COLOPHON

Title	Design aspects of submerged vanes
Author	J.A. van Zwol
Student no.	C9998340
Date	March 6, 2004
Version	Final version
Document	M.Sc. thesis, in partial fulfilment of the requirements for the degree of M.Sc. at Delft University of Technology
Contents	Report; Appendix A, B, C and D
Organisation	Delft University of Technology Faculty of Civil Engineering and Geosciences Section of Hydraulic Engineering http://www.tudelft.nl BUET-DUT linkage project partners: Bangladesh University of Engineering and Technology http://www.buet.ac.bd CICAT http://www.cicat.tudelft.nl WL | Delft Hydraulics http://www.wldelft.nl
Graduation committee	prof. drs. ir. J.K. Vrijling (Delft University of Technology) dr. ir. S. van Baars (Delft University of Technology) dr. ir. H.L. Fontijn (Delft University of Technology) ir. T.H.G. Jongeling (WL | Delft Hydraulics)
Accompanying documents	Zijlstra, R., J.A. van Zwol, 2003, *Measuring report; Experimental study of submerged vanes in the outdoor facility at BUET*, Delft University of Technology, The Netherlands

PREFACE

The document at hand is a thesis report in partial fulfilment of the requirements for the degree of M.Sc. at Delft University of Technology, Faculty of Civil Engineering and Geosciences. Last year, I was offered the opportunity to travel to Dhaka, Bangladesh, together with fellow-DUT student Robert Zijlstra, and to participate in an experimental study of submerged vanes in the framework of the BUET-DUT linkage project. In the period of March till June 2003, mobile bed tests were carried out in a straight rectangular flume by Robert Zijlstra, BUET-student Suman Saha and myself. The experiments were conducted in the outdoor facility at Bangladesh University of Engineering and Technology. Because the experiments were not preceded by earlier investigations and the experimental set up basically had to be built up from scratch, the task upon the researchers proved challenging, however, very rewarding and educative. In retrospect, my three-months stay in Bangladesh was by all means unforgettable, full of memories that I will cherish forever. Therefore, I would like to express my special thanks to Robert Zijlstra and Suman Saha for the successful co-operation and the great times spent together in Bangladesh.

I gratefully acknowledge the many useful comments and constructive suggestions of the members of my graduation committee: prof. drs. ir. J.K. Vrijling, dr. ir. S. van Baars, dr. ir. H.L. Fontijn and ir. T.H.G. Jongeling. Furthermore, I am very grateful to Jurriaan Lambeek for his guidance of the experiments during a couple of weeks and for the pleasant times spent both during and off working hours. I would also like to thank prof. M.M. Hossain for the fantastic co-operation, the staff of the fluid mechanics laboratory at BUET for their great assistance and Jahangir Alom for his aid before and during experimentation. Finally, I would like to thank C. Timmers and F. Post for support with regard to travel documents and accommodation, the Lamminga foundation for financial support, A. Felsenstein for hospitality extended to me during my stay in Bangladesh, and dr. ir. E. Mosselman, dr. ir. C.J. Sloff and dr. ir. H.L. Fontijn for advice during experiment preparations.

March 2004,

Boye van Zwol

SUMMARY

Submerged vanes are low aspect ratio flow-training structures mounted vertically on the riverbed at an angle to the prevailing flow. The vanes aim to generate a secondary circulation in the main flow and are designed to modify the near bed flow pattern and to re-distribute flow and sediment transport within the channel cross-section. Therefore, their application is related to riverbank protection, navigation and/or re-distribution of sediment and discharge.

In the last decades, many experiments have been conducted in the field of submerged vanes. Investigations by Odgaard and colleagues led to the development of design guidelines for vane systems. Results of recent studies, however, indicate that the theoretical relations by Odgaard et al. are subjected to shortcomings. The hypothesis can be raised that the theory of Odgaard does not account for the physics of the flow past submerged vanes adequately and consequently, fails to predict satisfactorily the lift and drag forces exerted on vanes (as found experimentally). Furthermore, the development of local scour at submerged vanes is still undefined, though of outmost importance to vane design.

In the period of March till June 2003, mobile bed tests were carried out in the outdoor facility at BUET, as part of an experimental investigation of submerged vanes in the framework of the BUET-DUT linkage project*. The experiments were designed to investigate the effects of vane height and angle of attack on scour development and flow field about a single thin, flat vane in steady flow through a straight flume of rectangular cross-section. Tested vanes were installed at angles of attack of 10°, 20°, 30° and 40° and at initial vane heights of 0.06 m. 0.12 m and 0.18 m. For all experiments, the vane length equalled 0.40 m. At vane location, the flow depth was kept at 0.30 m above initial bed level by a cross-section averaged velocity of 0.27 m/s. The model bed comprised fine sand with a median particle diameter of about 0.15 mm.

The results of near vane velocity measurements are used to test the hypothesis that the theory of Odgaard does not account for the physics of the flow past submerged vanes adequately. In analyses, it is found that flow separation occurs along the top edge as well as along the leading edge of the vanes. The primary vortex strengthens with increasing angle of attack. Findings with regard to the position of the centre of the vortex core in a cross-section through the trailing edge suggest that the primary vortex leaves from the surface of the suction side at a distance from the leading edge, which decreases with increasing angle of attack and increases with decreasing initial vane height. Vortex motion is seen to bring about modifications to the velocity distribution. The effect of re-distribution of the higher streamwise velocities toward the bed by vortex motion enlarges with increasing angle of attack. For tested vanes at angles of attack of 30° and 40°, the presence of the horseshoe vortex leg leaving from the trailing edge is identified, the strength of which decays within about twice the vane length downstream of the midst of the vane. Experimental results of the current research do not support the description of the flow past submerged vanes as presumed in the theory of Odgaard, in which the vortex sheet (resulting from an upward velocity component along the pressure side and a downward velocity component along the suction side) at the trailing edge rolls up to form a tip vortex springing from a position near the top of the vane. The hypothesis mentioned earlier seems well founded. The theory of Odgaard is developed for non-separated flow, where the strength of the circulation about the vane is calculated by assuming that the rear stagnation point is shifted to the trailing edge. Results of the current experiments demonstrate that the assumption that the circulation about the vane is established by the Kutta condition cannot be expected to hold for angles of attack higher than about 10°. In reality, significant flow separation occurs for vanes at conventional and higher angles of attack.

The main shortcoming of the theory of Odgaard with respect to prediction of the mean lift and drag forces exerted on a vane is that the model underlying the theory of Odgaard, the classical lifting line theory for finite wings by Prandtl, is inappropriate for low aspect ratio wings (and submerged vanes). Arguments that support the hypothesis that the theory of Odgaard does not account for the physics of the flow past submerged vanes adequately gave

* BUET: Bangladesh University of Engineering and Technology, Dhaka, Bangladesh; DUT: Delft University of Technology, Delft, The Netherlands.

rise to abandon the lifting line theory and to explore the analogy between submerged vanes and low aspect ratio wings. The characteristic feature of the flow about a slender low aspect ratio wing is the appearance of free shear layers that coil tightly about dividing surfaces of separation shed from the leading and side edges. It is seen that the vortical flows generated by submerged vanes and low aspect ratio wings show great similarities. It can be anticipated that the leading edge of a submerged vane plays an important role in the generation of the primary vortex.

Non-linear models based on theories for low aspect ratio wings by Bollay and by Gersten are derived for prediction of the mean lift and drag forces exerted on a sharp-edged slender vane protruding above a rigid bed. By the method of images, assuming that a single reflection of bound and trailing vorticity is sufficient to account for interference effect due to boundaries in an open channel, mathematical models are obtained that are equivalent to models by Bollay and Gersten. The mathematical models by Bollay and Gersten assume pre-determined shape and position of separated vortex flow over the lifting surface in the vortex wake, the latter of which is modelled as a wake composed of straight line vortices inclined at an angle to the lifting surface. The validity of the non-linear models is tested by comparison with experiment. It is concluded that the non-linear models give a decisive improvement on the theoretical relations for lift and drag developed by Odgaard et al. Use of the model based on theory by Bollay is advised for ratios of vane height to vane length lower than about 0.1. At higher ratios of vane height to vane length, the model based on theory by Gersten gives more accurate results. Due to lack of experimental results for higher ranges of angle of attack, the validity range is currently confined to an angle of attack of about 20°. Because the assumption that a single reflection of bound and trailing vorticity is sufficient to account for boundary interference effects breaks down with decreasing vane submergence, the ratio of vane height to flow depth should not be too high. The model based on Gersten is seen to hold approximately for ratios of vane height to flow depth up to at least 0.6.

The local scour depths at submerged vanes depend strongly on the alignment to the flow. At angles of attack of 30° and higher, it is observed that the strength of the horseshoe vortex leg along the pressure side is such that the vortex becomes effective in transporting material away from the scour hole. With increasing angle of attack, the location of maximum scour moves along the exposed side of the vane toward the trailing edge. At a ratio of vane height to flow depth of 0.4, maximum scour depths for angles of attack of 10° and 20° are seen to differ only marginally. However, for angles of attack of 30° and 40°, a strong increase in scour depth is observed. At an angle of attack of 20°, the maximum scour depth increases with increasing initial vane height; it appears that, at low and moderate angles of attack, the effect of induced downflow on scour depth becomes particularly appreciable if the ratio of initial vane height to flow depth is increased to higher than about 0.4. The use of scour relations for slender bridge piers to predict equilibrium scour depths for submerged vanes is evaluated, using scour relations for slender piers according to the CSU method and Breusers et al. In general, the agreement with experiment is rather unsatisfactory. For given test conditions, the CSU method is seen to predict the equilibrium scour depths better than the scour relation according to Breusers et al. The use of scour relations for slender bridge piers to calculate equilibrium scour depths at submerged vanes is not readily acceptable. The extreme values of ratio of length to thickness for submerged vanes do not relate to values for slender piers. In contrast to submerged vanes, bridge piers cause surface rollers, which weaken the downflow. Furthermore, scour relations for piers do not account for submergence, whereas results of the current research indicate that the dimensions of the scour hole depend on the initial vane height, at least for low angles of attack. At angles of attack of 30° and higher, the agreement between flows along the exposed sides of submerged vanes and bridge piers improves and thus, it may be expected that scour relations for bridge piers give more accurate predictions of equilibrium scour depths at submerged vanes at the higher ranges of angle of attack than at the lower ranges of angles of attack.

Vane efficiency can be expressed in terms of non-linear lift to drag. According to the model based on theory by Gersten, vortex lift and thus, the strength of the primary vortex increases non-linearly with increasing angle of attack. The increase in strength of the primary vortex is, however, accompanied with enlarged resistance to flow. Theoretically, the strength of the primary vortex also increases with decreasing ratio of vane height to flow depth. For vanes protruding relatively low above the bed, only a small ‘vortex cushion’ can be built up. More favourable conditions for the development of the primary vortex on the suction side exist for vanes protruding sufficiently high above the bed (ratio of vane height to flow depth lower than about 3 to 4) and for vanes at high angles of attack in deformable beds. If, for practical reasons, the initial vane height is bound to a relatively low maximum, it is advised to consider applying a higher angle of attack. Non-linear effects are larger for sharp-edged vanes than for vanes with rounded edges. An increase in the distance between pressure and suction side results in a decrease in tip flow and hence, a decrease in the strength of the primary vortex. It follows that submerged vanes should preferably be equipped with sharp leading and top edges and that the structural width should be reduced to a minimum. It is recognized that vanes require structural width, which may increase with increasing angle of attack as a result of enlarged load and scour depths. Furthermore, as a result of deficiencies associated with the form of the leading and top edges, profile drag and vane interaction, vane efficiency will generally be lower than predicted by the non-linear models based on theories by Bollay and Gersten. Therefore, the application of arrays of vanes at conventional angles of attack may not always lead to adequate and satisfying results.

The author feels that future experiments should concentrate on vanes at the higher ranges of angle of attack, despite enlarged scour holes, increased resistance to flow and the presence of additional vortical structures. At present, the extent to which the horseshoe vortex and possibly other vortices are counterproductive forces within the system governing the transverse transport of sediment has not been fully explored. Experimentally, it has been shown that these vortices decay downstream within a few vane lengths, while the primary vortex dominates over a much longer distance downstream of the vane. In case of a vane array, the strength of the horseshoe vortices in a state of equilibrium may be less than the strength of the horseshoe vortex for a single vane as the scour holes of neighbouring vanes may overlap. It is stressed that the suitability of scour holes to aid the intended purpose must not be ignored. To a certain degree, the presence of the scour hole leads to vortex stretching in transverse direction, thus increasing the effective width of each vane. It can be anticipated that for a system of vanes at high angles of attack both the transverse and longitudinal vane spacing may be enlarged. Hence, a smaller number of vanes may be sufficient to meet design objectives in terms of induced bed shear stresses than in the case vanes are laid out at conventional angles of attack. Furthermore, because of practical restrictions to minimum structural width and initial vane height, application of arrays of vanes at conventional angles of attack may not always lead to adequate and satisfying results. Finally, the effect of a vane system on induced change in energy slope is still uncertain and calls for further investigation. Existing relations need revision and improved relations are required to evaluate the effect of vane systems on resistance to flow.

TABLE OF CONTENTS

LIST OF SYMBOLS

a	=	function (Eq. 3.40)
a_{vn}, a_{vv}	=	universal constants tab. by Truckenbrodt (Eq. 5.47)
A	=	area covered by vane system
A, B, C	=	functions (Eq. 5.18)
AR	=	aspect ratio = b_w^2 / S_w
A_v	=	reciprocal vane density
A_{1n}, A_{2n}	=	universal constants tab. by Gersten (Eq. 5.66)
b	=	maximum span width; pier width (Eq. 6.2)
b_r	=	channel width
b_v	=	universal constants tab. by Truckenbrodt (Eq. 5.47)
b_w	=	wing span
B	=	function (Eq. 3.22)
c	=	chord length
c_D	=	sectional drag coefficient
c_L	=	sectional lift coefficient
c_v	=	universal constants tab. by Truckenbrodt (Eq. 5.47)
c_μ	=	mean chord length
C	=	Chézy coefficient
C_D	=	drag coefficient
C_L	=	lift coefficient
C_M	=	pitching moment coefficient
C_N	=	normal force coefficient
d	=	flow depth
$\overline{d}$	=	cross-section averaged flow depth
D	=	sediment grain size
E_{C_D}	=	estimated possible error in drag coefficient (Eq. 5.77)
E_{C_L}	=	estimated possible error in lift coefficient (Eq. 5.75)
f	=	Darcy-Weisbach friction factor
$f_1, f_2, .., f_6$	=	functions (Eq. 5.54)
F	=	function (Eq. 3.46)
$\overline{F}$	=	average measured force (Eq. 5.71)
F_D	=	drag force
F_L	=	lift force
F_N	=	normal force
Fr	=	Froude number
Fr_D	=	sediment Froude number
F_s, F_n	=	shear stress terms in s - and n - direction, resp.
$\overline{F_x}, \overline{F_y}$	=	average measured forces in streamwise and transverse direction, resp. (Eq. 5.72)
F_1, F_2, F_3	=	integrals (Eq. 5.10)
$F_1^{'}$	=	function (Eq. 5.18)
g	=	acceleration of gravity
g_1, g_2	=	functions (Eq. 5.59)
G	=	function (Eq. 3.30)
h_c	=	elevation of vortex core above bed (Eq. 3.38)
H	=	exposed vane height
i_b	=	slope of bed
i_w	=	slope of free water surface
$i(X, Z)$	=	influence function (Eq. 5.44)
I_1	=	Bessel function with imaginary order of 1 (Eq. 5.14)
I_1, I_2, I_3	=	integrals (Eq. 5.7)
$j(X, Z)$	=	influence function (Eq. 5.44)
J	=	linear operator (Eq. 5.51)
k	=	ratio $\overline{u}/u_b$; equivalent sand roughness
k_D	=	ratio of critical near bed velocity to critical shear velocity (Eq. 3.40)
K	=	function (Eq. 3.41)
K_i	=	factor (Eq. 6.4)
K_b	=	relative width factor (Eq. 6.4)
K_g	=	sediment grading factor (Eq. 6.4)
K_{gr}	=	interaction factor (Eq. 6.4)
K_s	=	pier shape factor (Eq. 6.4)
K_α	=	pier alignment factor (Eq. 6.4)
L	=	vane length
L_1, L_2	=	linear operators (Eq. 5.33)
m	=	friction parameter
m_H	=	lift curve slope coefficient for low aspect ratio rectangular wings by Helmbold
m_0	=	lift slope coefficient for thin airfoils
m_1, m_2	=	functions (Eq. 5.59)

N_n	=	number of vanes installed transversely at a distance of a water depth (Eq. 3.43)
r	=	distance from core axis (Fig. 3.1); radius of local curvature
r_i, r_o	=	innermost and outermost radii of curvature (Eq. 3.44)
r_0	=	depth-averaged turbulence intensity in streamwise direction
R	=	hydraulic radius
Re	=	Reynolds number
s	=	downstream co-ordinate (Fig. 3.1)
S	=	surface area
S_w	=	wing planform area
S_X, S_Y	=	standard deviation measured forces in streamwise and transverse direction, resp.
$t_{A,e}$	=	time at which $y_A = y_{A,e}$ (Eq. 6.1)
T_c	=	centrifugal force torque about section centroid (Eq. 3.44)
T_v	=	vane-induced torque about section centroid (Eq. 3.44)
u, v, w	=	time-averaged velocity components in s-, n- and z-directions, resp. (Fig. 3.1)
u, v, w	=	induced velocity components in x-, y- and z-direction, resp. (Section 5.3.2)
$\bar{u}, \bar{v}$	=	depth-averaged values of u and v
$\overline{u_H}$	=	vane height-averaged approach velocity (Eq. 5.72)
u_*	=	shear velocity
U, V, W	=	time-averaged velocity components in X-, Y- and Z-directions, respectively (Fig. 1.1)
U_∞	=	uniform free stream velocity
v_θ	=	tangential velocity component perpendicular to core axis (Fig. 3.1)
$\overline{w_x}$	=	chord-averaged tangential component of induced velocity (Eq. 5.19)
w_{x1}	=	tangential component of induced velocity due to bound vortices (Eq. 5.2)

w_{x2}	=	tangential component of induced velocity due to trailing vortices (Eq. 5.3)
w_{y1}	=	normal component of induced velocity due to bound vortices (Eq. 5.2)
w_{y2}	=	normal component of induced velocity due to trailing vortices (Eq. 5.3)
$x_{c/4}$	=	position of quarter-chord (Eq. 5.48)
y_A	=	scour depth at location A (Eq. 6.1)
$y_{A,e}$	=	equilibrium scour depth at location A (Eq. 6.1)
$y_{m,e}$	=	maximum equilibrium scour depth
z	=	vertical co-ordinate (Fig. 3.1)
z_0	=	level of zero velocity (Eq. 4.1)
α	=	angle of attack with respect to mean flow
α'	=	angle with tangent of channel centreline
α_i	=	induced angle of attack
α_{loc}	=	local angle of attack
β	=	factor associated with area-averaging
γ	=	vorticity distribution; coefficient (Eq. 6.1)
γ_0	=	constant (Eq. 5.8)
γ_1	=	linear part of vorticity distribution
γ_2	=	non-linear part of vorticity distribution
δ	=	deflection angle
δ_s, δ_n	=	vane spacing in streamwise and transverse direction, resp.
Δ	=	specific weight of submerged sediment
ε	=	eddy viscosity
θ	=	effective angle of inclination with respect to plate (Eq. 5.3)
Γ	=	strength of circulation
θ_{cr}	=	critical Shields stress
κ	=	Von Karman constant
λ	=	vane interaction coefficient
μ_F	=	actual average force (Eq. 5.71)
ξ	=	downstream distance along vortex line (Eq. 3.38)
ρ	=	fluid density
ρ_s	=	sediment density

σ_u	=	standard deviation of streamwise velocity component
τ	=	shear stress
$\bar{\tau}$	=	area-averaged shear stress
ϕ	=	angle of river bend
ω	=	ratio of projected area to volume for sediment particle normalized by ratio for sphere (Eq. 3.40)

Subscripts

b	=	near bed value
c	=	channel centreline value
i	=	induced
LE	=	leading edge value
n	=	transverse component
s	=	streamwise component; surface value
TE	=	trailing edge value
v	=	vane
0	=	initial, cross-section averaged, pre-vane parameter

1 INTRODUCTION

1.1 SUBMERGED VANES

Submerged vanes are low aspect ratio flow-training structures mounted vertically on the riverbed at an angle to the prevailing flow. The vanes aim to generate a secondary circulation in the main flow and are designed to modify the near bed flow pattern and to re-distribute flow and sediment transport within the channel cross-section. Therefore, the applicability of vanes is related to riverbank protection (protection against stream bank erosion), navigation (amelioration of shoaling in navigation channels) and/or re-distribution of sediment and discharge (exclusion of sediment from water intake structures) [14; 37; 39; 40; 42; 53]. Recently, experiments have been undertaken to investigate the potentials of vanes as means of beach protection [29]. Similarly to river-training applications, the vanes focus on the cause of sediment transport affecting mainly the long shore current velocity and, thus, slowing down the longitudinal transport rate locally.

Secondary or spiral flows result from unequally distributed transverse forces on the flow and are observed in channel bends, but can also be induced by structures installed at an angle of attack to the primary flow. The transverse sediment transport associated with spiral flow in river bends often is a major concern to river engineers as negative consequences with respect to navigability, riverbank protection and channel movements (river meandering) arise. Transverse morphological changes will not occur if secondary flows could be negated. Similarly, by introducing a secondary flow regime in a straight channel, channel bed changes can be forced in favour of – for example – water intakes. Vane-generated torques produce transverse shear stress components over a certain downstream bed area, which, in turn, induce transverse slopes on the bed. The popularity and use of submerged vanes have increased in the last decades compared to more traditional river-training structures as dikes and groins. Due to their relatively small structural dimensions and preferable orientation in the flow field, vanes are often a more flexible and cost-efficient alternative to achieve the required modifications of the flow field, while inducing less flow resistance.

1.2 STATE OF THE ART

Many experiments in the field of submerged vanes have been conducted in the last decades. Particularly researches by Odgaard and colleagues have drawn a great deal of attention, mainly because these investigations led to the development of design guidelines for vane systems. Results of recent studies [11; 24; 30], however, indicate that the theoretical relations developed by Odgaard et al. are subjected to shortcomings. From comparisons between measured and calculated lift and drag forces, Flokstra, De Groot and Struiksma and later Jongeling and Flokstra concluded that the theory of Odgaard fails to predict the forces exerted on a submerged vane satisfactorily, which supports the hypothesis that the existing theory does not account for the physics of the flow past a vane adequately. Although Odgaard and Spoljaric conducted experiments for vanes at low angles of attack exclusively, they stated that a low angle of incidence is advantageous over high angles of attack, which supposedly lead to unacceptably large scour holes [37]. Marelius and Sinha rightfully reminded the reader that continuously evolving flow fields and topographical features may result in vanes at higher angles of attack than originally intended. Experimentally, Marelius and Sinha found that the strength of the vane-induced primary vortex is a maximum for an angle of attack of 40° (under test conditions described in Section 2.3.4) and discerned a system of as many as two suction vortices and two horseshoe vortex legs in the direct vicinity of the vane.

The theory of Odgaard is developed for non-separated flow past vanes and holds for a restricted range of angle of attack only as flow separation occurs already at relatively low angles of attack. Efforts should be undertaken to achieve improved theoretical descriptions of the flow physics and consequently of the lift and drag forces exerted on vanes for a much wider range of angle of attack. Because changes in energy slope depend on induced flow resistance, a particular interest in the drag coefficient may exist in cases of mildly sloped rivers. At present, the development of local scour around submerged vanes is still undefined, though of outmost importance to vane design. The foundation should be able to sustain the maximum scour depth at the vane. In Bangladesh, failure of submerged vanes often occurred as a result of excessive scouring [20].

1.3 EXPERIMENTS BUET-DUT LINKAGE PROJECT

On September 16, 2000, the set-up of research topics in the third phase of the BUET-DUT[1] linkage project, one of which is the experimental investigation of the effect of vanes on river flow and morphology, has been discussed in a workshop. On October 6, 2001, the approach of the research with regard to submerged vane has been further discussed. The discussion resulted in a research proposal that is agreed upon by all parties involved. The main objective of the research is to increase knowledge of the hydraulic and morphologic processes around vanes. Hence, the design of vanes can be improved and the risks with regard to the expected performance of vanes for the purpose of river training can be reduced. Furthermore, the research aims to investigate whether the hydraulic and morphologic processes can be reproduced with the aid of a mathematical model (Delft-3D) [7; 8].

In the period of March till June 2003, researchers Saha, Zijlstra and Van Zwol conducted movable bed experiments in a straight flume of rectangular cross-section (flume width: about 2.45 m) at the outdoor facility at BUET. The experiments were designed to investigate the effects of initial vane height and angle of attack on scour development and flow field around a single thin, flat vane and on development of vane-induced accretion/erosion patterns farther downstream. By a discharge of 200 l/s, the cross-section averaged velocity in the flume equalled 0.27 m/s. At vane location, the water level was kept at 0.30 m above average initial bed level. The model bed comprised fine sand (median particle diameter: about 0.15 mm; see sieve curves in [57]). Throughout the experiments, sediment has been fed at the upstream of the flume by necessity. The midst of the tested vane was placed in the flume centreline at about 15 m from the upstream end of the flume (in X,Y-co-ordinates [cm]: 1500.0; 0.0). Figure 1.1 displays the co-ordinate system used during experimentation and the directions of positive velocity components.

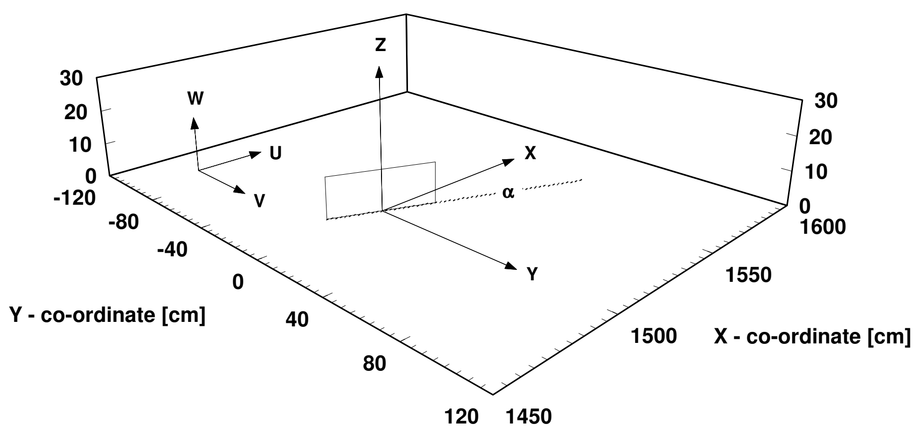

Figure 1.1: Co-ordinate system for experiments BUET-DUT linkage project

Experiment ID	$H_{v,0}$ [m]	α [degr.]
EXP.A1	0.12	10
EXP.A2	0.12	20
EXP.A3	0.12	30
EXP.A4	0.12	40
EXP.B2	0.06	20
EXP.B3	0.06	30
EXP.C2	0.18	20

Table 1.1: Vane dimensions and orientation

Table 1.1 presents dimensions and orientation of the tested vanes. For all experiments, the length of the tested vane equalled 0.40 m. Experiment series letters A, B and C indicate the initial vane height (A: 0.12 m; B: 0.06 m and C: 0.18 m), while the number following the series letter A, B or C indicates the angle of attack (1: 10°; 2: 20°; 3: 30° and 4: 40°). For example: for EXP.B2, the vane has been installed at an initial vane height of 0.06 m and an angle of attack of 20°. Reference is made to the measuring report [57] for more information.

[1] BUET: Bangladesh University of Engineering and Technology, Dhaka, Bangladesh; DUT: Delft University of Technology, Delft, The Netherlands.

1.4 DEFINITION OF PROBLEM

- On account of the results of recent experiments [11; 24; 30], the extent to which theoretical relations developed by Odgaard et al. are able to accurately predict the lift and drag forces exerted on submerged vanes is under discussion, so that application of the theory by vane design is possibly not or less appropriate.
- The theory of Odgaard applies for a restricted range of angle of attack only, while recent investigations [30] demonstrated that vanes at higher angles of attack lead to stronger vane-induced vortices. In certain situations, vanes at non-conventional angles of attack may, despite an increase of the load on a single vane, result in a more economical design by a reduction of the size of the vane field.
- Although local scour plays an important role by vane design, hardly any information is available about scour development at submerged vanes and the effects of local scour on the flow past vanes at initial vane height and angle of attack.

1.5 RESEARCH OBJECTIVES

- Validation of the capability of theoretical relations developed by Odgaard et al. to predict the lift and drag forces exerted on a submerged vane.
- Survey of the shortcomings of the existing theory of Odgaard and the effects of these shortcomings on vane design.
- Development of alternative relations for the lift and drag forces exerted on a submerged vane, striving for improvement of the capability to predict the lift and drag forces and enlargement of the range of angle of attack for which the relations hold.
- Evaluation of relations to predict scour depths for submerged vanes at initial vane height and angle of attack.

1.6 OUTLINE

In broad outlines, the contents of this report follow a path delineated by a cyclic model commonly applied in experimental studies, where results of comparisons between measured and predicted values are used to validate a theoretical model. As shown in Figure 1.2, analyses shall first concentrate on the characteristics of the flow past a submerged vane. Knowledge of the actual flow physics is essential when pursuing improved relations for the hydrodynamic forces exerted on a vane. For that purpose, the existing and widely adopted theory of Odgaard (Chapter 3) is used as a reference and a means to compare experimental results with. Hypothetically, the theory, which is based on the classical lifting line theory for finite wings, does not account for the flow physics in the direct vicinity of a submerged vane adequately and consequently fails to predict satisfactorily the lift and drag forces exerted on the vane (as found experimentally). The effects of vane height and angle of attack on the near vane flow field are investigated in analyses of the velocity measurements for the current experiments (Chapter 4). Results of the analyses and observations in previous experiments indicate that the model underlying the theory of Odgaard (Prandtl's lifting line theory) is inappropriate to describe the effects of flow physics in the direct vicinity of submerged vanes. A better perception of the flow about submerged vanes can be obtained by adopting advancements in aerodynamics for low aspect ratio wings. Thus, the effects of vane height and angle of attack may be better understood. In Chapter 5, the shortcomings of the theory of Odgaard with regard to the lift and drag forces are enumerated and new models are derived based on theory for low aspect ratio wings developed by Bollay and by Gersten. Using measurements of the forces acting on a vane protruding above a rigid bed by Odgaard and Spoljaric [35; 38], by Flokstra, De Groot and Struiksma [11] and by Jongeling and Flokstra [24], the validity of these non-linear models for the mean hydrodynamic forces is tested. In the remaining sections in Chapter 5, the effects of parameters on the flow past submerged vanes (and thus the effects on the mean forces exerted on the vanes) are investigated and attention is paid to pressure distribution and spread in lift and drag forces. At present, there is a lack of information about scour around submerged vanes, particularly at high angles of attack. Referring to the lack of experimental data for vanes, Hoffmans and Verheij [19] proposed to use scour relations for slender bridge piers aligned to the flow to predict equilibrium scour depths for submerged vanes. The local scour analyses in Chapter 6 concentrate on the effect of vane height and angle of attack on local scour. A description is given of the scour development as observed for the tested vanes and the use of scour relations for slender piers to predict scour depths at submerged vanes is evaluated. Based on the analogy between submerged vanes and low aspect ratio wings, support for which is given by the validity of the non-linear models for lift and drag forces, a great number of recommendations with regard to the design of vanes can be specified (Chapter 7). When translating analytical results to prototype conditions, it has to be kept in mind that the non-linear models apply to thin, flat vanes with sharp leading and top edges, while prototype vanes can have substantial structural widths. Furthermore, the effects of local scour, which do not necessarily have to be detrimental to the strength of the vane-induced vortices, should be taken into account. At present, no information is available about the effectiveness of an array of vanes at high angles of attack, while, despite enlarged scour hole dimensions, increased flow resistance and the formation of additional vortical structures, vanes at the higher ranges of angles of attack should receive more attention in future experiments as analyses suggest that vanes at high angles of attack may be more effective than vanes at conventional angles of attack. Elaborating on the path outlined by the cyclic model, efforts should be undertaken to modify the theory of Odgaard by implementing improved relations for the hydrodynamic coefficients and consequently for the strengths of the vane-induced vortices. Finally, conclusions and recommendations are summarized in Chapter 8.

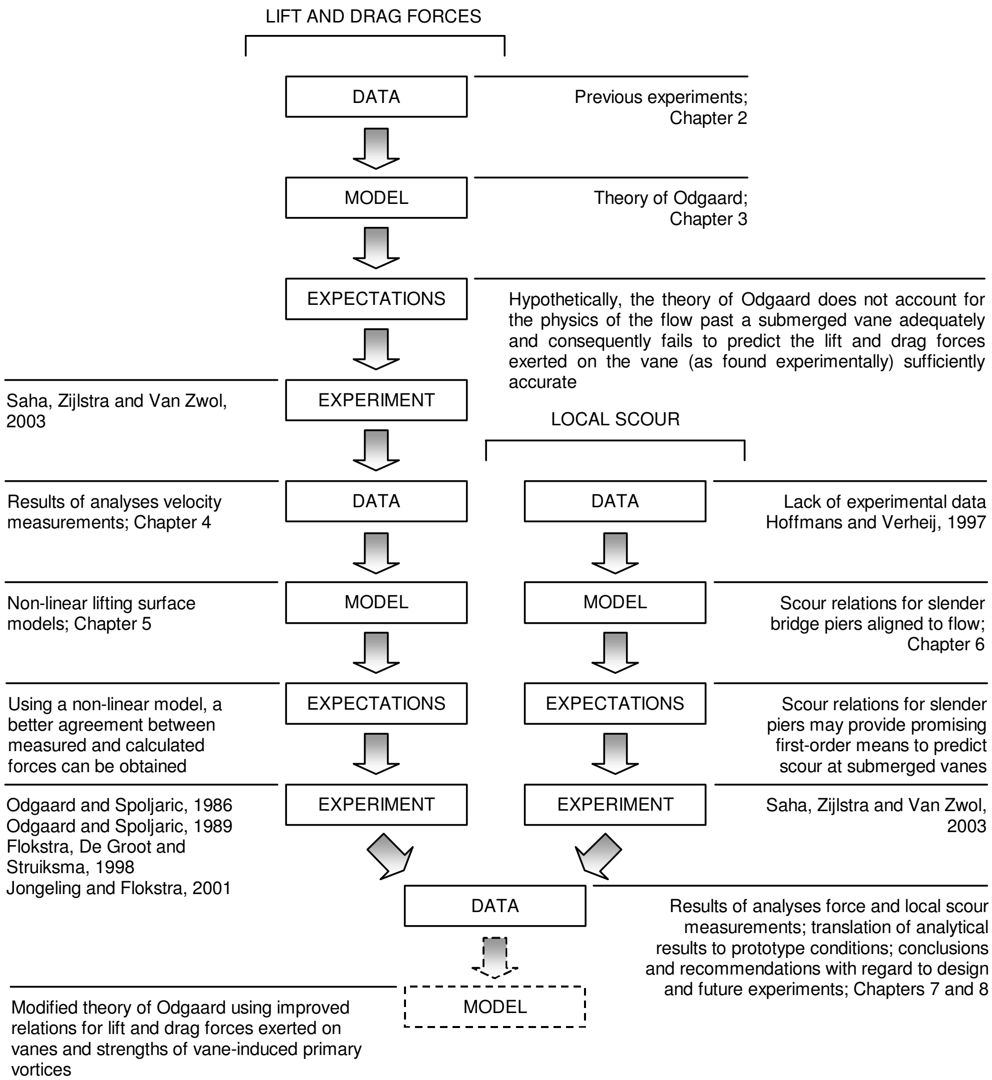

Figure 1.2: Outline

2 PREVIOUS EXPERIMENTS

2.1 INTRODUCTION

Many researches in the field of submerged vanes have been conducted in the last decades. Especially researches by Odgaard and colleagues have drawn a great deal of attention. His theory, based on experimental research [35; 38; 39; 41], is widely adopted by design of submerged vanes for flow and sediment control. The early and most recent design guidelines developed by Odgaard and colleagues are described in Chapter 3. Herein, summaries are presented of experiments of importance to the current research.

2.2 FIXED BED EXPERIMENTS

2.2.1 Odgaard and Spoljaric, 1986

Odgaard and Spoljaric developed a relation between vane characteristics and lift force acting on a low aspect ratio foil assuming that the lift force is a function of dynamic pressure, vane profile, aspect ratio, relative vane height and angle of incidence [35]. The validity of the developed relation has been tested experimentally with force measurements, by which tested vanes were mounted on a measuring frame. Different vane profiles were tested. However, Odgaard and Spoljaric only presented the results for a flat-plate vane with an aspect ratio of 0.3 at angles of attack of 5°, 10°, 15° and 20° and ratios of flow depth to vane height of 2, 3 and 4. The measured lift coefficients generally exceeded the theoretical values, by which deviations from theoretical lift coefficients increased with increasing angles of attack. Furthermore, an increase in lift coefficient was observed with increasing ratio of water depth to vane height, supposedly due to the nearness of the free water surface. Odgaard and Spoljaric concluded that the flat-plate vane is the least efficient vane shape in terms of lift force generated per unit lifting surface area.

2.2.2 Odgaard and Spoljaric, 1989

Odgaard and Spoljaric presented design bases for sediment control in straight (shoaling amelioration) and curved channels (river bend bank protection) [38]. Force experiments were conducted for thick and thin flat-plate vanes and cambered vanes with and without twist. Tested parameters were ratio of water depth to vane height, angle of attack, Froude number and vane shape. A relatively good agreement between measured and calculated lift and drag coefficients was found, except for thick, flat vanes. Furthermore, Odgaard and Spoljaric concluded that cambering and twist do not improve the lift characteristics. By dye injections, a more pronounced boundary layer separation was observed around cambered vanes than around thin, flat vanes. Referring to this observation, Odgaard and Spoljaric explained the less favourable measured lift characteristics of cambered vanes by stating that flow separation reduces the pressure difference between pressure and suction side and thus reduces lift. Also, the vertical lift component generated by the twisted vane could not be measured in their set-up [38]. The measured lift coefficients for thick, flat vanes were 25 to 40% lower than the predicted lift coefficients. Supposedly, an increase of vane thickness causes an increase of the size of the separation zone on the rear side of the vane and thus a decrease of lift. Odgaard and Spoljaric concluded that if, for practical reasons, a vane must be constructed with thickness, an airfoil shape would be most effective. Force measurements confirmed that the lift coefficient increases with decreasing ratio of water depth to vane height, supposedly due to the suppression of the tip vortex by the free surface, which results in an increase of the pressure difference between the vane surfaces. No measurable dependence of the drag coefficient on the ratio of flow depth to vane height was found [38]. Furthermore, the experimental results did not suggest a Froude number dependence under the tested flow conditions (ratio of flow depth to vane height lower than 2 and Froude numbers lower than 0.25).

2.2.3 Flokstra, De Groot and Struiksma, 1998

Because the theory developed by Odgaard et al. suggests that vane efficiency is only weakly dependent on vane length, while vane length is an important parameter with respect to construction costs, experiments have been conducted at WL | Delft Hydraulics, in which the lift and drag forces acting on sheet-wall and flat-plate vanes at an angle of attack of 17.5° have been measured [11]. For that purpose, the tested vanes were mounted on a frame, to which three force sensors were attached. In an undistorted model of the hydraulic conditions in the River Waal near Hulhuizen, The Netherlands (length scale: 25; roughness gravel bed: about 45 $m^{0.5}/s$; average flow velocity; 0.28 m/s; flow depth: 0.30 m), vanes at lengths of 0.24 m, 0.32 m, 0.40 m and 0.48 m were tested (vane height: 0.06 m). Additionally, the effect of upstream vanes on the hydrodynamic forces was tested. A strong variation of the lift force with time was observed: $0.3\overline{F_L} \leq F_L \leq 2.0\overline{F_L}$, in which $\overline{F_L}$ represents the time-averaged measured lift force (by a measuring duration of 120 seconds). From a comparison between measured and theoretical lift and drag coefficients, Flokstra, De Groot and Struiksma concluded that the measured lift and drag forces acting on the thin, flat vanes exceeded the theoretical values of the lift and drag forces by a factor 2 and 4, respectively. Furthermore, the experiments demonstrated that the lift and drag forces depend more strongly on vane length than the existing theory suggests. The lift and drag forces exerted on sheet-wall vanes were about 20% lower and 30 to 40% higher than the lift and drag forces acting on the thin, flat vanes, respectively. The shape of the trailing edge appeared to have a measurable effect on the lift force. Upstream vanes can affect lift and drag forces exerted on a submerged vane significantly, depending on the orientation of the upstream vane field.

2.2.4 Jongeling and Flokstra, 2001

Complementary to the studies described in Section 2.2.3, experiments have been conducted at WL | Delft Hydraulics to investigate the effect of vane height on the lift and drag forces exerted on sheet-wall and flat-plate vanes (test conditions as described in Section 2.2.3) [24]. Force measurements have been taken for vanes at heights of 0.03 m, 0.06 m, 0.09 m and 0.12 m (vane length: 0.40 m; angle of attack: 17.5°), accompanied with measurements of horizontal velocity components near and farther downstream of the tested vanes. The measured forces varied strongly with time: $0.2\overline{F_L} \leq F_L \leq 2.1\overline{F_L}$ and $0.6\overline{F_D} \leq F_D \leq 1.7\overline{F_D}$, in which $\overline{F_L}$ and $\overline{F_D}$ represent the time-averaged measured lift and drag force (by a measuring duration of 120 seconds), respectively. From a comparison between measured and calculated lift and drag coefficients for the thin, flat vanes, Jongeling and Flokstra concluded that the measured lift coefficients were a factor 1.7 to 2.5 higher than the theoretical lift coefficients, while the measured drag coefficients were a factor 2.3 to 3.8 higher than the theoretical drag coefficients. The lift and drag forces acting on sheet-wall vanes were about 10% lower and up to 50% higher than the lift and drag forces acting on equal-sized thin, flat vanes, respectively. The effect of the vane-induced circulation on the near bed transverse velocity component is stronger and extends farther downstream with increasing vane height. In the area directly downstream from the vane, however, small vanes may locally generate a higher near bed transverse velocity component than taller vanes. In general, the near bed transverse velocity component induced by thin, flat vanes is up to 10% higher than in case of sheet-wall vanes. The existing theory underestimates the maximum near bed transverse velocity component in the area directly downstream from the vane. Further downstream, the theory respectively underestimates and overestimates the effect of small and tall vanes on the near bed transverse velocity component. Analyses demonstrated that the theoretical relations developed by Odgaard et al. are unable to predict the lift and drag forces sufficiently accurate. The near bed transverse velocity component can be predicted more satisfactorily, but the predictability is still mediocre.

2.3 MOBILE BED EXPERIMENTS

2.3.1 Odgaard and Spoljaric, 1986

Odgaard and Spoljaric examined the effect of vanes on flow and bed topography in a straight, rectangular channel and developed relations to describe velocity and depth distribution (see Section 3.4) [37]. Herein, the streamwise variation of the transverse velocity component is obtained from the transverse component of the momentum equation, of which the solution is simplified by assuming a linear transverse velocity profile and a parabolic eddy viscosity profile. The effect of vanes on bed topography is obtained from a transverse force balance for sediment particles on the bed surface [36], which relates the transverse velocity component to the transverse vane-induced bed slope. The developed relations describing the velocity distribution downstream from a vane have been tested in a straight, rectangular flume (sediment: sand with median particle diameter of 0.4 mm; ratio of vane height to length of about 0.35 and positioned in the centreline at angles of attack of 10° to 20°) at lower than incipient motion velocities. The sand around the vane was given a light cement cap to avoid local scour. Near the vane a distinct s-shaped transverse velocity profile was observed, approaching a linear shape farther downstream. The measured near bed transverse velocity component in the centreline at a distance of a water depth downstream from the trailing edge indicated that downwash and hence, reduction of the effective angle of incidence due to vortices trailing the upper edge of the vane was negligible. A slightly faster than predicted rate of decay of the near bed transverse velocity component was observed, which may have been due to vane-induced turbulence not accounted for in the developed relations. Additionally, the effectiveness of a single vane (sediment: sand with median particle diameter of 0.4 mm; vane: positioned in the centreline at an angle of 15°; ratio of vane height to length: 0.4; ratio of flow depth to vane height: 2; cross-section averaged flow velocity: 0.30 m/s; bed survey after 5 hours of running) and lateral arrays of vanes in modifying the bed topography was tested in straight, rectangular flumes at higher than incipient motion velocities. Measured bed profiles have been compared to predicted bed profiles. The streamwise rate of decay of the near bed transverse velocity component was determined by means of strategic velocity measurements. Finally, a series of experiments have been conducted with streamwise symmetric vane arrays designed to generate a depth increase in the centre portion of the channel by means of counter rotating secondary circulations to study the potentials of vanes as means of providing and maintaining depth in navigation channels. Odgaard and Spoljaric concluded that the optimum angle is about 15°, because at angles higher than about 15°, flow separation becomes significant and excessive local scour occurs. It was stated that vane systems designed according to the developed guidelines succeed in generating depth changes by transporting sediment sideward rather than downstream without changing overall channel characteristics and cross-sectional area.

2.3.2 Odgaard and Wang, 1991

To test the theoretical design basis described in Section 3.2, Odgaard and Wang conducted experiments in curved and straight sediment-recirculating channels of rectangular cross-section (sediment: sand with median particle diameter of 0.41 mm) [42]. In the straight channel, vanes (initial vane height: 7.4 cm; vane length: 15.2 cm) were installed in arrays of four vanes, angled 20° toward the bank. In the curved flume, vanes (double-curved foils with a slight twist; initial vane height: 7.4 cm; vane length: 15.2 cm) were positioned in arrays of two or three vanes, angled 15° toward the outer bank. Measured and predicted velocity and depth distributions, with and without vanes, have been compared and showed good agreement. In the curved flume (discharge: 0.14 m^3/s; average flow depth: 17.8 cm), the vanes reduced the near bank values of depth and velocity from about 1.3 and 1.2 times the cross-section averaged values respectively to essentially the cross-section averaged values. In the straight flume (discharge: 0.15 m^3/s; average flow depth: 18.2 cm), the vanes reduced the depth near the right bank (in the vane field) by about 50% and increased the depth near the left bank by 20 to 30%. Importantly, vane-induced changes in the tests in both curved and straight flume occurred without significant changes of the surveyed bed area and of the longitudinal water surface slope (less than 10%), implying that vanes do not cause changes of the sediment transport capacity upstream and downstream from the vane field. It was also observed that the vane-induced redistribution of sediment within a cross-section is an irreversible process: a reduction in discharge does not result in a reduction in the volume of sediment accumulated in the vane field due to a too low sediment transport capacity at lower discharges.

2.3.3 Wang and Odgaard, 1993

Wang and Odgaard analysed the results of experiments for single vanes, vane pairs and vane arrays (angle of incidence: 20°; ratio of vane height to length: 0.5; ratio of vane height to flow depth: 0.5) in open sand bed channels [53]. From comparison between measured and calculated transverse velocity components, Wang and Odgaard concluded that the vane-induced transverse velocity is well represented with a Rankine-vortex type provided boundary effects and vane interference are taken into account. The measured maximum near bed transverse velocity component near the trailing edge of a single vane in a straight, rectangular flume is slightly more than the calculated velocity (using six vortex images). An explanation for the difference between measured and calculated transverse velocity is that the calculated transverse velocity does not include a contribution from the bound vortex (vertically around the vane). Using the depth-averaged eddy viscosity corresponding with the measured friction factor, the rate of decay of the vortex was simulated. Possibly because the calculation did not account for vane-generated eddy viscosity, the observed rate of decay exceeded the calculated rate. In tests with smaller relative vane heights, it was observed that the axis of the vortex tends to re-locate at mid-depth with increasing distance from the vane. Owing to the relatively large viscous near bed dissipation, the transverse velocity near the water surface becomes nearly equal in magnitude to the near bed velocity. As a result of the vortex motion, the streamwise velocity profile within a vane field is distorted relative to the profile in an ordinary open channel flow. Wang proposed an empirical relation in the form of a modified power-law velocity profile. Additionally, Wang derived equations using the depth-averaged, streamwise momentum equation to describe adjustments of the streamwise velocity resulting from transverse transport of momentum due to vortex motion, viscous diffusion and added flow resistance in the vane-covered area.

2.3.4 Marelius and Sinha, 1998

Although Odgaard and Spoljaric conducted experiments for vanes at low angles of attack exclusively, they concluded that a low angle of attack is advantageous over high angles of attack, which lead to unacceptably large scour holes [37]. In [30], Marelius and Sinha rightfully reminded the reader that continuously evolving flow fields and topographical features may result in vanes at higher angles of attack than originally intended. Furthermore, they state that the highly idealized analysis of flow through a fixed bed presents an overly simplified picture of the situation in the field. The suitability of relatively large scour holes to aid the intended purpose of the vanes has not been fully explored in previous studies. Marelius and Sinha investigated the characteristics of the flow field around vanes at low to high angle of attack in a straight flume of rectangular cross-section (sediment: uniform fine sand with a median particle diameter of 0.9 mm; flow velocity: about 90% of the critical velocity for bed sediment entrainment; flow depth: 0.40 m). Their study indicated that angles of attack between 25° and 50° should be considered too, since high angles of attack – compared to low angles of attack – lead to an acceleration of scour development and to stronger vane-induced vortices in the flow field. To obtain an approximate estimate of the optimum angle of attack, tests were conducted for thin, flat vanes (ratio of vane height to length: 0.5; ratio of vane height to flow depth: 0.3) at angles of attack of 25°, 36°, 45° and 57° for a minimum running time of 36 hours to allow for the formation of stable scour holes before detailed 3D-velocity measurements were taken at cross-sections at the trailing edge and at 0.48 m downstream from the midst of the tested vane. Marelius and Sinha chose the momentum of momentum at the downstream cross-section as a representative measure of the vortex strength and found an optimum angle of 40°. Finally, an experiment was conducted for a vane at the established optimum angle of attack by a total running time of 72 hours before detailed 3D-velocity measuring, taken at cross-sections spaced every 5 cm in the area of 0.40 m upstream and downstream of the midst of the tested vane. As opposed to the popularly assumed single vortex for low angles of attack, Marelius and Sinha found as many as two suction side vortices and two counter rotating horseshoe vortex legs in the immediate vicinity of the vane. The leading edge vortex leg decays quickly, while the trailing edge vortex leg persists over a longer distance. The stagnation line (defined by the change in direction of the transverse velocity component) on the pressure side near the upper edge is close to the leading edge of the vane. Hence, the trailing edge vortex leg is affected by a larger part of the pressure area than the leading edge vortex leg. Furthermore, the leading edge vortex leg is affected more by the low-pressure area at the suction side, which disrupts the circulation. In the direct vicinity of the vane, the combined effects of the system of vortices govern the transverse transport of sediment, where the weaker clockwise suction vortex is considered a small counterproductive force against transverse sediment movement. Farther downstream, only the primary vortex is effective. The rate of decay of the strength of the vortices was examined by calculating the moments of momentum at each cross-section with contributions of the transverse and vertical velocity components. As the flow leaves the scour hole, the primary vortex becomes ellipsoidal due to compression in vertical direction by the shoaling bed (vortex stretches in width-direction, thus increasing the effective vane-covered area). The contribution of the transverse velocity component to the moment of momentum decays exponentially, while the contribution of the vertical velocity component is dependent on shoaling and shows an almost linear decay.

2.4 FIELD TESTS

2.4.1 Odgaard and Mosconi, 1987

Odgaard and Mosconi developed a design basis for vane systems emplaced along the outer banks in river bends to counter the flow spiral and to direct the near bed current outward to the bank (see Section 3.4.2) [39]. The total lifting surface area required per unit surface area of channel bed results from equating the centrifugally induced torque to the vane-induced torque about the section centroid. The validity of the design procedure has been tested and verified in a curved, sediment-recirculating flume. Experimental results suggested that the relative vane height should remain in the range from 0.2 to 0.5 at all erosion causing stages. Vane length should be of the order of three to four times the vane height and vanes should be installed at an angle of 10° to 15° with the mean flow direction at bankfull flow. Furthermore, the transverse spacing of vanes and the distance from the outermost vane to the bank should be less than about twice the flow depth at bankfull flow. The design procedure was applied for a vane system in a bend of the Nishnabotna River, Iowa, USA. Odgaard and Mosconi described design and installation of the East Nishnabotna system, evaluated the performance and gave recommendations with regard to improvements to vane system designs. In retrospect, the vane system (though the design could have been improved) has effectively stabilized bed topography and reduced the channel migration rate by preventing near bank scour, reducing transverse bed slopes at high flows and reducing and redirecting near bank velocities.

2.4.2 Odgaard and Wang, 1991

In [42], Odgaard and Wang enumerated successful field installations (East Nishnabotna River, Iowa, USA; River Kuro, Japan [14]; Wapsipinicon River and Cedar River, Iowa, USA). The effectiveness of submerged vanes in ameliorating shoaling problems is demonstrated in the West Fork Cedar River, where the river was straightened and widened because of the construction of a bridge. In the course of time, the excavation upstream from the bridge had filled in and became vegetated. Subsequently, a sandbar developed causing the river to flow toward the bridge abutment, where it undermined and eroded the bank. Annual dredging was necessary to prevent the sand bar from growing larger. A system of vanes consisting of vertical sheet piles driven into the streambed and aligned at an angle of 20° with the mean flow direction was installed upstream from the bridge. As flow depth and velocity decreased along the previously eroding bank and increased along the centreline of the river, the design proved to be successful and permanent, while relatively inexpensive with regard to installation and maintenance costs.

3 THEORY OF ODGAARD

3.1 INTRODUCTION

Pursuing improved relations for the lift and drag forces exerted on a submerged vane, the existing and widely adopted theory of Odgaard may be used as a reference and a means to compare experimental results with. Hypothetically, the theory, based on the classical lifting line theory for finite wings by Prandtl, does not account for the flow physics in the direct vicinity of a submerged vane adequately and consequently fails to predict satisfactorily the lift and drag forces exerted on the vane (as found experimentally). Section 3.2 presents the most recent model for the design of a vane field developed by Odgaard and Wang [41; 52; 53]. In Section 3.3, the main design parameters according to Wang and Odgaard are identified. It is seen that a key role is attributed to the lift coefficient. Because the theory applies to channels of arbitrary planform, it is more general than models described in earlier publications [37; 39]. Furthermore, the theory developed by Odgaard and Wang accounts for vane interaction. However, compared to early models, the model is more complex, thus less suitable for preliminary design calculations. Therefore, the early models developed by Odgaard and Spoljaric [37] and by Odgaard and Mosconi [39] will be discussed briefly in Section 3.4. Finally, Section 3.5 deals with restrictions to application of the models.

3.2 RECENT MODEL

The vertical pressure gradients on the surfaces of a vane, by which the pressure increases from bottom to top on the suction side and decreases from bottom to top on the pressure side, causes the fluid along the suction side to acquire a downward velocity component. The resulting vortex sheet at the trailing edge rolls up to form a large vortex trailing from a position near the top of the vane (tip vortex). The vane-induced vortex is carried downstream with the flow, where it gives rise to a secondary circulation, which alters magnitude and direction of the bed shear stresses and causes a change in the distributions of velocity, depth and sediment transport in the vane-affected area. As a result, the bed aggrades in one part of the channel cross-section and degrades in another.

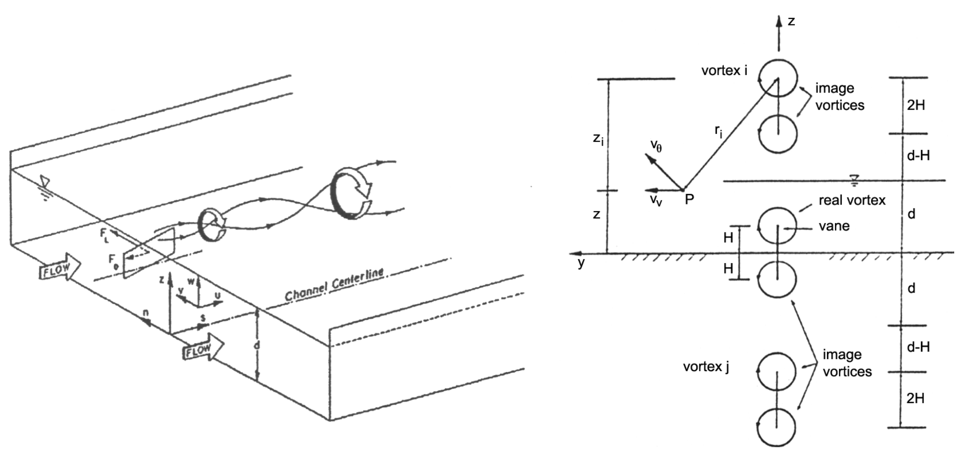

Figure 3.1: Co-ordinate system (left) and method of images (right); source: Odgaard and Wang, 1991

In order to predict the strength of vane-induced vortices, use is made of a model based on Prandtl's lifting line theory (Section A.3), by which one of the trailing vortices of a finite wing supposedly represents a vane-induced vortex. The circulation about the vane (bound vortex) is generated as a consequence of the action of viscosity in establishing the Kutta-condition at the trailing edge. Fluid elements in the resulting rotational flow in the boundary layer adjacent to the surface spill over the vane tip at a rate required to form a trailing vortex with strength equal to the circulation around the vane.

Sections 3.2.1 and 3.2.2 describe the theory with respect to changes in velocity distribution and bed shear stresses induced by a single vane. The bed area affected by a single vane is limited. In practice, the employment of vane arrays will often be required. A vane interaction model (Section 3.2.3) gives the total circulation induced by an array of equally sized and angled vanes. From this model, limits to the vane spacing can be derived lest a vane array generates a coherent circulation downstream. Finally, Section 3.2.3 summarizes the theory with regard to changes in vane-induced depth distribution. Figure 3.1 presents the co-ordinate system used throughout the description of the theory.

3.2.1 Velocity distribution and vane-induced bed shear stresses

The tip vortex resembles a Rankine vortex, which decays with distance downstream of the vane due to viscous diffusion. In an unbounded flow field the tangential velocity perpendicular to the core axis is described by

$$v_\theta = \frac{\Gamma_0}{2\pi r}\left[1 - e^{-\frac{u}{4\varepsilon s}r^2}\right] \tag{3.1}$$

The presence of bed and free surface in an open channel distorts the vortex. The effect of boundaries on the tangential velocity can be accounted for analytically by applying the method of images (Figure 3.1). Hence, the transverse component of the tangential velocity at distance z from the bed equals

$$v_n = \sum_{i=1}^{\infty}(-1)^{i+1}\frac{\Gamma_0}{2\pi r_i}\left[1 - e^{-\frac{u}{4\varepsilon s}r_i^2}\right]\frac{z_i - z}{r_i} + \sum_{j=1}^{\infty}(-1)^{j+1}\frac{\Gamma_0}{2\pi r_j}\left[1 - e^{-\frac{u}{4\varepsilon s}r_j^2}\right]\frac{z_j + z}{r_j} \tag{3.2}$$

in which the first summation includes contributions from the real vortex and images above the free surface and the second summation contributions from the images below the bed.

Calculations and experimental data [38] have shown that the core is about 0.2 times the vane height below the top elevation of the vane.

The initial circulation is calculated by using the Kutta-Joukowski theorem, which states that, in an inviscid, incompressible and uniform flow, the force acting per unit length on a cylinder of arbitrary cross-section perpendicular to the stream velocity equals the product of fluid density, stream velocity and circulation, and by applying Helmholtz's second theorem, according to which the initial circulation is equal to the vertical circulation around the vane (Section A.3). Assuming that there are as many vortices above the bed as there are below, the near bed transverse velocity component is obtained from Equation (3.2) with $z = 0$, reading

$$v_{vn} = \frac{F_L}{\pi\rho u H_v}\sum_{j=1}^{\infty}\frac{(-1)^{j+1}}{r_j}\left[1 - e^{-\frac{u}{4\varepsilon s}r_j^2}\right]\frac{z_j}{r_j} \tag{3.3}$$

Note that the transverse velocity component according to Equation (3.3) does not include the contribution from the bound circulation.

The vane-induced transverse bed shear stress follows from the assumption that the ratio of induced bed shear stress to streamwise bed shear stress equals the ratio of transverse near bed velocity component to streamwise near bed velocity component,

$$\frac{\tau_{vn}}{\tau_{bs}} = \frac{v_{vn}}{u_b} \tag{3.4}$$

Next, a power-law velocity distribution is adopted,

$$\frac{u}{\overline{u}} = \frac{m+1}{m}\left(\frac{z}{d}\right)^{\frac{1}{m}} \tag{3.5}$$

in which velocity profile exponent m is related to the Darcy-Weisbach friction factor f as

$$m = \kappa\sqrt{\frac{8}{f}} = \frac{\kappa\overline{u}}{\sqrt{g i_w d}} \tag{3.6}$$

The downstream decay of the vane-induced transverse bed shear stress and the near bed transverse velocity component is controlled by eddy viscosity. Because bed resistance is the main factor causing decay [38], the eddy viscosity is obtained from the power-law velocity profile and an assumed linearly distributed primary flow shear stress,

$$\tau_s = \tau_{bs}\left(1 - z/d\right) \tag{3.7}$$

$$\varepsilon = \frac{\kappa^2 \bar{u} d}{6m\left(1+1/m\right)\left(1-1/2m\right)\left(1-1/3m\right)} \tag{3.8}$$

3.2.2 Lift and drag forces exerted on the flow

The increment of lift force dF_L exerted on the flow by a vane element of height dz is given by

$$dF_L = \frac{1}{2} c_L \rho u^2 L_v dz \tag{3.9}$$

Thus, the lift force exerted on the flow by a foil of height H_v equals

$$F_L = \frac{1}{2} c_L \rho L_v \int_0^{H_v} u^2 dz \tag{3.10}$$

Similarly, the drag force exerted on the flow by a foil of height H_v equals

$$F_D = \frac{1}{2} c_D \rho L_v \int_0^{H_v} u^2 dz \tag{3.11}$$

Substituting Equation (3.5) into Equations (3.10) and (3.11), the lift and drag forces are

$$F_L = \frac{1}{2} c_L \rho L_v H_v \bar{u}^2 \frac{\left(m+1\right)^2}{m\left(m+2\right)} \left(\frac{H_v}{d}\right)^{\frac{2}{m}} \tag{3.12}$$

and

$$F_D = \frac{c_D}{c_L} F_L \tag{3.13}$$

By the Kutta-Joukowski theorem and by establishing the circulation by the Kutta-condition, the sectional lift coefficient for an inviscid, incompressible and uniform flow around a large aspect foil (2D) is given by $c_L = 2\pi\alpha$ (Section A.2). For a wing of finite span, however, the trailing vortices induce a downward velocity component (downwash), which disturbs the uniform approach flow and reduces the effective angle of attack. Assuming an elliptical spanwise distribution of the circulation, Prandtl determined that the induced angle of attack (the reduction of the effective angle of attack) yields (Section A.3)

$$\alpha_i = -\frac{c_L}{\pi AR} \tag{3.14}$$

Following Prantl's lifting line theory, it is assumed that the distribution of the vertical circulation around the vane is elliptical, maximum at the bed and zero at the top of the vane. The flow around a submerged vane is, however, not ideal. Furthermore, a submerged vane is a 'wall'-attached foil with a ratio of vane height to vane length of typically less than 1. Accounting for the presence of the bed, Odgaard and Spojaric assumed that the effective angle of attack is reduced by half the value of the induced angle of attack given by Equation (3.14) [35]; the rationale being that a vane has only one edge with tip vortices. Hence,

$$c_L = 2\pi\left(\alpha - \frac{c_L}{2\pi AR}\right) \equiv 2\pi\left(\alpha - \frac{c_L}{2\pi H_v/L_v}\right) = \frac{2\pi\alpha}{1 + L_v/H_v} \tag{3.15}$$

The (induced) drag coefficient is then given by

$$c_D = -c_L \frac{\alpha_i}{2} = \frac{c_L^2}{2\pi AR} = \frac{1}{2\pi}\frac{L_v}{H_v} c_L^2 \tag{3.16}$$

In [53], Wang derives Equation (3.15) alternatively by assuming that the vane and its image below the bed form a wing with a span of twice the vane height. Using Equation (A.24) (in Appendix A) and defining the aspect ratio of the wing composed by the vane and its image below the bed as

$$AR = \frac{b_w^2}{S_w} = \frac{(2H_v)^2}{2H_v L_v} = \frac{2H_v}{L_v} \tag{3.17}$$

the lift coefficient given by Equation (3.15) is retrieved:

$$c_L = m\alpha = \frac{m_0\alpha}{1 + m_0/(\pi AR)} = \frac{2\pi\alpha}{1 + L_v/H_v} \tag{3.18}$$

Using Equation (A.23), the corresponding drag coefficient yields

$$c_D = -c_L\alpha_i = \frac{c_L^2}{\pi AR} = \frac{1}{2\pi}\frac{L_v}{H_v}c_L^2 \tag{3.19}$$

3.2.3 Vane interaction and depth distribution

Though vane-interaction and induced depth distribution are less important to the current study, the description of the theory is continued in the remainder of this section, mainly to stress the importance of the lift coefficient as a key design parameter.

The bed area affected by a single vane is limited. The width of the affected area is increased if vanes are arranged in an array. However, the strength of the induced circulation is less than that obtained by simple superposition of individual vorticity fields on account of interaction between tip vortices. Wang developed an interaction model to describe the effect of interaction between tip vortices on the total induced circulation based on a model for biplanes [51]. For two finite wings placed in parallel, the vortex sheet induced by one of the wings produces a downwash velocity component along the span of the other wing, thus causing an additional reduction in effective angle of incidence. In favour of the interaction model for vane arrays, it is assumed that vanes are represented by lifting lines perpendicular to the approach flow and that each lifting line trails a vortex sheet with width equal to the wing span of twice the vane height. Furthermore, the wing shapes are assumed elliptical, so that the distribution of circulation along the span is elliptical. According to the model, the total circulation induced by an array of equally sized and angles vanes can be obtained by adding the circulations of individual vanes, provided the vanes are adjusted by an interaction coefficient, which is a function of vane spacing and vane dimensions. In order to generate a coherent circulation downstream, vane spacing should be less than about two to three times the vane height. If the vane spacing is larger, the vane array will generate a system of individual vortices and be less efficient. In practical terms, decay imposes a limitation to the longitudinal spacing of submerged vanes to sustain a certain induced circulation and induced bed shear stress downstream. The distance between arrays depends on design objectives in terms of limits on induced stresses.

Within a field of equally sized, angled and spaced vanes, the area-averaged induced bed shear stresses are $\bar{\tau}_{vn} = \frac{F_L\lambda\beta}{A_v}$ and $\bar{\tau}_{vs} = \frac{F_D\lambda\beta}{A_v}$, in which $A_v = \delta_n\delta_s$ and β is a factor arising from averaging processes [52]. Assuming that the vanes affect the flow field through the induced bed shear stresses, the developed relationship between vane characteristics and induced bed shear stresses is incorporated in the governing equations of motion and continuity equations of flow and sediment to obtain flow and depth distribution.

For general river conditions ($d/b_r < 1$ and $r/b_r > 1$), the vertical velocity component, w, is of the order of $v(d/r)$ or $u(d/b_r)(d/r)$ and all terms in the governing equations containing w can therefore be eliminated. The stress terms are then reduced to $F_s = (1/\rho)\partial\tau_s/\partial z$ and $F_n = (1/\rho)\partial\tau_n/\partial z$, by which the pressure terms can be written in terms of the water surface slope, since the equation of motion in z-direction is reduced to a hydrostatic condition.

Furthermore, it is assumed that the flow field is fully developed ($\partial/\partial s = 0$), implying that the depth-average of the transverse velocity component equals zero. Finally, by applying kinematic boundary conditions at the bed and at the free surface, the depth-averaged equations of motion read

$$\rho g i_{ws} d = \tau_{bs} + \tau_{vs} \tag{3.20}$$

and

$$\rho g i_{wn} d = \tau_{bn} - \tau_{vn} - \rho \bar{u}^2 \frac{d}{r} \tag{3.21}$$

with unknowns $\bar{u}$, i_{wn}, d and τ_{bn} (for straight channels: $r \to \infty$).

In consideration of the unknowns, an additional equation is obtained from a force balance for bed load particles on a transverse slope including lift, drag, gravity and friction force [36], which under fully developed conditions yields

$$\frac{d(d)}{dn} = -\frac{1}{B\sqrt{\theta_{cr} \rho g \Delta D_{50}}} \frac{\tau_{bn}}{\tau_{bs}} \tag{3.22}$$

in which B is a function of Coulomb friction and ratio of lift to drag ($3 \le B \le 6$; [21; 36]). By evaluating the equation of motion in n-direction and combining with Equation (3.21), a fourth and final equation is obtained, reading

$$\rho\left(u_s^2 - \bar{u}^2\right)\frac{d}{r} + \tau_{bn} - \tau_{vn} + \left(\frac{\partial \tau_n}{\partial z}\right)_s d = 0 \tag{3.23}$$

in which $u_s = \bar{u}(m+1)/m$.

The last term in Equation (3.23) is associated with twisting of the velocity profile caused by vanes and/or by centrifugal acceleration acting on the flow in river bends, which drives the faster moving surface flow toward the outer bank and the flow near the bed toward the inner bank. It is assumed that the velocity profile of the transverse velocity component can be described by a linear distribution resulting from centrifugally induced and vane-induced contributions,

$$v = 2\left(v_{vn} - v_b\right)\left(\frac{z}{d} - \frac{1}{2}\right) \tag{3.24}$$

in which v_b is the near bed value of the centrifugally induced transverse velocity. Then, $\tau_n = \rho\varepsilon\, \partial v/\partial z$ and the gradient of the streamwise shear stress at the water surface reads

$$\left(\frac{\partial \tau_n}{\partial z}\right)_s = -\frac{2\rho m \kappa \bar{u}}{(m+1)d}\left(v_{vn} - v_b\right) \tag{3.25}$$

as follows from Equations (3.7), (3.8) and (3.24), and the assumption that the eddy viscosity is isotropic. Substituting Equations (3.4) (with $u_b = \bar{u}/k$; [47]) and (3.25) into Equation (3.23) gives

$$\tau_{bn} = -\frac{\rho k (2m+1)(m+1)}{m^2\left[2m^2 + k(m+1)\right]} \bar{u}^2 \frac{d}{r} + \tau_{vn} \tag{3.26}$$

With $\tau_{bs} = \rho\kappa^2 \bar{u}^2 / m^2$ and Equation (3.26), Equations (3.20) and (3.22) are reduced to

$$\bar{u}^2 = \frac{m^2}{\kappa^2}\left(g i_w d - \frac{\tau_{vs}}{\rho}\right) \tag{3.27}$$

and

$$\frac{d(d)}{dn} = -\frac{m}{\rho\kappa\bar{u}B\sqrt{\theta_{cr} g\Delta D_{50}}}\tau_{bn} \tag{3.28}$$

From Equation (3.26), it follows that if vanes are to cancel out the secondary current in fully developed river bend flow, the vanes must generate a transverse bed shear stress equal to

$$\tau_{vn} = \frac{\rho k(2m+1)(m+1)}{m^2\left[2m^2 + k(m+1)\right]}\bar{u}^2\frac{d}{r} \tag{3.29}$$

With $\bar{\tau}_{vn} = \dfrac{F_L\lambda\beta}{A_v}$ and reciprocal vane density $A_v = \delta_n\delta_s = A/N$, the design relation [41] to eliminate the secondary current reads

$$\frac{NH_vL_v}{A} = \frac{2}{c_L}\frac{d}{r}G \tag{3.30}$$

in which $G = \dfrac{k}{\beta\lambda}\dfrac{(2m+1)(m+2)}{m(m+1)\left[2m^2 + k(m+1)\right]}\left(\dfrac{d}{H_v}\right)^{\frac{2}{m}}$ with vane interaction coefficient λ [52]. The design relation is similar to a relation developed in an earlier model by Odgaard and Mosconi [39]. Equation (3.28) is to be solved using a finite difference scheme, where computation should start at the bank farthest away from the vanes. The boundary condition is obtained from the continuity equation (in river bends normally the inner bank). Initially, the flow depth at the starting point is set equal to the pre-vane flow depth. The iteration process is continued until calculated distributions fulfil the boundary conditions.

3.3 DISCUSSION

Basic vane parameters in the theory described in Section 3.2 are initial vane height H_{v0}, ratio of vane height to vane length H_{v0}/L_v, angle of attack α, vane submergence T, longitudinal and transverse vane spacing δ_s and δ_n, and distance between outermost vane and bank δ_b. Basic flow and sediment parameters are pre-vane cross-section averaged flow depth d_0, flow velocity u_0, resistance parameter m, ratio of channel width to depth b_r/d_0, ratio of channel width to radius of curvature b_r/r and sediment Froude number Fr_D. The latter indicates the degree of mobility of sediment and is defined as $Fr_D = u_0/\sqrt{gD_{50}}$.

In general, vane-induced bed level changes increase with increasing sediment Froude number, vane height and angle of attack. Major uncertainties in calculations are associated with the transverse bed slope factor B, which represents sediment properties with regard to motion resistance, and velocity profile factor k. Experimental data have shown that B ranges from 3 to 6, possibly depending on sediment gradation [21].

To validate theory described in Section 3.2, laboratory tests were conducted in both straight and curved channels [42] (Section 2.3.2). It was concluded that the agreement between measured and calculated velocity and depth distributions, with and without vanes, is good. In [41], Odgaard and Wang presented a number of graphs to facilitate design of a vane system for bank protection in river bends. In calculations, the river banks are modelled as vertical and rigid walls (Figure 3.2). The design procedure can be described as a backward calculation, where the input consists mainly of the desired bed topology and vane lay-out and design are the outputs. It is assumed that induced re-distribution of sediment within the channel cross-section occurs during and immediately after high flows. Therefore, values of the parameters at bank-full flow stage are used in the design. Vanes would be installed at a relatively low flow stage when the bed profile is only slightly warped (Figure 3.2.A). Without vanes, scour depth

d_m would develop along the outer bank at design stage (bank-full stage) (see Figure 3.2.B). Locally, a change of depth can be achieved by installation of a vane system. In the case of protection of the outer bank against undermining by erosion, the design objective may be indicated by desired change of depth $d_m - d_v$. Figure 3.2.C presents a schematic of the bed profile at a subsequent low flow stage. In tests, Wang and Odgaard found that a reduction in discharge does not lead to a reduction in the volume of sediment accumulated in the vane field, because at the lower discharge, the sediment transport capacity in the vane field is too low to remove the sediment that accumulated at the higher discharge [42]. Therefore, they stated that vanes ensure that the near bank bed elevation obtained at design stage is maintained at all subsequent stages [41].

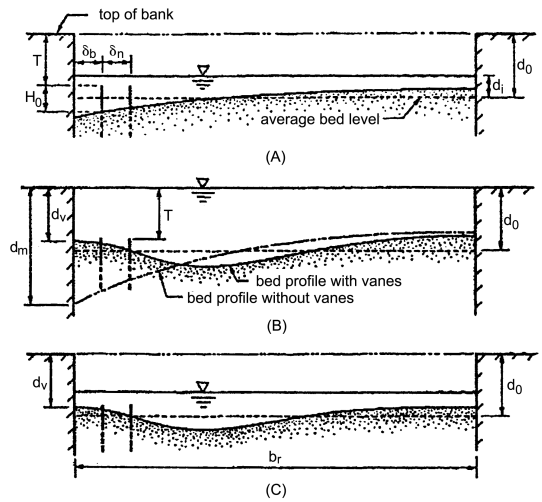

Figure 3.2: Primary design variables and flow sections at installation (A), design stage (B) and subsequent low flow stage (C); source: Odgaard and Wang, 1991

As an example, an imaginary vane system will be 'designed' for protection of the outer bank in a river bend, using the design graphs provided by Odgaard and Wang [41] and parameters, which correspond roughly to parameters for a river bend in the River IJssel, The Netherlands. It is understood that by possible employments of vane systems in Dutch rivers, sights are chiefly set on improvement of navigability at low flow stages. However, by re-distribution of sediment toward the outer bank, the navigation width at low flow stages may enlarge as seen in Figure 3.2.C, so that the design objectives of vanes as means of bank protection and shoaling amelioration in river bends are interrelated to some extent. Suppose that, at bank-full stage, the average channel width, flow depth, Chézy coefficient and velocity are b_r = 90 m, d_0 = 5.0 m, C = 36 m$^{0.5}$/s and u_0 = 1.4 m/s. The local radius of curvature is r = 500 m, while bed material supposedly comprises sand with median particle diameter D_{50} = 0.7 mm. Furthermore, assume velocity profile factor k = 1, bed slope factor B = 4 and critical Shields parameter θ_{cr} = 0.056. Hence, the sediment Froude number Fr_D = 16.9 and the resistance parameter m = 4.6 (with κ = 0.4). With $Fr_D\left(b_r/r\right)$ = 3.0, the scour depth along the outer bank at design stage (without vanes) can be estimated from Figure 3.3 [41]: d_m = 10.0 m. Suppose that the design objective reads a reduction of the near bank flow depth of $d_m - d_v$ = 5.0 m by the vane system at design stage (maintain flow depth along the outer bank equal to the average flow depth in the channel at all flow stages). The ratio of flow depth to channel width d_0/b_r = 0.05 is such that the vane-induced increases in bed level are (in theory) essentially independent of the ratio [41]. From Figure 3.4 (calculations are made for a section in between successive arrays; [41]), it follows that the above design objective can be met by applying at least three vanes (at H_{v0}/L_v = 0.3; α = 20°; $\delta_n = 3H_{v0}$ and $\delta_b = 1.5d_0$) per

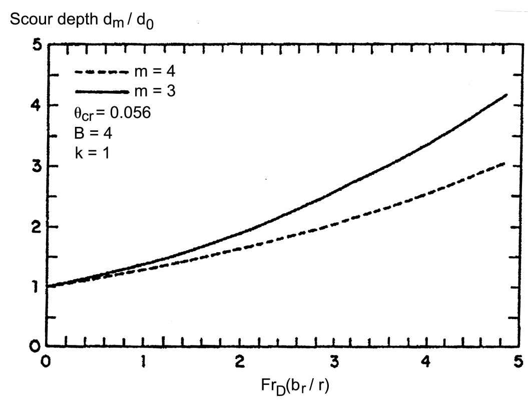

Figure 3.3: Scour depth at outer bank in river bend; source: Odgaard and Wang, 1991

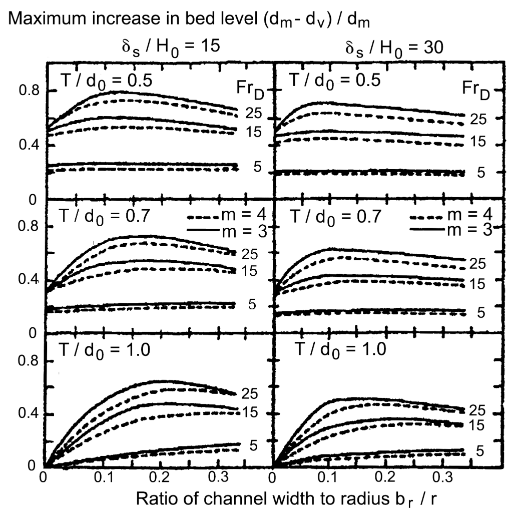

Figure 3.4: Calculated maximum increase in bed level along the outer bank for a three-vane array system (at H_0/L = 0.3; α = 20°; $\delta_n = 3H_0$; $\delta_b = 1.5d_0$); source: Odgaard and Wang, 1991

array, at T/d_0 = 0.5 and $\delta_s = 15H_{v0}$. The required initial vane height depends on the bed profile at the time of installation. Independent of eventual bed warping at installation, vane submergence T, defined as the distance between water level at design stage and top elevation of the vanes, should be maximally 2.5 m for these arrays in order to meet the design objective (if the bed at the bank is then horizontal, the vane height should be at least H_{v0} = 2.5 m). It is noted that vanes protruding relatively high above the bed may obstruct navigation at the lower flow stages, despite possible vane-induced decreases in bed level elevation in the channel mid-section. By increasing the angle of attack and/or the vane length, the maximum vane submergence can be enlarged and thus, the minimum initial vane height can be reduced. If the design objective is softened to a required reduction in the near bank flow depth at design stage of only $d_m - d_v$ = 4.0 m, a three-vane array system (with aforementioned vane dimensions and orientation) at T/d_0 = 0.7 suffices, so that the maximum vane submergence is increased to 3.5 m (and the minimum vane height H_{v0} is reduced to 1.5 m, if the bed at the bank is horizontal at installation). In consequence of the relaxation of the design objective, induced decreases in bed level elevation in the channel mid-section and thus, the effect of the vane system on navigation width at low flow stages may be inadequate. Compared to rivers abroad for which vanes have been applied, the major Dutch rivers show very mild slopes and modest flow velocities at design stage, resulting in relatively low sediment Froude numbers and relatively high values of the resistance parameter. Also, channel widths and radii of curvature are generally larger.

Odgaard and Wang assumed a linear distribution for both the centrifugally induced and the vane-induced transverse velocity component (see Equation (3.24)). De Vriend stressed that the assumed velocity profiles are mutually inconsistent, as the linear profile of the centrifugally induced transverse velocity component cannot be derived from a model from which the power-law velocity profile can be deduced [50]. Support for the linear distribution of the centrifugally induced velocity component is obtained from agreement with experimental data [36; 47]. Similarly, the assumption of a linear distribution of the vane-induced transverse velocity is supported by velocity measurements for experiments in a straight channel [37]. Near the vane, the vane-induced transverse velocity profile is distinctly s-shaped; farther downstream, the profile approaches a linear shape. The discrepancy between measured and assumed distribution is notable within a distance of 7 to 8 flow depths downstream. Odgaard and Spoljaric stated, however, that the streamwise variation of the vane-induced transverse velocity distribution is relatively insensitive to the shape of the transverse velocity profile [37].

Modifications of the flow field are expected to cause corresponding modifications of the bed shear stresses. Hence, the streamwise bed shear stress would reduce within the vane field and increase outside. In natural streams with movable beds, flow depth would decrease within the vane field and increase outside. Supposedly, the vane-induced transverse bed shear stress transports sediment into the vane-covered area, and develops and sustains a transverse bed slope throughout the vane-affected regions in the channel. In calculations, vane height is a variable whose steady-state value may approach zero in parts of the vane field [53], which implies that a part of the vane field is effective only during the development of the new depth distribution and may be buried afterward.

Sinha and Marelius [30; 48] already reminded the reader that the field design formulae presented in the previous section are based upon highly idealised theoretical analysis of flow through mostly straight rectangular channels, which presents an overly simplified picture of the situation in the field. The theory of Odgaard is developed for non-separated flow past submerged vanes. In the next chapters, it will be shown that the model underlying the theory, the classical lifting line theory by Prandtl, is inappropriate for submerged vanes. Apart from that, as described in Section A.3, only an untwisted elliptical planform at constant absolute angle of attack will yield an elliptical distribution of the bound circulation and constant sectional lift and drag coefficients along the span. As a result of the assumption that the circulation about the vane is established by the Kutta-condition, an infinite velocity at the leading edge remains, so that the flow field at the leading edge is predicted only approximately correct. On account of above-mentioned reasons, the existing theoretical descriptions of vane interaction and near vane flow physics are only approximately correct and cannot be expected to hold as soon as significant flow separation occurs. In [42], Odgaard and Wang recognized that agreement between experimental and theoretical depth distributions might be a bit deceptive, because flow separation actually occurs for vanes at conventional angles of attack, and induced circulation and bed shear stresses are probably different from calculated values. An explanation for observed agreement between theory and experiment is that, due to vortex motion, the streamwise velocity profile is distorted relative to the profile for a flow in an ordinary open channel [53]. Lack of a detailed description of the physics of the flow in the direct vicinity of the vane may have hindered further improvement of vane shape and performance. A better insight into the generation processes of vortices in the direct vane wakes is needed in order to develop an improved description of the near vane flow and improve vane performance.

Recently, efforts were undertaken to explore the possibilities of developing a fully 3D-numerical tool to simulate turbulent flows past submerged vanes in natural streams. In [42], Sinha and Marelius described their numerical model, which solves the 3D Reynolds-averaged Navier-Stokes and turbulence closure equations, and presented results of a simulation of the flow field in the direct vicinity of a single vane. To validate the numerical tool, results of an experimental study conducted earlier in a deformable bed straight channel were used [28]. Measured and calculated velocity distributions were seen to be in good general agreement. However, numerical predictions were found to be lacking in several areas. Particularly, at sections near the midst of the vane, the degree of agreement deteriorated as measurements indicated stronger primary and horseshoe vortices than predicted by the numerical model. If validated properly using detailed sets of currently non-existent flow and bathymetric data, numerical models provide an important alternative to investigate vane performance without resorting to more expensive, site-specific and tedious physical model studies [42]. Based on the analogy between submerged vanes and low aspect ratio wings (as described in Section 4.6), it is stressed that, in order to simulate correctly the flow past submerged vanes at high angles of attack, numerical models should probably represent flow interactions that reshape separated vorticity sheets into the rolled-up concentrated primary vortex, as practice in non-linear panel methods for slender low aspect ratio wings (see Section A.5.4).

3.4 EARLY MODELS

The theory developed by Odgaard and Wang [41; 53] and presented in Section 3.2 represents the most recent theory for design of vane fields. Because the theory applies to channels with any shape and planform, it is more general than models described in earlier papers [37; 39]. Furthermore, the theory developed by Odgaard and Wang takes into account the interaction between vanes in an array. However, compared to early models, the model is more complex, thus less suitable for first rough design calculations, and – at first sight – does not present real benefits with regard to conditions in the field owing to variations in parameters. Therefore, the early models developed by Odgaard and Spoljaric [37] and by Odgaard and Mosconi [39] are discussed briefly herein.

3.4.1 Odgaard and Spoljaric, 1986 and 1989

Odgaard and Spoljaric based the description of the streamwise variation of the transverse velocity components on the transverse component of the momentum equation [37], which – in the absence of lateral pressure gradients – reads

$$u\frac{\partial v}{\partial x}+v\frac{\partial v}{\partial y}+w\frac{\partial v}{\partial z}=\frac{\partial}{\partial z}\left(\varepsilon\frac{\partial v}{\partial z}\right) \tag{3.31}$$

Note that only one Reynolds-term is included in Equation (3.31) to control the decay of the (time-averaged) transverse velocity component, which means that decay due to fluid viscosity is neglected. The solution of Equation (3.31) is simplified by adopting a linear transverse flow velocity profile, given by

$$v=2v_s\left(\frac{z}{d}-\frac{1}{2}\right) \tag{3.32}$$

a parabolic eddy viscosity profile, given by

$$\varepsilon=\kappa u_* z\left(1-\frac{z}{d}\right) \tag{3.33}$$

and a transverse variation of the transverse velocity component at the water surface, given by

$$v_s=v_{sc}\cos\left(\pi\frac{n}{d}\right) \tag{3.34}$$

for $-d/2\le n\le d/2$. Inserting Equations (3.32), (3.33) and (3.34) in Equation (3.31) and assuming a constant flow depth, the solution of Equation (3.31) at the water surface and at the channel centreline reads

$$\frac{u_{sc}}{v_{so}}\frac{d\left(v_{sc}/v_{so}\right)}{d\left(s/d\right)}+\frac{2\kappa u_*}{v_{so}}\frac{v_{sc}}{v_{so}}=0 \tag{3.35}$$

in which v_{so} represents v_s at (s,n) = (0,0), where the origin is located at midst of vane. With $u_{sc}=\bar{u}_c+u_*/\kappa$, Equation (3.35) is solved to read

$$\frac{v_{sc}}{v_{so}}=e^{-\frac{2\kappa}{\sqrt{8/f}+1/\kappa}\frac{s}{d}} \tag{3.36}$$

in which $\sqrt{8/f}=\bar{u}_c/u_*$. The value of Darcy-Weisbach friction factor f typically ranges from 0.03 to 0.10. Thus, the vane-induced transverse velocity component is reduced by 50% at a distance downstream of the vane of typically 8 to 14 times the water depth [37]. To derive the downstream decay of the maximum vane-induced near bed transverse velocity component, Equation (3.36) can be rewritten, assuming $v_{bc}=-v_{sc}$ and $v_{bo}=u_{bo}\tan\alpha$ [38], in which v_{bo} and u_{bo} represent v_b and u_b at (s,n) = (0,0), respectively, to yield

$$\frac{v_{bc}}{u_{bo}}=\tan\alpha\cdot e^{-\frac{2\kappa}{\sqrt{8/f}+1/\kappa}\frac{s}{d}} \tag{3.37}$$

An alternative relation for the vane-induced near bed transverse velocity component can be obtained on the basis of vorticity equations, corresponding to the approach followed in favour of theoretical relations described in Section 3.2.1. Based on the initial circulation, Odgaard and Spoljaric [38] derived the following relation for the decay of the maximum vane-induced near bed transverse velocity component in a straight channel:

$$v_b=\frac{\Gamma_0}{2\pi h_c}\left[1-e^{-\frac{u}{4\varepsilon\xi}h_c^2}\right] \tag{3.38}$$

At ξ = 0, $v_b=u_b\tan\alpha$ (by approximation) and Equation (3.38) is reduced to

$$\frac{v_b}{u_b}=\tan\alpha\left\{1-e^{-\frac{1}{4}\frac{ud}{\varepsilon}\left(\frac{h_c}{d}\right)^2\frac{d}{\xi}}\right\} \tag{3.39}$$

Note that – in contrast to in the theory developed by Odgaard and Wang [41] – only the real vortex contributes to the maximum near bed transverse velocity component directly downstream of the vane. The relation between the near bed transverse velocity component (or the transverse velocity component at the water surface) and the transverse bed slope generated by the transverse bed shear stress component yields

$$i_{bn} = av_s \tag{3.40}$$

with $a = \dfrac{3\omega\sqrt{\theta_{cr}}}{2k_D\sqrt{g\Delta D}}$, in which ω is the ratio of projected surface area to volume for a sediment particle divided by that of a sphere of the same volume ($\omega = 1.27$ for ordinary sand) and k_D is the ratio of critical near bed velocity to critical shear velocity (k_D is of the order of unity). Substituting Equation (3.34) into Equation (3.40) gives

$$\frac{d(d)}{dn} = K\cos\left(\pi\frac{n}{\overline{d}}\right) \tag{3.41}$$

in which $K = av_{sc}$. Integration of Equation (3.41) gives

$$\frac{d-\overline{d}}{\overline{d}} = \frac{K}{\pi}\sin\left(\pi\frac{n}{\overline{d}}\right) \tag{3.42}$$

Superposition suggests that N_n vanes installed transversely by a distance equal to a water depth can generate a maximum change in flow depth of $\left(N_nK/\pi\right)\overline{d}$. Using Equation (3.36), the relation between changes in flow depths and longitudinal spacing of vane arrays reads

$$\frac{d-\overline{d}}{\overline{d}} = \frac{N_nK_o}{\pi}e^{-\frac{2\kappa}{\sqrt{8/f}+1/\kappa}\frac{\delta_s}{d}} \tag{3.43}$$

in which $K_o = av_{so} = av_{bo}$.

3.4.2 Odgaard and Mosconi, 1989

Odgaard and Mosconi stated that for fully developed flow in a curved channel of rectangular cross-section and constant curvature [39] and with the power-law velocity profile given by Equation (3.5), the centrifugal force torque about the section centroid acting on a volume with included angle ϕ yields (assuming a constant force due to the radial pressure gradient over the depth)

$$T_c = \int_{r_i}^{r_o}\int_0^d \rho\frac{u^2}{r}\left(z-\frac{d}{2}\right)r\phi dz dr = \frac{1}{2}\rho\overline{u}^2\frac{m+1}{m(m+2)}b\phi d^2 \tag{3.44}$$

The torque generated by N independent vanes about the section centroid is described by

$$T_v = N\int_0^{H_v}\left(\frac{d}{2}-z\right)dF_L = \frac{1}{4}c_L\rho\overline{u}^2L_vd^2\left(\frac{H_v}{d}\right)^{\frac{2+m}{m}}\left[\frac{(m+1)^2}{m(m+2)}-\frac{m+1}{m}\frac{H_v}{d}\right]N \tag{3.45}$$

Equating torques T_c and T_v implies elimination of the secondary flow. For that purpose, the total vane area (lifting surface) required per unit surface area of the channel bed reads

$$T_v = T_c \Rightarrow \frac{NH_vL_v}{r\phi b} = \frac{2}{c_L}\frac{d}{r}F \tag{3.46}$$

in which $F = \left(\dfrac{d}{H_v}\right)^{\frac{2}{m}}\left[(m+1)-(m+2)\dfrac{H_v}{d}\right]^{-1}$.

Odgaard and Mosconi [39] demonstrated that function F is relatively insensitive to variation in ratio of vane height to flow depth over a large range of values of H_v/d, so that vane operation is close to optimal over a wide range of flow stages, implying that discharge is not a key design parameter, but required only to calculate m. Because of the centrifugal acceleration causing a twist in the velocity distribution over the flow depth, the angle to be used for the calculation of c_L if vanes are installed at an angle of α' with the tangent of the channel centreline is $\alpha = \alpha' + \delta\left(1 - H_v/d\right)$ with $\delta = \arctan\left[\frac{1}{\kappa^2}\frac{m(m+1)}{m+2}\frac{d}{r}\right]$.

In favour of the theory, it is assumed that vane-induced lift forces can be averaged over the entire cross-section width. In practice, vanes in a river bend are only placed along the outer bank and the effect of vane-induced torque is identifiable only in and near the vane field. Furthermore, the developed theory did not account for interaction between vortices. Instead, guidelines were given for the lateral spacing of vanes and the distance between outermost vane and streambank.

3.5 RESTRICTIONS TO THEORY

In general, a range of angle of attack up to 20° is accepted for the angle of attack, although angles of attack up to 25° have been tested [41]. The optimum range is defined as 15° to 20°, as lift is reduced for lower angles of attack and flow separation and consequently drag become more and more pronounced with increasing angle of attack. Furthermore, local scour enlarges with increasing angle of attack. In [37], Odgaard and Spoljaric stated that the lift coefficient decreases with increasing angle of attack higher than about 20° due to flow separation. However, this statement will be invalidated on a theoretical basis in the next chapters. Equations (3.15) and (3.16) have been evaluated using force measurements for vanes with varying vane profiles installed at angles of attack up to 25° [37; 38]. For tested thin, flat vanes, the ratio of vane height to vane length equalled about 0.3. Note that all equations in the present chapter use angles in radians.

Odgaard and Spoljaric suggested $0.1 \le H_v/L_v \le 0.5$ [37]. Because the ratio of vane height to vane length is associated with a reduction of the effective angle of attack, vane dimensions directly affect the lift and drag coefficients. Therefore, the ratio of vane height to vane length is a key design parameter.

Odgaard and Mosconi found that the effect of vane submergence on vane-generated torque is relatively insensitive to variations in the ratio of vane height to flow depth over range $0.2 \le H_v/d \le 0.5$ [39]. Function F (Equation (3.46)) with respect to the vane height, giving the minimum lifting surface area required per unit surface area of channel bed, is a minimum at $H_v/d = 2(m+1)/(m+2)^2$ (for streambank protection in river bends). At design stage, Odgaard and Spoljaric suggested $0.4 \le H_v/d \le 0.5$ [37], while Odgaard and Mosconi [39] recommended $0.2 \le H_v/d \le 0.5$ for all erosion causing flow stages. Odgaard and Spoljaric observed an increase of the lift coefficient with increasing values of the ratio of vane height to flow depth owing to the free water surface, which increasingly suppresses the tip vortex, causing a reduction in downwash and hence, an increase in the effective angle of attack.

Transverse vane spacing should not exceed about $3H_v$ lest the vanes generate a coherent secondary circulation downstream. The interaction between vanes is almost negligible for a transverse vane spacing of $4H_v$ [52]; According to Odgaard and Wang [41], the optimum transverse vane spacing is about $2H_v$. Effects of vane-generated vortices are identifiable for more than 20 times the (initial) vane height. However, the longitudinal vane spacing depends on design objectives in terms of limits on induced stresses. Employment of multiple vanes in an array results in a wider vane-affected area, but also leads to a decrease in efficiency of the individual vanes due to vane interaction. Experiments presented by Odgaard and colleagues with vane arrays have been conducted only for up to four vanes in an array. In river bends, it is recommended to limit the distance of the outermost vane to bank to maximally twice the vane height as higher values may eventually lead to flanking of the vanes by the river flow, as observed by Odgaard and Mosconi [39].

4 ANALYSES OF VELOCITY MEASUREMENTS

4.1 INTRODUCTION

The present chapter deals with analyses of velocity measurements for the experiments in the framework of the BUET-DUT linkage project conducted in the period of March till June 2003 (Section 1.3). The horizontal and vertical velocity components have been measured by means of a programmable electro-magnetic velocity meter (P-EMS). According to technical specifications provided by supplier WL | Delft Hydraulics, the instrument is capable of measuring velocity components with an accuracy of +/- 0.01 m/s +/- 1% of measured values, provided the tilt angle of the probe <10°. During experimentation, a sampling rate of 10 Hz and an optimum measuring duration of 120 seconds has been selected. Therefore, at each measured location in the flow field, 1200 sample values have been taken, of which mean value, standard deviation, minimum and maximum value have been determined. In addition, data sets have been recorded and stored digitally. The P-EMS uses an intrusive technique to measure the velocity field. Measurement errors will therefore most likely be larger than in case use could have been made of instruments utilizing non-intrusive techniques. In defence, the technique applied is still superior to other intrusive techniques (for example: propeller meters), because the sampling volume is located at a lower depth than the probe and the instrument is equipped with an ellipsoidal probe, which minimizes disturbances to the flow field.

The P-EMS generates an electro-magnetic field, which ideally should not be disturbed. For an E30-probe, the influence area has a cylindrical shape with approximately a thickness of 5 mm and 50 mm diameter, situated just below the electrodes. In order to investigate the near vane flow field thoroughly, taking measurements directly next to the vane was desirable. The effect of the presence of the vane (made of a Perspex sheet) in the influence area of the probe has been tested under slack water conditions. Periodic oscillations with a frequency of about 1.4 Hz have been observed in records of measurements at locations directly next to the vane. The oscillations were clearly more apparent in records of the U-velocity component than in records of the V-velocity component. Amplitudes increased with increasing elevation of the measuring point. Moving in a direction away from the vane, the amplitudes diminished and the sampling character gradually transformed into irregular scatter, which could also be discerned in records of non-vane disturbed measurements. The oscillations hardly affected the mean values of the velocity components and because the analyses will concentrate on the mean values as representatives of quantities in the flow field, the findings did not directly give rise to omit measurements at locations directly next to the vane from measuring projects. As expected, no disturbances have been found in records of measurements in the cross-section at 3.0 cm downstream of the trailing edge, where the minimum distance between measuring location and trailing edge exceeded half the diameter of the proclaimed influence area of the E30-probe. In running water, disturbances to the flow field are bound to be larger when measuring in the direct vicinity of the vane than when measuring in a distant flow field due to enlarged interference of the probe. The extent to which disturbances occurred could not be detected and remains uncertain. The results of measurements at locations directly next to and in the wake of the vane should therefore be dealt with cautiously.

Velocity measurements should ideally be carried out in a state of equilibrium scour. Originally, it was assessed that a state of equilibrium scour could develop in a time span of about 8 hours running time. In the course of the first experiment (EXP.A3), it appeared that a longer time span should be adopted prior to velocity measuring as scour development continued. The process of erosion, which started near the leading edge of the vane, was seen to expand progressively towards the trailing edge. In consequence of the observations, the researchers decided to add measuring locations for scour monitoring and to prolong minimum running time prior to velocity measuring to 16 hours for angles of attack of 10° and 20°, and to 24 hours for angles of attack of 30° and 40°. A state of equilibrium has not been reached for all experiments. During the running time preceding velocity measuring, the upstream part of the scour stabilized in most cases. For EXP.A3, A4, B3 and C2, scour development continued gradually downstream along the exposed side of the vane during measuring. From the results of scour monitoring, it is seen that the scour depths locally increased only moderately with increasing running time. It is anticipated that the global characteristics of the flow field around the tested vanes would not change dramatically, if velocity measuring would have been delayed until all scour processes were completed. In the lee of the suction side, the bed levels were more or less stable as soon as the upstream part of the scour hole reached a state of stability. During velocity measuring, avalanches on the local rearward slope along the suction side as a result of gradually increasing scour depth at the trailing edge led to minor changes in bed level elevation only. Therefore, the current velocity measurements may be used to investigate characteristics of the flow field about submerged vanes qualitatively.

Measures have been taken to regulate the hydraulic boundary conditions optimally. However, due to limited capacities of instruments and model facility components in addition to several non-controllable circumstances, temporary and mostly small deviations from the selected hydraulic boundary conditions during experimentation were inevitable. The reader is referred to the accompanying measuring report [57] for more information about experiment procedures and measuring accuracies. On account of above-mentioned reasons, the results of velocity measurements shall be used in a qualitative sense primarily. The objectives of the analyses in this section may be summarized as to investigate qualitatively the effects of vane height and angle of attack on the flow past a single submerged vane in a movable bed and to identify the governing flow features. The analyses concentrate on a description of the time-averaged flow fields, for which purpose use is made of the mean measured values as representatives of quantities in the flow field.

4.2 APPROACH FLOW

The results of velocity measurements at X = 1360.0 cm within range –25.0 cm ≤ Y ≤ 25.0 cm for all experiments except for EXP.A2 (on account of a too low discharge during approach flow velocity measuring; Table 4.1) are used to determine (ideal) approach flow conditions. Figure 4.1 presents the average result of the selected measurements. Averagely, the V-velocity components are positive and increase with increasing height above initial bed level to values of up to 0.012 m/s, indicating that the approach flow formed an angle of about 2° with the X-axis or a systematic error in the zero-direction of the P-EMS. Compared to the angle of attack for tested vanes, measured deviations are moderate to minor (20% for an angle of attack of 10° (EXP.A1) to 5% for an angle of attack of 40° (EXP.A4).

Exp.	Date	X [cm]	Z [cm]	Avg. discharge reading [l/s]
A3	April 13, 2003	1350.0	2, 4, 6, 12, 27	200
A1	April 21, 2003	1360.0	2, 4, 6, 12, 21, 27	200
A4	April 28, 2003	1360.0	2, 4, 6, 12, 18, 21, 27	202
A2	May 5, 2003	1360.0	2, 4, 6, 12, 18, 27	194
B2	May 11, 2003	1360.0	2, 4, 6, 12, 18, 27	199
C2	May 18, 2003	1360.0	2, 4, 6, 12, 18, 27	201
B3	May 27, 2003	1360.0	2, 4, 6, 12, 18, 27	201

Table 4.1: Average discharge reading during approach flow measuring

By regression analysis applied to the measured velocity profile, a value of 0.281 m/s is found for the depth-averaged streamwise velocity component in the range –25.0 cm ≤ Y ≤ 25.0 cm. By a discharge of 200 l/s, the cross-section averaged streamwise velocity component equals 0.272 m/s. It is likely that the depth-averaged velocity in the mid-section of the flume was somewhat higher than the depth-averaged velocity near the sidewalls. Furthermore, in consideration of possible errors in discharge readings due to the nature of procedures applied by discharge calibration, discharge readings might structurally underestimate the magnitude of the actual discharge.

The measured velocity profile is compared to a theoretical logarithmic profile for steady state, uniform flow, reading

$$u(z) = \frac{u_*}{\kappa} \ln \frac{z}{z_0} = \frac{g\bar{u}}{\kappa\sqrt{C}} \ln \frac{z}{z_0} \tag{4.1}$$

In case of hydraulically rough beds, the level of zero velocity z_0 is determined by the bed roughness only (experimentally: $z_0 = k/33$) [22]. Assuming that equivalent sand roughness k equates the average observed ripple height of 0.03 m, the theoretical logarithmic profile as shown in Figure 4.1 is obtained (calculation with $C = 18\log(12R/k)$, using the value of the Chézy coefficient determined from average surface slope readings (C = 36.1 $m^{0.5}/s$; [57]) gives k = 0.029 m). The theoretical profile fits the measured profile quite well, especially in the lower regions not too far from the bed. At Z = 27 cm, the theoretical profile deviates less than 3% from the measured profile.

In the theory developed by Odgaard, a power-law profile is adopted for the vertical distribution of the streamwise velocity component (Equation (3.5)). When using C = 36.1 $m^{0.5}/s$ and a depth-averaged streamwise velocity component equal to the ideal cross-section averaged velocity of 0.272 m/s, the calculated power-law velocity profile deviates considerably from the measured profile. As shown in Figure 4.1, the power-law profile fits best to the measured velocity profile for C = 37 $m^{0.5}/s$ and $\overline{u}$ = 0.285 m/s.

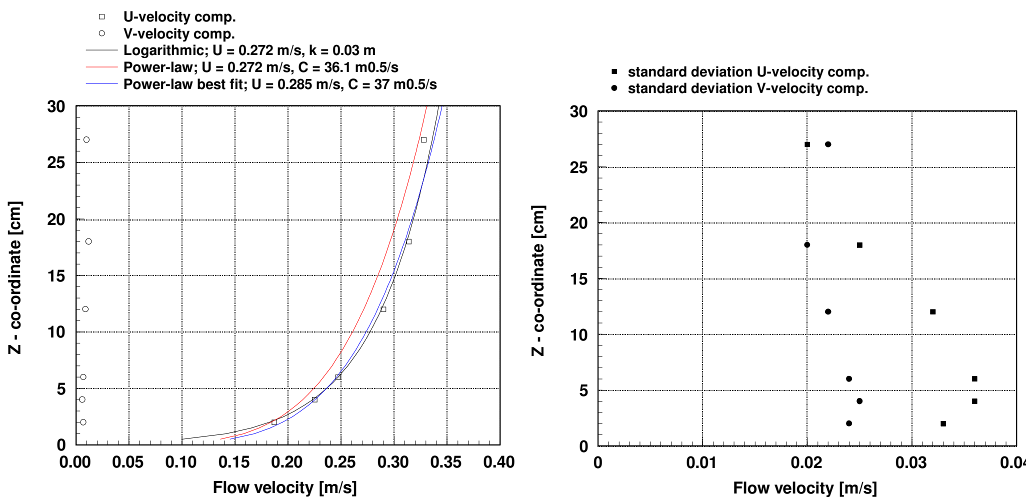

Figure 4.1: Approach flow velocity depth-profile (left) and turbulence depth-profile (right)

Figure 4.1 also presents the measured turbulence depth-profile in terms of the standard deviations of U- and V-velocity components (average standard deviations of the selected measurements). In general, the standard deviation of the V-velocity component is a factor 1.4 smaller than the standard deviation of the U-velocity component, but strikingly exceeds the value of the latter at Z = 27 cm, which suggests that there was a relatively high level of turbulence in the upper layers. It is, however, not excluded that the velocity measurements at Z = 27 cm, given the probe of the P-EMS, have been affected by the presence of the free surface. The depth-averaged turbulence intensity in X-direction, defined as

$$r_0 = \frac{1}{\overline{u}d}\int_0^d \sigma_u dz \tag{4.2}$$

equals 0.10 for $\overline{u}$ = 0.281 m/s and d = 0.30 m, which is a regular level of turbulence intensity for uniform flows.

4.3 NEAR VANE FLOW FIELD

The time-averaged results of near vane velocity measurements are presented in the figures in Appendix B. The figures include vector plots of the near vane U,V-velocity components, graphs of the U-velocity component in the lee of the vane, vector plots of the V,W-velocity components at X = X_{TE} + 3.0 cm (cross-section near the trailing edge) and at X = 1580.0 cm (cross-section at twice the vane length downstream from the midst of the vane), graphs of the U-, V- and W-velocity components at X = X_{TE} + 3.0 cm and at X = 1580.0 cm as functions of Y and Z, and vector plots of the velocity components parallel to the pressure side. Vector plots of the V,W-velocity components have been obtained by combining the results of measured U,V-velocity components and U,W-velocity components as the P-EMS is not capable of measuring 3D-velocity components simultaneously and therefore use had to be made of different probes to obtain all 3D-velocity components at a measuring point. In general, comparisons between U-velocity components measured with different probes showed mostly small deviations, which may be explained by the notion that the 3D-velocity components could not be measured simultaneously and consequently measurements has to be taken at different times. Furthermore, it can be anticipated that the different probes disturbed the spiral flow past the tested vanes differently. In order to minimise disturbance to the spiral flow during measuring, the positioning of the probe suitable for measuring of U,W-velocity components has been adjusted to the relative position of the measuring location to the core of the primary vortex in such a manner that the electrodes faced the vortex filament at all times. It is seen that the above-described measure could not prevent that some measurements have been affected by probe-induced disturbances too strongly to obtain approximate representatives of the actual velocity components, particularly in cases where measuring points were situated near the vortex filament (see also discussion in Section 4.5). The results of measurements of U,W-velocity components should therefore be dealt with cautiously. The vector plots of the velocity components parallel to the pressure and suction side result from measurements in planes parallel to the sides of the vane at a perpendicular distance to the side concerned of about 1.5 cm. The results of these measurements should therefore be dealt with cautiously too. However, as will be demonstrated in the following sections, results of measurements of velocity components parallel to the suction side may provide valuable information about the physics of the flow past submerged vanes. In the vector plots, the velocity components are projected to the surfaces of the pressure and suction sides for practical reasons.

From the vector plots of near vane U,V-velocity components, it can be observed that the flow approaching the vane is partly directed along the pressure side. The pressure side may be considered a stream surface essentially. Near the leading edge, streamlines curve toward low-pressure regions in the lee of the suction side. Flow separation occurs at the leading edge and gives rise to regions of strongly depressed time-averaged U-velocity components in the lee of the vane. These regions expand and intensify with increasing angle of attack and initial vane height. For vanes at relatively low angles of attack, the flow along the suction side probably reattaches at some distance downstream from the leading edge. For vanes at high angles of attack and for vanes protruding relatively high above the bed, regions of more or less adhering flow can be observed in the lee of the vane underneath regions of reduced U-velocity component. Driven by the pressure gradient between pressure and suction side, the flow along the pressure side near the top edge of the vane is directed upward. At and above the elevation of the upper edge, the flow slightly curves in negative direction. It is seen that the amounts of fluid masses involved in the flow over the top edge of the vane enlarge with increasing angle of attack and to a lesser extent with increasing initial vane height. Most probably, flow separation occurs along the sharp upper edge of the vane. It appears that the intersecting flows separated from the leading and top edges give rise to the generation of the primary vortex in the lee of the suction side at some distance from the leading edge. Moving downstream along the vane, a further development of the vortex can be observed. Within the regions of reduced U-velocity components, considerable masses of fluid are put into spiral motion. The core of the primary vortex is situated well inboard. As an example in which the above-mentioned findings can be discerned, Figure 4.2 presents results of measurements in the lee of the suction side for EXP.A2 (initial vane height: 0.12 m; angle of attack: 20°). The theory of Odgaard is developed for non-separated flow past vanes, where the strength of the circulation about the vane is calculated by assuming that the rear stagnation point is shifted to the trailing edge. The Kutta condition implies that there can be no velocity discontinuity at the trailing edge. Experimental results of the current research demonstrate that the assumption that the circulation about the vane is established by the Kutta condition cannot be expected to hold for angles of attack higher than about 10°.

The experimental results confirm findings about the elevation of the centre of the core of the primary vortex core reported by Odgaard and Spoljaric [38]. In the cross-section near the trailing edge, the elevation of the centre of the core is about 0.2 times the initial vane height below the top elevation of the tested vane, where the core diameter is defined as the distance

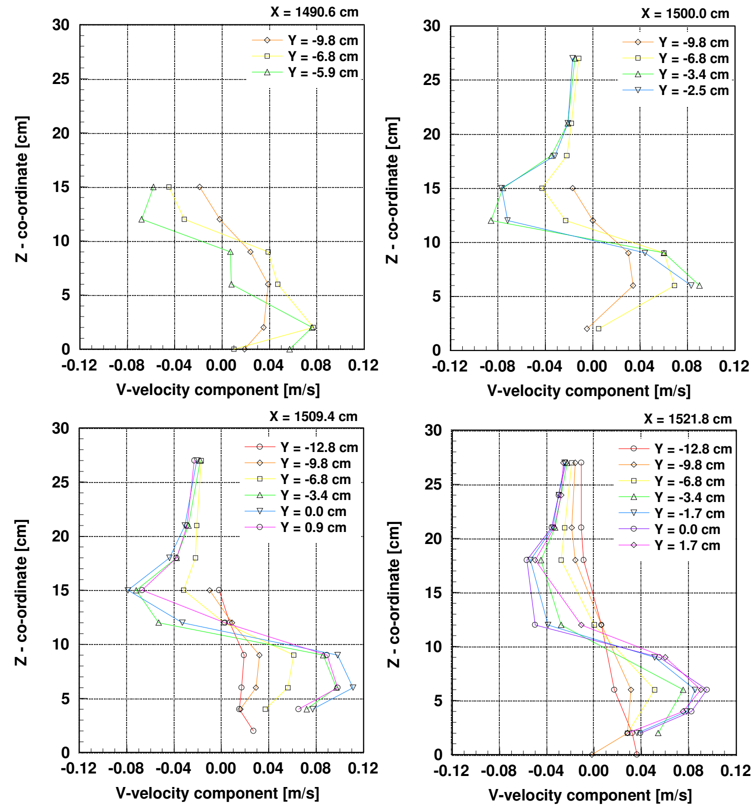

Figure 4.2: V-velocity components in the lee of the vane for EXP.A2

between absolute maximum induced V- or W-velocity components. Table 4.2 and Table 4.3 present maximum and minimum values of the measured mean V- and W-velocity components at $X = X_{TE} + 3.0$ cm and at X = 1580.0 cm. The measurements suggest that the centre of the core of the primary vortex in the cross-section near the trailing edge is averagely at about Y = 0 cm. It appears that the centre shifts slightly toward Y_{LE} with increasing angle of attack and to a lesser extent with increasing initial vane height, while the centre shifts toward Y_{TE} with decreasing initial vane height. These observations suggest that the primary vortex leaves from the surface of the suction side at a distance from the leading edge, which decreases with increasing angle of attack and increases with decreasing initial vane height (for given dimensions and orientation of the tested vanes; vane length: 0.40 m). Both induced velocities and diameter of the core increase with increasing angle of attack. It is seen that the primary vortex strengthens with increasing angle of attack. The core of the primary vortex appears to have a more ellipsoidal shape for vanes at relatively low initial vane height, probably as a result of boundary effects. The presence of the free surface may have affected the shape of the core similarly for EXP.C2. Experimental results for EXP.B2, B3 and C2 demonstrate that as the vortex travels downstream, the vortex filament tends to centre at mid-depth, thus confirming observations for low ratios of vane height to flow depth reported by Wang [52]. Noteworthy, results for EXP.C2 seem to indicate that the effect of the primary vortex on transverse transport of bed material for vanes at high ratio of vane height to flow depth is highest at some distance downstream from the vane as the vortex filament relocates toward mid-depth and the near bed transverse induced velocities gradually increase with distance downstream from the vane.

Graphs of U-velocity components at $X = X_{TE} + 3.0$ cm and at X = 1580.0 cm show the depression of the streamwise velocities associated with the primary vortex for all experiments. The depression becomes more pronounced with increasing angle of attack. For reasons of comparison, the depth-profile of the approach flow (Section 4.2) is included in graphs of the streamwise velocity component as a function of Z. As the vortex travels downstream, its strength decays and the depression of the streamwise velocities becomes less distinct. It is observed that the streamwise velocities in the flow field outside the core of the primary vortex, where the vertical velocity component is directed toward the bed, are higher than the values that may be observed locally in the absence of a vane. There, the higher velocities are brought down toward the bed as a result of induced vertical velocities. These modifications of the velocity distribution result in higher local streamwise bed shear stresses than in the flow field where the vertical velocity component is directed toward the free surface and were first reported by Odgaard and Wang [42]. The reader is referred to [56] for more information about the effect of these modifications of the velocity distribution on morphology.

EXP.ID	MAX/MIN	X [cm]	Y [cm]	Z [cm	U [m/s]	V [m/s]	ANG(V/U) [2] [degr.]
EXP.A1	MAX	1522.6	-3.5	6	0.260	0.065	14.0
		1580.0	6.5	2	0.176	0.043	13.7
	MIN	1522.6	-3.5	18	0.314	-0.028	-5.1
		1580.0	0.0	18	0.291	-0.017	-3.3
EXP.A2	MAX	1521.8	0.0	6	0.235	0.095	22.0
		1580.0	0.0	2	0.264	0.047	10.1
	MIN	1521.8	0.0	18	0.314	-0.057	-10.3
		1580.0	0.0	18	0.276	-0.047	-9.7
EXP.A3	MAX	1520.3	-5.0	2	0.214	0.128	30.9
		1580.0	5.0	2	0.230	0.082	19.6
	MIN	1520.3	-5.0	15	0.246	-0.090	-20.1
		1580.0	0.0	21	0.247	-0.051	-11.7
EXP.A4	MAX	1518.3	-6.4	-2	0.150	0.155	45.9
	MIN	1518.3	-6.4	15	0.209	-0.072	-19.0
EXP.B2	MAX	1521.8	3.4	2	0.096	0.080	39.8
		1580.0	3.4	2	0.191	0.036	10.7
	MIN	1521.8	-1.7	6	0.205	-0.035	-9.7
		1580.0	3.4	15	0.289	-0.018	-3.6
EXP.B3	MAX	1520.3	-2.5	-6	0.181	0.227 [3]	51.4
		1580.0	2.5	2	0.174	0.068	21.3
	MIN	1520.3	-2.5	9	0.254	-0.072	-15.8
		1580.0	0.0	12	0.203	-0.045	-12.5
EXP.C2	MAX	1521.8	-3.4	12	0.238	0.118	26.4
		1580.0	-1.7	6	0.270	0.069	14.3
	MIN	1521.8	-1.7	21	0.290	-0.097	-18.5
		1580.0	-1.7	21	0.208	-0.077	-20.3

Table 4.2: Maximum and minimum values of measured mean V-velocity components

EXP.ID	MAX/MIN	X [cm]	Y [cm]	Z [cm	U [m/s]	W [m/s]	ANG(W/U) [4] [degr.]
EXP.A1	MAX	1522.6	3.5	12	0.235	0.047	11.3
		1580.0	3.5	12	0.225	0.027	6.8
	MIN	1522.6	-6.5	12	0.289	-0.049	-9.6
		1580.0	-6.5	12	0.285	-0.023	-4.6
EXP.A2	MAX	1521.8	1.7	9	0.219	0.064	16.3
	MIN	1521.8	-3.4	12	0.243	-0.094	-21.1
EXP.A3	MAX	1520.3	0.0	9	0.091	0.098	47.1
		1580.0	5.0	6	0.178	0.073	22.3
	MIN	1520.3	-10.0	9	0.307	-0.106	-19.0
		1580.0	-7.5	6	0.280	-0.058	-11.7
EXP.A4	MAX	1518.3	6.4	2	0.041	0.063	56.9
	MIN	1518.3	-12.9	6	0.161	-0.078	-25.8
		1518.3	15.9	-14	0.179	-0.109 [5]	-31.3
EXP.B2	MAX	1521.8	3.4	2	0.124	0.080	32.8
	MIN	1521.8	-1.7	4	0.213	-0.053	-14.0
EXP.B3	MAX	1520.3	2.5	2	0.133	0.081	31.3
	MIN	1520.3	-5.0	0	0.138	-0.095	-34.5
EXP.C2	MAX	1521.8	3.4	12	0.226	0.087	21.1
	MIN	1521.8	-3.4	18	0.214	-0.089	-22.6

Table 4.3: Maximum and minimum values of measured mean W-velocity components

[2] Angle between measured mean U- and V-velocity components.
[3] Measurement taken at point near local bed; possibly affected strongly by probe-induced disturbance to flow.
[4] Angle between measured mean U- and W-velocity components.
[5] Measured W-velocity component is associated with trailing edge horseshoe vortex leg.

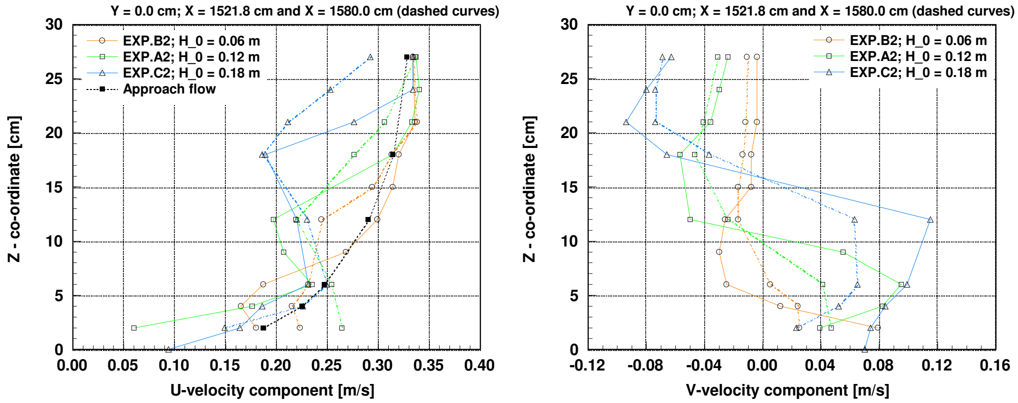

Figure 4.3: Depth-profiles U,V-velocity components at an angle of attack of 20° with varying vane heights

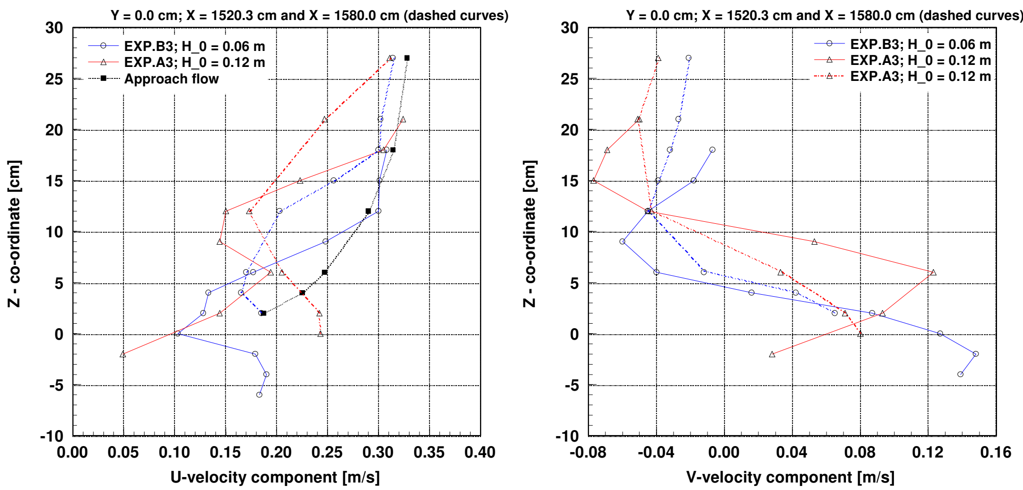

Figure 4.4: Depth-profiles U,V-velocity components at an angle of attack of 30° with varying vane heights

From comparisons of the U-velocity components at $X = X_{TE} + 3.0$ cm and at X = 1580.0 cm, it is seen that the near bed streamwise velocities in the earlier-defined regions in the flow field increase over at least the length of this itinerary. The effect of re-distribution of the higher velocities toward the bed by vortex motion enlarges with increasing angle of attack as vanes at higher angles of attack induce higher vertical velocity components. Peaks in U-velocity component in layers below the top elevation of the vane near Y_{TE}, as seen in graphs of the U-velocity component in the cross-section near the trailing edge, are associated with the flow along the exposed side of the vane (pressure side) and cannot be discerned at some distance downstream of the vane.

Figure 4.3 and Figure 4.4 present distributions of the U- and V-velocity components in the centreline (Y = 0.0 cm) at $X = X_{TE} + 3.0$ cm and X = 1580.0 cm for tested vanes at varying initial vane heights. The graphs confirm findings mentioned earlier, namely the tendency of the primary vortex to expand over the entire flow depth as it travels downstream of the vane. It appears that, at an angle of attack of 20°, vane effectiveness in terms of induced near bed transverse velocity component is poor if the ratio of vane height to flow depth is restricted to about 0.2 (EXP.B2). At an angle of attack of 30°, on the other hand, single vanes seem to be quite effective even for even low ratios of vane height to flow depth. Figure 4.5 and Figure 4.6 present distributions of the U- and V-velocity components in the centreline (Y = 0.0 cm) at $X = X_{TE} + 3.0$ cm and X = 1580.0 cm for tested vanes at varying angles of attack. It is seen that the depression of the streamwise velocity component intensifies with increasing angle of attack. The measured distributions of the transverse velocity component also demonstrate that strength and stability of the primary vortex, and hence, vane effectiveness increase with increasing angle of attack. Observations of vane-induced bed level changes support this finding. The distribution of the V-velocity component is distinctly s-shaped at $X = X_{TE} + 3.0$ cm and X = 1580.0 cm; the assumption of a linear distribution holds improvingly with distance downstream of the vane.

Experimental results for angles of attack of 30° and 40° (EXP.A3, A4 and B3) indicate the presence of a horseshoe vortex. Marelius and Sinha already reported the presence of a horseshoe vortex for a single vane at an angle of attack of 40° [30]. The results of the current research suggest that such a vortex is generated also at an angle of attack as low as 30°. The observed scour development for EXP.C2 may provide a reason to believe that a horseshoe vortex occurred for the tested vane at an angle of attack of 20° and a ratio of vane height to flow depth of 0.6 as well, but no vortices (except for the primary vortex) could be identified from the limited number of measurements for EXP.C2. By a detailed experimental study, Marelius and Sinha found as many as two suction side vortices (one of which can be identified as the primary vortex) and two horseshoe vortex legs. According to Marelius and Sinha, the horseshoe vortex forms two counter-rotating vortex legs at the edges of the vane. The vortex leg leaving from the leading edge decays quickly, while the vortex leg leaving from the trailing edge persists over a longer distance. Marelius and Sinha explained the difference in decay rates by stating that the horseshoe vortex leg leaving from the trailing edge is affected by a smaller portion of the exposed surface of the vane and by the strong low-pressure regions on the suction side. Adopting nomenclature by Marelius and Sinha, the presence of the weaker suction vortex and the vortex leg leaving from the leading edge have not been found in the current research, probably due to the use of inferior instruments and a less detailed measuring project. However, the experimental results confirm the presence of the counter-rotating (compared to the sense of direction of the primary vortex) horseshoe vortex leg leaving from the trailing edge, the strength of which increases with increasing angle of attack. In conformance with observations by Marelius and Sinha, measurements at X = 1580.0 cm suggest that the horseshoe vortex leg leaving from the trailing edge decays within about twice the vane length downstream of the midst of the vane. The discussion about the presence of secondary vortices in the flow field past submerged vanes will be continued in Section 4.6.

The limited number of available measurements of velocity components in planes parallel to the pressure and suction sides can be explained by the fact that it was initially assessed that these measurements would not provide much additional information, particularly in consideration of possible inaccuracies due to probe-induced disturbances to flow. It appears, however, that the results may reveal interesting features of the physics of the flow past the tested vanes, as will be discussed in Section 4.6. In contrast to other velocity measurements, a measuring duration of only 60 seconds has been applied for measurements of the velocity components in planes parallel to the sides of the vane. It is observed that the directions of the measured velocity vectors in the plane parallel to the pressure side qualitatively correspond to directions of strings attached to the vane as presented by Marelius and Sinha [30]. Near the top edges of the tested vanes, the flow is directed upward, while the flow is largely directed toward the bed over the most portion of the exposed surface. From the vector plots of the velocity components parallel to the suctions side, some remarkable observations can be made. Firstly, the velocity vectors near the leading edge at the top elevation of the vane have downward directions without exceptions, while at greater distance from the leading edge the flow is directed toward the free surface. Measurements suggest regions of stagnated and even reversed flow below the top elevation of the vane near the leading edge for vanes at the higher angles of attack (EXP.A3, A4 and B3) and a smoother type of flow for vanes at the lower angles of attack (EXP.A1, A2, B2 and C2). It appears that there is a more or less adhering near bed flow along the suction side for vanes protruding relatively high above the bed (EXP.C2) and for vanes at high angle of attack (EXP.A3, A4 and B3). In Section 4.6, the above discussion will be continued.

4.4 DOWNSTREAM FLOW FIELD

A limited number of measurements have been taken near the local bed in cross-sections at X = 1660.0 cm and X = 1820.0 cm. In general, the results show a high degree of scatter and do not provide very useful information. The expected Gaussian distributions of the near bed transverse velocity component can be observed distinctly in rare cases only (Figure B.1.18), probably as a result of ripple effects. Preferably, measurements in these downstream cross-sections should have been taken at higher elevation. Fixed bed experiments probably provide easier conditions to investigate the distribution of the near bed transverse velocity component. Here, it is mentioned that the results of measurements in the downstream flow field are not very relevant to the current research. Measurements and observations of induced bed level changes indicate that the primary vortex persists over a long distance downstream from the vane. As the vortex travels downstream, the vortex filament tends to centre at mid-depth and may curve slightly in lateral direction.

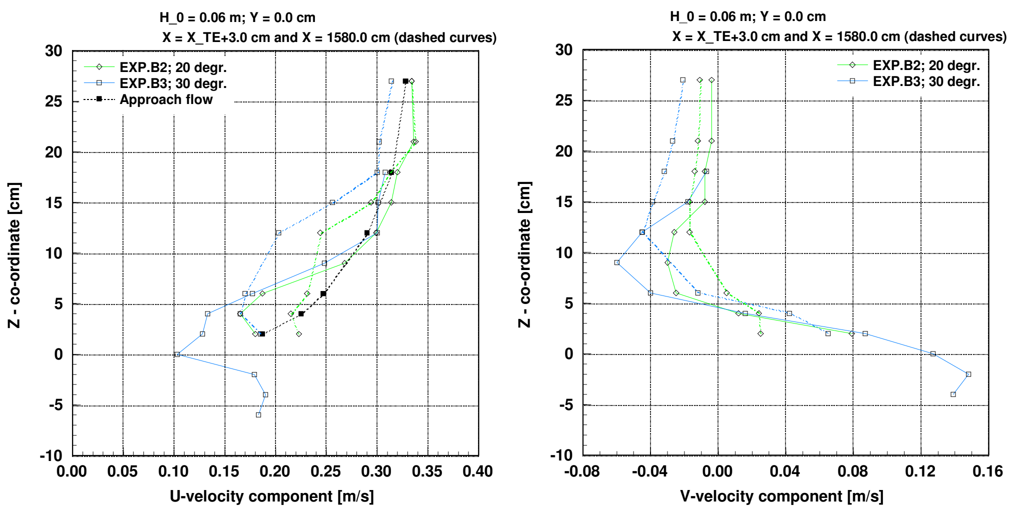

Figure 4.5: Depth-profiles U,V-velocity components at a vane height of 0.06 m with varying angles of attack

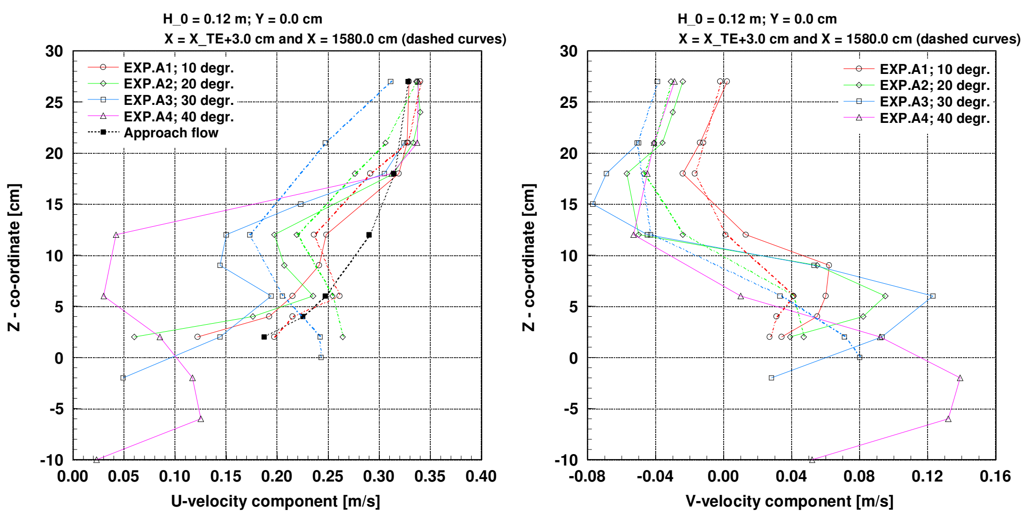

Figure 4.6: Depth-profiles U,V-velocity components at a vane height of 0.12 m with varying angles of attack

4.5 COMPARISON WITH THEORY OF ODGAARD

Because dimensions and orientation of the tested vanes comply with values for which the theory of Odgaard applies and because observed scour depths were relatively small, results of measurements at $X = X_{TE} + 3.0$ cm and at $X = 1580.0$ cm for EXP.A1, A2 and B2 are compared with calculated values of the V- and W-velocity components, using Equation (3.1) and a total of six image and real vortices (see figures in Appendix C). It is understood that the resemblance between the primary vortex and a Rankine vortex improves with distance downstream of the vane. At $X = X_{TE} + 3.0$ cm, deviations may be explained partly by the notion that the calculated velocity components do not include the contribution from the bound circulation [53]. In consideration of the magnitude of measured velocity components and possible inaccuracies, the agreement between measured and predicted velocity components is reasonable. It appears, however, that Equation (3.1) fails to predict the velocity components at about the elevation of the centre of the core of the primary vortex adequately. At elevations above and below the centre of the core, the agreement is generally better. From the graphs, it is seen that certain measurements of the W-velocity component taken inside the core of the primary vortex gave erroneous values as the results of these measurements clearly deviate from general trends. In view of the vortex motion, the erroneous results may be explained by procedures applied when approaching the core of the primary vortex with the probe of the velocity meter (see Section 4.5) and consequently must be ignored.

4.6 ANALOGY BETWEEN VANES AND LOW ASPECT RATIO WINGS

In analyses of the near vane velocity measurements (Section 4.3), several findings indicate that the theory of Odgaard cannot be expected to hold for angles of attack higher than about 10°. Experimental results of the current research do not support the description of the flow past submerged vanes as presumed in favour of the theory, in which the vortex sheet (resulting from an upward velocity component along the pressure side and a downward velocity component along the suction side) at the trailing edge rolls up to form a large vortex springing from a position near the top of the vane (tip vortex). Instead, findings suggest that the leading edge plays an important role in the generation of the primary vortex. Hence, the hypothesis that the theory of Odgaard fails to account for the physics of the flow past submerged vanes adequately seems to be well founded. Below, arguments that support the hypothesis are summarized:

- The theory of Odgaard is developed for non-separated flow past vanes, where the strength of the circulation about the vane is calculated by assuming that the rear stagnation point is shifted to the trailing edge. Relying on experimental findings for plates aligned to the flow, it can be anticipated that flow separation occurs at an angle of attack as low as about 5°. The Kutta condition implies that there can be no velocity discontinuity at the trailing edge. Experimental results of the current research demonstrate that the assumption that the circulation about the vane is established by the Kutta condition cannot be expected to hold for angles of attack higher than about 10°. In [42], Odgaard and Wang recognized that observed agreements between theoretical and experimental depth distributions might be a bit deceptive. In reality, flow separation occurs for vanes at conventional angles of attack, and induced circulation and bed shear stresses are probably different from calculated values. Odgaard and Wang explained the relative good agreement between theory and experiment by stating that, while flow separation reduces the transverse induced bed shear stress component, it increases the streamwise component by a comparable amount. Nevertheless, matter of fact is that the theoretical description of the physics of the flow past submerged vanes is inappropriate and consequently, the theory of Odgaard fails to predict the lift and drag forces exerted on submerged vanes (as found experimentally) satisfactorily.
- Experimental results of the current research indicate that the centre of the core of the primary vortex in the cross-section near the trailing edge is not at Y_{TE}, but rather the centre of the core is situated at about the centreline. It appears that the centre shifts slightly toward Y_{LE} with increasing angle of attack and to a lesser extent with increasing initial vane height, while it shifts toward Y_{TE} with decreasing initial vane height. These findings suggest that the primary vortex leaves from the surface of the suction side at a distance from the leading edge, which decreases with increasing angle of attack and increases with decreasing initial vane height (for given dimensions and orientation of the tested vanes; vane length: 0.40 m).
- In tests with a deformable bed, Marelius and Sinha found that the strength of the primary vortex at a downstream cross-section is a maximum at about 40° (vane length: 0.24 m; initial vane height: 0.12 m; flow depth: 0.40 m) [30]. The observation that the strength of the primary vortex increases with increasing angle of attack is confirmed by experimental results of the current research. The model underlying the theory of Odgaard, the classical lifting line theory for finite wings by Prandtl, is appropriate for wings at moderate to high aspect ratio, which generally stall at an angle of attack of 20° to 25°. Apparently, the lift force exerted on a submerged vane increases for ranges of angle of attack of up to 40°.
- Force measurements conducted at WL | Delft Hydraulics [11; 24] show that the theory of Odgaard fails to predict the lift and drag forces exerted on a vane at an angle of attack of 17.5° (for varying vane lengths and vane heights) satisfactorily. Because force measuring provides an excellent means to test the validity of the theoretical description of the flow physics, support is found for the hypothesis that the theory of Odgaard does not account for the physics of the flow past submerged vanes adequately.

- Measurements of the velocity components in planes parallel to the suction side suggest that the leading edge plays an important role in the generation of the primary vortex. In the remainder of this section, attention is paid to the effect of the leading edge on the physics of the flow about low aspect ratio wings. In the author's opinion, a similar role can be attributed to the leading edge of a submerged vane.

Above-mentioned reasons give cause for abandonment of the classical lifting line theory by Prandtl and exploration of the analogy between vortical flows induced by submerged vanes and low aspect ratio wings. The characteristic feature of the flow about a slender low aspect ratio wing is the appearance of free shear layers that coil tightly around dividing surfaces of separation shed from the leading and side edges.

In 1935, Winter presented the results of an extensive investigation of the flow pattern about low aspect ratio plates, which included force measurements, pressure measurements and flow visualization [55]. Thin, flat plates (thickness: 3.5 mm; upper surface well ground; tapered leading edge) as well as (mostly symmetrical) cambered models were tested in a wind tunnel. For flat rectangular plates, Winter distinguished ranges of aspect ratio and angle of attack, within which the flow pattern shows uniform characteristics. Below, Winter's conclusions and results for plates within ranges of aspect ratio are summarized, which correspond to ranges of aspect ratio for submerged vanes [6]:

- Thin, flat rectangular plate at aspect ratio within the range $0.1 < AR < 2.0$:

At very low angles of attack, the flow is practically adhering; there is tip flow, but the resulting flow separation is insignificant. On the pressure side, outwardly directed velocities can be observed, which increase with increasing angle of attack and decreasing aspect ratio. Generally, an increasing cross flow is discerned near the side and leading edges. On the suction side, a 'vortex cushion' is formed as a result of flow separation. The dimensions of the vortex cushion depend mainly on angle of attack and aspect ratio. At relatively high aspect ratio, the vortex cushion can spread out along the entire chord length, while it remains confined to the forward part of the plate for low aspect ratios. At higher angles of attack, the flow may be considered as divided into 'wing centre flow' (mainly adhering flow accompanied with separation) and 'wing tip flow' (fluid at the side edges flows spirally, taking the form of a 'vortex braid'). With decreasing aspect ratio, the latter type of flow predominates more and more. For equal angles of attack, an increase in the diameter of the side trailing vortices can be observed with decreasing aspect ratio. The induced transverse flows at the after part on the suction side reduce the tendency toward separation as considerable masses of fluid are involved in the vortex motion along the side edges. The main flow begins to adhere again at the downstream end of the stagnation region, from which streamlines spread out in all directions. With increasing angle of attack, the stagnation region extends farther downstream. At relatively high aspect ratio, separated flow takes place and a strong decrease in the normal force is observed when the stagnation region has expanded to the downstream end of the plate. At relatively low aspect ratio, the process of separation sets in more gradually, starting from the side edges. In case of relatively long plates, the diameter of the trailing vortices can augment up to a degree, where apparently no more fluid can be rolled up at the plate ends, and flow separation sets in at the after part of the plate.

- Thin, flat rectangular plate at aspect ratio within the range $0.0 < AR < 0.1$:

At very low angles of attack, a smooth airfoil type of flow takes place. The trailing vortices travel downstream nearly parallel to the plane of the plate. As a consequence of the limited span width, only a small vortex cushion can be built up. At higher angles of attack, the after parts of the curled trailing vortices become unstable as the diameter has become to large compared to the width of the plate and the vortices eventually break off. The distance along which the rolled-up side vortices adhere to the plate decreases with increasing angle of attack. Downstream of the position of the break, the flow separates without spiral formation.

In 1967, Wickens presented the results of an experimental investigation of the aerodynamic characteristics of a slender rectangular plate with an aspect ratio of 0.25 (dimensions: 6ft0", 1ft6" and 0ft3/8" in thickness; all edges consisted of a double bevel of 60° induced angle) [54].

---

[6] In Section 5.3, the aspect ratio for rectangular vanes will be defined as $AR = 2H_v / L_v$.

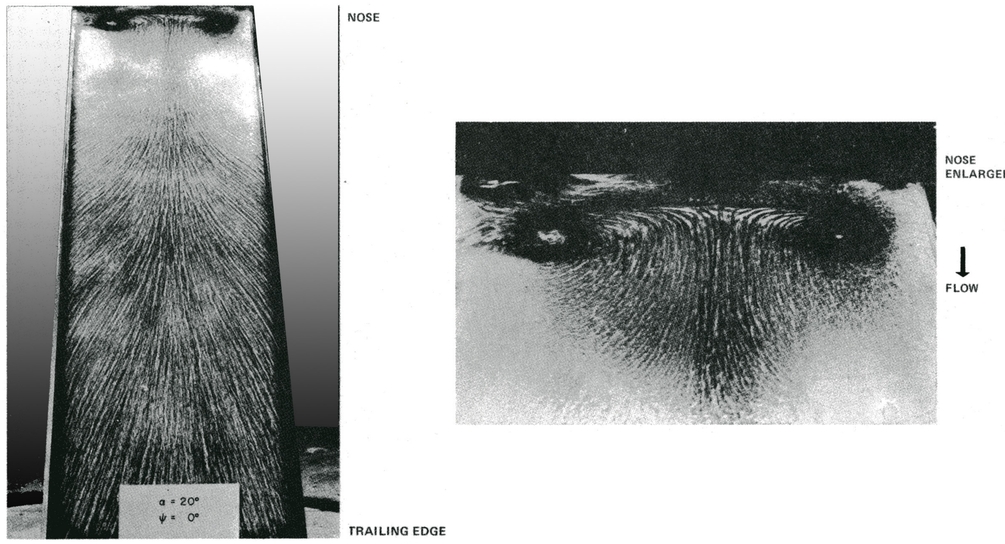

Figure 4.7: Upper surface flow streamlines on a slender rectangular plate at an angle of attack of 20° and zero yaw angle; source: Wickens, 1967

Figure 4.7 presents upper surface flow streamlines on the plate at an angle of attack of 20° and zero yaw angle, obtained with the aid of the chalk and kerosene technique. Flow visualization revealed a bubble-type separation from the leading edge with reattachment at some distance downstream. Primary separation occurred along the side edges; there did not appear to be any secondary separation on the plate at an angle of attack of 20°. Figure 4.8 presents Wickens' interpretation of the observed surface streamlines. The flow pattern near the leading edge is due to local separation and reattachment. Line OA represents a primary attachment line along which the incident flow impinges after having been drawn into the vortex field above the plate. Flow attachment also occurs along the normal leading edge and on the lower surface along the plate centreline. Downstream of boundary streamlines OE and OE', the main flow attaches to the line OA progressing outwards toward the side edges. Upstream of streamlines OE and OE', flow reattaches at the bubble.

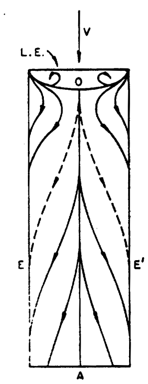

Figure 4.8: Interpretation surface flow streamlines; source: Wickens, 1967

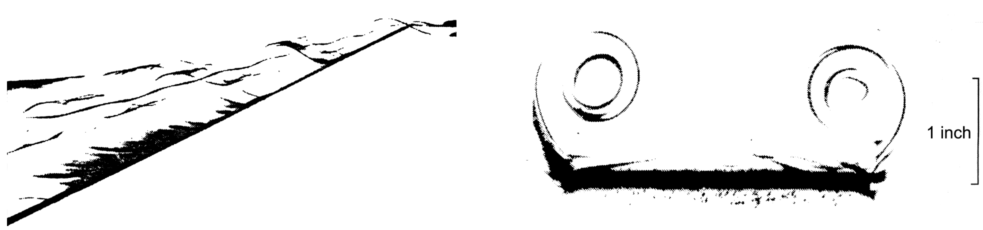

Figure 4.9: Dye filaments in rolled-up vortex sheet (left) and in vertical plane through trailing edge (right); source: Wickens, 1967 (photographs inverted)

Figure 4.9 (left) shows the flow pattern above a rectangular flat plate (chord length: 1ft) at an angle of attack of 20°, visualized by filaments of fluorescent dye issued from holes drilled in the surface. The velocity in the water tunnel was such that the flow in the shear layers was laminar. The spiral flow formed by the dye filaments represents the vortex sheet and deforms with the sheet during the process of rolling up. The individual dye filaments leave the edge of the plate and gradually spiral toward the vortex core. Figure 4.9 (right) presents a view at the vertical plane through the trailing edge in upstream direction, where a slit beam of light normal to the main flow illuminated the flow at a Reynolds number of $5{\cdot}10^3$. Wickens observed that the identity of the separate turns within the spiral is lost owing to turbulence at Reynolds numbers higher than about $1{\cdot}10^5$.

By smoke injections at the forward corner along one edge, Wickens examined the vortex core, characterized by intense rotation, very low pressure and viscous diffussion. The vortex core is located at the centre of the spiral flow above the plate. Wickens found that the vortex core is nearly linear in form, and inclined at an angle of approximately half the angle of attack with respect to the plate. Close to the trailing edge, the core starts to align itself with the free stream.

In [43], Peake and Tobak re-evaluated the oil-flow pattern on the leeward side of the slender rectangular wing from experimental results by Wickens, presented in Figure 4.7, by adopting the notions of singular points (nodes and saddle points) to create sequences of plausible flow structures and to deduce mean flow characteristics and flow mechanisms. The singular points may be regarded as the elemental constituents of a 'flow grammar' for cases of 3D-flow separation provided by the assumption of continuous vector fields of skin friction lines and external flow streamlines, coupled with simple topology laws. Singular points in the pattern of skin friction lines occur at isolated points on the surface, where the orthogonal vector quantities tangential to the surface vorticity and skin friction become identically zero, and are classified into nodes (nodal points and foci) and saddle points, defined accordingly:

- A nodal point of attachment is a source of a continuous pattern of skin friction lines. At a nodal point of attachment, all of the skin friction lines are directed outward away from the node.
- A nodal point of separation is a sink for the collection of skin friction lines. At a nodal point of separation, all of the skin friction lines are directed inward toward the node.
- A focus differs from a nodal point in that it has no common tangent line. An infinite number of skin friction lines spiral around the singular point, either away from it (a focus of attachment) or into it (a focus of separation).
- At a saddle point, there are only two particular lines that pass through the singular point. The directions on either side of the singular point are inward on the one particular line and outward on the other particular line. The particular lines (called lines of separation) act as barriers in the field of skin friction lines; all of the other skin friction lines do not pass the singular point and take directions consistent with the directions of the adjacent particular lines. The separation line is the location along which the boundary layer detaches from the body surface. The particular surface (termed a dividing surface) in the flow, anchored to the body along the separation line, prevents the converging boundary layers on each side of the separation line from coalescing and rolls up in its passage downstream. The saddle point in the pattern of skin friction lines is also the source of external streamlines that exist on the dividing surface.

The appearance of a focus on the surface is associated with the presence of a saddle point. Together, they provide a mechanism through which surface vortex lines can be extended into the fluid to form a dividing surface about a central core, first hypothesized by Legendre [27]. Beginning at a saddle point on the surface, the dividing surface extends the function of a line of separation into the flow, separating the set of limiting streamlines that have risen from near the surface on one side of the line of separation from the set arisen from the other side. The focus extends into the fluid as a concentrated vortex filament. The adjacent dividing surfaces (to which the focus on the surface is attached through saddle points) roll up with the same sense of rotation as the vortex filament. When one of these dividing surfaces extends downstream, it quickly draws the vortex filament into its core. Hence, the extension into the fluid of the focus on the body surface serves as the vortical core about which the dividing surface coils. Peake and Tobak termed the surface on which surface vortex lines extend into the fluid and coil around the extension of the focus a 'horn-type dividing surface' [43].

The surface vortex lines form a system of lines orthogonal at every point to the system of skin friction lines. Thus, it is in principle possible to describe the flow in the vicinity of singular points alternatively in terms of a pattern of skin friction lines or a pattern of surface vortex lines. Because the mean streamlines in a plane above a body surface are the solutions of an equation that is a direct counterpart of the equation for skin friction lines on that surface, the rules governing skin friction behaviour can be easily adapted and extended to yield similar rules governing flow behaviour (see [43]). Nodes and saddle points within the flow, excluding the boundary surface, are labelled N and S, respectively, whereas singular points on the boundary surface are defined as half-nodes N' and half-saddles S'.

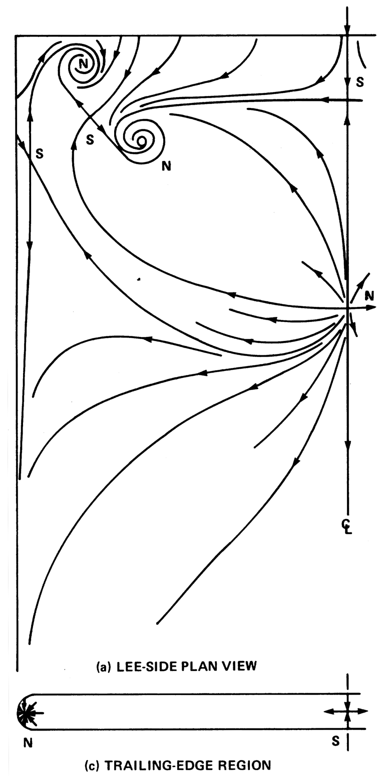

Figure 4.10: Interpretation of pattern of skin friction lines; source: Peake and Tobak, 1980

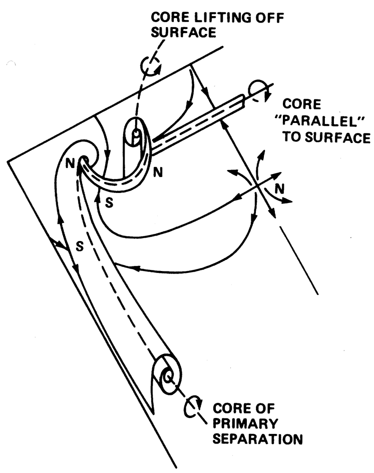

Figure 4.11: Perspective; source: Peake and Tobak, 1980

Supporting the views by Lighthill and Legendre, Peake and Tobak stated that oil streak flow visualization surface patterns are best interpreted as being representatives of skin friction lines [43]. The use of skin friction lines has distinct advantages, as, even in the vicinity of the lines of separation, skin friction lines are defined uniquely everywhere on the surface. Furthermore, the pattern of skin friction lines can be viewed as a continuous vector field. Beneath the core of the coiled-up dividing surface, a line of inflexion points will be observed in the pattern of skin friction lines interspersing the separation line (on either side of which are converging skin friction lines) and an associated reattachment line (on either side of which are diverging skin friction lines). The localized pattern of inflexion points evidences the existence of a coiled-up dividing surface. Although the quality of the photograph presented in Figure 4.7 is rather poor, one can distinguish patterns of inflexion points and regions of converging and diverging oil streak lines.

Figure 4.10 presents the interpretation of the flow about the slender rectangular wing as proposed by Peake and Tobak, based on a deduction from Figure 4.7 of the pattern of skin friction lines. There are four foci, one nodal point of attachment and five saddle points on the leeward surface. The windward surface contains one nodal point of attachment. Assuming that all of the skin friction lines except the particular ones on the centreline of the wing go into nodal points of separation, one at each tip of the wing trailing edge, while the particular lines on the centreline go into a saddle point at the trailing edge, there are in total eight nodes and six saddle points. Hence, the difference in numbers of nodes and saddle points equals two, which is in accordance with the topological rule for skin friction lines on a 3D-body simply connected and immersed in a flow that is uniform far upstream [9; 28] (Davey and Lighthill have noted that of all the possible patterns of skin friction lines on the surface of a body only those whose number of nodes (nodal points and foci) exceeds the number of saddle points by two are admissible). Each of the five saddle points on the leeward surface separates the flows from adjacent pairs of nodes. Springing from the saddle points are dividing surfaces, as seen in the perspective in Figure 4.11. Supposedly, the primary separation on each side of the centreline consists of the dividing surface which runs into the focus nearest the edge of the wing, taking the form of a 'horn-type dividing surface'. For flow about a wing of infinite span (2D-flow), the dividing surface springing from the saddle point on the centreline with corresponding reattachment would extend indefinitely spanwise and would represent a leading edge separation bubble. Peake and Tobak reasoned that, with reducing span, the dividing surface would first turn downstream as a result of the adverse spanwise pressure gradient. With a further reduction in span, the dividing surface will be forced to roll up around a focus as the downstream path is blocked by an adverse streamwise pressure gradient (see the focus/saddle point-combination near the centreline in Figure 4.10). Hence, an isolated vortex filament emanates from the focus into the flow and passes downstream, while the dividing surface would have extended downstream in the absence of adverse pressure gradients to form the site of a primary or secondary separation. Therefore, the flow depicted in Figure 4.10 must have been preceded by a sequence of less complicated structures containing a smaller number of singular points over intervals of lower angles of attack. Peake and Tobak [43] delineated a possible sequence of patterns of skin friction lines corres-ponding to structures that involve only a primary separation, leading to the pattern of skin friction lines in Figure 4.10. The initial pattern in the postulated sequence contains one focus. With increasing inci-dence, the subsequent surface pattern supposedly contains a pair of foci. At angles of attack in the range for which Figure 4.10 presents the appropriate pattern, there are four foci in the pattern of skin friction lines. Peake and Tobak reckoned that over a next range of angle of attack, a pair of secondary separations should appear on the leeward surface. A physically plausible pattern can be obtained by introducing another nodal point of attachment on either side of the nodal point on the centreline. The focus nearest the centreline in Figure 4.12 is then also connected to the line of secondary separation through a saddle point, so that the vortex filament emerging from the focus is no longer isolated, but may act as the core of a horn-type dividing surface that extends the line of secondary separation into the flow.

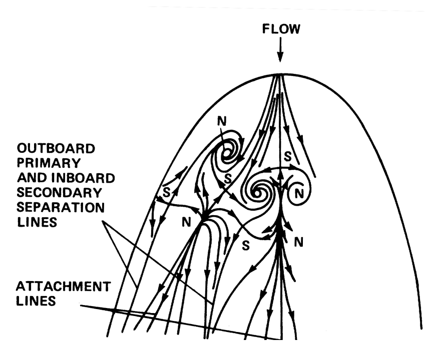

Figure 4.12: Pattern of skin friction lines with primary and secondary separation; source: Peake and Tobak, 1980

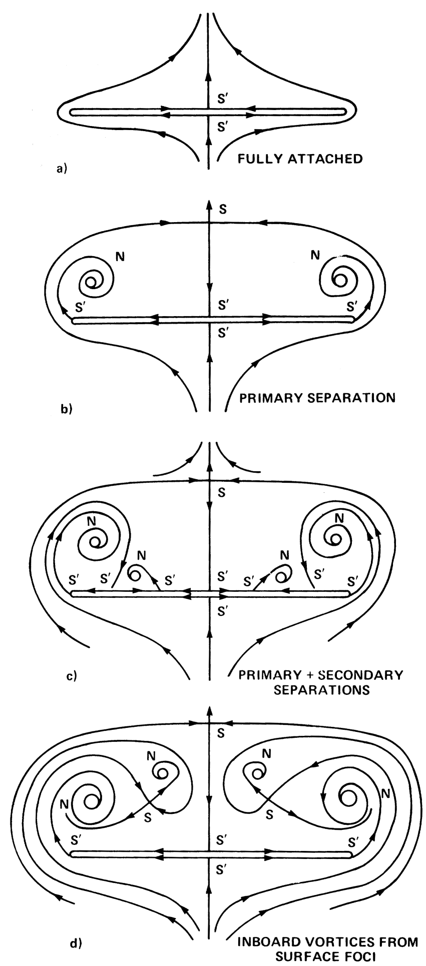

Figure 4.13: Cross flow streamlines near trailing edge; source: Peake and Tobak, 1980

Figure 4.13 presents cross flow streamline patterns in a cross flow plane near the trailing edge consistent with the postulated patterns of skin friction lines. Figure 4.13.A shows non-separated flow. Flows with primary separations, consistent with Figure 4.10 and structures over intervals of lower angles of attack in the sequence postulated by Peake and Tobak, are shown in Figure 4.13.B. Figure 4.13.C presents cross flow streamline patterns for flows with secondary separations, consistent with Figure 4.12. Finally, Figure 4.13.D applies when the isolated vortices springing from foci on the surface (see Figure 4.10) appear in the cross flow plane.

The main difference between a submerged vane and a slender low aspect ratio wing is obviously that a submerged vane is mounted vertically on a riverbed. For 3D bodies connected to a plane wall, it has been found experimentally that separation lines encircle the front face of the obstacle, from which surfaces spring to form the legs of horseshoe vortices, depending on the scale of the boundary layer relative to the obstacle cross-section. Hence, the presence of horseshoe vortex legs can be anticipated for vanes at angle of attack, the strength of which increases with increasing angle of attack as the effective width of the vane increases accordingly. The horseshoe vortex leg leaving from the trailing edge could be identified by the results of near vane velocity measurements for vanes at an angle of attack of 30° and 40° (see also Figure 4.15). For a vane at an angle of attack of 40°, Marelius and Sinha [30] reported the presence of horseshoe vortex legs leaving from the edges of the vane and two suction side vortices (Figure 4.14). The stronger of the suction vortices is clearly associated with primary separation (primary vortex). Based on the described results of analyses of the patterns of skin friction lines on surfaces of low aspect ratio wings by Peake and Tobak, the presence of the weaker and counter rotating (relative to the sense of rotation of the primary vortex) suction vortex may be explained by secondary separation or by the appearance of an isolated vortex springing from a focus on the suction side of the vane (compare Figure 4.14 with Figure 4.13).

It is seen that the characteristics of the flows about submerged vanes and slender low aspect ratio wings show great similarities. For flows about low aspect ratio wings, a key role is attributed to the leading edge. Similarly, the leading edge of a submerged vane appears to play an important role in the generation of the primary vortex along the suction side. New theoretical descriptions of the physics of the flow past submerged vanes must account for leading edge separation.

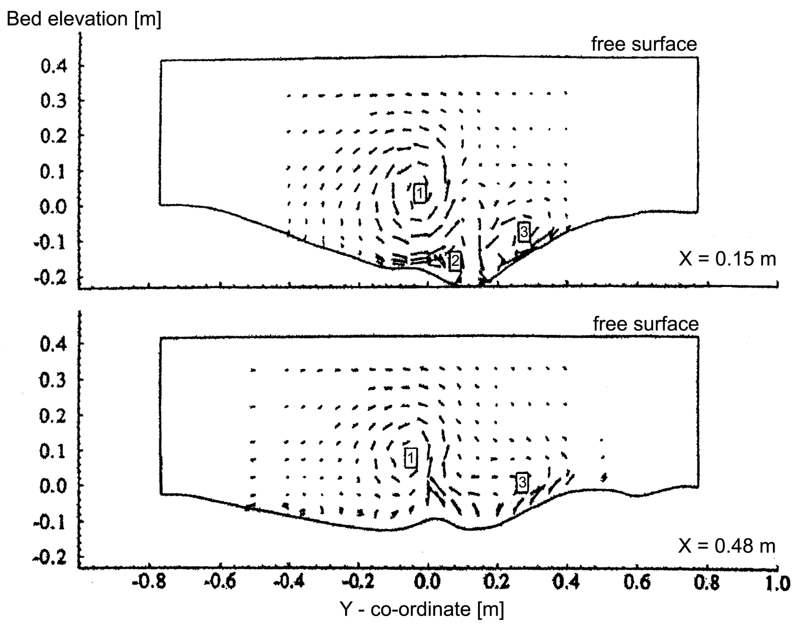

Figure 4.14: Velocity vectors at downstream cross-sections for vane at an angle of attack of 40° (vane length: 0.24 m; initial vane height: 0.12 m) by Marelius and Sinha; vortices identified as (1) counterclockwise suction side vortex, (2) clockwise suction vortex and (3) horseshoe vortex leg leaving from trailing edge; source: Marelius and Sinha, 1998

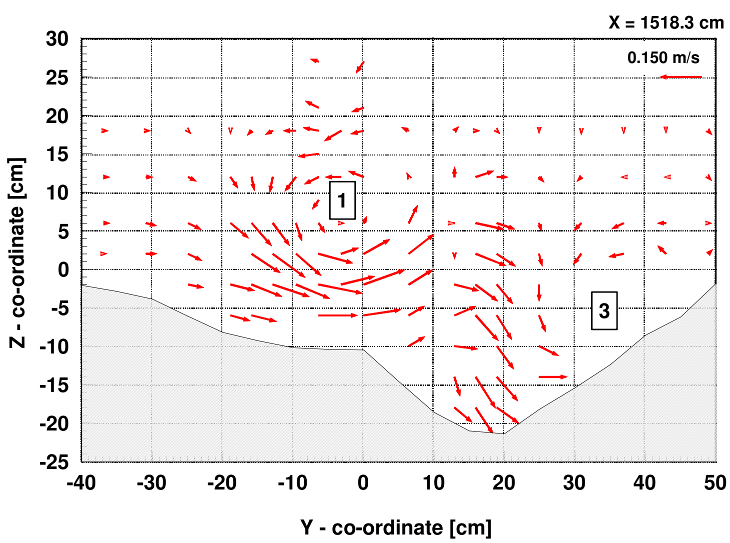

Figure 4.15: Velocity vectors at cross-section near trailing edge for EXP.A4 (angle of attack: 40°; vane length: 0.40 m; initial vane height: 0.12 m); vortices identified as (1) primary vortex and (3) horseshoe vortex leg leaving from trailing edge

5 LIFT AND DRAG FORCES

5.1 INTRODUCTION

The present chapter concentrates on the lift and drag forces exerted on submerged vanes. Force measurements conducted at WL | Delft Hydraulics [11; 24] show that the existing theoretical relations developed by Odgaard and et. fail to predict the lift and drag forces (as found experimentally) satisfactorily. Hypothetically, the theory of Odgaard does not account for the physics of the flow past submerged vanes adequately. In Section 4.6, the analogy between vortical flows induced by vanes and low aspect ratio wings has been explored. It is expected that the leading edge plays an important role in the generation of the primary vortex. The shortcomings of the theory of Odgaard with regard to the lift and drag forces acting on vanes are enumerated in Section 5.2. Section 5.3 describes new models to predict the mean lift and drag forces, which in view of the observed similarities in flows about vanes and slender low aspect ratio wings are based on theories for low aspect ratio wings by Bollay and by Gersten. A finite wing of given aspect ratio generates lift and counterrotating vortical structures. For a low aspect ratio wing, the vortices may be present over most of the wing area and affect the aerodynamic coefficients notably. Wings at aspect ratios of less than about 1.5 can be considered to hold linear and non-linear sources of lift. Linear lift is created by circulation about the airfoil and can be typically regarded as lift for the higher aspect ratio wings. Non-linear lift results from the generation of low-pressure cells on the upper surface of the wing. The non-linear effect increases with increasing angle of attack and is considered to be responsible for the relatively high stall angles of attack for low aspect ratio wings. In case of submerged vanes, the vortex sheets separated from the leading and top edges roll up to form primary vortices over a distance well within the length of a vane. Therefore, submerged vanes are expected to generate non-linear lift forces similarly. The validity of the new models derived from non-linear theories by Bollay and Gersten is tested by comparisons between measured and calculated lift and drag coefficients. Section 5.4 presents available force data for submerged vanes, while the results of comparisons are described in Section 5.5. Section 5.6 deals with the effects of several parameters on the mean lift and drag forces. Finally, attention is paid to expected pressure distributions and spread in hydrodynamic forces in Section 5.7.

5.2 SHORTCOMINGS THEORY OF ODGAARD WITH RESPECT TO MEAN LIFT AND DRAG FORCES

In the model underlying Prandtl's lifting line theory, an infinite number of infinitesimally weak horseshoe vortices are superimposed as to generate a lifting line and a trailing vortex sheet, which induces downwash at the lifting line (see Figure A.2). In the 3D-flow over a finite wing at moderate to high aspect ratio, the streamlines leaving the trailing edge from the upper and lower surfaces are generally in different directions. As a result of the pressure gradient, there is a spanwise flow component from wing tip to root on the upper surface and a spanwise flow component from root to wing tip on the lower surface. Theoretically, the discontinuity in the tangential velocity at the trailing edge is allowed across a vortex sheet. In reality, the different velocities at the trailing edge generate a thin region of shear flow with large vorticity. A sheet of vorticity actually trails downstream from the trailing edge of a finite wing, which tends to roll up at the edges to form tip vortices. Therefore, the classical lifting line theory is physically consistent with the actual flow downstream of a finite wing at moderate to high aspect ratio.

Figure 5.1.A presents the generation of rolled-up tip vortices in the wake of a finite lifting wing at medium to high aspect ratio at up to moderate angles of attack. The vortices, which are shed from the side and trailing edges, roll up downstream of the trailing edge into tip vortices. The generation of these vortices starts already at relatively low angles of attack and the strength and size of the vortices increase with increasing angle of attack. The near wake characteristics can be calculated by assuming that the tip vortices have a viscous core that reaches an asymptotic size within a few span lengths downstream of the trailing edges and from there on extend with a constant core diameter. Outside of the viscous vortex cores, the flow is dominated by the vortex flow and may be considered mainly inviscid. At low and moderate angle of attack, the effect of the rolled-up tip vortices on the aerodynamic characteristics of the high aspect ratio wing is small, so that at low subsonic velocities, the

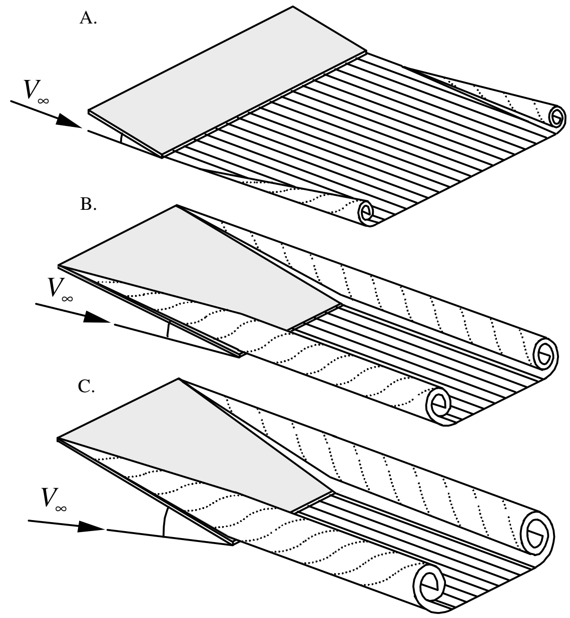

Figure 5.1: Vortex formation for high aspect ratio wings (A) and low aspect ratio wings (B; C)

variation of the aerodynamic coefficients remains linear. With increasing angle of attack, separation regions develop over the wing, involving a dramatic loss of lift (stall). Therefore, Prandtl's linear lifting line theory is appropriate for moderate to high aspect ratio wings at angles of attack up to stall.

The flow field about a sharp-edged slender low aspect ratio wing is radically different from that about the high aspect ratio wing. As the aspect ratio is decreased, boundary layers separate at the leading edges and the consequent free shear layers are swept inboard and upward, coiling up over the wing surface to form two primary vortices. For low aspect ratio wings, these rolled-up vortices are fairly extensive regions of rotational flow with reduced total pressure (Figure 5.1.B). The induced flow due to the vortices causes the generation of additional aerodynamic forces, resulting in the non-linear variation of the aerodynamic coefficients with increasing angles of attack. The viscous boundary layer attached to the surface tends to separate from the surface in regions of adverse pressure gradients. Initially, the separated flow from a flat surface reattaches further downstream, forming a 'separation bubble' or 'cushion' near the leading edge. As the angle of attack is increased, the separated shear layer does not reattach and flows into the free stream. The free shear layers tend to roll up into vortices and form various 3D-vortical flows, taking the form of the rolled-up leading edge vortex and/or other vortex types. When the angle of attack is increased even further, secondary vortices, as well as more complicated separated flows, may be observed (see also Section 4.6).

The non-linear variation of the aerodynamic coefficients for low aspect ratio wings cannot be obtained with Prandtl's lifting line theory. Therefore, the use of the classical lifting line theory (or any linear wing theory, for that matter) to calculate the lift and drag forces exerted on submerged vanes based on the analogy between the vortical flows generated by wings and submerged vanes seems inappropriate. In the remainder of this section, the shortcomings of the theory of Odgaard with regard to the prediction of the lift and drag forces exerted on submerged vanes are enumerated.

5.2.1 Lift distribution

According to the theory of Odgaard (Section 3.2), the lift and drag coefficients are calculated following Prandtl's classical lifting line theory, which, as described in Section A.3, assumes an elliptical lift distribution. For wings with an elliptical distribution of the circulation, constant lift curve slope and absolute angle of attack, the magnitude of the induced spanwise downwash is constant and the sectional lift and drag coefficients do not vary along the span. Only an untwisted elliptical wing planform will yield an elliptical lift distribution at all angles of attack up to stall. Clearly, submerged vanes do not have an elliptical planform and, thus, will not yield an elliptical lift distribution. However, in reality, an elliptical lift distribution gives a reasonable approximation for induced drag for an arbitrary finite wing at moderate to high aspect ratio, as demonstrated by among others Glauert, who used a Fourier series expansion to relate the lift and drag coefficients for an elliptical planform to the coefficients for an elliptical planform [18].

5.2.2 Profile drag

Equation (3.16) accounts for induced drag only (drag due to downwash), not for the total drag acting on a vane. Profile drag, which consists of the viscous-dominated contributions of skin friction and pressure drag due to flow separation, must to be added. The profile drag coefficient depends on vane shape and is not influenced by the aspect ratio.

5.2.3 Effect of aspect ratio

To check the validity of the statement that the properties of wings of arbitrary planform can be approximated by the properties of an elliptical wing (Section 5.2.1), Prandtl conducted experiments in a wind tunnel with untwisted rectangular wings at aspect ratios varying from 1 to 7. For high aspect ratios, the approximation appeared valid, but plots of measured wing lift coefficient versus geometrical angle of attack and wing drag coefficient showed a noticeable curvature for the rectangular wing at the lower aspect ratios. The curvature becomes more pronounced as the aspect ratio decreases further; the assumption that the lift curve slope is independent of the angle of attack becomes more and more invalid with decreasing aspect ratio. For very low aspect ratios, the experimental lift curves indicate a curvature concavely upward, as can be seen in Figure 5.2, which presents results of force measurements for rectangular plates by Winter [55] (normal force coefficient versus angle of attack; tapered leading edges; numbers designating the curves give the inverse aspect ratio).

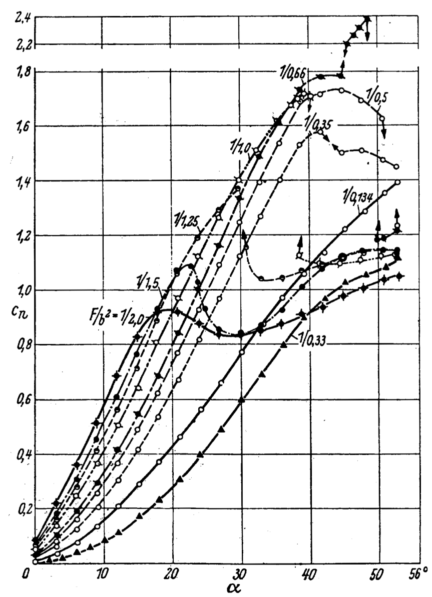

Figure 5.2: Normal force coefficient versus angle of attack for thin rectangular plates; source: Winter, 1935

The lifting line theory is inappropriate for low aspect ratio rectangular wings. Submerged vanes have aspect ratios of typically less than 1. Therefore, it is incorrect to apply the lifting line theory to predict the mean lift and drag forces exerted on a submerged vane. Instead, a more sophisticated model should be used (Section 5.3).

The observation that the lifting line theory holds closely for moderate and high aspect ratio wings, but gives less reasonable results for aspect ratios of approximately less than 4, has led to the development of linear surface theories (Section A.4), which hold approximately down to aspect ratios of the order unity. Already in 1925, Blenk stated that the upward curvature is caused by an additional effect, which becomes significant at very low aspect ratios, and that this effect cannot be obtained by means of the existing linear theories [2].

5.3 NON-LINEAR LIFTING SURFACE MODELS FOR FLAT-PLATE VANES

Observations and experimental results have demonstrated that the non-linear variation of the aerodynamic coefficients as a function of the angle of attack, is caused by the effects of rolled-up free vortices generated by the vortex sheets, which are separated from the leading and side edges. Because linear theories cannot predict a non-linear dependence of lift and pitching moment on the angle of attack, theories were required to estimate the wing loading as a non-linear function of incidence. One basic concept is that, when vorticity is shed forward of the trailing edge, the vorticity is displaced from the wing so as to diminish its contribution to the downwash at the surface. In consequence, extra vorticity or lift is required to maintain tangential flow there. Possibly the first analytical method to determine the non-linear effects of incidence on such lines is the non-linear lifting surface theory for rectangular wings developed by Bollay [3]. Bollay's mathematical model has a continuous distribution of vortices trailing from the wing tips along straight lines inclined at an arbitrary, but constant, angle to the wing surface, implying a uniform spanwise loading and flow separation at the wing tips (Section A.5.2). In 1961, Gersten published a non-linear theory that is in principle applicable to any wing planform in steady incompressible flow. In Gersten's mathematical model, the trailing vorticity is shed from each point of the lifting surface at an angle of exactly half the angle of attack to the plane of the wing (Section A.5.3). It has been demonstrated that releasing free trailing vortices from the surface and/or from the leading and side edges generates non-linear lift forces. The induced flow, arising from the trailing vortices whose trajectories cover the lifting surface, causes the additional lift force.

The non-linear lifting surface theories developed by Bollay and Gersten may be of interest for submerged vanes with respect to prediction of the mean lift and drag forces. By regarding a vane protruding above a rigid bed as a semi-span wing and by applying the method of images to account for interference effects of the boundaries in an open channel, vorticity models can be generated, which are equivalent to the mathematical models of Bollay and Gersten. Once equivalent mathematical models were derived, no further adjustments to theories developed by Bollay and Gersten were found necessary at this stage (possible improvements of the mathematical models can be designated; however, all at the cost of simplicity of analyses). Thus, adopting the theories by Bollay and Gersten, relations can be derived to calculate the hydrodynamic coefficients of submerged vanes for idealized conditions with respect to the free stream and the bed above which the vane protrudes. In Section 5.3.1, a description is given of the model for a sharp-edged slender vane based on theory by Bollay. Section 5.3.2 presents a model for a sharp-edged slender vane based on non-linear theory by Gersten.

The properties of a physically possible inviscid flow are governed by the continuity equation (conservation of mass) and Euler's equation of motion. If an additional kinematical condition of irrotational flow is imposed, the flow field equation in terms of velocity potential can be determined by solving linear equations of motions with prescribed boundary conditions, thus avoiding problems associated with the non-linearity of Euler's equation [25]. The mathematical models by Bollay and Gersten address the problem of steady flow about a sharp-edged wing of negligible thickness in an inviscid, incompressible fluid by constructing the flow field by the synthesis of elementary vortex flows. As explained in Section A.1, vortex flow is irrotational everywhere except at the centre of the vortex, at which there is an infinitesimal region of infinite vorticity with a finite circulation. Therefore, the flow, as described by the mathematical models, is irrotational outside the vortex sheets formed by the wing and its wake. Rotational flow occurs throughout a wake of finite constant cross-section. Nevertheless, in consideration of the observed agreement between theory and experiment for low aspect ratio wings, the mathematical models may be sufficiently appropriate and the approximation that allows the theories to use linear equations of motion, while introducing terms involving the square of the incidence may be justified, so that the flow at the wing can be built up as a superposition of elementary potential flows [15]. It is emphasized that the method of images, as used to construct mathematical models for submerged vanes equivalent to the models by Bollay and Gersten, is also based on the superposition principle (the flow resulting from superposition of incompressible, irrotational flows is also incompressible and irrotational [25]). Use of the method is impaired in appreciable regions of rotational flow, such as in the large wakes behind blunt bodies. In the mathematical models, the regions of rotational flow in the wake are confined to the vortex sheet through the top edge of the vane exclusively (mathematical model by Bollay) or pre-dominantly (mathematical model by Gersten; the model predicts – in accordance with empirical observations for sharp-edged thin wings – that the free vortices trail mainly from the side edges (Section A.5.3)). It is therefore assumed that the use of the method of images is acceptable.

In reality, the vortex sheets separated from the leading and side edges of a sharp-edged thin plate immediately roll up into a pair of concentrated vortices with viscous cores. Outside of the vortex cores, the flow field may be considered mainly inviscid. By the agreement between theory and experiment for wings at low aspect ratio, it has been shown that the effects of the vortex sheets assumed in the theories developed by Bollay and Gersten are approximately equivalent to the effects of a single vortex core.

The analytical methods developed by Bollay and Gersten assume pre-determined shape and position of the separated vortex flow over the lifting surface and in its wake. The vortex wakes are modelled as wakes composed of straight line vortices inclined at a pre-determined angle above the surface. The flow interactions that reshape the vortex layer into the rolled-up concentrated vortices are not represented. Therefore, the methods are not able to simulate this important feature of flow over slender lifting surfaces at high angle of attack. In order to simulate correctly the flow at high angles of attack, shapes and positions of the free vortex sheets and the rolled-up concentrated vortices, which are not known a priori, must be determined by including the results of the interaction of the flow induced by the configuration and the velocities induced by the trailing vortices. In non-linear panel methods, the free vortices are allowed to separate from the lifting surface. These methods can also be modified to include in the calculations the determination of shape and position of the free rolled-up vortex lines or sheets (Section A.5.4). In contrast to these methods, the analytical methods of Bollay and Gersten do not require heavy computer processing. Still, they give a reasonable to good agreement with experimental results for low aspect ratio wings. Especially for primary design calculations for vanes with basic rectangular planforms, the relative merit of non-linear panel methods is doubtful.

5.3.1 Model based on theory developed by Bollay, 1939

Description of mathematical model

Consider a rectangular flat-plate submerged vane of negligible thickness at an angle of attack with the free stream velocity. For purposes of mathematical analyses, the solid body of the vane is replaced by a system of bound of vortices (Figure 5.3), the strength of which is determined by the boundary condition that the vane surface is a stream surface and there is no flow through the plate. The flow-tangency condition implies that the normal component of the free stream velocity must be cancelled by the normal component of the induced velocities at any point on the vane surface. At the top edge, each bound vortex is assumed to leave as a straight trailing vortex line in a plane through the top edge of the vane at angle θ with respect to the vane surface. The origin is chosen in the midst of the vane at bed level and the current variables along vane length and vane height are denoted by ξ and η, respectively.

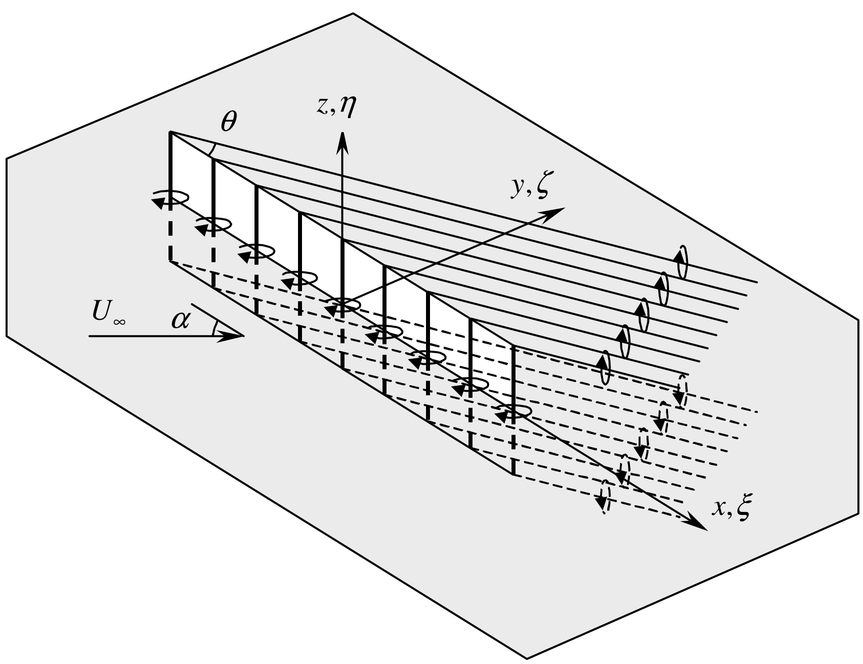

Figure 5.3: Vorticity model based on theory developed by Bollay

The interference effect of boundaries in an open channel composed by bed and free surface on the velocities induced by the bound and free trailing vortices can be accounted for analytically by applying the method of images. If the vorticity model designed to replace the vane is mirrored in the plane of the bed, a system of horseshoe vortices results. Strictly speaking, the method of images demands the generation of more mirror images of the real and image vortices by reflections in the planes of the bed and the free surface, but for the sake of simplicity, it is assumed that a single reflection in the plane of the bed is sufficient to account for interference effects. Because the trailing vortices of the vorticity model replacing the vane and its image below the bed counterrotate and are at equal distance from the bed, the resulting system of horseshoe vortices satisfies the boundary condition imposed by the presence of the bed, which states that there can be no flow through the bed. Note that the second boundary condition is satisfied as long as each (image) trailing vortex above the bed in the mathematical model has a counterrotating image vortex of equal strength below the bed. Hence, the number of (image) vortices accommodated in the mathematical model is of significance only with respect to the calculated induced velocity in the flow field, not with respect to the satisfaction of the boundary condition imposed by the presence of the bed. By the Biot-Savart law, the longer the distance between a vortex filament and an arbitrary point in the flow field, the smaller the effect of the particular vortex filament on the magnitude of the induced velocity due to all vortex filaments in that point. Therefore, the assumption of a single reflection of the bound and trailing vortices replacing the vane may be reasonable. To simplify analysis, it is further assumed that:

- the free stream is inviscid, incompressible and of uniform velocity, which is assumed constant over the flow depth,
- the vorticity distribution is constant along the height of the vane, but may vary along the length of the vane,
- the component of the induced velocity normal to the free stream direction (downwash) is constant along the height of the vane and equal to the value at the origin,
- the trailing vortex sheet remains in the plane through the top edge of the vane and the trailing vortices follow straight lines at an effective inclination with respect to the plate,
- the bed above which the vane protrudes is flat and rigid.

Derivation of hydrodynamic coefficients

The aspect ratio of the rectangular plate composed by vane and image below the bed is defined as

$$AR = \frac{2H_v}{L_v} \tag{5.1}$$

First, the velocities induced by bound and trailing vortices along the centreline of the plate are calculated by the Biot-Savart law for any point along the chord with length L_v. The induced velocity normal to the plate due to the bound vortices w_{y1} is obtained from the integrated effect of the bound vortices over the chord length. In the plane of the bound vortices, the tangential induced velocity w_x is zero. At infinitesimal distances on both sides of the plate, however, the tangential induced velocities w_{x1} are non-zero. After normalizing x and ξ by $L_v/2$, the induced velocities at the plate due to the bound vortices read

$$\begin{aligned} w_{y1} &= \frac{AR}{2\pi}\int_{-1}^{1}\frac{\gamma(\xi)}{x-\xi}\frac{1}{\sqrt{AR^2+(x-\xi)^2}}d\xi \\ w_{x1} &= \pm\frac{\gamma(x)}{2} \end{aligned} \tag{5.2}$$

The induced velocities due to the trailing vortices normal to the plate w_{y2} and tangential to the plate w_{x2} are obtained from the integrated effect of the trailing vortices from both ends of the span, and yield (in dimensionless co-ordinates)

$$\begin{aligned} w_{y2} &= \frac{AR\cos\theta}{2\pi}\int_{-1}^{1}\frac{\gamma(\xi)}{AR^2+(x-\xi)^2\sin^2\theta}\left[\frac{(x-\xi)\cos\theta}{\sqrt{AR^2+(x-\xi)^2}}+1\right]d\xi \\ w_{x2} &= w_{y2}\tan\theta \end{aligned} \tag{5.3}$$

The integral equation, which determines the strength of the vorticity along the chord $\gamma(\xi)$ can be found by expressing the flow-tangency condition,

$$w_{y1}(x) + w_{y2}(x) = U_\infty \sin\alpha \tag{5.4}$$

If instead of finding the pressure distribution over the plate, the problem is restricted to finding the total force only, the integral equation only has to be satisfied in the mean. Expressing the condition that the mean value of the induced velocity over the chord must equal the normal component of the free stream velocity,

$$\frac{1}{2}\int_{-1}^{1}\left[w_{y1}(x)+w_{y2}(x)\right]dx=U_\infty \sin\alpha \tag{5.5}$$

or, interchanging the order of integration of x and ξ,

$$\frac{AR}{4\pi}\int_{-1}^{1}\gamma(\xi)d\xi I_1+\frac{AR}{4\pi}\int_{-1}^{1}\gamma(\xi)\cos\theta d\xi I_2+\frac{AR}{4\pi}\int_{-1}^{1}\gamma(\xi)\cos^2\theta d\xi I_3=U_\infty\sin\alpha \tag{5.6}$$

in which

$$\begin{aligned}
I_1&=\int_{-1}^{1}\frac{dx}{(x-\xi)\sqrt{AR^2+(x-\xi)^2}}\\
&=\frac{1}{AR}\ln\left[\frac{AR+\sqrt{AR^2+(1+\xi)^2}}{AR+\sqrt{AR^2+(1-\xi)^2}}\frac{1-\xi}{1+\xi}\right]\\
I_2&=\int_{-1}^{1}\frac{dx}{AR^2+(x-\xi)^2\sin^2\theta}\\
&=\frac{1}{AR\sin\theta}\left[\tan^{-1}\left(\frac{(1+\xi)\sin\theta}{AR}\right)+\tan^{-1}\left(\frac{(1-\xi)\sin\theta}{AR}\right)\right]\\
I_3&=\int_{-1}^{1}\frac{(x-\xi)dx}{\left[AR^2+(x-\xi)^2\sin^2\theta\right]\sqrt{AR^2+(x-\xi)^2}}\\
&=\frac{-1}{AR\sin\theta\cos\theta}\left[\tan^{-1}\left(\frac{\tan\theta}{AR}\sqrt{AR^2+(1+\xi)^2}\right)-\tan^{-1}\left(\frac{\tan\theta}{AR}\sqrt{AR^2+(1-\xi)^2}\right)\right]
\end{aligned} \tag{5.7}$$

Assuming that the chordwise vorticity distribution may be given by [4]

$$\gamma(\xi)=\gamma_0\sqrt{\frac{1-\xi}{1+\xi}} \tag{5.8}$$

which holds for flat-plate wings at high aspect ratio, constant γ_0 can be determined by substituting Equation (5.8) into Equation (5.6),

$$\frac{\gamma_0}{4\pi}F_1+\frac{\gamma_0\cos\theta}{4\pi\sin\theta}F_2-\frac{\gamma_0\cos\theta}{4\pi\sin\theta}F_3=U_\infty\sin\alpha \tag{5.9}$$

in which

$$\begin{aligned}
F_1&=\int_{-1}^{1}\sqrt{\frac{1-\xi}{1+\xi}}\left[\ln\frac{AR+\sqrt{AR^2+(1+\xi)^2}}{AR+\sqrt{AR^2+(1-\xi)^2}}-\ln\frac{1+\xi}{1-\xi}\right]d\xi\\
F_2&=\int_{-1}^{1}\sqrt{\frac{1-\xi}{1+\xi}}\left[\tan^{-1}\left(\frac{(1+\xi)\sin\theta}{AR}\right)+\tan^{-1}\left(\frac{(1-\xi)\sin\theta}{AR}\right)\right]d\xi\\
F_3&=\int_{-1}^{1}\sqrt{\frac{1-\xi}{1+\xi}}\left[\tan^{-1}\left(\frac{\tan\theta}{AR}\sqrt{AR^2+(1+\xi)^2}\right)-\tan^{-1}\left(\frac{\tan\theta}{AR}\sqrt{AR^2+(1-\xi)^2}\right)\right]d\xi
\end{aligned} \tag{5.10}$$

Solving Equation (5.10) for the constant γ_0 gives [4],

$$\gamma_0 = \frac{4\pi U_\infty \sin\alpha}{F_1 + F_2 \cot\theta - F_3 \cot\theta} \tag{5.11}$$

so that the problem is reduced to solving integrals F_1, F_2 and F_3.

The first part of integral F_1 is not integrable by elementary methods. Therefore, the integral is solved by means of an expansion approximation under assumptions that restrict the validity of the analysis to plates of $AR < 1$ [4]:

$$\ln\left(AR + \sqrt{AR^2 + p^2}\right) \approx \ln\left(AR + p\right) + ke^{-\lambda p} \tag{5.12}$$

with $p = 1 \pm \xi$, where the constants k and λ are determined to fit the difference curve of

$$\left[\ln\left(AR + \sqrt{AR^2 + p^2}\right) - \ln\left(AR + p\right)\right] \tag{5.13}$$

at $p = 0$ and $p = AR$. Integral F_2 can be evaluated exactly using the method of contour integration. An expansion approximation is again applied to solve integral F_3 under the same assumptions made in evaluating integral F_1. The resulting evaluated integrals are [4]

$$\begin{aligned}
F_1 &= \frac{2\pi AR}{AR+2} + \frac{4\pi}{AR+2}\sqrt{\frac{AR}{AR+2}}\,\frac{\sqrt{\frac{AR}{AR+2}}+2}{\left(\sqrt{\frac{AR}{AR+2}}+1\right)^2} + 4.35e^{-\frac{1.302}{AR}} I_1\left(\frac{1.302}{AR}\right) \\
F_2 &= 2\pi \tan^{-1}\mu - 4\pi \tan^{-1}\left(\frac{\sin\left(\frac{1}{2}\tan^{-1}\mu\right)}{\sqrt[4]{1+\mu^2} + \cos\left(\frac{1}{2}\tan^{-1}\mu\right)}\right) \\
F_3 &= 4\pi\left[\frac{1}{\nu} - \frac{1}{\nu}\frac{\cos\left(\frac{1}{2}\tan^{-1}\nu\right)}{\sqrt[4]{1+\nu^2}} - \frac{\sin\left(\frac{1}{2}\tan^{-1}\nu\right)}{\sqrt[4]{1+\nu^2}}\right] + 2\pi\theta e^{-\lambda} I_1\left(\lambda\right)
\end{aligned} \tag{5.14}$$

in which $I_1\left(\lambda\right)$ represents a Bessel function with imaginary argument of the order of 1 with

$$\lambda = -\frac{1}{AR}\ln\left[\frac{\tan^{-1}\left(\sqrt{2}\tan\theta\right)}{\theta} - 1\right] \tag{5.15}$$

and in which

$$\begin{aligned}
\mu &= \frac{2\sin\theta}{AR} \\
\nu &= \frac{2\tan\theta}{AR}
\end{aligned} \tag{5.16}$$

Note that F_3 can be expressed as the sum of two terms that are functions of ν and λ. By defining new parameters, Equation (5.11) can be rewritten to

$$\gamma_0 = \frac{U_\infty \sin\alpha}{F_1'\left(AR\right) + \cot\theta\left[A\left(\mu\right) + B\left(\nu\right) - \theta C\left(\lambda\right)\right]} \tag{5.17}$$

in which

$$
\begin{aligned}
&F_1'(AR)=\frac{F_1}{4\pi}\\
&A(\mu)=\frac{F_2}{4\pi}\\
&B(\nu)=-\frac{1}{\nu}+\frac{1}{\nu}\frac{\cos\left(\frac{1}{2}\tan^{-1}\nu\right)}{\sqrt[4]{1+\nu^2}}+\frac{\sin\left(\frac{1}{2}\tan^{-1}\nu\right)}{\sqrt[4]{1+\nu^2}}\\
&C(\lambda)=\frac{1}{2}e^{-\lambda}I_1(\lambda)
\end{aligned}
\tag{5.18}
$$

In the high aspect ratio wing theory, which assumes low angles of attack, the effect of the induced velocity tangential to the plate is neglected. Because the angles of attack may run up to 45° before low aspect ratio wings 'stall', it is necessary to consider the tangential induced velocities in the calculation of the forces acting. The bound vortices induce a velocity tangential to the plate of $\gamma(x)/2$ at the suction side and of $-\gamma(x)/2$ at the pressure side. The mean value at the plate due to the bound vortices is therefore zero. The trailing vortices, however, induce tangential velocity w_{x2} given by Equation (5.3) along the plate. The mean value of the tangential induced velocity over the chord is then given as

$$
\begin{aligned}
\overline{w_x}&=\frac{\gamma_0}{4\pi}\left[F_2-F_3\right]=\gamma_0\left[A(\mu)+B(\nu)-\theta C(\lambda)\right]\\
&=U_\infty\sin\alpha\tan\theta-F_1'(AR)\gamma_0\tan\theta
\end{aligned}
\tag{5.19}
$$

The inclination of the trailing vortices with respect to the plate θ is determined by Helmholtz's vortex law, which states that a free vortex filament follows the fluid particles. Thus, the vortex will lie along the resultant velocity vector. In the foregoing analysis, the inclination of the resultant velocity vector has been assumed constant. As an approximation of the mean value of the effective inclination, the effective inclination θ at which the vortices supposedly leave the plate is chosen, supported by the idea that the vortices right near the plate are the most effective in determining the local downwash. With these approximations, the resultant velocity vector at the side of the plate can be determined. Expressing the fact that the induced velocities at the sides of the plate are exactly half as much as the induced velocities would be at the centre of a plate of twice the span, because only the opposite vortex sheet can induce velocities in x- and y-directions in the plane of the side of the plate, the mean values of the induced velocities at the sides of the plate yield [4]

$$
\begin{aligned}
&\overline{w_{y1}}=\frac{\gamma_0}{4\pi}\frac{F_1(2AR)}{2}=\gamma_0\frac{F_1'(2AR)}{2}\\
&\overline{w_{y2}}=\frac{\gamma_0\cos\theta}{4\pi\sin\theta}\left[\frac{F_2(2AR)-F_3(2AR)}{2}\right]=\frac{\gamma_0\cot\theta}{2}\left[A\left(\frac{\mu}{2}\right)+B\left(\frac{\nu}{2}\right)-\theta C\left(\frac{\lambda}{2}\right)\right]\\
&\overline{w_{x1}}=\frac{1}{2L_v}\int_{-L_v/2}^{L_v/2}\frac{\gamma(\xi)}{2}d\xi=\frac{\pi}{8}\gamma_0\\
&\overline{w_{x2}}=\overline{w_{y2}}\tan\theta
\end{aligned}
\tag{5.20}
$$

The inclination of the resultant velocity vector reads

$$\tan\theta = \frac{U_\infty \sin\alpha - \overline{w_{y1}} - \overline{w_{y2}}}{U_\infty \cos\alpha + \overline{w_{x1}} + \overline{w_{x2}}}$$
$$= \frac{\sin\alpha - \dfrac{\gamma_0}{2U_\infty}\left[F_1'(2AR) + \cot\theta\left(A\left(\dfrac{\mu}{2}\right) + B\left(\dfrac{\nu}{2}\right) - \theta C\left(\dfrac{\lambda}{2}\right)\right)\right]}{\cos\alpha + \dfrac{\gamma_0}{2U_\infty}\left[\dfrac{\pi}{4} + \left(A\left(\dfrac{\mu}{2}\right) + B\left(\dfrac{\nu}{2}\right) - \theta C\left(\dfrac{\lambda}{2}\right)\right)\right]} \tag{5.21}$$

By applying the formula for the force on a vortex, the normal force acting on the plate F_N is calculated as

$$F_N = 2\rho\left(U_\infty \cos\alpha + \overline{w_x}\right)\Gamma H_v \tag{5.22}$$

in which

$$\Gamma = \int_{-L_v/2}^{L_v/2} \gamma(\xi)d\xi = \gamma_0 \int_{-L_v/2}^{L_v/2} \sqrt{\frac{L_v/2 - \xi}{L_v/2 + \xi}}d\xi = \frac{\pi}{2}\gamma_0 L_v \tag{5.23}$$

The normal force coefficient is defined as

$$C_N = \frac{F_N}{\frac{1}{2}\rho U_\infty^2 2H_v L_v} \tag{5.24}$$

By substituting Equations (5.17), (5.19) and (5.22) into Equation (5.24), the formula for the normal force coefficient finally reads

$$C_N = \pi\frac{\gamma_0}{U_\infty}\left[\cos\alpha + \sin\alpha\tan\theta - F_1'(AR)\frac{\gamma_0}{U_\infty}\tan\theta\right] \tag{5.25}$$

Calculation procedure

For convenience, the formulae required for the calculation of the normal force coefficient are summarized on the next page. Because γ_0/U_∞ is a function of θ, Equation (5.21) can only be solved for θ by iteration. As a first approximation, it is advised to assume $\theta = \alpha/2$, calculate γ_0/U_∞ and functions A, B and C, and then obtain a new expression for $\tan\theta$. The iteration process should be repeated until the assumed and resultant values for θ agree. Figure 5.4 presents plots of functions $F_1'(AR)$, $A(\mu)$, $B(\nu)$ and $C(\lambda)$. Note that all angles used in evaluating Equations (5.26) and (5.27) are in radians.

$$C_N = \pi\frac{\gamma_0}{U_\infty}\left[\cos\alpha + \sin\alpha\tan\theta - F_1'(AR)\frac{\gamma_0}{U_\infty}\tan\theta\right]$$
$$\frac{\gamma_0}{U_\infty} = \frac{\sin\alpha}{F_1'(AR) + \cot\theta\left[A(\mu) + B(\nu) - \theta C(\lambda)\right]} \tag{5.26}$$
$$\tan\theta = \frac{\sin\alpha - \dfrac{\gamma_0}{2U_\infty}\left[F_1'(2AR) + \cot\theta\left(A\left(\dfrac{\mu}{2}\right) + B\left(\dfrac{\nu}{2}\right) - \theta C\left(\dfrac{\lambda}{2}\right)\right)\right]}{\cos\alpha + \dfrac{\gamma_0}{2U_\infty}\left[\dfrac{\pi}{4} + \left(A\left(\dfrac{\mu}{2}\right) + B\left(\dfrac{\nu}{2}\right) - \theta C\left(\dfrac{\lambda}{2}\right)\right)\right]}$$

in which

$$F_1'(AR)=\frac{AR}{2(AR+2)}+\frac{1}{AR+2}\sqrt{\frac{AR}{AR+2}}\frac{\sqrt{\frac{AR}{AR+2}}+2}{\left(\sqrt{\frac{AR}{AR+2}}+1\right)^2}+\frac{\ln 2}{2}e^{-\frac{1.302}{AR}}I_1\left(\frac{1.302}{AR}\right)$$

$$A(\mu)=\frac{1}{2}\tan^{-1}\mu-\tan^{-1}\left(\frac{\sin\left(\frac{1}{2}\tan^{-1}\mu\right)}{\sqrt[4]{1+\mu^2}+\cos\left(\frac{1}{2}\tan^{-1}\mu\right)}\right)$$

$$B(\nu)=-\frac{1}{\nu}+\frac{1}{\nu}\frac{\cos\left(\frac{1}{2}\tan^{-1}\nu\right)}{\sqrt[4]{1+\nu^2}}+\frac{\sin\left(\frac{1}{2}\tan^{-1}\nu\right)}{\sqrt[4]{1+\nu^2}}$$

$$C(\lambda)=\frac{1}{2}e^{-\lambda}I_1(\lambda) \tag{5.27}$$

$$\mu=\frac{2\sin\theta}{AR}$$

$$\nu=\frac{2\tan\theta}{AR}$$

$$AR=\frac{2H_v}{L_v}$$

where $I_1(\lambda)$ is a Bessel function with imaginary argument of the order of 1.

Figure 5.5 presents the effective inclination θ, the angle with respect to the plate at which the trailing vortices leave the plate, in terms of the aspect ratio. Notice the peculiar increase of the value of θ with the aspect ratio, with a maximum at about $AR=0.35$ for mediocre angles of attack. Figure 5.5 also displays a plot of the normal force coefficient versus the angle of attack. The results of calculations of the normal force coefficients for the limiting cases of plates at infinite aspect ratio (finite chord and infinite span) and at zero aspect ratio (finite span and infinite chord) are included. For a flat plate of zero aspect ratio, the normal force coefficient yields

$$C_{N_{AR=0}}=2\sin^2\alpha \tag{5.28}$$

Equation (5.28) suggests that a vane at extremely low aspect ratio behaves similar to a so-called Newtonian flat plate, which experiences a normal force proportional to the time rate of change of momentum of fluid particles colliding with the plate. The component of the free stream velocity normal to surface S is $U_\infty \sin\alpha$. From Newton's second law, with mass of flow incident on surface equal to $\rho S U_\infty \sin\alpha$ and time rate of change of momentum equal to $U_\infty \sin\alpha$, the normal force on the plate yields

$$F_N=\rho\left(U_\infty \sin\alpha\right)^2 S \quad \Rightarrow \quad C_N=2\sin^2\alpha \tag{5.29}$$

By extrapolation of experimental values of the normal force coefficient to zero aspect ratio, the validity of Equation (5.28) has been confirmed. It is seen that the theory correctly predicts the normal force coefficient in the limiting case of zero aspect ratio. In contrast to the limiting case of infinite aspect ratio, the result for the limiting case of zero aspect ratio depends greatly on angle θ, which suggests that, at low aspect ratios, the assumption that the free vortices leave at some angle with respect to the surface is of basic importance [4].

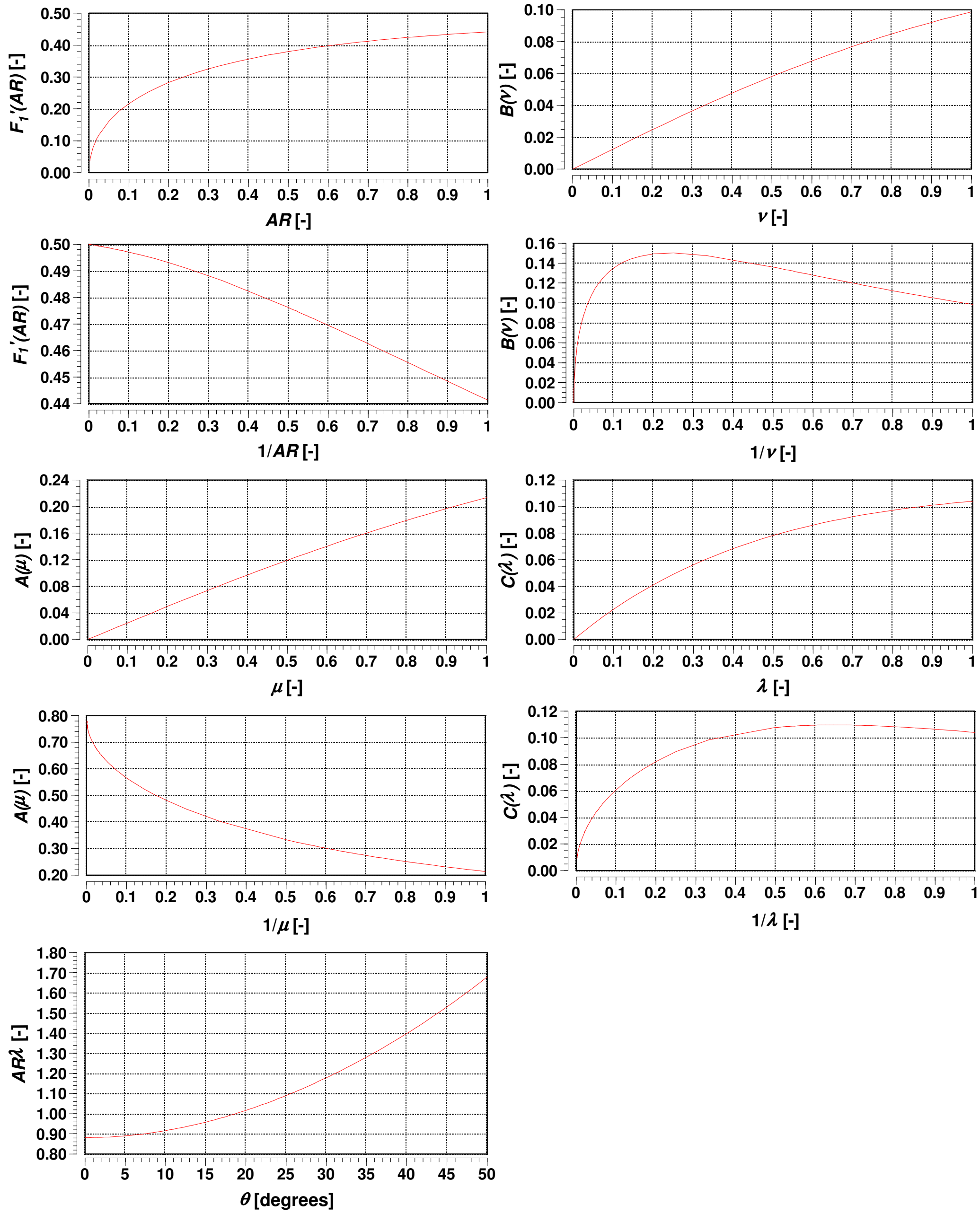

Figure 5.4: Plots of functions A, B and C

Discussion

The validity of several fundamental assumptions is verified by experimental results for low aspect ratio wings. The assumption of a constant lift distribution across the span is verified exactly for the zero aspect ratio wing [4] and pressure measurements by Winter [55] indicate that the assumption is still good even at $AR = 1$. The assumed chordwise vorticity distribution along the chord (Equation (5.8)) also seems reasonable from measurements at $AR = 1$. Measured pressure distributions indicate that the actual solution of the integral equation for the chordwise vorticity distribution is quite complicated, so that the assumption of some mean distribution as given by Equation (5.8) is reasonable in view of the necessity to approach the actual distribution theoretically. In comparisons to experimental results for rectangular wings at low and intermediate aspect ratio (Section A.5.2), a very good agreement is obtained with the non-linear theory by Bollay at extremely low aspect ratios. With increasing aspect ratio, calculated normal force coefficients depart more and more from experimental values.

Discrepancies are probably due to the approximation used for the effective inclination at which the trailing vortices leave. For $AR > 2$, the linear lifting line theory fits better with experimental data. The non-linear theory by Bollay here no longer holds as the assumption of a constant lift distribution along the span breaks down and the approximations used in expanding the integrals become less satisfactory at high aspect ratios.

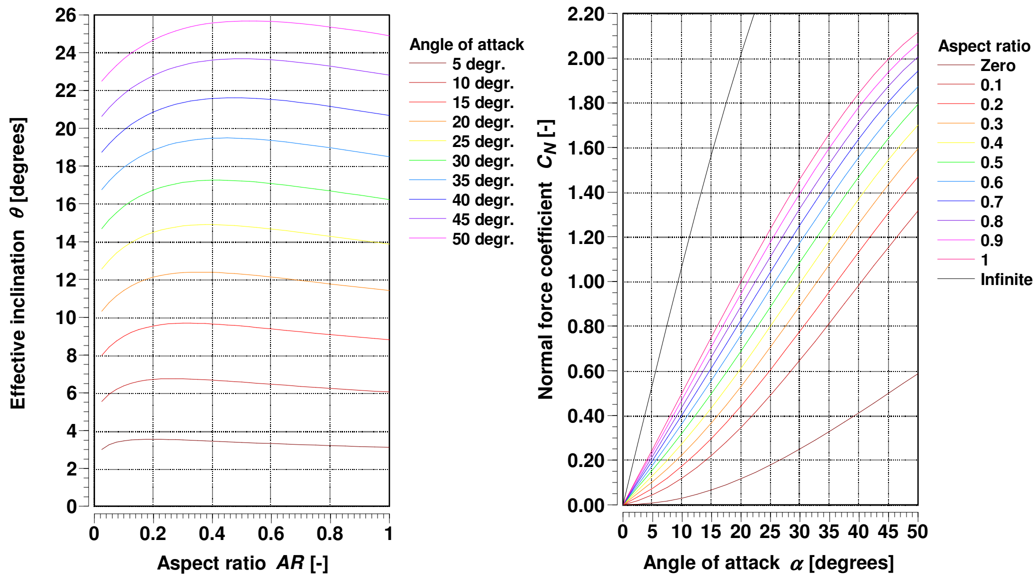

Figure 5.5: Plots of effective inclination (left) and normal force coefficient (right)

The assumption that the trailing vortices leave at an angle with respect to the plate for low aspect ratios seems to be verified by flow pictures taken by Winter [55]. For low angles of attacks, a smooth type of flow is discerned, which explains the reasonable agreement of the lifting line theory with regard to the initial tangents of the curves in Figure A.6. At high angles of attack, however, a strong tip flow occurs with vortices leaving the plate at the sides, which actually roll up immediately into a single vortex core. Apparently, the vortex sheets assumed in the non-linear theory developed by Bollay are unstable, but, by the agreement between theory and experimental data, their effects are approximately equivalent to a single vortex core.

By assuming that the trailing vortices follow straight lines at an effective inclination with respect to the plate, the Helmholtz' condition (Section A.3) that vortex filaments must follow streamlines is partially violated. Due to the effects of velocity perturbations, the trailing vortices are not actually straight lines but lie along curved paths. It is emphasized that the lifting line theory by Prandtl (Section A.3), which assumes the trailing vortices to be carried along the direction of the undisturbed flow, similarly violates Helmholtz' vortex laws.

A number of refinements to the current mathematical model for submerged vanes based on theory by Bollay can be designated, however, all at the cost of simplicity of analysis:

- Obviously, the assumption that a single reflection of the bound and free trailing vortices in the plane of the bed is sufficient to account for interference effects of boundaries breaks down with increasing ratio of vane height to flow depth. In order to expand the range of relative vane submergence, for which interference effects caused by both bed and free surface are accounted for adequately, the mathematical model should be improved by applying reflections in the plane of the free surface as well as in the plane of the bed, using a low Froude number approximation, which allows the free surface to be taken as a rigid boundary. However, the calculation of induced velocities corresponding to all real and image vortices would then be complicated considerably. At design stage, the ratio of vane height to flow depth should be in the range of 0.4 to 0.5, according to Odgaard and Spoljaric [37]. Possibly, in view of the findings in Section 5.5, the assumption that a single reflection of the vortices in the plane of the bed is sufficient to account for interference effects of boundaries is still reasonable at ratios of vane height to flow depth up to 0.5.

- A better method of determining the effective inclination of trailing vortices might improve agreement with experimental results. In the present analysis, the inclination of the trailing vortices with respect to the plate is determined by Helmholtz's vortex law, which states that a free vortex follows the fluid particles. Thus, the vortex will lie along the resultant velocity vector. The inclination of the resultant velocity vector and therefore, the directions of the vortex trajectories vary in space. However, in the theory developed by Bollay, the inclination of the resultant velocity vector is assumed constant. As an approximation of the mean value of the effective inclination, the inclination at which the vortices leave the plate is chosen, supported by the idea that the vortices right near the plate are the most effective in determining the local downwash. Furthermore, as an approximation, it is assumed that the trailing vortices remain in the planes through the top edge of the vane, thus neglecting the component of the induced velocity in z-direction (Figure 5.3) when applying the Helmholtz condition.

Based on observed agreements between theory and experiment for wings at low aspect ratios (Section A.5.2), it is expected that the model based on non-linear theory by Bollay predicts satisfactorily the normal force coefficient on a sharp-edged, slender rectangular vane protruding above a rigid bed at an aspect ratio lower than 0.2 (ratio of vane height to vane length lower than 0.1) and an angle of attack up to 30° to 40°, provided the ratio of vane height to flow depth is not too high.

5.3.2 Model based on theory developed by Gersten, 1961

Description of mathematical model

Consider a flat-plate submerged vane of negligible thickness and arbitrary planform at an angle with respect to the free stream velocity. According to practice in the linear lifting surface theory, regard the plate as consisting of infinitesimal lifting elements (Figure A.7). In the linear theory by Truckenbrodt [49], the lifting elements have a chordwise vorticity distribution and free vortices leaving the trailing edge in the plane of the element.

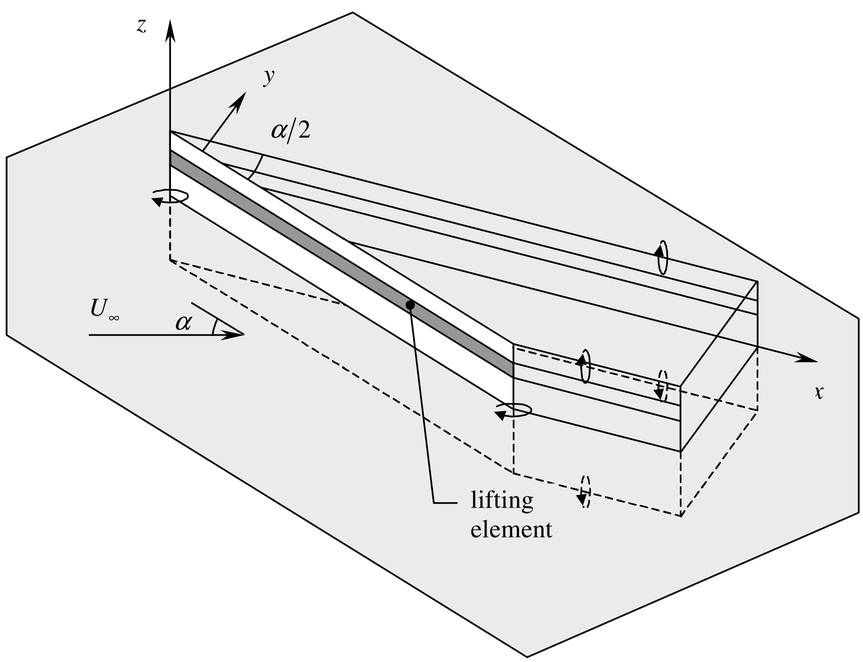

Figure 5.6: Vorticity model based on theory developed by Gersten

Gersten proposed to alter the vorticity model of the lifting element by Truckenbrodt into a lifting element model based on theory developed by Bollay (Section 5.3.1), where the trailing vortices are no longer forced to remain in the plane of the element, but incline at an angle of exactly half the angle of attack with respect to the element surface (Figure 5.7) [16]. In effect, Gersten has applied Bollay's mathematical model to each lifting element. All the vorticity is shed instantly in planar sheets inclined at an angle of half the angle of attack with respect to the plate. Thus, rotational flow occurs throughout a wake of finite constant cross-section.

Figure 5.6 presents a schematic of Gersten's mathematical model applied to a rectangular submerged vane under the assumption that reflecting all the vorticity of the lifting elements by the method of images in the plane of the bed only is sufficient to account for interference effects due to boundaries in an open channel. Hence, the effect of image vortices in the plane of the free surface on the induced velocity in the flow field is neglected. Because the trailing vortices of each lifting element and of its image below the bed counterrotate and are placed at equal distance from the plane of the bed, the resulting system of bound and free trailing vortices satisfies the boundary condition imposed by the presence of the bed, which states that there can be no flow through the plane of the bed. It is further assumed that:

- the free stream is inviscid, incompressible and of uniform velocity, which is assumed constant over the flow depth,
- the plate is of negligible thickness, but may have small arbitrary incidence, camber and twist whose squares can be ignored,
- the bed above which the vane protrudes is flat an rigid,
- the flow is irrotational outside the vortex sheet formed by vane and wake,
- all the vorticity is shed in planar sheets; i.e., the trailing vortices follow straight lines at an angle of $\alpha/2$ with respect to the plate,
- the squares and products of perturbations u/U_∞, v/U_∞ and w/U_∞ are negligible.

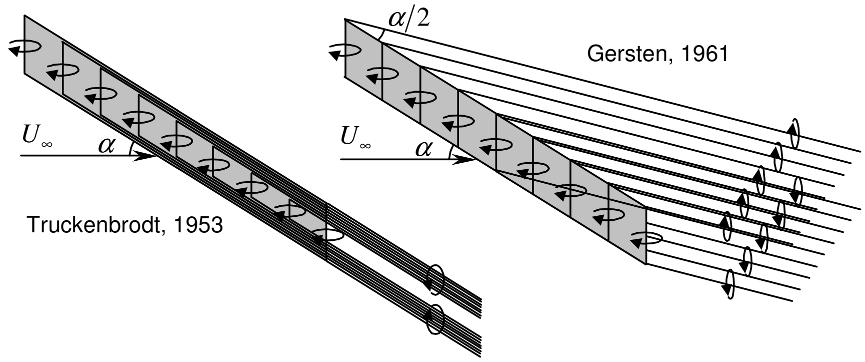

Figure 5.7: Lifting elements according to Truckenbrodt, 1953 and Gersten, 1961

The main task is to calculate the induced velocity at the plate surface by the mathematical model, so that the vorticity distribution can be found by the flow-tangency condition, which states that the direction of the resultant velocity of free stream and induced velocity is tangential to the surface at every point on the plate. Because the chordwise induced velocity is small compared to the chordwise component of the free stream velocity, the angle of the resultant velocity at the plate surface equates the induced angle of attack, given by [16]

$$\alpha_i = -\frac{v}{U_\infty} \tag{5.30}$$

in which v represent the induced velocity component normal to the plate surface. In the limit $\alpha \to 0$, the mathematical model approximates a model equivalent to the mathematical model in linear lifting surface theory.

For a constant vorticity distribution $\gamma(x,z)$ and using linear lifting surface theory, the induced angle of attack at the plate surface yields [16]

$$\alpha_i = L_1(\gamma) \tag{5.31}$$

and the flow tangency-condition then becomes

$$\alpha_{loc} = \alpha_i = L_1(\gamma) \tag{5.32}$$

in which L_1 represents a linear operator (in fact, a complex Doppler-integral) with properties

$$L_1(r\gamma) = rL_1(\gamma)$$
$$L_1(\gamma_1 + \gamma_2) = L_1(\gamma_1) + L_1(\gamma_2) \tag{5.33}$$

In order to determine the flow-tangency condition for the non-linear mathematical model, Equation (5.30) must be expanded in terms that also depend on the angle of attack. By rising additional terms in powers of the angle of attack, the flow-tangency condition becomes [16]

$$\alpha_{loc} = \alpha_i = L_1(\gamma) + \frac{\alpha}{|\alpha|}\alpha L_2(\gamma) + \ldots \tag{5.34}$$

in which operator L_2 has the same properties as linear operator L_1. Equation (5.34) can be solved by assuming that the vorticity distribution may be divided into a linear part γ_1 and a non-linear part γ_2 as

$$\gamma = \gamma_1\alpha + \gamma_2\frac{\alpha}{|\alpha|}\alpha^2 \tag{5.35}$$

Using the properties of the operators given by Equation (5.33), γ_1 and γ_2 are evaluated by

$$L_1(\gamma_1) = \frac{\alpha_{loc}}{\alpha} \tag{5.36}$$

and

$$L_1(\gamma_2) = -\frac{\alpha_{loc}}{\alpha}L_2(\gamma_1) \tag{5.37}$$

Equation (5.36) is identical to the linear lifting surface equation, which can therefore be solved for γ_1 accordingly. The non-linear part of the assumed vorticity distribution can then be calculated by solving Equation (5.37) for γ_2. Finally, the lift and pitching moment coefficients follow from

$$C_L = C_N = \frac{2}{SU_\infty}\iint_S \gamma(x,z)dxdz$$
$$C_M = -\frac{2}{Sc_\mu U_\infty}\iint_S x\gamma(x,z)\,dxdz \tag{5.38}$$

in which $c_\mu = \frac{1}{S}\int_{-b/2}^{b/2} c^2 dz$ with $S = \frac{b^2}{AR}$.

Derivation of hydrodynamic coefficients

For the evaluation of the linear terms, Gersten used the linear surface theory for wings of arbitrary planform developed by Truckenbrodt [49], which assumes a constant distribution of vorticity at the wing surface. Figure 5.8 shows a representation of a submerged vane as a semi-span wing model according to the linear lifting surface theory of Truckenbrodt.

Assuming a constant vorticity distribution $\gamma(x',z')$ at the plate surface, an elementary horseshoe vortex of strength $\gamma(x',z')dx'$ trails at every point on the surface (Figure 5.8). All horseshoe vortices starting at line x' induce a velocity component in y-direction (normal to the plate) in point $P(x,0,z)$, whose magnitude can be calculated by the Biot-Savart law,

$$dv(x,z) = -\frac{1}{4\pi} \int\limits_{\substack{-b/2 \\ Cauchy}}^{b/2} \frac{\frac{d}{dz'}\left[\gamma(x',z')\left(1+\frac{x-x'}{R}\right)\right]dx'}{z-z'} dz' \tag{5.39}$$

in which $R=\sqrt{(x-x')^2+(z-z')^2}$ and the integral is a Cauchy principal value integral (the calculation of the induced velocity components v and w in the vortex sheet ($y=0$) requires special treatment at $z=z'$; see [16]) defined as

$$\int\limits_{\substack{-b/2 \\ Cauchy}}^{b/2} \ldots dz' = \lim_{\varepsilon \to 0} \left\{ \int\limits_{-b/2}^{z-\varepsilon} \ldots dz' + \int\limits_{z+\varepsilon}^{b/2} \ldots dz' \right\} \tag{5.40}$$

The induced angle of attack results from the integrated effect of $dv(x,z)$ in x'-direction. After changing the order of integration [16],

$$\alpha_i = -\frac{v}{U_\infty} = \frac{1}{4\pi U_\infty} \int\limits_{\substack{-b/2 \\ Cauchy}}^{b/2} \int\limits_{x_v}^{x_h} \frac{\frac{d}{dz'}\left[\gamma(x',z')\left(1+\frac{x-x'}{R}\right)\right]}{z-z'} dx'dz' \tag{5.41}$$

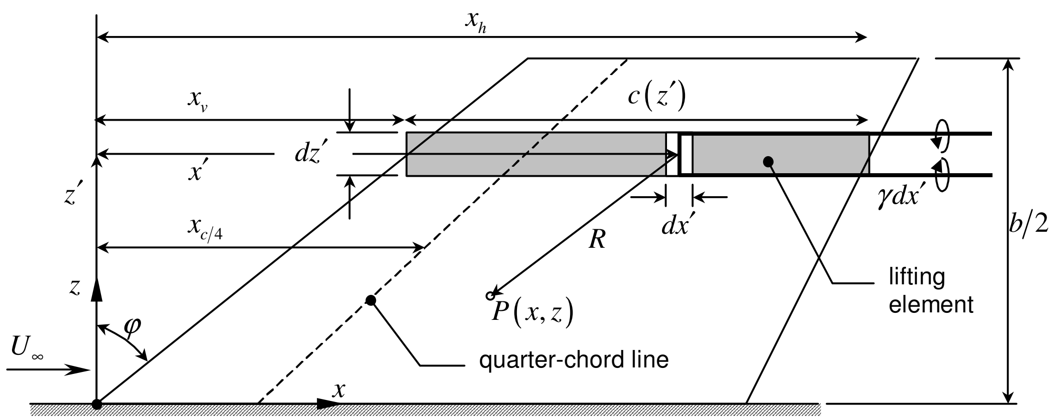

Figure 5.8: Representation of a vane as a semi-wing according to linear theory by Truckenbrodt

It is assumed that the vorticity distribution $\gamma(x,z)$ may be given by

$$\gamma(\varphi,\vartheta) = \frac{2}{\pi}\frac{bU_\infty}{c(\vartheta)}\left[\gamma(\vartheta)\cot\frac{\varphi}{2} + 4\mu(\vartheta)\left(\cot\frac{\varphi}{2} - 2\sin\varphi\right)\right] \tag{5.42}$$

with $\frac{1}{2}(1-\cos\varphi) = \frac{x'-x_v(z')}{c(z')}$ and $\cos\vartheta = \eta' = \frac{2z'}{b}$.

The vorticity distribution in x'-direction for a constant z' arises from the first and second Birnbaum normal distributions [32], the strength of which varies along the span (the use of Birnbaum normal distributions may be explained historically by successful applications in early theories for wings of quite arbitrary planform [49]). The Birnbaum normal distributions are determined by vorticity distribution $\gamma(\vartheta)$ and pitching moment distribution $\mu(\vartheta)$. Hence, the analysis now focuses on finding functions $\gamma(\vartheta)$ and $\mu(\vartheta)$.

Introducing dimensionless co-ordinates $\xi = \frac{x}{b/2}$, $\eta = \frac{y}{b/2}$, $\xi' = \frac{x'}{b/2}$ and $\eta' = \frac{y'}{b/2}$, the flow-tangency condition in the linear theory of Truckenbrodt [49] reads

$$\alpha(\xi,\eta) = \alpha_i(\xi,\eta) = -\frac{v}{U_\infty} = L(\gamma,\mu) = \frac{1}{2\pi}\int_{\substack{-1\\ Cauchy}}^{1} \frac{\frac{d}{d\eta'}(i\gamma + j\mu)}{\eta - \eta'} d\eta' \tag{5.43}$$

in which the influence functions $i(X,Z)$ and $j(X,Z)$ yield

$$\begin{aligned} i(X,Z) &= \frac{2}{\pi c}\int_{x_v}^{x_h} \cot\frac{\varphi}{2}\left(1 + \frac{x - x'}{R}\right) dx' \\ j(X,Z) &= \frac{8}{\pi c}\int_{x_v}^{x_h} \left(\cot\frac{\varphi}{2} - 2\sin\varphi\right)\left(1 + \frac{x - x'}{R}\right) dx' \\ X &= \frac{x - x_v(z')}{c(z')} \\ Z &= \frac{z - z'}{c(z')} \end{aligned} \tag{5.44}$$

Because both $\gamma(\eta)$ and $\mu(\eta)$ are unknown, Equation (5.43) must be satisfied at two different lines on the plate surface. In the linear theory of Truckenbrodt, the backside of the planform (designated by *) and the quarter-chord line (designated by **) are selected:

$$\begin{aligned} \alpha^*(\eta) &= L^*(\gamma,\mu) = \frac{1}{2\pi}\int_{\substack{-1\\ Cauchy}}^{1} \frac{\frac{d}{d\eta'}(i^*\gamma + j^*\mu)}{\eta - \eta'} d\eta' \\ \alpha^{**}(\eta) &= L^{**}(\gamma,\mu) = \frac{1}{2\pi}\int_{\substack{-1\\ Cauchy}}^{1} \frac{\frac{d}{d\eta'}(i^{**}\gamma + j^{**}\mu)}{\eta - \eta'} d\eta' \end{aligned} \tag{5.45}$$

By adopting Multhopp quadrature formulae [31] to express functions $i^*\gamma$, $i^{**}\gamma$, $j^*\gamma$ and $j^{**}\mu$, which may be given by

$$\begin{aligned} \int_{-1}^{1} h(\eta) d\eta &= \frac{\pi}{m+1}\sum_{n=1}^{m} h(\eta_n)\sin\frac{n\pi}{m+1} \\ \frac{1}{2\pi}\int_{\substack{-1\\ Cauchy}}^{1} \frac{\frac{dh}{d\eta'}}{\eta - \eta'} d\eta' &= \frac{1}{a_{vv}}\left(h_v - \sum_{n=1}^{m} a_{vn} h_{vn}\Big|_{n\neq v}\right) \end{aligned} \tag{5.46}$$

in which $h(\eta)$ represents the function to evaluate, and assuming $\gamma = g_1\alpha$ and $\mu = m_1\alpha$, the solution for $g_1(\eta)$ and $m_1(\eta)$ in Equation (5.45) is presented by Truckenbrodt [49] as

$$a_{vv}\frac{\alpha_v^*}{\alpha}=\left[2+b_v\left(\frac{b}{2c_v}\right)^{\frac{3}{2}}\right]g_{1v}-\sum_{n=1}^{m}a_{vn}i_{vn}^*g_{1n}\Big|_{n\neq v}-12b_v\left(\frac{b}{2c_v}\right)^{\frac{3}{2}}m_{1v}-\sum_{n=1}^{m}a_{vn}j_{vn}^*m_{1n}\Big|_{n\neq v}$$

$$a_{vv}\frac{\alpha_v^{**}}{\alpha}=\left[1.2180+c_v\left(\frac{b}{2c_v}\right)^2\right]g_{1v}-\sum_{n=1}^{m}a_{vn}i_{vn}^{**}g_{1n}\Big|_{n\neq v} \tag{5.47}$$

$$+\left[3.3006+6c_v\left(\frac{b}{2c_v}\right)^2\right]-\sum_{n=1}^{m}a_{vn}j_{vn}^{**}m_{1n}\Big|_{n\neq v}$$

in which a_{vn}, a_{vv}, b_v and c_v represent universal constants, tabulated by Truckenbrodt for $m=7$ and $m=15$ [49] and g_{1n}, m_{1n} and g_{1v}, m_{1v} are the function values at stations $\eta_n=\cos\frac{n\pi}{m+1}$ and $\eta_v=\cos\frac{v\pi}{m+1}$ ($v=1,2,\ldots,m$), respectively. Thus, Equation (5.45) can be solved for and $g_1(\eta)$ and $m_1(\eta)$, by which a linear system of equations is obtained for functions g_{1v} and m_{1v} ($v=1,2,\ldots,m$).

The linear part of the lift and pitching moment coefficients then follow from

$$\left(\frac{dC_L}{d\alpha}\right)_{\alpha=0}=AR\int_{-1}^{1}g_1(\eta)\,d\eta$$

$$\left(\frac{dC_M}{d\alpha}\right)_{\alpha=0}=-AR\int_{-1}^{1}g_1(\eta)\frac{x_{c/4}}{c_\mu}d\eta+AR\int_{-1}^{1}m_1(\eta)\frac{c(\eta)}{c_\mu}d\eta \tag{5.48}$$

in which $x_{c/4}(\eta)$ represents the position of the local quarter-chord and $c_\mu=\frac{1}{S}\int_{-b/2}^{b/2}c^2dz$.

Again, the integrals in Equation (5.48) can be expressed in the Multhopp quadrature formulae (Equation (5.46)).

The essential difference between the linear theory and the non-linear theory developed by Gersten arises from the alteration of the vorticity model of the lifting elements. The trailing vortices are no longer forced to remain in the plane of the element surface, but incline at an angle of $\alpha/2$ with respect to the plate. It can be shown (see [16]) that by the Biot-Savart law, the vortex sheet formed by all horseshoe vortices with distribution $\gamma(x',z')dx'$ along z' originating from x' induces a velocity component in y-direction at point $P(x,z)$, where the distance between point P and the trailing vortex sheet is $-(x-x')\alpha/2$ (Figure 5.8), whose magnitude is given by

$$dv=-\frac{1}{4\pi}\int_{\substack{-b/2\\ Cauchy}}^{b/2}\frac{\frac{d}{dz'}\left[\gamma(x',z')\left(1+\frac{x-x'}{R}\right)\right]}{z-z'}dz'dx'$$

$$-\frac{1}{8}\frac{\alpha}{|\alpha|}\alpha\left(1+\frac{x-x'}{|x-x'|}\right)(x-x')\frac{\partial^2}{\partial z^2}\gamma(x',z)\,dx' \tag{5.49}$$

The total induced velocity in point $P\left(x, y=-(\alpha/2)x, z\right)$ results from the integrated effect of dv in x'-direction. After changing the order of integration and differentiation,

$$
\begin{aligned}
v(x,z) &= \frac{1}{4\pi} \underset{Cauchy}{\int_{-b/2}^{b/2}} \int_{x_v}^{x_h} \frac{\dfrac{d}{dz'}\left[\gamma(x',z')\left(1+\dfrac{x-x'}{R}\right)\right]dx'}{z-z'}dz' \\
&- \frac{1}{8}\frac{\alpha}{|\alpha|}\alpha\frac{\partial}{\partial z^2}\int_{x_v}^{x_h}\left(1+\frac{x-x'}{|x-x'|}\right)(x-x')\gamma(x',z)\,dx'
\end{aligned}
\tag{5.50}
$$

Under the assumption for the vorticity distribution given by Equation (5.42), the flow-tangency condition (in dimensionless co-ordinates) in the non-linear theory of Gersten becomes [16]

$$\alpha(\xi,\eta) = \alpha_i(\xi,\eta) = -\frac{v}{U_\infty} = L(\gamma,\mu) + \frac{\alpha}{|\alpha|}\alpha\frac{d^2 J(\gamma,\mu)}{d\eta^2} \tag{5.51}$$

in which $L(\gamma,\mu)$ and $J(\gamma,\mu)$ are linear operators with properties given by Equation(5.33). Operator $L(\gamma,\mu)$ is identical to the operator in the linear lifting surface theory. For operator $J(\gamma,\mu)$ applies

$$J(\gamma,\mu) = \frac{1}{\pi}\frac{c(\eta)}{b}\left[\gamma(\eta)J_1(\eta) + 4\mu(\eta)J_2(\eta)\right] \tag{5.52}$$

with

$$
\begin{aligned}
J_1(\eta) &= \frac{1}{2}\int_0^{\varphi}(1+\cos\varphi')(\cos\varphi'-\cos\varphi)\,d\varphi' \\
J_2(\eta) &= \frac{1}{2}\int_0^{\varphi}\left(1+\cos\varphi'-2\sin^2\varphi\right)(\cos\varphi'-\cos\varphi)\,d\varphi'
\end{aligned}
\tag{5.53}
$$

in which

$$
\begin{aligned}
\frac{x-x_v}{c} &= \frac{1}{2}(1-\cos\varphi) \\
\frac{x'-x_v}{c} &= \frac{1}{2}(1-\cos\varphi')
\end{aligned}
\tag{5.54}
$$

Differentiation of Equation (5.52) gives

$$
\begin{aligned}
\frac{d^2 J}{d\eta^2} &= f_1(\gamma,\mu) + f_2(\gamma,\mu)\frac{dc}{dz} + f_3(\gamma,\mu)\frac{dx_v}{dz} + f_4(\gamma,\mu)\frac{dc}{dz}\frac{dx_v}{dz} \\
&+ f_5(\gamma,\mu)\left(\frac{dc}{dz}\right)^2 + f_6(\gamma,\mu)\left(\frac{dx_v}{dz}\right)^2
\end{aligned}
\tag{5.55}
$$

The terms with dc/dz and dx_v/dz in Equation (5.55) represent the effects of taper ratio and sweepage, respectively. In accordance with practice in the linear theory of Truckenbrodt, the flow-tangency given by Equation (5.51) must be satisfied at the backside of the planform (designated by *) and at the quarter-chord line (designated by **):

$$
\begin{aligned}
\alpha^*(\eta) &= L^*(\gamma,\mu) + \frac{\alpha}{|\alpha|}\alpha\frac{d^2 J^*(\gamma,\mu)}{d\eta^2} \\
\alpha^{**}(\eta) &= L^{**}(\gamma,\mu) + \frac{\alpha}{|\alpha|}\alpha\frac{d^2 J^{**}(\gamma,\mu)}{d\eta^2}
\end{aligned}
\tag{5.56}
$$

Using elementary integration and differentiation methods, Gersten found [16]

$$
\begin{aligned}
f_1^*(\gamma,\mu) &= \frac{3}{4}\frac{c}{b}\frac{d^2\gamma}{d\eta^2}+\frac{c}{b}\frac{d^2\mu}{d\eta^2} \\
f_2^*(\gamma,\mu) &= -\frac{1}{4}\frac{d\gamma}{d\eta}+\frac{d\mu}{d\eta} \\
f_3^*(\gamma,\mu) &= -\frac{d\gamma}{d\eta} \\
f_4^*(\gamma,\mu) &= f_5^*(\gamma,\mu)=f_6^*(\gamma,\mu)=0
\end{aligned}
\tag{5.57}
$$

and

$$
\begin{aligned}
f_1^{**}(\gamma,\mu) &= \frac{3\sqrt{3}}{16\pi}\frac{c}{b}\frac{d^2\gamma}{d\eta^2}+\frac{1}{3}\frac{c}{b}\frac{d^2\mu}{d\eta^2} \\
f_2^{**}(\gamma,\mu) &= -\left(\frac{\sqrt{3}}{16\pi}-\frac{1}{12}\right)\frac{d\gamma}{d\eta}+\left(\frac{3\sqrt{3}}{4\pi}-\frac{1}{3}\right)\frac{d\mu}{d\eta} \\
f_3^{**}(\gamma,\mu) &= -\left(\frac{1}{3}+\frac{\sqrt{3}}{2\pi}\right)\frac{d\gamma}{d\eta}-\frac{3\sqrt{3}}{\pi}\frac{d\mu}{d\eta} \\
f_4^{**}(\gamma,\mu) &= \frac{\sqrt{3}}{4\pi}\frac{b}{c}\gamma \\
f_5^{**}(\gamma,\mu) &= \frac{\sqrt{3}}{32\pi}\frac{b}{c}\gamma \\
f_6^{**}(\gamma,\mu) &= \frac{\sqrt{3}}{2\pi}\frac{b}{c}\gamma
\end{aligned}
\tag{5.58}
$$

Hence, the values of $\frac{d^2J^*(\gamma,\mu)}{d\eta^2}$ and $\frac{d^2J^{**}(\gamma,\mu)}{d\eta^2}$ in Equation (5.56) can be expressed in terms of the functions given by Equations (5.57) and (5.58) by Equation (5.55).

In order to solve Equation (5.56), it is assumed that

$$
\begin{aligned}
\gamma(\eta) &= g_1(\eta)\alpha+g_2(\eta)\frac{\alpha}{|\alpha|}\alpha^2 \\
\mu(\eta) &= m_1(\eta)\alpha+m_2(\eta)\frac{\alpha}{|\alpha|}\alpha^2
\end{aligned}
\tag{5.59}
$$

By neglecting terms that depend on the third power of the angle of attack and using properties of the linear operators,

$$L\left(\left(r_1g_1+r_2g_2\right),\left(r_1m_1+r_2m_2\right)\right)=r_1L\left(g_1,m_1\right)+r_2L\left(g_2,m_2\right) \tag{5.60}$$

substituting Equation (5.59) in Equation (5.56) gives

$$
\begin{aligned}
L^*(g_1,m_1) &= \frac{\alpha^*(\eta)}{\alpha} \\
L^{**}(g_1,m_1) &= \frac{\alpha^{**}(\eta)}{\alpha}
\end{aligned}
\tag{5.61}
$$

and

$$L^*\left(g_2,m_2\right)=-\frac{\alpha^*\left(\eta\right)}{\alpha}\frac{d^2J^*\left(g_1,m_1\right)}{d\eta^2}$$
$$L^{**}\left(g_2,m_2\right)=-\frac{\alpha^{**}\left(\eta\right)}{\alpha}\frac{d^2J^{**}\left(g_1,m_1\right)}{d\eta^2} \tag{5.62}$$

The operators given by Equation (5.61) are identical to the operators in the linear lifting surface theory. Therefore, the integrals can be solved for $g_1\left(\eta\right)$ and $m_1\left(\eta\right)$ with the aid of methods described in the linear lifting surface theory. Next, using the calculated values of $g_1\left(\eta\right)$ and $m_1\left(\eta\right)$, Equation (5.62) can be solved for $g_2\left(\eta\right)$ and $m_2\left(\eta\right)$. From the calculated functions $g_1\left(\eta\right)$, $m_1\left(\eta\right)$, $g_2\left(\eta\right)$ and $m_2\left(\eta\right)$, the lift coefficient and the pitching moment coefficient can be determined as

$$C_L=\left(\frac{dC_L}{d\alpha}\right)_{\alpha=0}\alpha+C_1\frac{\alpha}{|\alpha|}\alpha^2$$
$$C_M=\left(\frac{dC_M}{d\alpha}\right)_{\alpha=0}\alpha+C_2\frac{\alpha}{|\alpha|}\alpha^2 \tag{5.63}$$

in which

$$\left(\frac{dC_L}{d\alpha}\right)_{\alpha=0}=AR\int_{-1}^{1}g_1\left(\eta\right)d\eta$$
$$\left(\frac{dC_M}{d\alpha}\right)_{\alpha=0}=-AR\int_{-1}^{1}g_1\left(\eta\right)\frac{x_{c/4}\left(\eta\right)}{c_\mu}d\eta+AR\int_{-1}^{1}m_1\left(\eta\right)\frac{c\left(\eta\right)}{c_\mu}d\eta$$
$$C_1=AR\int_{-1}^{1}g_2\left(\eta\right)d\eta$$
$$C_2=-AR\int_{-1}^{1}g_2\left(\eta\right)\frac{x_{c/4}\left(\eta\right)}{c_\mu}d\eta+AR\int_{-1}^{1}m_2\left(\eta\right)\frac{c\left(\eta\right)}{c_\mu}d\eta \tag{5.64}$$

For plates with sharp leading edges, the induced drag coefficient approximately yields

$$C_{Di}=C_L\alpha \tag{5.65}$$

Calculation procedure

Instead of solving the integral equations, the functions are, in practice, only calculated for a finite number of discrete spanwise stations m equal to the number of lifting elements across the span; the flow-tangency given by Equation (5.56) is satisfied only at the selected stations, by which linear systems of equations are obtained for the unknowns g_{1v}, m_{1v}, g_{2v} and m_{2v} ($v=1,2,\ldots,m$).

First, for a given planform (composed by vane and image below the bed), calculate influence functions i_{vn} and j_{vn} at stations $\eta_n=\cos\left(n\pi/\left(m+1\right)\right)$ at the backside and at the quarter-chord line by Equation (5.44). Then, Equation (5.61) can be solved for functions $g_1\left(\eta\right)$ and $m_1\left(\eta\right)$, using Equation (5.47) and universal constants a_{vn}, a_{vv}, b_v and c_v ($v=1,2,\ldots,m$), as tabulated by Truckenbrodt [49]. Evaluate the linear system of equations thus obtained to determine the values of functions g_{1v} and m_{1v} ($v=1,2,\ldots,m$).

Next, calculate the values of $\dfrac{d^2 J^*(g_1, m_1)}{d\eta^2}$ and $\dfrac{d^2 J^{**}(g_1, m_1)}{d\eta^2}$ by Equations (5.55), (5.57) and (5.58). The first and second order differentials of $g_1(\eta)$ and $m_1(\eta)$ in Equations (5.57) and (5.58) may be written as

$$\begin{aligned}
\frac{dg_1(\eta)}{d\eta} &= \sum_{n=1}^{m} A_{1n} g_{1n} \\
\frac{d^2 g_1(\eta)}{d\eta^2} &= \sum_{n=1}^{m} A_{2n} g_{1n} \\
\frac{dm_1(\eta)}{d\eta} &= \sum_{n=1}^{m} A_{1n} m_{1n} \\
\frac{d^2 m_1(\eta)}{d\eta^2} &= \sum_{n=1}^{m} A_{2n} m_{1n}
\end{aligned} \tag{5.66}$$

In [16], Gersten has tabulated the universal constant A_{1n} and A_{2n} for $m = 7$ and $m = 15$. Finally, Equation (5.62) can now be solved for $g_2(\eta)$, $m_2(\eta)$ analogous to the evaluation of Equation (5.61), by which a linear system of equations results for g_{2v} and m_{2v}. Evaluate the system of equations to determine the values of g_{2v} and m_{2v} ($v = 1, 2, \ldots, m$).

The lift, drag and pitching moment coefficients can then be calculated by Equations (5.63), (5.64) and (5.65), using the Multhopp quadrature formulae [31] given by Equation (5.46). The aspect ratio of the plate (composed by vane and image below the bed) with maximum span b and surface area S is given by

$$AR = \frac{b^2}{S} \tag{5.67}$$

For rectangular vanes with vane height H_v and vane length L_v, aspect ratio $AR = \dfrac{2H_v}{L_v}$.

Figure 5.9 presents plots of functions $(dC_L/d\alpha)_{\alpha=0}$, $(dC_M/d\alpha)_{\alpha=0}$, C_1 and C_2 versus the aspect ratio for sharp-edged, slender rectangular vanes (using 15 lifting elements across the span). For low aspect ratios, the linear lift curve slope coefficient according to the linear theory by Truckenbrodt approximates the lift curve slope coefficient determined by slender wing theory [45],

$$\left(\frac{dC_L}{d\alpha}\right)_{\alpha=0} \approx \frac{\pi}{2} AR \tag{5.68}$$

and agrees well with the linear lift curve slope coefficient m_H for low aspect ratio rectangular wings by Helmbold [1], which reads

$$m_H = \frac{m_0}{\sqrt{1 + \left(m_0/(\pi AR)\right)^2} + m_0/(\pi AR)} = \frac{2\pi}{\sqrt{1 + 4/AR^2} + 2/AR} \tag{5.69}$$

Though it is understood that the lifting line theory is inappropriate for low aspect ratio wings, the lift curve slope coefficient according to Prandtl's lifting line theory is included for reasons of comparison. Note that the theory of Odgaard, which (incorrectly) uses the lifting line theory to calculate the mean lift and drag forces exerted on a submerged vane, overestimates the linear lift coefficient considerably and does not account for non-linear lift. From Figure 5.9, it is seen that the non-linear lift curve slope coefficient C_1 is a maximum for $AR = 0$ and decreases significantly with increasing aspect ratio.

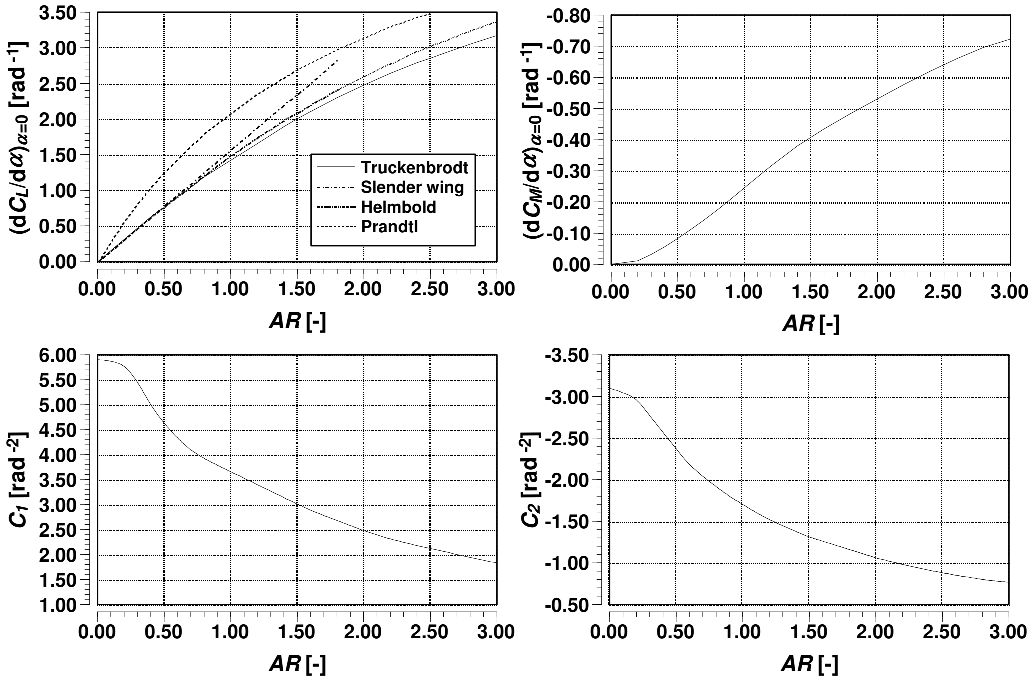

Figure 5.9: Linear and non-linear lift curve slope coefficients and pitching moment curve slope coefficients for a rectangular planform according to Gersten

Figure 5.10 presents plots of the lift coefficient and the ratio of non-linear to linear lift for slender rectangular vanes according to the model based on theory developed by Gersten. For comparison, the linear lift coefficients (according to Truckenbrodt) are included. As shown in Figure 5.10, the non-linear effect increases with increasing angle of attack and decreasing aspect ratio. The model based on theory by Gersten suggests that non-linear lift (or vortex lift) can become dominant over linear lift already at relatively low angles of attack.

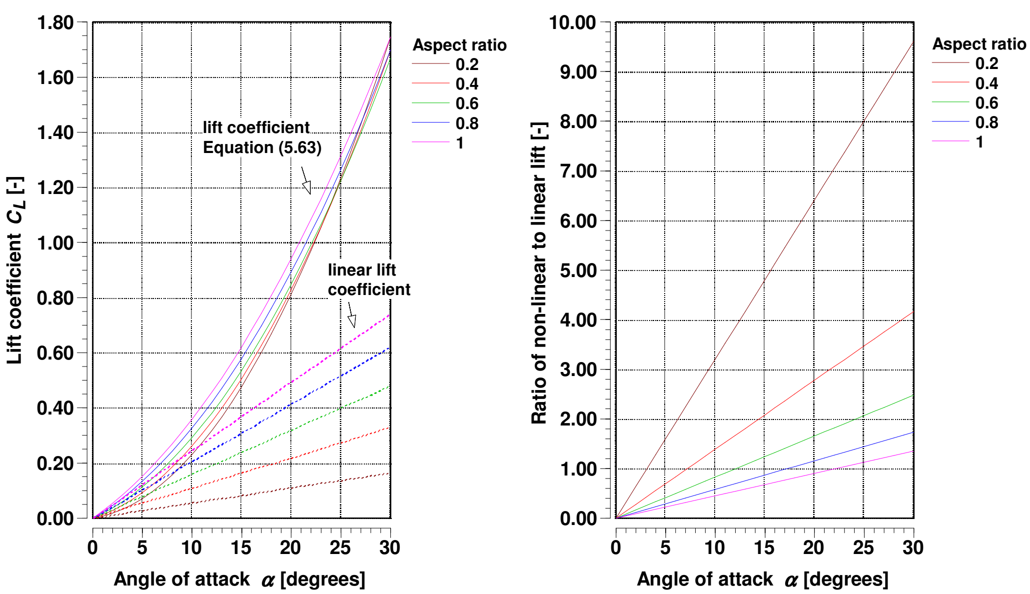

Figure 5.10: Lift coefficient and ratio of non-linear to linear theoretical lift versus angle of attack

Discussion

A critical assessment of the non-linear theory developed by Gersten is carried out by Garner and Lehrian [15], who, however, substituted Multhopp's linear theory [32] in place of the linear lifting surface theory by Truckenbrodt [49] (from the account of Gersten's non-linear theory described by Equations (5.30) to (5.38), it can be seen that any linear theory can be used to calculate the linear part of the vorticity distribution). Garner and Lehrian designated a number of possible sources of error, associated with simplifications inherent in the theory:

- In the mathematical model by Gersten, all trailing vorticity is shed in planar sheets inclined at an angle of half the angle of attack with respect to the surface. The flow at the wing surface is built up as a superposition of elementary potential flows. In reality, flow separation involves singularities along separation lines in the wing surface, where free vortices originate. In the mathematical model, it supposed without physical justification that the free vortices are shed at all points of the upper surface. Furthermore, there is a discontinuity of half the angle of attack between the tangential surface flow and the direction in which vorticity is assumed to be convected [15].
- For rectangular wings, Garner and Lehrian varied the number of spanwise stations in their adaptation of Gersten's method and found that calculations failed to converge as the number of spanwise stations increases. The divergence was attributed to an approximate expansion for the upwash at the wing surface induced by an elementary planar vortex sheet inclined at an angle of half the angle of attack to the wing [16], which is necessary to achieve a tractable method for a wing of arbitrary planform and appears in Equation (5.49). Garner and Lehrian stated that the approximation becomes increasingly suspect as the wing tip is approached [15].
- Gersten's method lacks a provision to account for the rolling-up process of the vortex sheets into concentrated vortices [15].

In Section A.5.3, comparisons for lift, drag and pitching moment coefficients with experimental results for a sharp-edged rectangular flat-plate at an aspect ratio of 0.5 are presented. The agreement between theory and experiment is rather good. For slender wings at low aspect ratios, Gersten's method gives a decisive improvement on linear theory. It is seen that the dependence of the aerodynamic coefficients on angle of attack is predicted adequately. Furthermore, comparisons with experiment show that realistic estimates of the spanwise lift distribution can be obtained. In accordance with experiment, the lift coefficient is practically constant over a large part of the span. A dramatic decrease in lift is observed near the edges, indicating that there are no free vortices trailing from the wing surface for most of the wing. The mathematical model, on which the non-linear theory by Gersten is based, predicts – in accordance with empirical observations – that the free vortices trail mainly from the side edges, where the vortices affect the lift distribution considerably. The success of the method for prediction of the load distribution on rectangular wings suggests that the first source of error, as designated by Garner and Lehrian, may be unimportant. In Gersten's method, the flow-tangency condition is to be satisfied at the lifting surface, but the streamline vortex condition is relaxed. The choice of the angle with respect to the lifting surface is suggested by results of the non-linear theory developed by Bollay. From Figure 5.5, it can be seen that for very low aspect ratios, the trailing vortices are inclined at an angle approximately equal to $\alpha/2$ with respect to the plate. For aspect ratios $AR<1$ and $5° \le \alpha \le 50°$, Bollay predicts that the mean effective inclination angle θ is up to about 5% to 40% larger. In Gersten's method, there is no flow condition that can be applied as an independent check on the angle of inclination. For incompressible flow, the value $\alpha/2$ is, however, justified empirically by the comparisons between measured and calculated lift. The effect of the different relative angles of the straight line vortex trajectories is investigated by Ermolenko and Barinov, who found that the value of $\alpha/2$ for the inclination of the vortices relative to the wing surface is about the average of the local inclination of the shed vortices along the chord of the wing [10].

Because numerical solutions are obtained by collocation (i.e., the flow-tangency condition is satisfied at the selected control stations only), the second possible source of error designated by Garner and Lehrian (convergence problems at the wing tip) is avoided in Gersten's method by resticting the number of spanwise stations [15]. By the agreement between theory and experiment for rectangular wings, it is believed that the third and final source of error (lack of provision for the rolling-up process) does not play a significant role for rectangular planforms. For more complex configurations, lack of provision for the rolling-up process into concentrated vortices in Gersten's method can be held responsible for discrepancies [15]. At present, there are methods that simulate the rolling-up process by certain iterative procedures [45] (see also Section A.5.4).

The linear part of the assumed vorticity distribution γ_1 is determined from the integral equation of linear theory as a linear function of the angle of incidence (Equation (5.36)) and is consequently used to calculate the non-linear part of the vorticity distribution γ_2 (Equation (5.37)). The integral equation of linear theory are not very restrictive in α, because linear lifting surface theory can be a good approximation in cases of non-separated flow at fairly high angles of attack (Section A.4). Given the above-described approach in the non-linear theory by Gersten, it can be reasoned that predicted loadings and thus, the calculated coefficients become less and less accurate with increasing angle of attack. Comparisons with experiment for wings at low aspect ratios show that the non-linear theory by Gersten holds approximately for angles of attack up to at least 30° [15; 16] (for practical reasons, there is generally no interest in higher angles of attack in aerodynamics; comparisons are therefore presented for a range of angle of attack up to about 30° only, while measurements by Winter [55] indicate that the lift coefficient on sharp-edged rectangular plates at relatively low aspect ratios increases further in higher ranges of angle of attack (Figure 5.2)). It is seen that, when there are leading edge vortices and extensive regions of separated flow, the non-linear theory gives a decisive improvement on linear lifting surface theory. For a sharp-edged flat-plate in an inviscid flow, there is no leading edge suction force; the lift and induced drag coefficients can be determined from the normal force as $C_L = C_N \cos\alpha$ and $C_{Di} = C_N \sin\alpha$. For low angles of attack, the lift and drag coefficients yield $C_L = C_N$ and $C_{Di} = C_L\alpha$, respectively (Eq. (5.38) and (5.65)). Of course, the approximation holds less and less with increasing angle of attack.

In contrast to the non-linear theory by Bollay (Section 5.3.1), Gersten's method fails to predict the observed behaviour of zero aspect ratio wing (finite span and infinite chord) correctly. It is expected that the model based on theory by Gersten overestimates the lift and drag coefficients on submerged vanes at extremely low aspect ratios, say lower than 0.2. Similarly to the non-linear theory by Bollay (and the lifting line theory by Prandtl), the mathematical model by Gersten violates the Helmholtz' vortex laws by assuming that the trailing vortices follow straight lines (see discussion in Section 5.3.1). Again, the assumption that a single reflection of the bound and free trailing vortices in the plane of the bed is sufficient to account for interference effects of boundaries breaks down with increasing ratio of vane height to flow depth. In order to expand the range of relative vane submergence, for which interference effects caused by both bed and free surface are accounted for adequately, the mathematical model should be improved by applying reflections in the plane of the free surface as well as in the plane of the bed, using a low Froude number approximation, which allows the free surface to be taken as a rigid boundary. Possibly, in view of the findings in Section 5.5, the assumption that a single reflection of the vortices in the plane of the bed is sufficient to account for interference effects of boundaries is still reasonable at ratios of vane height to flow depth up to 0.5.

Based on observed agreements between theory and experiment for wings at low aspect ratios (Section A.5.3), it is expected that the model based on non-linear theory by Gersten predicts satisfactorily the lift and drag coefficients on a sharp-edged, slender rectangular vane protruding above a rigid bed at an aspect ratio higher than 0.2 (ratio of vane height to vane length lower than 0.1) and an angle of attack up to 30° to 40°, provided the ratio of vane height to flow depth is not too high.

5.4 AVAILABLE EXPERIMENTAL FORCE DATA

5.4.1 Odgaard and Spoljaric, 1986

In 1986, Odgaard and Spoljaric presented results of force-measuring experiments conducted in a rectangular, glass-walled tilting flume [35]. Figure 5.11 presents a schematic of the set-up. The tested vane were mounted on a flat plate, suspended in such a manner that it could move freely in any direction and levelled with the fixed, false bottom in the channel. Both vane mount and false bottom were made of metal sheets with a glued on layer of 0.3 mm quarts sand. Under running water conditions, the frame of the vane mount exerted a force on two load cells (one of which was employed to record lift, the other to record drag). The load cells were interfaced with a data acquisition and control system, allowing for online data processing and calibration control. Different vane profiles were tested. Odgaard and Spoljaric, however, only presented the results for a flat-plate vane (length: 21.5 cm; height: 6.4 cm) at angles of attack of 5°, 10, 15° and 20° and flow depth to vane height-ratios of 2, 3 and 4 (Figure 5.11). The lift and drag coefficients have been determined with Equations (3.10) and (3.11), using

$$\bar{u}^2 = \frac{1}{H_v} \int_0^{H_v} u^2 dz \tag{5.70}$$

in which the velocity distribution was measured on the centreline just upstream from the vane at all three flow depths and compared to Equation (3.5), showing good agreement. Each point in Figure 5.11 is the average value from several tests with different flow velocities (within range 1 to 3 fps). Some scatter was discerned, but data analysis confirmed that the effect of the ratio of flow depth to vane height on the measured lift coefficients is significant and that there is no dependence on flow velocity.

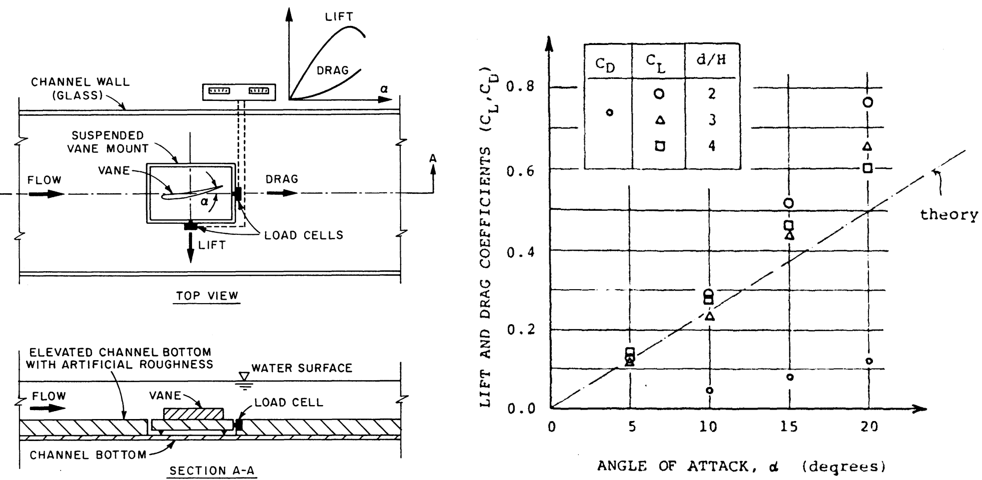

Figure 5.11: Test set-up (left) and measured lift and drag coefficients for a flat-plate vane (right); source: Odgaard and Spoljaric, 1986

5.4.2 Odgaard and Spoljaric, 1989

It appears that the set-up in the force measuring experiments presented by Odgaard and Spoljaric in 1989 [38] corresponded with the set-up in their experiments conducted in 1986 (see also Figure 5.11). In [38], however, more information is given about the set-up. The clearance between the plate surface on which the tested vanes were mounted and the surrounding sand coated panels measured 1.5 mm. Length and width of the vane mount were 0.45 m and 0.35 m, respectively. The lift and drag forces have been measured by means of miniature 50 g compression load cells. Thin and thick flat-plate vanes, and cambered vanes with and without twist have been tested (Figure 5.12). The length and height of the thin flat-plate vane were about 17 cm and 5 cm, respectively. Depth and velocities were varied within the ranges 10 to 25 cm and 10 to 30 cm/s. The friction factor ranged from 0.016 to 0.020, which corresponds to a power-law exponent in Equation (3.5) from 8 to 9. Each point in Figure 5.13 represents the average value for velocities within the range 10 to 30 cm/s, where individual values were within 10% of the average values.

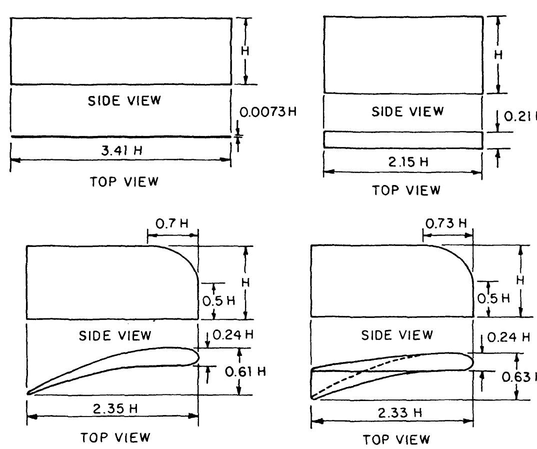

Figure 5.12: Tested vanes; source: Odgaard and Spoljaric, 1989

5.4.3 Flokstra, De Groot and Struiksma, 1998

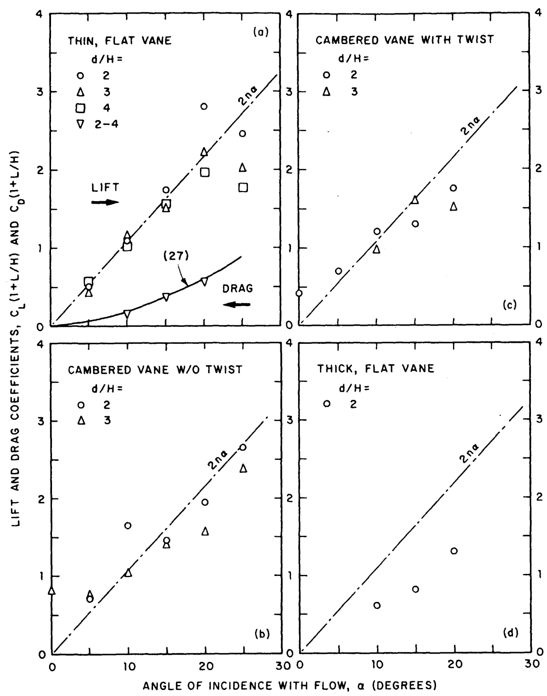

Figure 5.13: Measured lift and drag coefficients; source: Odgaard and Spoljaric, 1989

Hydraulic conditions in the flume have been regulated as to meet conditions in the River Waal near Hulhuizen, The Netherlands, optimally (depth: 0.30 m; depth-averaged velocity: about 0.28 m/s; bed roughness: about 45 $m^{0.5}/s$). In accordance with the set-up applied by Odgaard and Spoljaric in their experiments (Sections 5.4.1 and 5.4.2), the metal plate, on which the tested vanes were mounted, was equipped with a layer of glued on gravel to match the bed roughness upstream and downstream of the vane. Allowing for horizontal movements, the vane mount was supported by three members inside a box, which also accommodated a measuring frame with three force sensors. The positioning of the force sensors was selected such that one sensor recorded drag, while the other sensors measured lift. Experiments have been conducted for sheet-wall and flat-plate vanes at an angle of attack of 17.5° with lengths of 0.24 m, 0.32 m, 0.40 m and 0.48 m, by which the vane protruded 0.06 m above the gravel layer. Additionally, the effect of upstream vanes on the lift and drag forces has been investigated. Based on analysis of force measurements for different measuring durations under equal hydraulic conditions, a measuring duration of 120 s was selected. Measures were taken to improve uniformity in the approach flow.

5.4.4 Jongeling and Flokstra, 2001

Under the hydraulic conditions and using the set-up described in Section 5.4.3, experiments were conducted at WL | Delft Hydraulics in 1999 to investigate the effect of vane height on the lift and drag forces exerted on sheet-wall and flat-plate vanes with a vane length of 0.40 m at an angle of attack of 17.5°. The tested vanes protruded 0.03 m, 0.06 m, 0.09 m and 0.12 m above the gravel layer.

5.4.5 Error analysis

Unfortunately, Odgaard and Spoljaric did not provide much information about accuracies of their measurements in (further indicated as measurements OS1986 and OS1989). Therefore, no information is available about instrument calibration and correction procedures to account for shear stresses exerted on the vane mount. Tables 5.1 and 5.2 present lift and drag coefficients for measurements OS1986 and OS1989, mostly collected manually from the graphs presented in [35] and [38]. The set-up and procedures in the experiments by WL | Delft Hydraulics (further indicated as measurements WL1998 and WL2001) are on the other

H_v [m]	L_v [m]	α [degr.]	d/H_v [-]	C_L [-]	C_D [-]
0.064	0.215	5	2	0.13	
0.064	0.215	10	2	0.29	0.05
0.064	0.215	15	2	0.52	0.08
0.064	0.215	20	2	0.77 [7]	0.12
0.064	0.215	5	3	0.11	
0.064	0.215	10	3	0.23	0.05
0.064	0.215	15	3	0.44	0.08
0.064	0.215	20	3	0.65 [7]	0.12
0.064	0.215	5	4	0.14	
0.064	0.215	10	4	0.27	0.05
0.064	0.215	15	4	0.46	0.08
0.064	0.215	20	4	0.60	0.12

Table 5.1: Measured lift and drag coefficients for flat-plate vane; measurements OS1986

[7] The value of the measured lift coefficient is given by the authors in [35].

H_v [m]	L_v [m]	α [degr.]	d/H_v [-]	C_L [-]	C_D [-]
0.05	0.171	5	2	0.12	
0.05	0.171	10	2	0.25	0.04
0.05	0.171	15	2	0.40	0.08
0.05	0.171	20	2	0.64 [8]	0.13
0.05	0.171	25	2	0.56	
0.05	0.171	5	3	0.10	
0.05	0.171	10	3	0.26	0.04
0.05	0.171	15	3	0.34	0.08
0.05	0.171	20	3	0.51	0.13
0.05	0.171	25	3	0.46	
0.05	0.171	5	4	0.13	
0.05	0.171	10	4	0.23	0.04
0.05	0.171	15	4	0.36	0.08
0.05	0.171	20	4	0.45 [8]	0.13
0.05	0.171	25	4	0.40	

Table 5.2: Measured lift and drag coefficients for flat-plate vane; measurements OS1989

hand well documented. Report [11] also includes a list of possible errors by calculation of the lift and drag coefficients. A summary of the error analysis for measurements WL1998 and WL2001 is given in the discussion below. Additionally, effects of several non-systematic errors on the calculated lift and drag coefficients are examined. The measured lift and drag forces varied strongly in time, due partially to deviations from ideal approach flow conditions. Free stream turbulence leads to variations in the magnitudes of the vane height-averaged approach velocity and the angle of attack. Due to the nature of experimental procedures, approach flow conditions may have varied slightly per experiment. Force measurements in the absence of a mounted vane suggest a possible variation in approach flow velocity of about 2% [11]. In calibration tests, the force-measuring instrument turned out to be more accurate than 0.5% of the regulated measuring range [24]. The forces measured by the force sensors did not comprise the forces exerted on the vane alone. Because the force sensors were attached to the vane mount, the forces resulting from shear stresses on the hydraulically rough metal plate have been measured too. An estimate of the magnitude of the shear force can be obtained from the assumption that the drag force measured in the absence of a vane may be rotated proportionally to the angle of attack [11]. Assuming that the angle between shear forces on the vane mount and flume centre-axis averagely equalled half the angle of attack, measured lift forces should be reduced by about 0.011 N. In consideration of the magnitude of measured lift forces, a reduction by 0.011 N implies a systematic error of up to 5% for measurements WL1998 and of up to 17% for measurements WL2001. The measured lift and drag forces presented in [11] and [24] have been reduced by the values of the shear forces on the metal plate in the absence of a vane, where the shear force component in transverse direction practically measured zero. As a consequence, it is expected that the thus corrected lift and drag forces are slightly overrated and underrated, respectively.

The turbulent lift and drag forces have been recorded by a measuring duration of 120 s. In order to obtain statistically reliable estimates of the actual average forces, measurements were repeated 10 times per experiment (with intervals of 2 to 5 minutes) [11]. The measured standard deviation is an estimate of the actual standard deviation. Using a Student t-distribution to describe the spread of the calculated average force, the change that

$$\left|\overline{F} - \mu_F\right| \leq 0.71S \tag{5.71}$$

equals 95% by 10 independent measurements [11]. For thin, flat vanes, the standard deviation varied to maximally 0.011 N for measurements WL1998 and 0.017 N for measurements WL2001. Repetitions of several experiments demonstrated that the calculated average force could be reproduced quite accurately [11].

The lift and drag coefficients have been derived from the measured forces (corrected for the shear forces exerted on the vane mount in the absence of a vane), using

$$C_L = \frac{\overline{F_y}}{\frac{1}{2}\rho \overline{u_H}^2 L_v H_v} \tag{5.72}$$

[8] The value of the measured lift coefficient is given by the authors in [38].

and

$$C_D = \frac{\overline{F_x}}{\frac{1}{2}\rho \overline{u_H}^2 L_v H_v} \tag{5.73}$$

in which the vane height-averaged velocity $\overline{u_H}$ is calculated from the power law profile given in Equation (3.5), as

$$\overline{u_H} = \bar{u}\frac{m+1}{\sqrt{m(m+2)}}\left(\frac{H_v}{d}\right)^{\frac{1}{m}} \tag{5.74}$$

Approach flow velocity measurements did not agree well with the power law distribution. Best fits gave bed roughness values, which could not be retrieved from surface slope readings and shear force measurements on an empty vane mount [24]. Therefore, Tables 5.3 and 5.4 also present the lift and drag coefficients calculated for values of the vane height-averaged velocity resulting from curve fitting.

				CF [9]					CF	
H_v [m]	L_v [m]	α [degr.]	$\overline{u_H}$ [m/s]	$\overline{u_H}$ [m/s]	$\overline{F_y}$ [N]	$\overline{F_x}$ [N]	C_L [-]	C_D [-]	C_L [-]	C_D [-]
0.06	0.24	17.5	0.202 [10]	0.198	0.210	0.075	0.71	0.26	0.74	0.27
0.06	0.32	17.5	0.202	0.198	0.255	0.093	0.65	0.24	0.68	0.25
0.06	0.40	17.5	0.202	0.198	0.293	0.107	0.60	0.22	0.62	0.23
0.06	0.48	17.5	0.202	0.198	0.344	0.127	0.59	0.22	0.61	0.22

Table 5.3: Measured lift and drag coefficients for flat-plate vane; measurements WL1998

			PL [11]	CF			PL		CF	
H_v [m]	L_v [m]	α [degr.]	$\overline{u_H}$ [m/s]	$\overline{u_H}$ [m/s]	$\overline{F_y}$ [N]	$\overline{F_x}$ [N]	C_L [-]	C_D [-]	C_L [-]	C_D [-]
0.03	0.40	17.5	0.189	0.164	0.072	0.031	0.34	0.14	0.45	0.19
0.06	0.40	17.5	0.213	0.194	0.311	0.111	0.57	0.20	0.69	0.25
0.09	0.40	17.5	0.229	0.213	0.652	0.212	0.69	0.22	0.80	0.26
0.12	0.40	17.5	0.241	0.228	1.019	0.338	0.73	0.24	0.82	0.27

Table 5.4: Measured lift and drag coefficients for flat-plate vane; measurements WL2001

As mentioned above, the forces presented in Tables 5.3 and 5.4 have been corrected by the values of the shear forces exerted on an empty vane mount. In the presence of a vane, the shear forces have most likely rotated proportionally to the angle of attack. If no corrections are applied to account for the rotation of the shear forces, systematic errors result. Tables 5.5 and 5.6 display measured forces and calculated lift and drag coefficients corrected for shear forces on the vane mount in the presence of a vane, assuming that the angle between shear forces and flume centre-axis averagely equated half the angle of attack.

				CF					CF	
H_v [m]	L_v [m]	α [degr.]	$\overline{u_H}$ [m/s]	$\overline{u_H}$ [m/s]	$\overline{F_y}$ [N]	$\overline{F_x}$ [N]	C_L [-]	C_D [-]	C_L [-]	C_D [-]
0.06	0.24	17.5	0.202	0.198	0.198	0.076	0.70	0.26	0.70	0.27
0.06	0.32	17.5	0.202	0.198	0.243	0.094	0.64	0.24	0.64	0.25
0.06	0.40	17.5	0.202	0.198	0.281	0.108	0.60	0.22	0.60	0.23
0.06	0.48	17.5	0.202	0.198	0.332	0.128	0.59	0.22	0.59	0.23

Table 5.5: Measured lift and drag coefficients for flat-plate vane corrected; measurements WL1998

[9] CF: using a curve-fit on approach flow velocity measurements.
[10] The value of the vane height-averaged approach velocity used in the calculations could not be found in [11], but is retrieved through calculations in reversed order.
[11] PL: using a power-law distribution.

			PL	CF			PL		CF	
H_v [m]	L_v [m]	α [degr.]	$\overline{u_H}$ [m/s]	$\overline{u_H}$ [m/s]	$\overline{F_y}$ [N]	$\overline{F_x}$ [N]	C_L [-]	C_D [-]	C_L [-]	C_D [-]
0.03	0.40	17.5	0.189	0.164	0.060	0.032	0.28	0.15	0.37	0.20
0.06	0.40	17.5	0.213	0.194	0.299	0.112	0.55	0.21	0.66	0.25
0.09	0.40	17.5	0.229	0.213	0.640	0.213	0.68	0.23	0.78	0.26
0.12	0.40	17.5	0.241	0.228	1.007	0.339	0.72	0.24	0.81	0.27

Table 5.6: Measured lift and drag coefficients for flat-plate vane corrected; measurements WL2001

In order to examine the effects of non-systematic errors on the calculated lift and drag coefficients, the possible errors due to deviations in vane height-averaged velocity, angle of attack and actual average force need to be quantified reasonably. Estimates are presented in Tables 5.7 and 5.8. The maximum possible error in lift coefficient is determined as

$$\sum E_{C_L} = E_{C_L 1} + E_{C_L 2} + E_{C_L 3} \tag{5.75}$$

in which $E_{C_L 1}$ represents the error contribution due to the use of a deviating vane height-averaged velocity, assuming that the actual velocity averagely exceeded the curve-fitted value by 4%; $E_{C_L 2}$ represents the error contribution due to the use of a deviating angle of attack, assuming that the actual angle of attack differed averagely 2° from the angle at which the vanes were installed with respect to the flume axis (17.5°), and $E_{C_L 3}$ represents the error contribution due to the use of a deviating average force, assuming that the maximum possible difference between measured and actual average force is given by Equation (5.71). In accordance with Equation (5.63), error contribution $E_{C_L 2}$ is estimated as

$$E_{C_{L2}} = \left(\frac{dC_L}{d\alpha}\right)_{\alpha=0} \Delta\alpha + C_1\left(\Delta\alpha\right)^2 \tag{5.76}$$

in which $\Delta\alpha$ represents the difference between actual angle of attack and angle of attack used in the calculation of the lift coefficient. In accordance with Equation (5.65), the maximum possible error of the calculated drag coefficient is determined as

$$\sum E_{C_D} = \left(E_{C_L 1} + E_{C_L 2}\right)\alpha + E_{C_D 1} \tag{5.77}$$

in which $E_{C_D 1}$ represents the error contribution due to the use of a deviating average force, assuming that the maximum possible difference between measured and actual average force is given by Equation (5.71). The conclusion can be drawn that the major uncertainties with regard to the calculated lift and drag coefficients are associated with corrections for shear forces on the vane mount in the presence of a vane and approach flow conditions.

H_v [m]	L_v [m]	α [degr.]	S_X [N]	S_Y [N]	$E_{C_L 1}$ [-]	$E_{C_L 2}$ [-]	$E_{C_L 3}$ [-]	$E_{C_D 1}$ [-]	ΣE_{C_L} [-]	ΣE_{C_D} [-]
0.06	0.24	17.5	0.005	0.006	0.05	0.03	0.02	0.01	0.10	0.04
0.06	0.32	17.5	0.005	0.009	0.05	0.03	0.02	0.01	0.09	0.03
0.06	0.40	17.5	0.007	0.011	0.05	0.02	0.02	0.01	0.08	0.03
0.06	0.48	17.5	0.004	0.007	0.04	0.02	0.01	0.01	0.07	0.02

Table 5.7: Estimated maximum possible errors of lift and drag coefficients; measurements WL1998

H_v [m]	L_v [m]	α [degr.]	S_X [N]	S_Y [N]	$E_{C_L 1}$ [-]	$E_{C_L 2}$ [-]	$E_{C_L 3}$ [-]	$E_{C_D 1}$ [-]	ΣE_{C_L} [-]	ΣE_{C_D} [-]
0.03	0.40	17.5	0.002	0.002	0.03	0.02	0.01	0.01	0.05	0.02
0.06	0.40	17.5	0.003	0.006	0.05	0.02	0.01	0.00	0.08	0.03
0.09	0.40	17.5	0.008	0.017	0.06	0.03	0.01	0.01	0.10	0.03
0.12	0.40	17.5	0.007	0.007[12]	0.06	0.04	0.00	0.00	0.10	0.03

Table 5.8: Estimated maximum possible errors of lift and drag coefficients; measurements WL2001

[12] The actual value of the standard deviation is higher as the maximum recorded force in transverse direction exceeded the full-scale value of 1.074 N [24].

5.5 COMPARISON NON-LINEAR MODELS WITH EXPERIMENT

Tables 5.9 upto and including 5.12 and Figure 5.14 present comparisons between calculated and measured mean lift and drag coefficients. The reader is reminded that the number of available force measurements is limited, which imposes serious restrictions to the drawing of conclusions. It is highly recommended to conduct additional force measurements to verify the conclusions and findings presented in this report.

At relatively low angles of attack, the theoretical lift and drag coefficients by Odgaard agree well with experiment, while at higher angles of attack a less satisfying agreement is observed and theoretical lift coefficients show unacceptable discrepancies with measurements OS1986 and in particular with measurements WL1998 and WL2001. The poorer agreement between calculated and measured lift coefficient with increasing angle of attack is to be anticipated, as the theory of Odgaard does not account for non-linear effects and the non-linear contribution to lift increases with increasing angle of attack. The lift coefficients calculated with the non-linear models based on theory developed by Bollay (Section 5.3.1) and by Gersten (Section 5.3.2) are seen to agree reasonably to good with experimental results at low and high ranges of angle of attack, particularly with measurements WL1998 and WL2001 and to a lesser extent with measurements OS1986. At first sight surprisingly, a comparison of the theoretical lift coefficients with measurements OS1989 shows a poor agreement between measured coefficients and coefficients calculated with the non-linear models at the higher angles of attack and suggests that the measured lift curve is given more accurately by the theory of Odgaard. There are, however, reasons to believe that this observation may be explained by the dimensions of the tested vane.

A more thorough examination of data and experimental set-up brings to light several striking matters, some of which may explain why the lift curves for measurements OS1986 and in particular for measurements OS1989 correspond roughly with the theoretical curve given by Odgaard. Firstly, the tested vanes have been given low vane heights: 0.064 m (OS1986) and 0.05 m (OS1989). Hypothetically, when the vane height is decreased to a degree (or when the strength of the primary vortex increases to a degree) where further development along the suction side is disturbed by the presence of the bed, the region where the flow is more or less attached and directed rearwards toward, the trailing edge collapses, affecting the linear contribution to lift, while stagnating the development of the primary vortex. With increasing angle of attack, the strength of the primary vortex might even decrease due to increasing effects caused by the presence of the bed. The disturbed development of the primary vortex results in a smaller non-linear contribution to lift than the contribution of a vortex that can develop to full growth along the suction side by selection of a taller vane at equal aspect ratio. The core of the undisturbed vortex grows with increasing angle of attack. It is therefore assessed that disturbances can take place already at relatively low angles of attack for vanes protruding relatively low above the bed, especially in the case of a rigid bed. Possibly, the existence of other flow structures at the higher angles of attack causes disturbances to the formation and development of the primary vortex along the suction side. Another reason could be that the horseshoe vortex leg along the pressure side increases in strength and thus reduces the pressure difference between pressure and suction side.

Examine lift coefficients for measurements OS1989 with increasing angle of attack. At angles of attack of 15° and higher, the measured lift forces deviate significantly from the forces predicted on the basis of the non-linear models. At an angle of attack of 25°, a decrease in lift is observed. Based on, among others, experimental results by Marelius ([30]; Section 2.3.4), one may expect that the lift force exerted on a submerged vane is a maximum at an angle of attack of the order of 40°. Hence, there is reason to believe that for the selected vane height, the presence of the bed affected the progress of the primary vortex already appreciably at an angle of attack as low as 15°, and that the measured lift coefficients may be explained by relatively low linear and non-linear contributions to lift due to disturbances caused by the presence of the bed. Note also the poor agreement between calculated lift coefficient using the non-linear model based on theory by Gersten and the measured lift coefficient for a vane height of 0.03 m (measurements WL2001). Here, on the other hand, the model based on theory developed by Bollay gives a better result, which, given the extremely low aspect ratio of the tested vane, is not that remarkable (use of the model based on theory by Bollay is advised for ratios of vane height to vane length of less than about 0.1 (Section 5.3.1)).

It appears that the aforementioned reasons can only explain partly why measurements WL1998 and WL2001 relate reasonably to good to coefficients calculated with the non-linear models and a weaker agreement is observed with measurements OS1986 and in particular with measurements OS1989. Apparently, the remaining part must be explained by measuring accuracies, differences between experimental equipment and procedures and corrections to obtained force data (corrections for shear forces exerted on the vane mount and zero-shifts). Here, as an example of how uncontrollable and seemingly small differences in test conditions are seen to affect the experimental results, the reader's attention is drawn to the slight difference in results for a vane height of 0.06 m in measurements WL1998 and WL2001, obtained for equal vane dimensions and test settings.

				Experiment		Odgaard		Bollay		Gersten	
H_v	L_v	d/H_v	α	C_L	C_D	C_L	C_{Di}	C_L	C_{Di}	C_L	C_{Di}
[m]	[m]	[-]	[degr.]	[-]	[-]	[-]	[-]	[-]	[-]	[-]	[-]
0.064	0.215	2.0	5	0.13		0.13	0.01	0.18	0.02	0.11	0.01
0.064	0.215	2.0	10	0.29	0.05	0.25	0.03	0.36	0.06	0.30	0.05
0.064	0.215	2.0	15	0.52	0.08	0.38	0.08	0.54	0.14	0.54	0.14
0.064	0.215	2.0	20	0.77	0.12	0.50	0.14	0.71	0.26	0.86	0.30
0.064	0.215	3.0	5	0.11		0.13	0.01	0.18	0.02	0.11	0.01
0.064	0.215	3.0	10	0.23	0.05	0.25	0.03	0.36	0.06	0.30	0.05
0.064	0.215	3.0	15	0.44	0.08	0.38	0.08	0.54	0.14	0.54	0.14
0.064	0.215	3.0	20	0.65	0.12	0.50	0.14	0.71	0.26	0.86	0.30
0.064	0.215	4.0	5	0.14		0.13	0.01	0.18	0.02	0.11	0.01
0.064	0.215	4.0	10	0.27	0.05	0.25	0.03	0.36	0.06	0.30	0.05
0.064	0.215	4.0	15	0.46	0.08	0.38	0.08	0.54	0.14	0.54	0.14
0.064	0.215	4.0	20	0.60	0.12	0.50	0.14	0.71	0.26	0.86	0.30

Table 5.9: Comparison measured and calculated coefficients for flat-plate vane; measurements OS1986

				Experiment		Odgaard		Bollay		Gersten	
H_v	L_v	d/H_v	α	C_L	C_D	C_L	C_{Di}	C_L	C_{Di}	C_L	C_{Di}
[m]	[m]	[-]	[degr.]	[-]	[-]	[-]	[-]	[-]	[-]	[-]	[-]
0.05	0.171	2.0	5	0.12		0.12	0.01	0.18	0.02	0.11	0.01
0.05	0.171	2.0	10	0.25	0.04	0.25	0.03	0.35	0.06	0.29	0.05
0.05	0.171	2.0	15	0.40	0.08	0.37	0.08	0.53	0.14	0.54	0.14
0.05	0.171	2.0	20	0.64	0.13	0.50	0.13	0.71	0.26	0.86	0.30
0.05	0.171	2.0	25	0.56		0.62	0.21	0.87	0.40	1.24	0.54
0.05	0.171	3.0	5	0.10		0.12	0.01	0.18	0.02	0.11	0.01
0.05	0.171	3.0	10	0.26	0.04	0.25	0.03	0.35	0.06	0.29	0.05
0.05	0.171	3.0	15	0.34	0.08	0.37	0.08	0.53	0.14	0.54	0.14
0.05	0.171	3.0	20	0.51	0.13	0.50	0.13	0.71	0.26	0.86	0.30
0.05	0.171	3.0	25	0.46		0.62	0.21	0.87	0.40	1.24	0.54
0.05	0.171	4.0	5	0.13		0.12	0.01	0.18	0.02	0.11	0.01
0.05	0.171	4.0	10	0.23	0.04	0.25	0.03	0.35	0.06	0.29	0.05
0.05	0.171	4.0	15	0.36	0.08	0.37	0.08	0.53	0.14	0.54	0.14
0.05	0.171	4.0	20	0.45	0.13	0.50	0.13	0.71	0.26	0.86	0.30
0.05	0.171	4.0	25	0.40		0.62	0.21	0.87	0.40	1.24	0.54

Table 5.10: Comparison measured and calculated coefficients for flat-plate vane; measurements OS1989

				Experiment		Odgaard		Bollay		Gersten	
H_v	L_v	d/H_v	α	C_L	C_D	C_L	C_{Di}	C_L	C_{Di}	C_L	C_{Di}
[m]	[m]	[-]	[degr.]	[-]	[-]	[-]	[-]	[-]	[-]	[-]	[-]
0.06	0.240	5.0	17.5	0.70	0.27	0.38	0.09	0.57	0.18	0.67	0.21
0.06	0.320	5.0	17.5	0.64	0.25	0.30	0.08	0.48	0.15	0.66	0.20
0.06	0.400	5.0	17.5	0.60	0.23	0.25	0.07	0.43	0.13	0.65	0.20
0.06	0.480	5.0	17.5	0.59	0.23	0.21	0.06	0.39	0.12	0.64	0.20

Table 5.11: Comparison measured and calculated coefficients for flat-plate vane; measurements WL1998

				Experiment		Odgaard		Bollay		Gersten	
H_v [m]	L_v [m]	d/H_v [-]	α [degr.]	C_L [-]	C_D [-]	C_L [-]	C_{Di} [-]	C_L [-]	C_{Di} [-]	C_L [-]	C_{Di} [-]
0.03	0.400	10.0	17.5	0.37	0.20	0.13	0.04	0.31	0.10	0.61	0.19
0.06	0.400	5.0	17.5	0.66	0.25	0.25	0.07	0.43	0.13	0.65	0.20
0.09	0.400	3.3	17.5	0.78	0.26	0.35	0.09	0.53	0.17	0.67	0.20
0.12	0.400	2.5	17.5	0.81	0.27	0.44	0.10	0.63	0.20	0.69	0.21

Table 5.12: Comparison measured and calculated coefficients for flat-plate vane; measurements WL2001

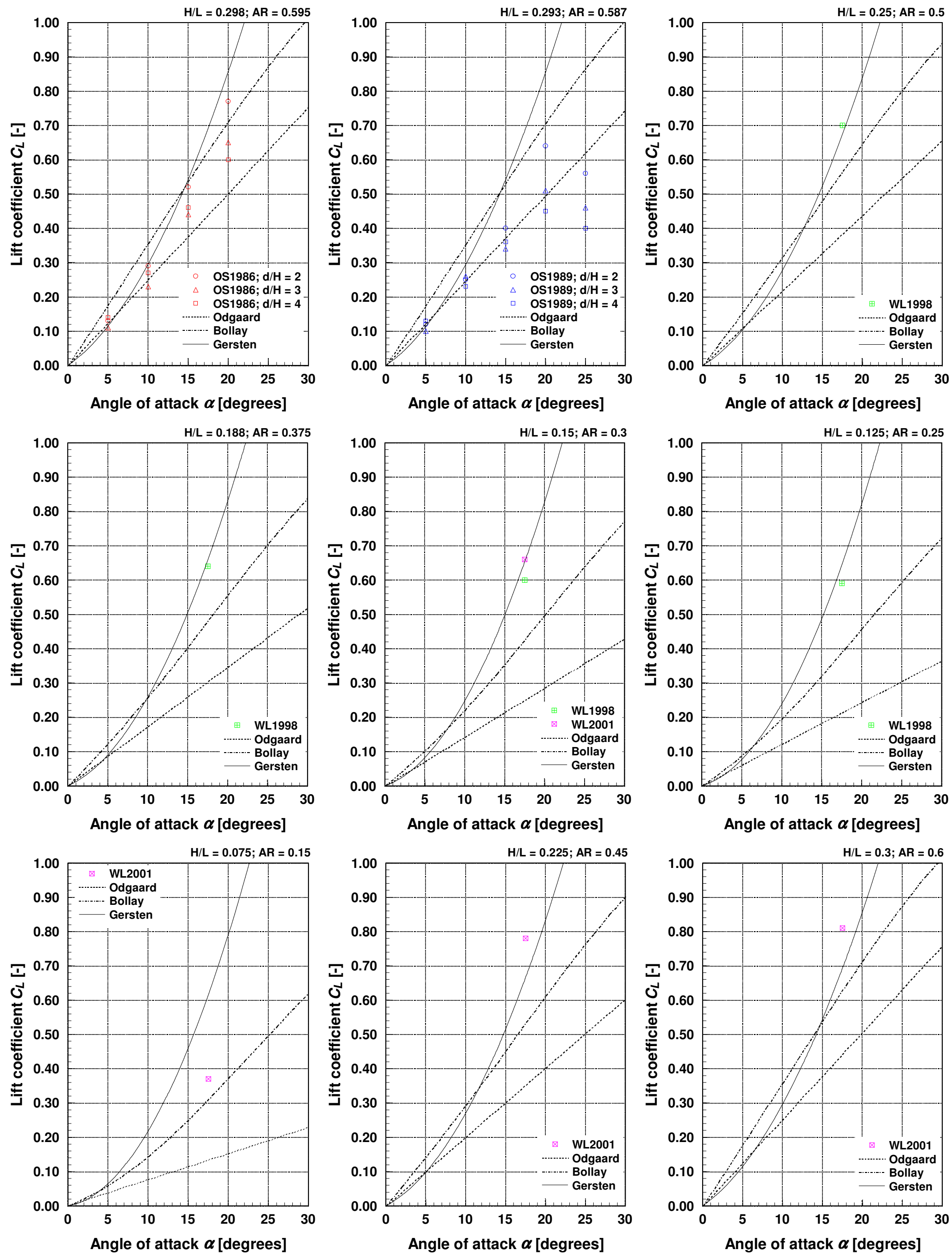

Figure 5.14: Comparison measured and calculated lift coefficients

Odgaard and Spoljaric reported that the lift coefficient increases with decreasing ratio of flow depth to vane height [35]. They explained this trend by stating that the pressure difference between the vane surfaces increases as a result of the suppression of the tip vortex by the free surface. No measurable dependence of the drag coefficient on the ratio of flow depth to vane height was found. If there is an effect of the ratio of flow depth to vane height on lift, it is seen that the ratio of flow depth to vane height has not affected measurements WL2001 evenly. Figure 5.16 shows that the variation in the ratio of flow depth to vane height resulted from a varying flow depth by equal vane dimensions and discharges in the experiments conducted by Odgaard and Spoljaric and from a varying vane height by equal flow depth and discharge in experiments conducted at WL | Delft Hydraulics. For measurements WL2001, the vane submergence was such that strong suppression of the primary vortex by the free surface seems unlikely, even at low ratios of flow depth to vane height. A better indicator of the possible effect of suppression of the primary vortex by the free surface may be the ratio of vane submergence to radius of the undisturbed vortex core. Especially in the lower regions, there are strong gradients in the actual depth-distribution of the approach flow velocity. With increasing vane height, there are less pronounced gradients in the distribution of the approach flow velocity not to far from the top edge of the vane. Maybe, the conditions for preservation of the 'separation bubble', from which fluid is drawn to the low-pressure regions of the primary vortex and put into spiral motion, are then more favourable. For measurements WL2001, the discrepancy between measured lift coefficients and lift coefficients calculated by use of the model based on theory developed by Gersten is a minimum for a vane height of 0.06 m and increases with increasing vane height. The limited number of available results, however, does not permit the drawing of conclusions on this subject.

Compared to measurements WL1998 and WL2001, measurements OS1986 and OS1989 show low drag coefficients at the higher angles of attack. This observation may indicate that the primary vortex indeed could not develop undisturbed along the suction side by the presence of the bed. Unfortunately, Odgaard and Spoljaric did not present the results of drag measurements at an angle of attack of 25°. Strikingly, Odgaard and Spoljaric did not find a measurable dependence of the drag coefficient on the ratio of flow depth to vane height, whereas the lift coefficient was seen to depend on the ratio of flow depth to vane height. For low aspect ratio plates, an increase in lift is usually accompanied with an increase in drag. A good agreement between measured and theoretical non-linear (induced) drag coefficients for measurements WL1998 and WL2001 and for measurements OS1986 and OS1989 at low angles of attack. Note that the theoretical models estimate the induced drag (drag due to lift) only; profile drag must be added to the induced drag to obtain the total drag (Section 5.2.2). For thin, flat plates at relatively high angles of attack, induced drag is clearly the main contributor to the total drag.

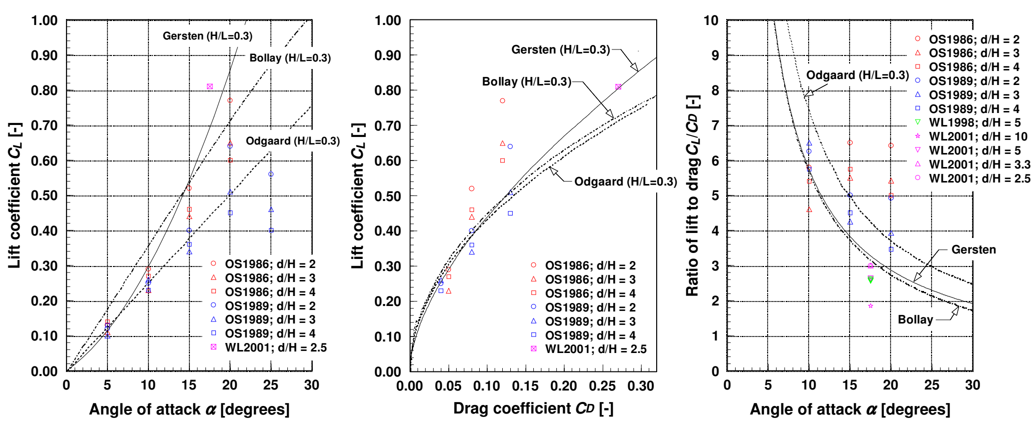

Figure 5.15: Comparison measurements OS1986, OS1989, WL1998 and WL2001

Figure 5.15 presents a comparison between the available experimental results for a ratio of vane height to vane length of approximately 0.6. The polar plot (lift versus drag) shows that, as a consequence of the relatively low measured drag forces, measurements OS1986 and OS1998 suggest high efficiency (relatively high ratio of lift to drag coefficient). Experimental results by WL | Delft Hydraulics indicate that, by approximation, the curvature of the polar corresponds to the expected non-linear behaviour of the lift and drag forces exerted on a sharp-edged, slender vane: the primary vortex influences the pressure distribution on the suction side and gives rise to a substantial non-linear lift contribution that partially compensates for the additional drag due to the loss of the leading edge suction force. In the graph on the right, the ratio of lift to drag is plotted versus the angle of attack. Measurements OS1986 and OS1989 suggest high vane efficiency at angle of attack. Measurements WL1998 and WL2001 show levels of vane efficiency that, broadly speaking, agree better with expected ratios of lift to drag for slender submerged vanes at angle of attack. Note that the curves, designated Odgaard, Bollay and Gersten, do not account for profile drag and thus indicate slightly overestimated ratios of lift to drag at a given angle of attack.

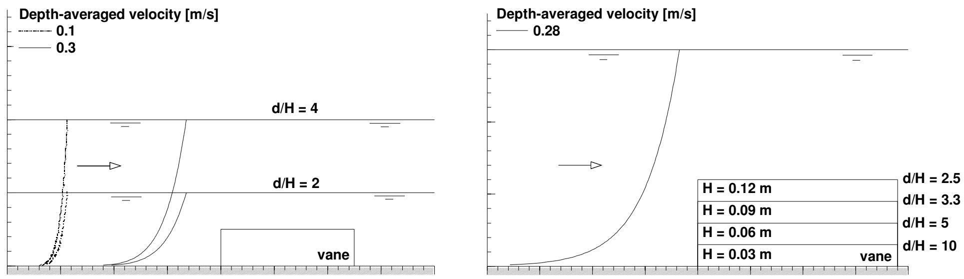

Figure 5.16: Ratio of water depth to vane height measurements OS1989 (left) and WL2001 (right)

5.6 EFFECTS ON MEAN LIFT AND DRAG FORCES

Pressure distributions and mean hydrodynamic forces acting on hydraulic structures may be presented in terms of the piezometric head coefficient or, in cases unaffected by gravity, the pressure coefficient. In general, the dimensionless coefficients are functions of many independent parameters. For the pressure distributions and the hydrodynamic forces exerted on submerged vanes, boundary geometry and roughness, approach flow conditions, vane geometry, gravity effects (Froude number) and viscosity effects (Reynolds number) may play a role. Herein, the effects of these parameters are investigated.

Flow processes in air and water can be treated analogously as long as compressibility effects are negligible and free surface or cavitation effects do not play a role [34]. Within these limits, it is possible to gratefully adopt achievements in aerodynamics to predict the mean hydrodynamic forces exerted on submerged vanes.

5.6.1 Effect of gravity

The theory of Odgaard (Section 3.2) is based on a low Froude number approximation, which allows the free surface to be taken as a rigid boundary [38]. In their experiments, Odgaard and Spoljaric varied the Froude number to investigate gravity effects. Experimental results did not suggest a Froude number dependence under the flow conditions tested (ratio of flow depth to vane height > 2 and Froude number < 0.25) [38].

5.6.2 Effect of viscosity

From experimental results for Reynolds chord numbers ranging from $0.3 \cdot 10^6$ to $1.7 \cdot 10^6$, Wickens concluded that the forces and therefore the flow pattern about flat plates are practically independent of the Reynolds number [54]. The flow pattern about cambered models, however, may depend on the Reynolds number. Submerged vanes typically have Reynolds chord numbers of the order of 10^4 to 10^6. Because flow separation is fixed along the sharp edges of thin flat-plates, it is expected that the dependence of slender submerged vanes on the Reynolds chord number is negligible. Noteworthy, no viscosity effects have been observed in the range of Reynolds number of $4 \cdot 10^3$ to $1 \cdot 10^7$ for flat-plates of infinite aspect ratio in turbulence free cross flows, since drag depends mainly on the conditions of flow separation and the location of separation is fixed along sharp edges for angular bodies [34]. An increase in dependence of the mean lift and drag forces on the Reynolds chord number is expected for cambered vanes that protrude relatively high above the bed at low angles of attack, as the flow along lower regions on the suction side may be essentially adhering and the location of separation may depend on the Reynolds chord number.

5.6.3 Effect of bed and roughness

In the non-linear models for flat-plate vanes described in Sections 5.3.1 and 5.3.2, it is assumed that the bed is smooth, plane and rigid. For practical reasons, force measurements OS1986, OS1989, WL1998 and WL2001 have been taken for vanes protruding above rigid beds, where the vane mounts have been coated to ensure that the local roughness equalled the roughness of the surrounding model bed. Hence, bed roughness has affected the force measurements. For a submerged vane protruding above a riverbed, the bed affects the velocity distribution and can give rise to flow separation in the form of a horseshoe vortex in front of the vane, the strength of which depends mainly on the geometric angle of attack. The effects of bed roughness can be explained in terms of increased turbulence and change in velocity profile. At high angles of attack, the strength of vortices resulting from flow separation in front of the structure may be considerable as shown by Marelius and Sinha [30] and by results of the current research. At present, there is almost no information about possible counter-productive effects of these and other counterrotating vortices induced at high angles of attack, except that it has been observed that the horseshoe vortex leaving from the trailing edge and the weaker suction vortex decay within a distance downstream of the midst of the vane of about twice the vane length. Particularly at high angles of attack, however, the strength and stability of the primary vortex is such that the presence of the counterrotating vortices may be overcome. Furthermore, the suitability of scour holes to aid the intended purpose must not be ignored. The reader is referred to Chapter 6 for more information about scour at submerged vanes.

5.6.4 Effect of approach flow conditions

Flow depth

According to Odgaard and Spoljaric, the lift coefficient increases with decreasing ratio of flow depth to vane height due to suppression of the tip vortex by the free surface [35; 38]. No measurable dependence of the drag coefficient on the ratio of flow depth to vane height was found. As described in Section 5.5, measurements WL2001 do not suggest evenly significant effects of the ratio of flow depth to vane height on the lift coefficient (Figure 5.15). For measurements WL2001, however, vane submergence was such that suppression of the vortex by the free surface seems unlikely, even at low ratios of flow depth to vane height (Figure 5.16). It is expected that suppression of the tip vortex by the free surface does not affect the lift coefficient significantly in not all too shallow waters. Therefore, the ratio of flow depth to vane height is not a correct measure for possible suppression effects (see also Section 5.5). In the author's opinion, the selection of the initial vane height plays a more important role by vane design. Preferably, vanes should protrude sufficiently high above the bed to provide optimum conditions for the development of the primary vortex along the suction side (Section 5.6.5).

Free stream turbulence

Free stream turbulence can alter conditions of flow separation and reattachment in cases of angular and cylindrical bodies [34]. In general, turbulence is seen to lead to higher streamline curvature right after separation. In several wind tunnel tests at low Reynolds chord numbers, it has been found that an increase in free stream turbulence intensity reduces the drag on airfoils and slightly increases the maximum lift coefficient [44]. The slight increase in airfoil performance with increasing turbulence intensity at relatively low angles of attack is ascribed to earlier flow reattachment (a shorter 'separation bubble'). At higher angles of attack, at which the flow about the airfoil is mostly separated, an increase in drag coefficient is observed with increasing turbulence intensity. In water tunnel tests at a Reynolds chord number of $6 \cdot 10^4$, Pelletier and Meuller [44] found a negligible effect of the turbulence intensity on the aerodynamic coefficients of a thin flat-plate at an aspect ratio of 1.0. Flow visualization by use of hydrogen bubbles did not indicate the presence of flow reattachment after separation. Therefore, and because turbulence intensity usually affects the location of separation and reattachment, the results were not expected to be significantly affected by varying turbulence intensity for the tested thin plate. Based on the above-described findings, it is expected that regular turbulence intensities do not affect the lift and drag coefficients of slender submerged vanes strongly, as the flow about submerged vanes is mostly separated at practical ranges of angle of attack.

Yaw angle

At present, no information is available about the flow pattern about a submerged vane where the approach flow contains substantial vertical velocity components. Taking advantage of the supposed analogy between the vortical flows about slender submerged vanes and low aspect ratio wings, one may refer to results of aerodynamic investigations on the matter. Figure 5.17 shows Wickens' interpretation of the flow about a thin flat-plate at an aspect ratio of 0.25 and an angle of attack of 20°, yawed to 16°. Wickens postulated that the (conjectural) primary attachment line OA in Figure 5.17 originates close to the plate centreline, but progresses across the plate and intersects the leeward edge at mid-chord approximately [54]. Line AA' (nearest the leeward edge) and line OA divide the regions where the flow enters either the windward or the leeward vortex system. Presumably, secondary and tertiary separation occurs inboard of the edge on the windward side of the plate. Two vortices of the same sign, but of different strengths, shed from the leeward edge, roll up into two separate cores at the trailing edge [54]. The primary leeward vortex originates at the forward corner, the secondary vortex presumably at the point of intersection of line OA with the leeward edge. Fluid flowing along the leeward side of the plate is drawn into either vortex, as the cross flow divides at the line dividing the leeward and windward flow on the curved surface of the leeward vortex sheet between the primary or secondary vortices. Relying on experimental results for a yawed low aspect ratio wing by Wickens, secondary and/or tertiary separation is likely for submerged vanes at yaw angle. Possible detrimental effects of vertical velocity components in the approach flow on vane performance (supposing that the primary vortex is beneficial to vane performance) depend on the strengths and signs of additional vortical structures, but it is anticipated that the strengths of possible additional structures are small compared to the strength of the primary vortex.

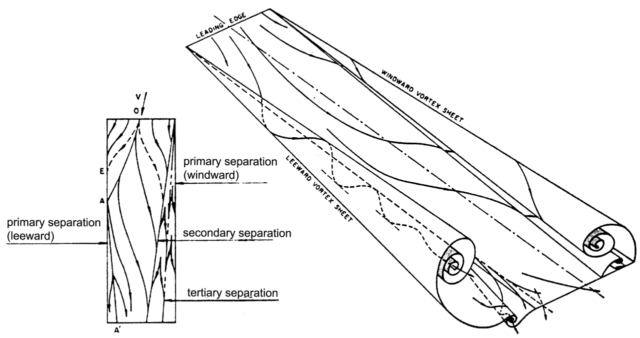

Figure 5.17: Windward and leeward vortex sheets for a yawed thin, rectangular flat-plate; source: Wickens, 1967

5.6.5 Effect of vane geometry

Aspect ratio

The effect of aspect ratio on the mean lift and drag coefficients for a thin, flat vane with rectangular planform is seen to be given reasonably to good by the non-linear models based on theories developed by Bollay and Gersten (Section 5.5). For aspect ratios lower than about 0.2 (ratios of vane height to vane length lower than 0.1), use of the model based on theory developed by Bollay (Section 5.3.1) is advised. For higher aspect ratios, the model based on theory developed by Gersten (Section 5.3.2) gives a better agreement with experimental results, whereas the model based on theory by Bollay only gives the order of magnitude (with maximum discrepancies in lift coefficient with measurements WL1998 and WL2001 of the order of 35%). Keep in mind that the limited number of force measurements available restricts the drawing of conclusions. It is recommended to conduct additional force measurements for thin, flat vanes and to use the results to verify findings with regard to the mean lift and drag force. Preferably, measuring projects should include force measurements at high angles of attack up to 50°. With the aid of experimental data for vanes at high angles of attack, the validity ranges of the models based on theories developed by Bollay and Gersten can be defined. At present, the upper limit of the validity ranges of both models is confined to an angle of attack of about 20°. Here, it is stressed that, in spite of increases in drag and local scour, attention should be given to vanes at the higher ranges of angle of attack, because it is expected that the non-linear effects increase with increasing angle of attack. Presumably, vanes at higher angles of attack induce stronger and more stable primary vortices (provided the vanes protrude sufficiently high above the bed, so that the primary vortex can develop to full growth along the suction side) than vanes at conventional angles of attack. Referring to experimental results by Winter [55] (for low aspect ratio flat-plates) and by Marelius and Sinha [30] (for a thin flat-plate vane), it is expected that the lift exerted on a submerged thin, flat vane with rectangular planform (excluding forces in lift direction due to possible horseshoe vortices) is a maximum at an angle of attack increasing from about 40° for an aspect ratio of 1.0 to higher than 55° for an aspect ratio of 0.1, provided the vane protrudes sufficiently high above the bed.

The initial vane height may play an important role by vane effectiveness. It appears that the presence of a layer of more or less adhering flow below the regions of depressed streamwise velocity component is beneficial to the development of the primary vortex. Measurements of the forces exerted on vanes protruding above rigid beds at angles of attack up to 20° suggest an optimum development of the primary vortex for ratios of flow depth to vane height of lower than about 3. The reader is referred to Section 7.3 for more information about the effect of vane height on vane effectiveness.

Form of leading and top edges

Figure 5.18 presents experimental results by Winter [55] for a thin, flat rectangular plate at an aspect ratio of 0.5 and a Reynolds chord number of $6 \cdot 10^5$ with varying forms of the leading and side edges. Because non-linear effects are mainly due to flow separation and the generation of vortices at the leading and side edges, the non-linear contribution to lift is larger for sharp-edged plates than for plates with rounded edges (the linear contribution to lift is estimated by use of the linear lifting surface theory by Truckenbrodt [49] (linear curve)). The separated flow shed from the sharp leading edge reattaches at some distance downstream. Specifically at low aspect ratios, stagnating fluid inside the 'separation bubble' near the leading edge flows toward the low-pressure regions of the edge vortices and gets involved in the spiral motion downstream, thus, increasing the size of regions of separated flow near the side edges and the strengths of the edge vortices. The non-linear effects increase with decreasing aspect ratio and increasing angle of attack. The form of the side edges appears to be less important. Independent of the form of the side edges, there is tip flow and flow separation along the side edges. However, rounding of the side edges is seen to have a small detrimental effect on lift. An increase of the distance between the pressure and suction side will bring about a decrease in tip flow and hence a decrease in the non-linear effects. The author of this report feels that the well functioning of a submerged vane is primarily associated with the generation of a strong and stable primary vortex, a measure of which may be the non-linear contribution to lift exerted on the vane. In other words, a submerged vane should be designed in such a manner that the conditions regarding the shape of the vane to bring about the non-linear lift contribution are optimal. It follows that submerged vanes should preferably be equipped with sharp leading and top edges and that the structural width should be reduced to a minimum.

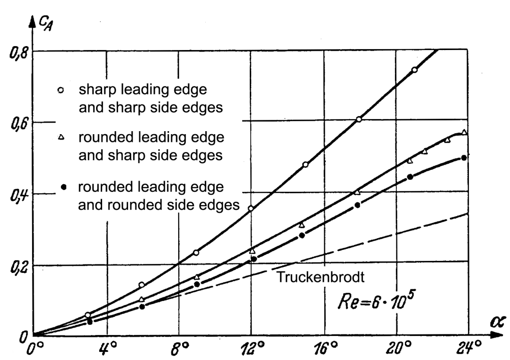

Figure 5.18: Experimental results by Winter for a thin, flat rectangular plate with varying forms of leading and side edges; source: Gersten, 1961

Due to the expansion of the flow around the leading edge, there is a low pressure over the front face of the leading edge (in an inviscid, incompressible flow). The expansion strengthens with decreasing profile thickness, so that the leading edge suction force (the product of pressure over the front face and plate thickness) reaches a finite magnitude in the limit of zero thickness. Of course, very thin plates fail to create a significant suction force and a force in drag direction results. Note that due to the absence of a leading edge suction force for very thin plates, it is allowed to determine the (induced) drag coefficient from the normal force coefficient as $C_{Di} = C_N \sin\alpha$ (Sections 5.3.1 and 5.3.2). Airfoil-shaped and slender bodies with rounded leading edges, however, achieve a larger part of the suction force at least at low angles of attack, resulting in improved polars (lift versus drag).

Thick vanes

Figure 5.13 presents experimental results by Odgaard and Spoljaric for thick, flat vanes (thickness ratio: about 10%) at an aspect ratio of 0.93. Odgaard and Spoljaric stated that an increase of vane thickness causes an increase of the size of the separation zone at the rear side of the vane and thus a decrease of lift [38]. The results are also presented in Figure 5.19, in which curves are added for comparison with a thin, flat vane at equal aspect ratio. First, it is noted that the aspect ratio of the tested thick, flat vanes is rather high; the selected plate dimensions are not suitable to model an adequate submerged vane as the non-linear contribution to lift will be relatively small at an aspect ratio of about 0.9 and at practical ranges of angle of attack, even for a thin, flat plate. Evidently, thick vanes are less efficient than thin vanes. The leading edge of the thick, flat vanes is blunt, while a sharp edge (or at least a tapered edge) is preferred. Furthermore, the increase in distance between the pressure and suction side by the profile thickness causes a decrease in tip flow. All of the above-mentioned deficiencies disturb the generation of a strong and stable primary vortex, which manifests itself in force measurements by a relatively small vortex lift contribution.

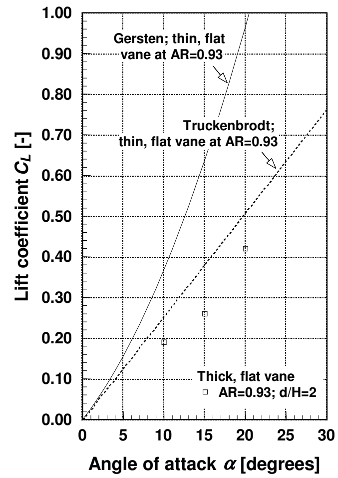

Figure 5.19: Comparison thick, flat vanes and thin, flat vanes; measurements OS1989

Cambered vanes

Experimental results by Odgaard and Spoljaric for cambered vanes with and without twist (thickness ratio: about 10%) at an aspect ratio of about 0.9 are presented in Figure 5.13. Unfortunately, the results of drag measurements have not been included. Initially, cambered vanes were selected as test vanes, based on the knowledge that cambering reduces induced drag and thus increases wing efficiency for high aspect ratio wings. From the results, Odgaard and Spoljaric [38] concluded that cambering and twist do not improve the lift characteristics. By dye injections, a more pronounced boundary layer separation was observed around cambered vanes than around thin, flat vanes. Referring to this observation, Odgaard and Spoljaric explained the less favourable measured lift characteristics of cambered vanes by stating that flow separation reduces the pressure difference between pressure and suction side and thus reduces lift [38]. Also, the vertical lift component generated by the twisted vane could not be measured in their set-up. Figure 5.20 presents results of force measurements on a cambered wing with rectangular planform at an aspect ratio of 0.5 (Göttingen profile 409; thickness ratio: 12.7%) by Winter [55]. Up to a lift coefficient of about 0.55, the polars almost coincide with the polars of flat rectangular plates (see Figure 5.20; effect of camber is often attributed to the 'separation bubble' near the leading edge of a thin, flat plat at low angles of attack), while above a critical angle of attack of about 23°, the polars show a strong increase in drag and hence, are found to be less efficient in the higher ranges of angle of attack. In spite of increased separation, the flow essentially adheres to the profile. The effect of camber is seen to lead to a 'smoother' flow along the centreline of the profile, which reduces the formation of vortices. Furthermore, compared with thin models, the distance between the pressure and the suction side is increased by the profile thickness, bringing about a decrease in tip flow. The results by Odgaard and Spoljaric for cambered models are also presented in Figure 5.21, in which curves are added for comparison with thin,

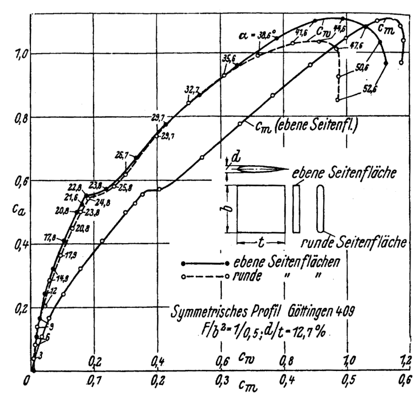

Figure 5.20: Polar plots for cambered wings at an aspect ratio of 0.5; source: Winter, 1935

flat vanes. Note again that the aspect ratio of the airfoil-shaped vanes is rather high; the selected dimensions are not suitable to model an adequate submerged vane. At angles of attack beyond about 10°, the measured lift coefficients for the cambered models are considerably lower than the (expected) lift coefficients for a thin, flat plate of equal aspect ratio. Based on the perception of the flow about submerged vanes described in Section 4.6, the author of this report objects to the explanation for the observed less favourable lift characteristics of cambered vanes (compared with thin, flat vanes) postulated by Odgaard and Spoljaric. The less favourable lift characteristics of cambered vanes are due to the disturbance of the effect of the edge vortex on lift by the thicker top edges. From the experimental results by Winter for a cambered wing with rectangular planform at low aspect ratios and the analogy between submerged vanes and low aspect ratio wings, one might expect that the lift curves of thin, flat vanes and cambered vanes do not spread to an extent as seen in Figure 5.21. There is reason to believe that the observed lift development is caused by the selected, relatively small vane height (see discussion in Section 5.5). Hypothetically, with increasing vane height, there would have developed a stronger, more or less adhering flow along the regions on the suction side below the regions of separated flow near the top edge. For the selected vane height, it is assessed that the regions of separated flow covered most of the suction side surface at the higher angles of attack (possibly up to a degree at which the generation of the primary vortex was disturbed by the presence of the bed) and that there could not develop an essentially adhering flow along the suction side with corresponding lift contribution. Still, cambered vanes tend to disturb the formation of a strong and stable primary vortex, and thus are less adequate vanes than thin, flat vanes. However, if, for practical reasons, a vane must have a substantial structural width, cambered profiles should not be ruled out. It is recommended to conduct additional force measurements for cambered vanes, preferably with taller profiles and at lower aspect ratios.

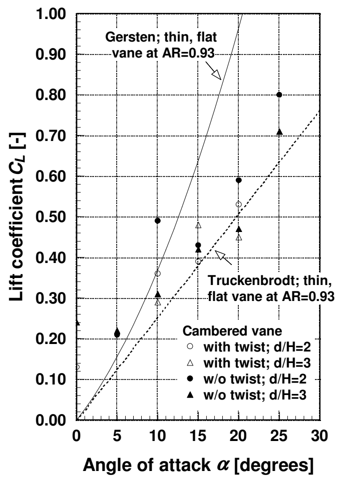

Figure 5.21: Comparison cambered vanes and thin, flat vanes; measurements OS1989

Sheet-wall vanes

Figure 5.22 presents a comparison between thin, flat vanes and sheet-wall vanes at an angle of attack of 17.5° (measurements WL1998 and WL2001). Relative to the measured lift and drag forces for thin, flat vanes, the measured lift and drag forces on sheet-wall vanes (corrected for shear stresses on the vane mount) are up to 21% lower and up to 66% higher, respectively. It is expected that the relative increase in drag for sheet-wall vanes is due mainly to an increase in profile drag. Theoretically, the non-linear contribution to the lift acting on a thin, flat vane according to the model based on theory developed by Gersten, given by the difference in lift coefficients by the curves designated Gersten and Truckenbrodt, represents the additional vortex lift and may be regarded as a measure of the strength of the primary vortex. From lift coefficient versus vane length/height plots, the conclusion cannot be drawn that the tested sheet-wall vanes induced significantly weaker primary vortices. Especially for the taller sheet-wall vanes tested (measurements WL2001), the measured lift forces agree reasonably with measured lift forces on thin, flat vanes with equal dimensions. Noteworthy, downstream velocity measurements did not show large differences between the maximum transverse velocity components for thin, flat vanes and sheet-wall vanes. Like the flat-plate vane, the sheet-wall vane is equipped with sharp edges along the leading and top edge, so that the location of flow separation is fixed. Hence, the slender sheet-wall vane in principle complies with the key ingredient to the generation of a strong and stable primary vortex. However, as a consequence of the relative increase in drag, the efficiency of a sheet-wall vane, given by the ratio of lift to drag, is clearly poorer compared to the efficiency of a thin, flat vane.

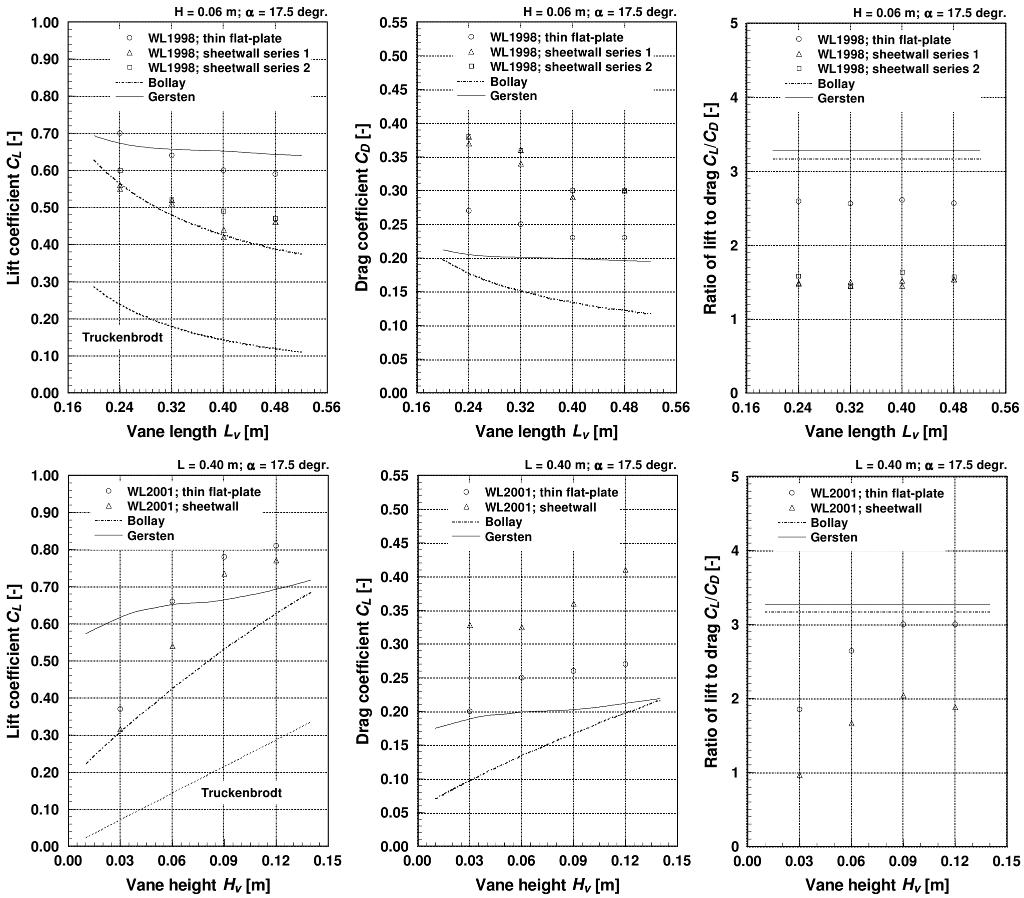

Figure 5.22: Comparison sheet-wall vanes and thin, flat vanes; measurements WL1998 and WL2001

5.7 PRESSURE DISTRIBUTION AND PRESSURE FLUCTUATIONS

Since the pressure side of a submerged vane is essentially a stream surface (in the absence of a strongly developed horseshoe vortex), it is expected that the pressure distribution on the pressure side is a continuous curve. The suction side, on the contrary, is predominantly covered with vortex layers and is therefore subject to a non-uniform and time-varying pressure distribution. Force measurements conducted at WL | Delft Hydraulics indicate strong variations in the lift and drag forces exerted on a thin, flat vane at an angle of attack of 17.5° [11; 24]: globally, $0.2\overline{F_L} \le F_L \le 2.1\overline{F_L}$ and $0.6\overline{F_D} \le F_D \le 1.7\overline{F_D}$, in which $\overline{F_L}$ and $\overline{F_D}$ represent the time-averaged measured lift and drag forces (by a measuring duration of 120 seconds).

Figures 5.23 and 5.24 present experimental results of surface pressure measurements for a thin, flat plate at an aspect ratio of 0.25 and an angle of attack of 20° by Wickens [54]. Pressure holes (diameter: 0.06”) were drilled at selected chordwise and spanwise locations and the plate was equipped with a small nose flap in order to suppress flow separation and pressure fluctuations downstream of the leading edge. Figure 5.23 presents 3D-illustrations of the aerodynamic load for yaw angles of 0° and 16°, Figure 5.24 shows the measured spanwise distributions on the upper and lower surfaces for yaw angles of 0°, 8° and 16°. It is seen that the lift is carried mainly near the leading and side edges underneath the rolled-up vortices. At yaw angles, the pressure decreases even more (negative pressure) on the suction side at the windward edge as the windward vortex strengthens. The pressure peak induced by the vortex moves in spanwise direction and is located underneath the rolled-up core. The load on the leeward side diminishes, because the leeward vortex moves away from the plate. It is also seen that the lower surface pressure coefficients do not change as severely as the upper surface pressure coefficients with yaw angle. The windward pressures are higher than the leeward pressures due to the higher effective incidence on the windward side. Based on the experimental results of surface pressure measurements for low aspect ratio wings by Wickens [54] and Winter [55], it is expected that the hydrodynamic load on a slender submerged vane includes large pressure peaks in regions near the leading edge and near the top edge underneath the primary vortex and that intense pressure fluctuations occur in these regions. Especially at the higher angles of attack, local pressure fluctuations due to the horseshoe vortex leg along the pressure side of the vane may also demand the designer's attention. All regions at which pressure fluctuations are augmented due to the generation of vortices ought to be inspected and checked for excessive tensions.

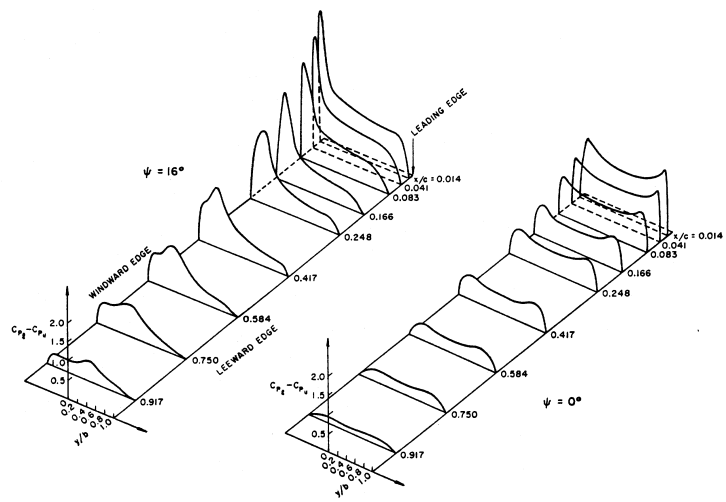

Figure 5.23: Aerodynamic load distribution on a thin, flat plate at varying yaw angle; source: Wickens, 1967

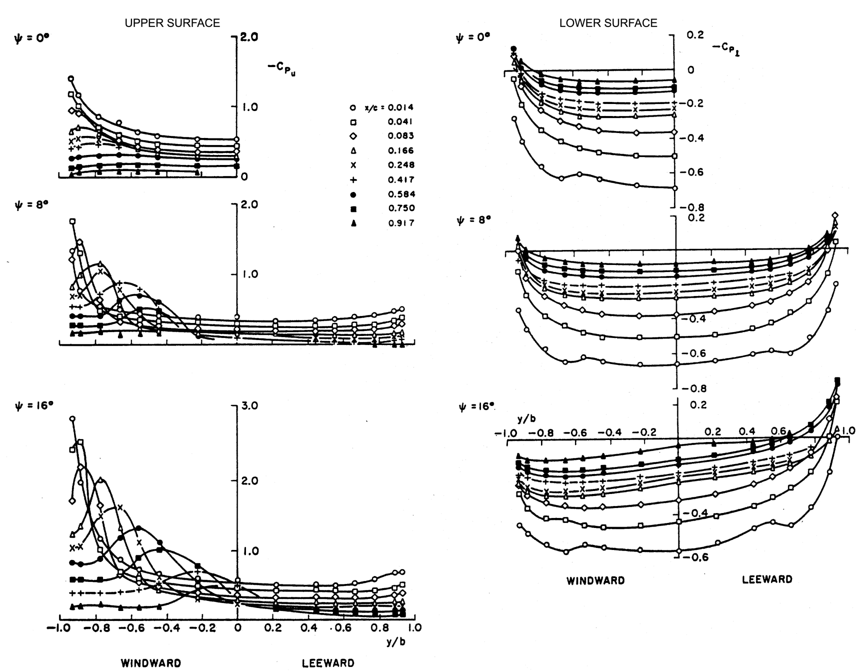

Figure 5.24: Spanwise pressure distributions at varying yaw angle; source: Wickens, 1967

6 ANALYSIS OF LOCAL SCOUR MEASUREMENTS

6.1 INTRODUCTION

An important reason to start up a rather extensive series of scour tests in the framework of the BUET-DUT linkage project has been the lack of information about scour development around submerged vanes. The current experiments have been designed to investigate the effect of vane height and angle of attack on local scour and the effect of local scour on the physics of the flow past a single vane. Most of the previous experiments have been conducted for fixed beds, while in some mobile bed tests scour is avoided by giving the sediment around the vanes a light cement cap. Referring to the lack of information about scour at submerged vanes, Hoffmans and Verheij proposed to use relations for scour at slender bridge piers aligned to the flow to predict equilibrium scour depths for submerged vanes [19].

In the following sections, the results of the scour tests conducted in the period of March to June 2003 are presented and analysed. Section 6.2 gives a description of the observed scour development. In Section 6.3, the use of scour relations for slender bridge piers to estimate equilibrium scour depths around submerged vanes, as proposed by Hoffmans and Verheij, is evaluated by a comparison between predicted and measured scour depths. Finally, Section 6.4 deals with measures to reduce scour at submerged vanes.

During experimentation, the development of local scour around the tested vanes has been monitored by measurements of the local water depth at three locations along the exposed side of the vane: at the leading edge (location A), at the midst of the vane (location B) and at the trailing edge (location C). For that purpose, use has been made of a simple rod equipped with a small footplate. In consideration of the nature of the measuring procedures applied, water depth readings have been rounded off to multiples of 0.5 cm. The accuracy of the error-sensitive local scour readings is of the order of 1.0 cm. Bed level measurements provide a more accurate means to determine local scour depths, but due to the labour-intensive nature of measuring only a limited number of bed level data sets are available. As no advanced equipment was accessible, bed level measurements have been carried out manually by means of a self-designed instrument made out of an IPE100 beam, which spanned the flume width and rested upon the flume sidewalls. In the mid-section of the beam, the flanges have been perforated at an interval of 25 mm, while in the outer sections an interval of 50 mm has been applied. Local bed levels have been determined by manually lowering gauges of equal length until their sharpened tips hit the bed locally and by subsequently reading the lengths of the gauges above beam level. Rubber cascades in between the flanges prevented the gauges from penetrating the model bed. Bed level measuring has been carried out under reduced water level conditions for reasons of better visibility. It is assessed that the possible error in local bed elevation obtained from a bed level data set maximally equals 0.7 cm. The reader is referred to the accompanying measuring report [57] for more information about scour monitoring, bed level measuring and measuring accuracies.

6.2 SCOUR DEVELOPMENT

Scour development commences near the leading edge of the submerged vane, at which stage the eroded material is transported downstream by the flow. Soon after commencement of scouring, a relatively shallow scour pattern is formed around the leading edge of the vane, taking the shape of a spherical shell with increasing radius. Because the velocity decreases from the top of the vane downwards, the stagnation pressures also decrease from the top of the vane downwards. The downward pressure gradient gives rise to downflow at the face of the submerged vane, which erodes a groove in front of and along the pressure side of the vane. As a result of flow separation at the upstream rim of the scour hole excavated by the downflow, a horseshoe vortex develops. Particularly for vanes at angles of attack of 30° and higher, it is observed that the strength of the horseshoe vortex leg along the pressure side of the vane is such that the vortex becomes effective in transporting material away from the scour hole. The eroded material is then transported downstream by the combined action of accelerated flow and the spiral motion of the horseshoe vortex leg along the pressure side of the vane.

For a flat rectangular vane at an angle of attack of 40°, Marelius and Sinha reported that the combined effects of suction and horseshoe vortices govern the transverse transport in the immediate vicinity of the vane (see Figure 4.14) [30]. They found that the horseshoe vortex leg leaving from the leading edge decays quickly, while the vortex leg leaving from the trailing edge (horseshoe vortex leg along the pressure side of the vane) persists over a longer distance. The difference in decay rates is explained by the location of the stagnation line on the pressure side of the vane, which indicates that the horseshoe vortex leg leaving from the trailing edge is affected by a larger portion of the pressure side surface. The vortex leg leaving from the leading edge is affected more by the strong low pressure are on the suction side of the vane, which disrupts the circulation. The counterrotating suction vortex (compared to the sense of rotation of the primary (suction) vortex) is expected to result in a small counterproductive force only. At a distance of twice the vane length downstream from the midst of the vane, the suction and horseshoe vortex lose their identity and convert into general turbulence. Hence, farther downstream only the primary (suction) vortex is effective. Above-mentioned findings are verified by experimental results of the current research. Note, however, that the leading edge horseshoe vortex leg and the small counterrotating suction vortex have not been identified, probably due to the use of inferior instruments and a less detailed measuring grid, which suggests that the vortices are relatively weak and insignificant. For angles of attack of 30° and 40°, the presence of the horseshoe vortex leg leaving from the trailing edge is distinctly identified.

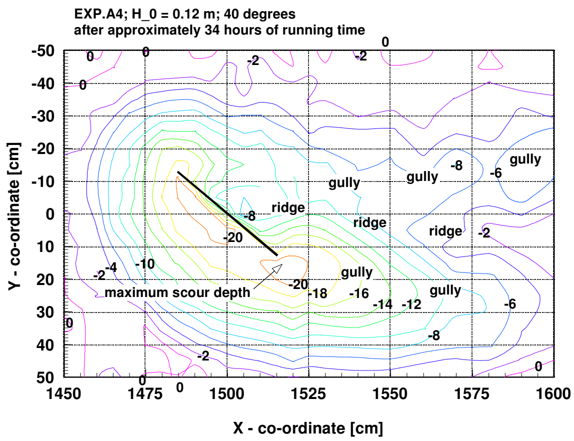

Figure 6.1: Local scour hole around tested vane at an angle of attack of 40° after approximately 34 hours of running time

The local scour depth is seen to depend strongly on the alignment to flow. Hence, the scour depth is a function of the projected width of the submerged vane (width normal to the flow). With increasing angle of attack, the location of maximum scour moves along the exposed pressure side of the vane towards the trailing edge. For the tested vanes with ratio of vane length to vane width equal to 80, the scour depth at the rear ultimately exceeds the scour depth at the front for angles of attack of 30° and higher. Figure 6.1 presents scour hole dimensions for EXP.A4 (vane height: 0.12 m; angle of attack: 40°) after approximately 34 hours of running time (obtained from bed level measurements). At this stage of scour development, the scour depth is a maximum near the trailing edge. Figure 6.2 presents scour development along the pressure and suction sides of the vane for EXP.A4 (presented scour depths have been estimated by visual observations using indicators applied to the vane; therefore, limited accuracy). The scour pattern along the suction side of the vane shows minimum scour at about the three-quarter chord with slopes continuing to the maximum

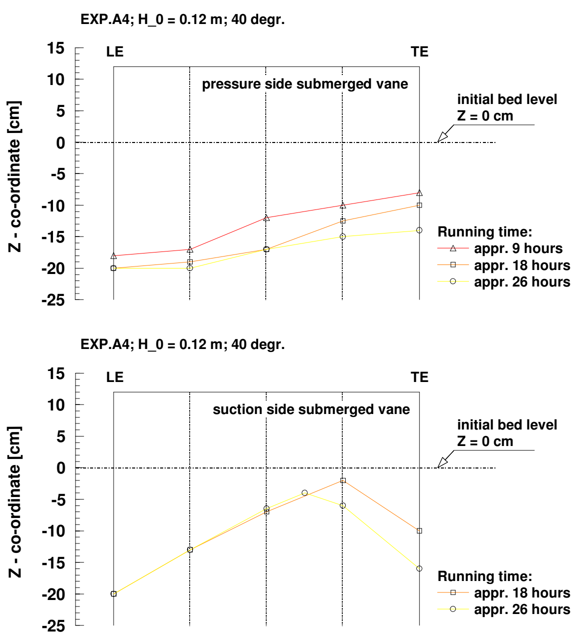

Figure 6.2: Scour development along the pressure and suction side for tested vane at an angle of attack of 40°

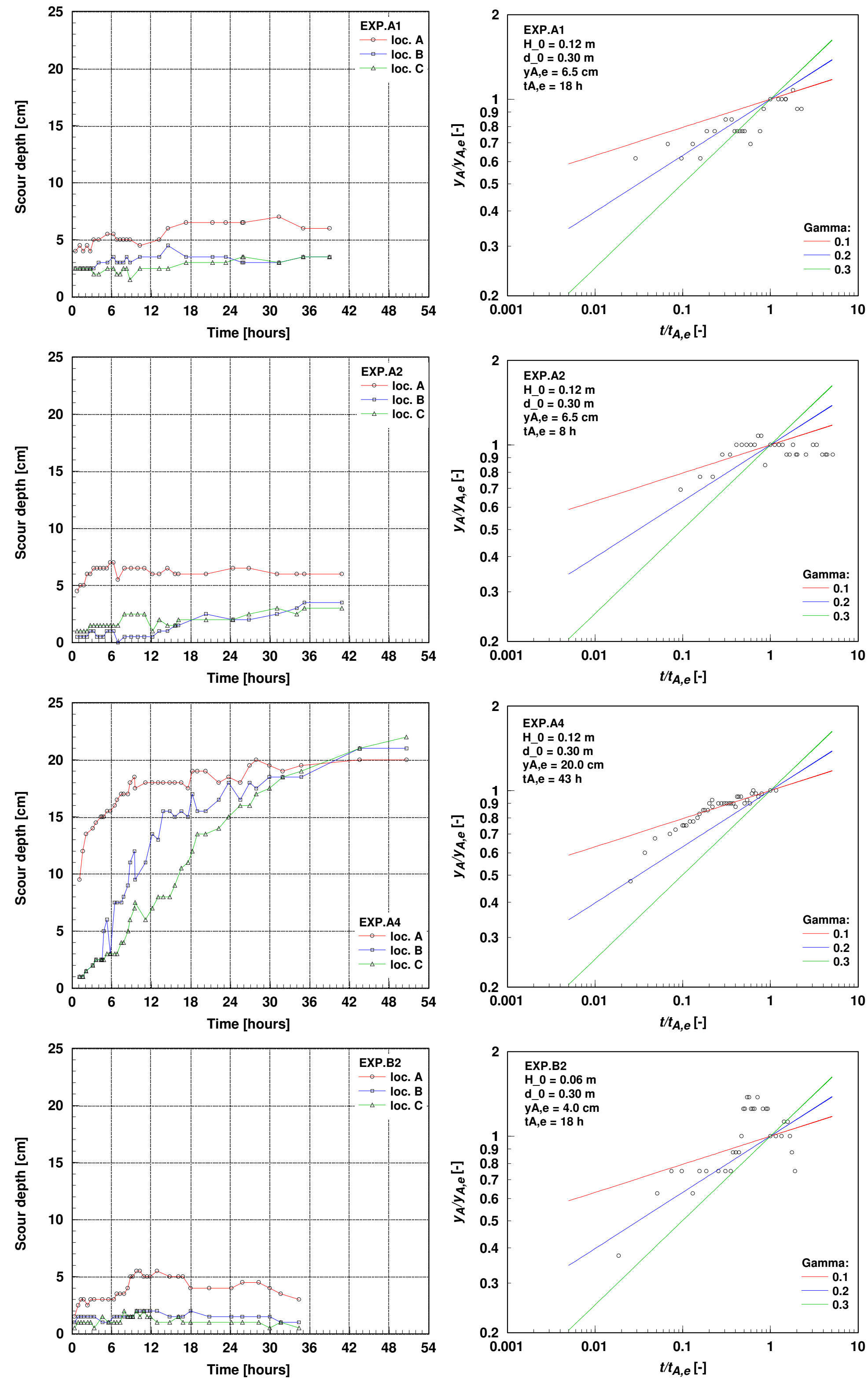
EXP.A1
loc. A
loc. B
loc. C
Scour depth [cm]
Time [hours]
EXP.A1
H_0 = 0.12 m
d_0 = 0.30 m
yA,e = 6.5 cm
tA,e = 18 h
Gamma:
0.1
0.2
0.3
$y_A/y_{A,e}$ [-]
$t/t_{A,e}$ [-]
EXP.A2
loc. A
loc. B
loc. C
Scour depth [cm]
Time [hours]
EXP.A2
H_0 = 0.12 m
d_0 = 0.30 m
yA,e = 6.5 cm
tA,e = 8 h
Gamma:
0.1
0.2
0.3
$y_A/y_{A,e}$ [-]
$t/t_{A,e}$ [-]
EXP.A4
loc. A
loc. B
loc. C
Scour depth [cm]
Time [hours]
EXP.A4
H_0 = 0.12 m
d_0 = 0.30 m
yA,e = 20.0 cm
tA,e = 43 h
Gamma:
0.1
0.2
0.3
$y_A/y_{A,e}$ [-]
$t/t_{A,e}$ [-]
EXP.B2
loc. A
loc. B
loc. C
Scour depth [cm]
Time [hours]
EXP.B2
H_0 = 0.06 m
d_0 = 0.30 m
yA,e = 4.0 cm
tA,e = 18 h
Gamma:
0.1
0.2
0.3
$y_A/y_{A,e}$ [-]
$t/t_{A,e}$ [-]

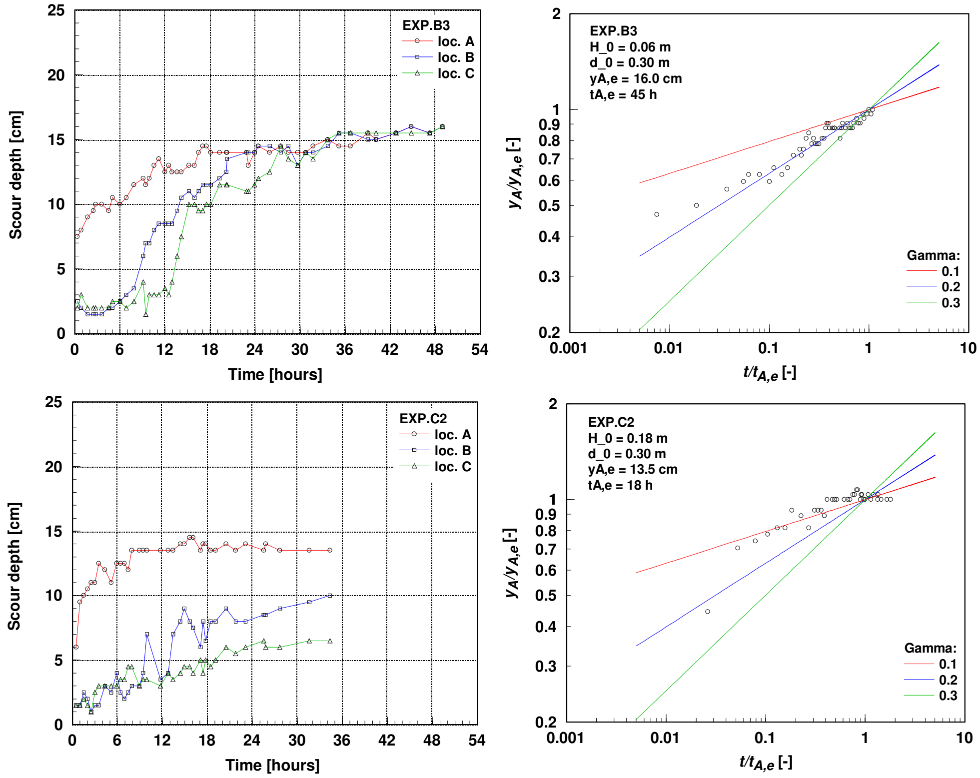

Figure 6.3: Scour development at locations A, B and C along the exposed side of the vane

	$H_{v,0}$ [m]	α [degr.]	$y_{A,e}$ [cm]	$t_{A,e}$ [hours]
EXP.A1	0.12	10	6.5	18
EXP.A2	0.12	20	6.5	8
EXP.A3	0.12	30	N/A	N/A
EXP.A4	0.12	40	20.0	43
EXP.B2	0.06	20	4.0	18
EXP.B3	0.06	30	16.0	45
EXP.C2	0.18	20	13.5	18

Table 6.1: Estimates of equilibrium scour depths and characteristic times at location A

scour depths near the leading and trailing edges. In time, as the location of maximum scour moves towards the trailing edge, the location of minimum scour along the suction side moves towards the leading edge as a result of local avalanches of the rearward slope. It is observed that the location of minimum scour along the suction side at about the three-quarter chord is a general trend. Another general trend consists of the formation of a small ridge dividing the gullies due to the erosion capacity of the flows along the pressure and suction side, which particularly became visible for the higher angles of attack (EXP.A3, B3 and A4; see Figure 6.1) and the higher initial vane heights (EXP.C2). In general, the upstream part of the scour hole stabilizes first. At locations B and C along the pressure side, scouring takes place in the later stages of scour development. Table 6.1 presents estimates of the equilibrium scour depths at location A and of the characteristic times at which the maximum scour depth equates the equilibrium scour depth at location A, based on local scour measurements. These times may be regarded as times required to reach a state of stability in the upstream part of the scour hole.

By approximation, the scour process at location A as a function of time in the development phase can be given by the relation:

$$\frac{y_A}{y_{A,e}} = \left(\frac{t}{t_{A,e}}\right)^{\gamma} \tag{6.1}$$

in which y_A represents the scour depth at location A at time t and $y_{A,e}$ is the equilibrium scour depth at location A at time $t_{A,e}$. From Figure 6.3, it is seen that the values of coefficient γ range from 0.1 to 0.2 for all experiments. In Appendix D, plots are given of the scour hole dimensions obtained from bed level measurements.

6.3 EQUILIBRIUM SCOUR DEPTH

Due to the lack of information about scour around submerged vanes, Hoffmans and Verheij proposed to use design relations for scour at bridge piers to predict equilibrium scour depths at submerged vanes [19]. The schematisation of an array of vanes as a sill is dissuaded, because the ratio of vane spacing to vane thickness is generally such that the vanes act as individual structures with regard to scour. The effect of vanes is therefore more similar to that of a bridge pier than to the effect of a sill. The resemblance between submerged vanes and piers with regard to scour emerges in the resemblance between the shapes of the local scour holes (see local scour plots in Appendix D). Hoffmans and Verheij stated that submerged vanes differ mainly from pier structures in that only a part of the flow energy is converted into scour-causing vortices in the case of submerged vanes (hypothetically, a greater part of the energy is converted into a vortex that counteracts the helical flow in a river bend). Hence, they assessed that a submerged vane causes less scour than a bridge pier and applied a reduction factor for submerged vanes.

	$H_{v,0}$ [m]	α [degr.]	Running time preceding bed level measuring [hours]	Maximum scour depth (estimate of equilibrium scour depth) [cm]	Location maximum scour (X;Y) [cm]
EXP.A1	0.12	10	38.9	7.6	(1480.0;-5.0)
EXP.A2	0.12	20	15.6 [13]	6.6	(1485.0;0.0)
EXP.A3	0.12	30	43.7	15.2	(1500.0;5.0)
EXP.A4	0.12	40	50.6	22.7	(1520.0;20.0)
EXP.B2	0.06	20	34.6	4.1	(1490.0;-2.5)
EXP.B3	0.06	30	39.6	17.3	(1490.0;-2.5)
EXP.C2	0.18	20	34.6	14.2	(1485.0;0.0)

Table 6.2: Estimates of equilibrium scour depths

From Figure 6.3, the conclusion can be drawn that a state of equilibrium scour has not been reached for all experiments. It appears that the upstream part of the scour hole has reached a state of stability for all experiments. Particularly for EXP.A3, A4, B3 and C2, however, it is anticipated that the scour processes downstream of the leading edge have not completed entirely within the durations of the experiments. Table 6.2 presents estimates of the equilibrium scour depths, where the maximum scour depths obtained from bed level measurements (from unprocessed data sets) are used as estimates of the equilibrium scour depths. The reader should therefore bear in mind that these values might underestimate the actual equilibrium scour depths. Difficulties are encountered with the definition of the maximum scour depth as distinct from fluctuations in bed level. Analyses of longitudinal bed profiles, however, do not suggest significant bed disturbances at vane location [57]. Theoretically, the flume was not susceptible to the formation of alternating bars, resulting from oscillations in the interaction between model bed and flow regime, and the presence of these bars is not discerned in the measured longitudinal bed profiles. A comparison between maximum scour depths from bed level measurements and local scour monitoring teaches that

[13] From a second data set of measurements taken after a running time of approximately 41 hours, a maximum scour depth of 5.3 cm can be determined. For EXP.A2, a scour depth of 6.6 cm is considered a better estimate of the equilibrium scour depth.

the values are more or less of the same order of magnitude. Note that the locations of maximum scour depth do not necessarily agree with scour monitoring locations A, B and C.

Here, the use of scour relations for bridge piers to predict the equilibrium scour around submerged vanes in steady flow is evaluated. A scour relation for bridge piers by Breusers et al. [6] and the Colorado State University method (CSU) [23] are applied to the case of submerged vanes. Based on experimental data for live bed scour, Breusers et al. concluded that the scour depth around bridge piers may be described by

$$y_{m,e} = 1.5 K_i b \tanh\left(d_0/b\right) \tag{6.2}$$

The Colorado State University method for the prediction of the equilibrium scour depth at bridge piers may read

$$y_{m,e} = 2.0 K_i d_0 Fr^{0.43}\left(b/d_0\right)^{0.65} \tag{6.3}$$

in which $Fr = U_0/\left(gd_0\right)^{0.5}$ represents the upstream Froude number. The factor K_i in Equations (6.2) and (6.3) accounts for several parameters that affect the flow pattern and the local scour process around bridge piers. Usually, the case of a single circular bridge pier is used as a reference, in which case factor K_i may be expressed as

$$K_i = K_s K_\alpha K_b K_g K_{gr} \tag{6.4}$$

Herein, factor K_s accounts for the effect of pier shape on the equilibrium scour depth. Based on shape coefficients for piers aligned to the flow according to Dietz [19], K_s = 1.0 for the tested flat rectangular vanes with $L_v/b = 80$. Factor K_α describes the effect of pier alignment to the flow. The values of factor K_α for the tested vanes can be estimated using a relation given by Froehlich [13], which reads

$$K_\alpha = \left(\cos\alpha + L_v/b\sin\alpha\right)^{0.62} \tag{6.5}$$

and agrees reasonably with results by Laursen and Toch [26] and by Nakagawa and Suzuki [33] for piers with a rectangular horizontal cross-section. Equation (6.5) specifies that the local scour depth depends strongly on the alignment of the pier to the flow. For circular bridge piers, the development and equilibrium depth of local scour are modified by the relative size of pier and sediment. If the grains are large compared to the groove excavated by the downflow, the erosion process is impeded. Reduction factor K_b approaches a limiting value at about b/D_{50} = 50 (see [5]). Factor K_g accounts for the effect of sediment grading on scour depth, where sediment grading is supposedly characterised by the geometric standard deviation $\sigma_g = D_{84}/D_{50}$. From the results of sediment sieving, the gradation of the sediment used may be given by D_{50} = 170 μm and D_{84} = 245 μm [57]. For b/D_{50} = 29 and σ_g = 1.4, the values of factors K_b and K_g yield 0.95 and 0.9, respectively (see [5]). Factor K_{gr} describes the effect of the presence of a group of piers on the local scour depths. According to Wang [41], the optimum transverse vane spacing is about $2H_v$ (for angles of attack up to about 25°) and the vane spacing should not exceed $3H_v$. For a group of two circular piers perpendicular to the flow, the mutual influence on the maximum scour depth is negligible if the pier spacing is greater than about eight diameters. In general, the ratio of transverse vane spacing to vane thickness amply exceeds 8, which suggests that there is no interaction between vanes in an array with regard to scour. At present, no information is available about the optimum vane spacing for vanes at relatively high angles of attack. Experimental results of the current research show that the scour hole around a submerged vane can expand to a maximum width up to about $4L_v\sin\alpha$ for high angles of attack and for vanes protruding relatively high above the bed. It can be anticipated that, in an array of equal-sized and equal-angled vanes at high angle of attack or at low vane submergence, the scour holes of neighbouring vanes will overlap considerably if vane spacing is limited to $< 3H_{v,0}$. Possibly, the assumption that vanes act as individual structures with regard to scour then no longer holds due to interaction effects. Additional experiments are required to establish guidelines with regard to the optimum transverse vane spacing for vanes at high angles of attack and the effect of vane spacing on scour depth. An intriguing research objective in such experiments would be to investigate the strength of the horseshoe vortex leg leaving from the trailing edge in case the scour holes of neighbouring vanes overlap. The current research concentrates on single vanes only, thus K_{gr} = 1.0. For slender bridge piers, the effect of flow depth on the equilibrium scour depth is negligible [5]. It is therefore expected that the flow depth does not affect the equilibrium scour depth around submerged vanes either.

Under live bed conditions, the range between maximum and minimum values of local scour depths is approximately equal to the height of bed features under given flow conditions. For design purposes, Breusers et al. [5] proposed to equate the maximum scour depth to the sum of the average equilibrium scour depth and half of the dune height. In as far as a state of equilibrium was reached during experimentation, the range between maximum and minimum equilibrium scour depths appeared small (compared to the magnitude of possible measuring errors), possibly due to a rather low bed load transport rate. Here, it is assumed that the contribution of bed features passing past the tested vanes is negligible and that the maximum measured scour depths represent average equilibrium scour depths.

	$H_{v,0}$ [m]	α [degr.]	Experiment $y_{m,e}$ [cm]	Breusers $y_{m,e}$ [cm]	CSU $y_{m,e}$ [cm]
EXP.A1	0.12	10	7.6	3.4	8.7
EXP.A2	0.12	20	6.6	5.1	12.9
EXP.A3	0.12	30	15.2	6.4	16.2
EXP.A4	0.12	40	22.7	7.4	18.9
EXP.B2	0.06	20	4.1	5.1	12.9
EXP.B3	0.06	30	17.3	6.4	16.2
EXP.C2	0.18	20	14.2	5.1	12.9

Table 6.3: Comparison between measured and calculated equilibrium scour depths

Table 4.1 and Figure 6.4 present a comparison between measured and calculated equilibrium scour depths. Note that no reduction factor has been applied to compensate for loss of flow energy that is converted into scour-causing vortices, as proposed by Hoffmans and Verheij. The agreement between calculated and measured scour depth is rather unsatisfactory. For the given conditions, the CSU method is seen to predict the equilibrium scour depths better than the relation for scour at slender bridge piers according to Breusers et al. Particularly at the higher angles of attack, the discrepancies between measured and calculated scour depths are smaller if use is made of the CSU method. For the given conditions, significant discrepancies exist in the scour depths predicted by the different scour relations for slender bridge piers. It is important to realise that the relations have been designed and verified for scour at slender bridge piers, and not for submerged vanes. Because of the lack of experimental data for scour at submerged vanes, the use of a scour relation for bridge piers to calculate the equilibrium scour depth for submerged vanes is not readily acceptable. First and foremost, the extreme values of the ratio of length to thickness for submerged vanes do not relate to values for slender bridge piers. It can be anticipated that, at relatively low angles of attack, the extent of flow separation in front of the structure is larger for (slender) bridge piers than for submerged vanes, as the structural widths of piers

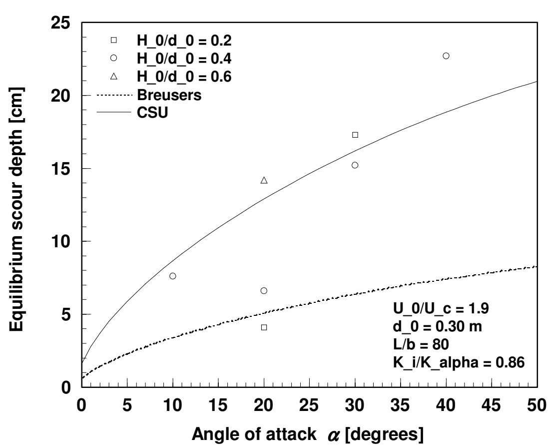

Figure 6.4: Comparison between measured and calculated equilibrium scour depths

and submerged do not agree. At the higher ranges of angle of attack, the agreement between flows along the exposed sides of bridge piers and submerged vanes improves. For angles of attack higher than about 30°, the presence of strongly developed horseshoe vortices can be observed for both bridge piers and submerged vanes. With increasing angle of attack, the effect of pier width on scour diminishes and scour depth becomes a function of the projected width (width of the structure normal to the flow) mainly. Hence, it can be expected that scour relations for slender bridge piers aligned to the flow give more accurate predictions of the equilibrium scour depths for submerged vanes at the higher ranges of angle of attack than at the lower ranges of angle of attack. Secondly, in contrast to a submerged vane, a bridge pier causes a surface roller, which, compared to the horseshoe vortex at the base of the pier, has an opposite sense of direction. With decreasing flow depth, the surface roller becomes more dominant and weakens the downflow. On the other hand, driven by the pressure gradient between the pressure and suction side, the flow near the top edge is directed upwards along the pressure side of the vane. Nearer to the bed, the flow at the leading edge and along the pressure side has a downward direction. For relatively low angles of attack, the cross-flow covers a relatively large portion of the exposed surface and the application of a reduction factor seems justified (supporting the proposal by Hoffmans and Verheij, although possibly on different grounds). Finally, the scour relations for slender bridge piers do not account for submergence, whereas the results of the current research indicate that the scour hole dimensions depend on the initial vane height (at least for relatively low angles of attack). At an angle of attack of 20°, the maximum scour depth is seen to increase with increasing initial vane height. Strikingly, an increase in the ratio of initial vane height to initial water depth from 0.4 to 0.6 resulted in an increase in local scour depth that is disproportionate to the increase in scour depth for an increase of the ratio from 0.2 to 0.4. Apparently, as velocity measurements do not indicate the presence of a strongly developed horseshoe vortex leg leaving from the trailing edge at an initial vane height of 0.18 m (EXP.C2), the observed enlargement in scour depth must be attributed to a disproportionate increase in downflow. At an initial vane height of 0.12 m, the scour depths for angles of attack of 10° and 20° are seen to differ only marginally. However, for angles of attack of 30° and 40°, a strong increase in scour depth is observed, demonstrating clearly the capacity of a strongly developed horseshoe vortex to transport bed material downstream. The data set of scour depths displays a seemingly striking result for the tested vanes at an angle of attack of 30° (EXP.A3 and B3), as the presented maximum scour depth for an initial vane height of 0.06 m (EXP.B3) exceeds the scour depth for an initial vane height of 0.12 m (EXP.A3). For EXP.A3, however, the maximum scour depth (estimate of the average equilibrium scour depth) is obtained from a data set of bed level measurements taken manually at a relatively small number of measuring locations only after a running time of approximately 44 hours. Possibly, the maximum scour depth actually occurred at a location that was not included in the restricted measuring project for that data set. As a result, the difference between equilibrium scour depths for EXP.A3 and B3 may be overestimated. In a clear water scour test for a thin, flat rectangular vane at an angle of attack of 40° (initial vane height: 0.12 m; vane length: 0.24 m; initial water depth: 0.40 m; sediment: uniform sand of equivalent median diameter of 0.9 mm), Marelius and Sinha found a maximum scour depth of 0.24 m (read from graph shown as Figure 4.14) near the trailing edge after a running time of 72 hours. The result of the current research for the tested vane at equal initial vane height and angle of attack (EXP.A4) agrees well with the equilibrium scour depth as found by Marelius and Sinha, which supports the hypothesis that the equilibrium scour depth is a function of the angle of attack and of the initial vane height mainly. The comparison seems to indicate that vane length plays a less dominant role with regard to scour and although the current experiments were not designed to test the effect of vane length on local scour, the expectancy is proclaimed that the effect of vane length on local scour is considerably subordinate to the effects of angle of attack and initial vane height. The experimental results for angles of attack of 30° and 40° suggest that the assumption by Hoffmans and Verheij (see discussion above) that submerged vanes cause less scour than bridge piers and that a reduction factor may be applied to the calculated scour depth using relations for scour at slender bridge piers does not hold for vanes at the higher ranges of angle of attack.

At present, the limited number of available experimental results for submerged vanes does not allow for the generation of alternative scour relations. However, experimentation in the framework of the BUET-DUT linkage project has been continued at BUET after Zijlstra and

Van Zwol ended their stay in Dhaka, Bangladesh, and is currently still ongoing. It is highly recommended to collect the experimental data of these scour tests and to re-evaluate the use of scour relations for slender bridge piers to predict the equilibrium scour depths at vanes.

6.4 MEASURES TO REDUCE LOCAL SCOUR

The maximum scour depth at submerged vanes is seen to depend mainly on angle of attack and initial vane height. Hypothetically, the effect of vane length on local scour is considerably subordinate to the effects of angle of attack and initial vane height. In general, the load exerted on vanes at high angles of attack and on vanes protruding high above the bed calls for substantial installation depths and structural widths. If, for a given vane design, the expected scour depths are considered unacceptable, the most obvious measures to reduce local scour would be to reduce the angle of attack and to reduce the initial vane height. In the author's opinion, however, these measures obstruct the well functioning of vanes. On the other hand, a large structural width similarly hinders the generation of strong and stable primary vortices, which leaves the designer of a vane field with great dilemmas. Besides, most of the existing design guidelines are based on the theory of Odgaard and are given for vanes at angles of attack up to about 20° only. Based on analyses of the experimental results, the author supports views by Marelius and Sinha and feels that future experiments should concentrate on vanes at the higher angles of attack, despite enlarged scour holes, increased resistance to flow and the presence of additional vortical structures. At present, the extent to which the horseshoe vortex and possibly other vortices are counterproductive forces within the system governing the transverse transport of sediment has not been fully explored. Experimentally, it has been shown that these vortices decay downstream within a few vane lengths, while the primary vortex dominates over a much longer distance downstream of the vane, which demonstrates that vanes at high angles of attack induce strong and stable primary vortices (provided the vanes are well-designed). In case of a vane array, the strength of the horseshoe vortices in a state of equilibrium may be less than the strength of the horseshoe vortex for a single vane as the scour holes of neighbouring vanes may overlap. To a certain degree, the presence of the scour hole leads to vortex stretching in transverse direction, thus increasing the effective width of each vane. It can be anticipated that for a system of vanes at high angles of attack both the transverse and longitudinal vane spacing may be enlarged. Hence, a smaller number of vanes may be sufficient to meet design objectives in terms of induced bed shear stresses than in the case that the vanes are laid out at lower angles of attack. Furthermore, for reasons given in the next chapter, the application of arrays of vanes at conventional angles of attack may not always lead to adequate and satisfying results.

Usually, no bed protection is applied for submerged vanes. It is stressed that the suitability of scour holes to aid the intended purpose must not be ignored. If for practical reasons the initial vane height is bound to a relatively low maximum (ratio of initial vane height to initial water depth lower than about 0.4), it is recommended to consider applying an angle of attack of at least 30°. For the given test conditions, experimental results for EXP.B3 in contrast to the results for EXP.B2 show that the bed levels along the suction side of the vane ultimately drop below initial bed level due to the combined effects of the horseshoe vortex legs and velocities induced by the primary (and secondary) vortex, thus creating conditions for the primary vortex to develop optimally or at least improvingly. Alternative solutions inspired on the standard vane design may overcome the practical problems caused by scour, but are mostly highly experimental and may bring about other specific problems or impede with the well functioning of a vane. Before changes to the standard design are undertaken, the effects of vanes at high angles of attack should be further explored. Finally, the reader is reminded that, if well-designed, vanes provide a permanent solution as opposed to dredging. The costs in the construction phase associated with installation depth for vanes at high angles of attack may be overcome if one regards the estimated overall costs of several alternatives and vanes appear to be the more economical solution.

7 OPTIMUM VANE DIMENSIONS AND ORIENTATION

7.1 INTRODUCTION

The present chapter concentrates on the effects of dimensions and orientation of submerged vanes on vane effectiveness. Herein, a restriction is made to vane structures that intend to meet the design objectives in terms of induced bed shear stresses by the generation of a secondary circulation in the downstream flow field, as opposed to – for example – 'deflecting walls'. The performance of such vanes can be evaluated by the capability to induce strong and stable primary vortices at design stage. In principle, the analyses of the physics of the flow past submerged vanes presented in Chapter 4 and the non-linear models for prediction of the mean lift and drag forces described in Section 5.3 exclusively hold for the case of a single vane for steady flow in an open channel of rectangular cross-section. However, by approximation, the results may be used to proclaim expectancies regarding the effectiveness of a system of equally sized and equally angled vanes in the field.

7.2 ANGLE OF ATTACK

In Section 5.3, non-linear models are described for prediction of the mean lift and drag forces exerted on sharp-edged slender vanes. The models are based on theories for low aspect ratio wings by Bollay and Gersten. From comparison with experimental force measurements for thin, flat vanes, it is seen that the non-linear models give a decisive improvement on relations developed by Odgaard et al. Particularly with measurements WL1998 and WL2001, a rather good agreement between measured and calculated lift and drag coefficients is observed (Section 5.5). Use of the model model based on theory by Bollay is advised for ratios of vane height to vane length lower than about 0.1. At higher ratios of vane height to vane length, the model based on theory by Gersten gives more accurate results. It should be mentioned that the models apply to the case of a single vane protruding above a rigid bed for steady flow of uniform, depth-constant free stream velocity. Furthermore, because the assumption that a single reflection of the bound and trailing vorticity in the plane of the bed by the method of images is sufficient to account for boundary interference effects breaks down with increasing ratio of vane height to flow depth (Section 5.3), the ratio of vane height to flow depth should not be all to high. At present, the upper limit of the validity ranges of both models is confined to an angle of attack of about 20° due to the lack of experimental results for the higher ranges of angle of attack. The model based on theory by Gersten is seen to hold approximately for ratios of vane height to flow depth up to at least 0.6. Note that the non-linear models account for sharp-edged thin flat-plates and that the models predict induced drag only (profile drag is not accounted for (Section 5.2.2)). In reality, vanes are mounted on a riverbed and require structural width. The effect of local scour on the mean lift and drag forces is not accounted for. However, the results of the non-linear models may be used as first order approximates for the determination of the strength of vane-generated primary vortices. Herein, it is assumed that the efficiency of a single vane at angle of attack is representative of the efficiency of a system of equally sized and equally angled vanes. Due to profile drag, deficiencies associated with structural width and form of leading and top edges, and vane interaction, vane efficiency will generally be lower than predicted by the non-linear models.

Figure 7.1 presents plots of the ratio of lift to drag (according to Odgaard et al. and the non-linear models based on theories by Bollay and Gersten) and the ratio of non-linear lift to drag (according to the model based on theory by Gersten) versus the angle of attack. Because submerged vanes aim to generate a secondary circulation in the main flow, preferably at a minimum of flow resistance, and the strength of the circulation is related to the lift force exerted on vanes, vane efficiency can be expressed in terms of ratio of lift to drag. As seen in Figure 7.1, the theory of Odgaard suggests high vane efficiency (relatively high ratios of lift to drag at angle of attack). Furthermore, according to Odgaard et al., vane efficiency in terms of ratio of lift to drag increases with increasing ratio of vane height to vane length. Results of experiments conducted at WL | Delft Hydraulics [11; 24], however, indicate that the curvature of polars (lift versus drag) approximately corresponds to the expected non-linear behaviour of the lift and drag forces exerted on sharp-edged slender vanes as described by the non-linear models (Figure 5.15): the primary vortex influences the pressure distribution on the suction side and gives rise to a substantial non-linear lift contribution that partially compensates for the additional drag due to loss of the leading edge suction force (Section 5.5). In the author's opinion, vane efficiency is expressed more correctly in terms of ratio of non-linear lift to drag, as non-linear lift (or vortex lift) is an enhanced measure of the strength and stability of the vane-induced primary vortex. It is assessed that the effect of trailing vorticity associated with linear lift on vane effectiveness is small to negligible. According to the model based on theory by Gersten, the ratio of non-linear lift to drag decreases with increasing angle of attack and increasing aspect ratio (Figure 7.1 (right)). Theoretically, vortex lift and thus, the strength of the primary vortex increases non-linearly with increasing angle of attack (Figure 7.2). The increase in non-linear lift is, however, accompanied by a strong increase in induced drag, which implies enlarged resistance to flow. Odgaard and Mosconi [39] derived a relation to evaluate the effect of a system of vanes emplaced along the outer bank in a river bend on induced change in energy slope. Because the relation adopts the theoretical relations for lift and drag coefficients by Odgaard et al., it probably needs revision. Improved relations are needed to evaluate the effect of vane systems on flow resistance.

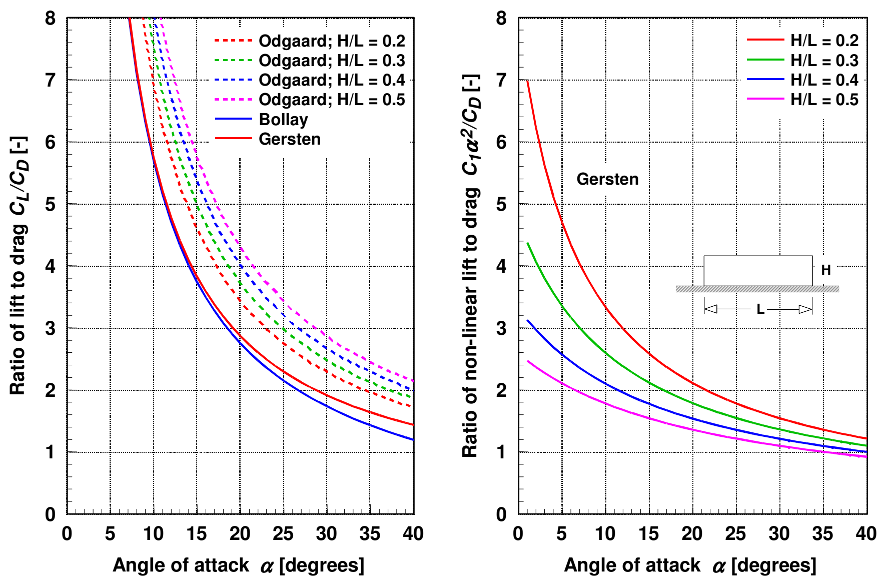

Figure 7.1: Vane efficiency in terms of ratio of lift to drag according to Odgaard and models based on Bollay and Gersten (left) and in terms of ratio of non-linear lift to drag according to model based on Gersten (right)

An explanation for the reasonable agreement between measured and calculated V- and W- velocity components, as observed in Section 4.5, is that, at low angles of attack, the non-linear lift coefficient is approximately of the order of the lift coefficient calculated with theoretical relations by Odgaard et al. Efforts should be undertaken to investigate whether the theory of Odgaard can be improved by implementation of relations for lift and drag coefficients given by the model based on theory by Gersten, by which the strength of induced circulation is related to the non-linear lift coefficient. Possibly, the range of angle of attack for which the theory of Odgaard holds can thus be expanded.

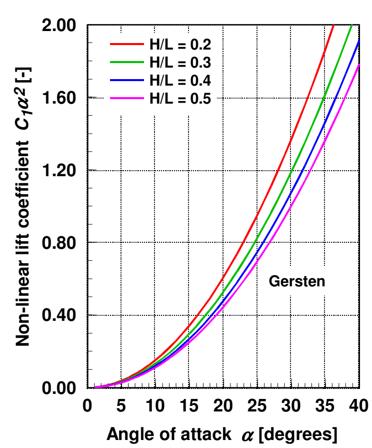

Figure 7.2: Non-linear lift coefficient according to model based on theory by Gersten

It is seen that the designer of a vane system is confronted with dilemmas. Unacceptable vane-induced resistance to flow and scour depths will generally confine the upper limit to angle of attack. Local scour depths and the load acting on vanes increase with increasing angle of attack. Therefore, vanes at the higher ranges of angle of attack may require substantial structural width and installation depth. Despite enlarged scour holes, increased flow resistance and presence of additional vortical structures, future experiments should concentrate on vanes at high ranges of angle of attack for reasons described in Section 6.4. Perhaps, both transverse and longitudinal vane spacing may be enlarged for a system of vanes at high angles of attack. A smaller number of vanes may be sufficient to meet design objectives in terms of induced bed shear stresses than in case vanes are laid out at conventional angles of attack. The lower limit to angle of attack may be defined by effectiveness of individual vanes and initial vane height. At relatively low angles of attack, the effectiveness of the individual vanes is low as the strength of the vane-induced vortices is relatively small and hence, a relatively large number of vanes may be required to meet the design objectives. If for practical reasons, the ratio of vane height to flow depth is bound to a maximum lower than about 0.4, it is advised to consider applying a higher angle of attack (Section 6.4).

7.3 INITIAL VANE HEIGHT AND VANE LENGTH

As shown in Figure 7.1, the theoretical non-linear lift coefficient and vane efficiency increase with decreasing aspect ratio. It is expected that the lift force exerted on slender vanes with rectangular planform is a maximum at an angle of attack increasing from about 40° for a ratio of vane height to vane length of 0.5 to higher than 55° for a ratio of vane height to vane length of 0.05, provided the vane protrudes sufficiently high above the bed. With decreasing aspect ratio, tip flow predominates the flow on the suction side more and more and an increase of the diameter of the rolled up primary vortex can be observed. However, for vanes protruding relatively low above the bed, only a small vortex cushion can be built up. It appears that the presence of a layer of more or less adhering flow underneath the regions of depressed streamwise velocity component is beneficial to the development of the primary vortex. Such layers of mainly adhering flow accompanied with flow separation occur for vanes protruding sufficiently high above the bed (from experiment: at angles of attack up to 20°, ratios of flow depth to vane height lower than about 3 to 4) and for vanes at the higher angles of attack emplaced in deformable beds. If, for practical reasons, the initial vane height is bound to a relatively low maximum, it is recommended to consider applying a higher angle of attack. For given test conditions, experimental results for EXP.B2 and B3 indicate that the effectiveness of the tested vanes at low initial vane height improved considerably by the increase in angle of attack, which may be explained by the observation that the minimum exposed vane height along the suction side ultimately exceeded the initial vane height at an angle of attack of 30° due to the combined effects of horseshoe vortex and primary vortex. Therefore, the conditions for the development of the primary vortex enhanced for EXP.B3, whereas conditions for the generation of the leading edge vortex remained sub-optimal for EXP.B2. Results for EXP.C2 suggest that the effect of the primary vortex on transverse transport of bed material for vanes at high ratio of vane height to flow depth is highest at some distance downstream from the vane as the vortex filament relocates toward mid-depth and the near bed transverse induced velocities gradually increase with distance downstream of the vane. In case of relatively long vanes, the diameter of the primary vortex at high angles of attack may hypothetically augment up to a degree, where apparently no more fluid can be rolled up and the after parts of the rolled up primary vortex become unstable, eventually resulting in the breaking off of the primary vortex. The above discussion points out that there are upper and lower limits to initial vane height and vane length. Odgaard and Spoljaric suggested that the ratio of vane height to vane length should be in the range from 0.1 to 0.5 [37] (Section 3.5). Here, it is stated that the given range is adequate, be it that the non-linear contribution to lift is clearly more inefficient at ratios of vane height to vane length of the order of 0.5. At design stage, Odgaard and Spoljaric proposed that the ratio of vane height to flow depth should be about 0.4 to 0.5 [37], while Odgaard and Mosconi recommend that this ratio should be in the range from 0.2 to 0.5 for all erosion causing flow stages [39] (Section 3.5).

7.4 FORM OF LEADING AND TOP EDGES

The leading edge of a submerged vane plays an important role in the generation of the primary vortex (Section 5.6.5). Because non-linear effects are due to flow separation and generation of vortices at the leading and top edges, the non-linear contribution to lift is larger for sharp-edged vanes than for vanes with rounded edges. Particularly the form of the leading edge is important; the form of the top edge is probably less important. Independent of the form of the top edge, there is tip flow and flow separation along the top edge of the vane. Rounding of the top edge probably brings about a small detrimental effect on non-linear lift. An increase of the distance between pressure and suction side results in a decrease in tip flow and hence, a decrease in non-linear effects. The well functioning of a submerged vane can be associated primarily with the generation of a strong primary vortex. Submerged vanes should be designed in such a manner that the conditions with respect to vane shape to bring about non-linear effects are optimal. It follows that submerged vanes should preferably be equipped with sharp leading and top edges and that the structural width should be reduced to a minimum.

7.5 VANE SHAPE

Section 5.6.5 already dealt with effects of vane shape on the mean lift and drag coefficients. As mentioned in Section 7.4, vanes should preferably be slender and equipped with sharp leading and top edges. The leading edge of a thick, flat vane is blunt and the profile thickness decreases tip flow. These deficiencies disturb the formation of the primary vortex. Cambering and twist probably do not improve the lift characteristics of vanes. The effect of camber is to bring about a 'smoother' type of flow over a larger portion of the suction side than for thin, flat vanes. For a predominantly more or less adhering flow, however, the formation of the primary vortex is reduced. Furthermore, relative to thin, flat vanes, the distance between pressure and suction side is increased by the profile thickness. Compared to thin flat-plates, sheet-wall vanes generate less lift and significantly more drag. Measurements WL1998 and WL2001 for thin, flat vanes and sheet-wall vanes at an angle of attack of 17.5° show that the lift and drag forces on sheet-wall vanes are up to 21% lower and up to 66% larger, respectively, than the forces acting on thin, flat vanes. The relative increase in drag for sheet-wall vanes may be explained largely by an increase in profile drag. The conclusion cannot be drawn that the tested sheet-wall vanes generated much weaker primary vortices. Especially for the taller sheet-wall vanes (measurements WL2001), the measured lift forces agree reasonably with measured lift forces on thin, flat vanes of equal dimensions. Like thin flat-plates, sheet-wall vanes are equipped with sharp edges along the leading and top edge, so that the location of flow separation is fixed. Hence, slender sheet-wall vanes in principle comply with the key ingredients to the generation of primary vortices. However, as a consequence of the relative increase in drag, the efficiency of a sheet-wall vane is clearly poorer compared to that of a thin, flat vane.

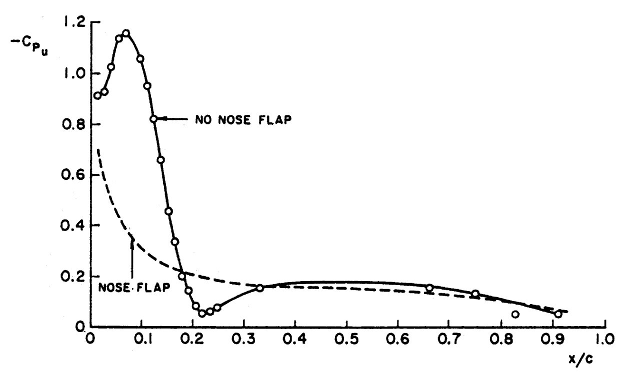

Figure 7.3: Chordwise distributions of upper surface pressures for a flat-plate wing at an angle of attack of 20° with and without nose flap; source: Wickens, 1967

It is recognized that vanes require structural width, which may increase with increasing angle of attack as a result of enlarged load and scour depths. Consequently, vane efficiency is lower than predicted by the non-linear models based on theories by Bollay and Gersten. Therefore, the application of arrays of vanes at conventional angles of attack may not always lead to adequate and satisfying results. The detrimental effects of structural width on tip flow can be compensated for by selecting a higher angle of attack. Tapering of the leading and top edges can also be considered, though probably less effective. The reader is reminded that vanes are rather sensitive to approach flow conditions (see also [39]). If possible, measures ought to be taken to ensure that the angle of incidence remains constant and to prevent adverse flanking in meandering rivers. Continuously evolving flow field and topographical features may result in vanes at different ranges of angle of attack than originally intended [30].

Finally, it is mentioned that, if there is a need to suppress flow separation from the leading edge, the application of a small nose flap can be considered, such that the angle of incidence between approach flow and nose flap is slightly smaller than the angle of attack with respect to the vane, to which the nose flap is attached. The length of a nose flap would be of the order of a tenth of the vane length. Supposedly, a nose flap suppresses flow separation from the leading edge and reduces pressure fluctuations downstream of the leading edge (see also Section 5.7). The formation of the primary vortex would still take place, but the load exerted on the vane diminishes. Hypothetically, vanes induce less flow resistance, if equipped with a nose flap. A disadvantage associated with the use of a nose flap could, however, be the effect on transverse vane spacing, as the size of the vane-induced wake and thus, the effective width is reduced to some extent. Figure 7.3 presents chordwise distributions of the upper surface pressures for a thin, flat-plate wing at an angle of attack of 20° with and without a small nose flap attached, as measured by Wickens [54] (see also Section 4.6). From comparison, it is seen that without the nose flap, the distribution of the upper surface pressures is dominated by the separated region for a distance downstream of about a third of the chord length. The pressures near the leading edge can be reduced considerably if a nose flap is present to suppress separation. The suitability of a small nose flap to reduce pressure fluctuations and induced drag for submerged vanes has not been investigated as of yet, but could be an interesting research objective for future experiments.

7.6 APPLICATIONS

Figure 7.4 presents several typical vane lay-outs for streambank protection and shoaling control in straight and curved channels as proposed Odgaard and Wang [42]. A lay-out of a vane system designed for protection of the outermost bank (or a property at the outermost bank) in a river bend is given in Figure 7.4.A. The vane-induced circulation locally counteracts the spiral flow in the river bend. Protection of the outermost bank is obtained by deflecting the main current toward the centre channel section. In order to locally reduce the amplitude of alternate bars or meanders, a vane lay-out as presented in Figure 7.4.B can be employed. By installing vanes in the existing low flow channel immediately upstream of the meander apex, such that the outermost vanes edge the desired channel, the vane system would move the low flow channel away from the eroding bank and reduce impact at high flow stages. A similar lay-out can be employed to maintain a navigation channel in a straight channel (Figure 7.4.C). A typical vane lay-out would consist of vanes installed opposite from the vanes on the other side of the desired navigation channel, so that a continuous berm is established along the banks. Often, shoaling problems arise at intakes as a result of a reduction in downstream velocity and sediment transport capacity at the intake (Figure 7.4.D). To improve conditions for the withdrawal of water, the vane lay-out should be designed to increase flow depth and velocity upstream of the intake. Preferably, the induced increase in downstream velocity exceeds the decrease associated with the withdrawal. The width of the vane field must be sufficient that the induced aggradations

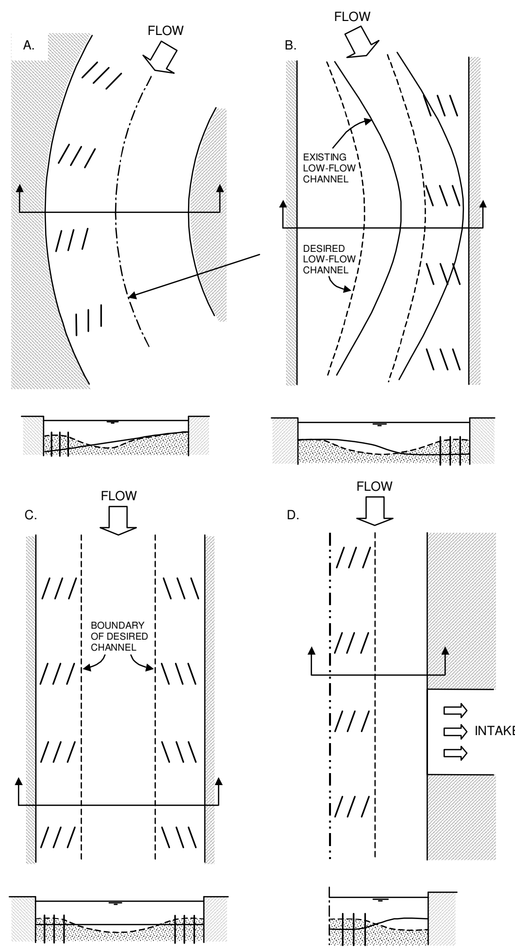

Figure 7.4: Typical vane lay-outs for streambank protection and shoaling control in a river bend (A), in a channel with alternate bars or meanders (B), in a navigation channel (C) and at a water intake (D)

within the field lead to a sufficient increase in discharge along the intake. The given lay-out not only accommodates the flows into the intake, it also reduces the amount of sediment withdrawn.

It is noted that, in some field tests [14; 40], efforts were undertaken to reduce flow separation at the leading edge by rounding of the nose. Odgaard and Wang stated that flow separation inhibits the generation of circulation [42]. The findings presented in the previous chapters, however, contradict this statement. There is sound reason to believe that rounding of the leading edge may in fact disturb the formation of strong primary vortices. It can be anticipated that flow separation occurs irrespective of the form of the leading edge, even at conventional angles of attack. However, by accommodating vanes with a sharp leading edge, the location of flow separation is fixed and consequently, the conditions for the generation of the primary vortices enhance.

Finally, to investigate the effect of local scour and hydraulic load on installation depth, the example of the imaginary vane system 'designed' in Section 3.3 is continued with. Relevant parameters, vane dimensions and (intended) orientation with respect to the main current are summarized in Table 7.1. In order to determine the minimum installation depth, the schematisation shown in Figure 7.5 is used. Supposedly, the near bank bed is horizontal at the time of installation (at a low flow stage; see also Section 3.3). Maximum local scour and hydraulic load are expected at bank-full stage. In computations, it is assumed that the scour depth at the suction side equals the scour depth at the pressure side, thus neglecting neutral to passive lateral stresses at the suction side in possible soil layers above level $z = z_0 - y_m$. Suppose that the vanes are to be constructed from sheet piling and that it is specified that the lateral displacement may not exceed 16 mm.

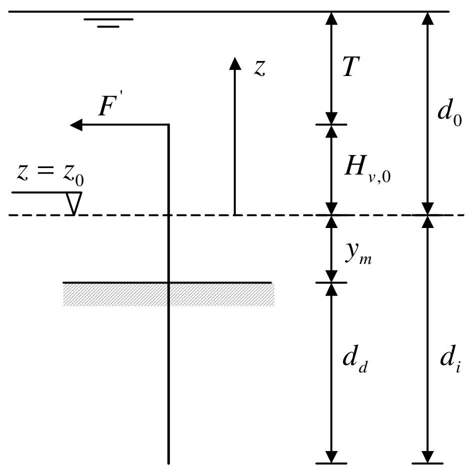

Figure 7.5: Schematisation at bank-full stage

Load F' is estimated with aid of the model based on theory by Gersten (Section 5.3.2), using initial vane height H_{v0} in calculations. Note that other forces may act on the vanes (for instance: impact forces of ice and debris at low flow stages, forces associated with sheet pile driving and navigation (jet stream and return flow)), however, these are not accounted for herein. Furthermore, no safety factors have been applied to the calculated forces, though the use of safety factors seems justified in consideration of insecurities with regard to initial vane height and flow velocity. Besides, the model based on theory by Gersten does not account for profile drag and therefore underestimates the drag force acting on sheet-wall vanes. Because of continuously evolving features in the field, the vanes may be exposed to higher than intended angles of attack. In calculations, it is assumed that the range of angle of attack at bank-full stage is confined by a maximum angle of attack of 30°. In Section 5.7, it was hypothesized that the lift on submerged vanes is carried mainly near the leading and top edges. Assuming that the pressure distribution is such that 75% of the hydraulic load is carried on the lifting surface over half the vane length downstream of the leading edge, the schematised load F', obtained accordingly, equals 7.5 kN/m (Table 7.1).

Estimates of maximum scour depth y_m are obtained using scour relations for slender bridge piers according to the CSU method and Breusers et al. (Section 6.3), where the maximum scour depth is defined as the sum of the average equilibrium scour depth $y_{m,e}$ and half the dune height, assuming that the dune height equals 0.5 m. Again, the range of angle of attack at bank-full stage is supposedly confined by a maximum angle of attack of 30°. Although, for the transverse vane spacing established in Section 3.3, the scour holes of individual vanes are likely to overlap at the higher ranges of angle of attack, it is assumed that K_{gr} = 1.0. According to the CSU method, the maximum scour depth equals 4.2 m, while the scour relation by Breusers et al. predicts a maximum scour depth of 2.3 m (Table 7.1). The use of scour relations for slender bridge piers aligned to the flow to predict equilibrium scour depths at submerged vanes is not readily acceptable (Section 6.3). Based on experimental results of the current research, it is assessed that the schematised scour depth y_m equals 3.0 m.

H_{v0}	= 2.7 m	d_0	= 5.0 m
L_v	= 9.0 m	u_0	= 1.4 m/s
α	= 20°	D_{50}	= 0.7 mm
b	= 0.25 m	σ_g	= 1.8
Model based on theory by Gersten (Section 5.3.2):		F_L	= 40.1 kN (α = 30°)
		F_D	= 21.0 kN (α = 30°)
		F_N	= 45.2 kN (α = 30°)
		$F^{'}$	= 7.5 kN/m
Fr	= 0.20	K_g	= 0.9
K_s	= 1.0	K_{gr}	= 1.0 (assumed)
K_α	= 6.2 (α = 30°)	y_d	= 0.5 m (dune height)
K_b	= 1.0		
Breusers et al. (Eq. 6.2):		y_m	= $y_{m,e} + y_d/2$ = 2.3 m
Colorado State University method (Eq. 6.3):		y_m	= $y_{m,e} + y_d/2$ = 4.2 m

Table 7.1: Estimates of hydraulic load and maximum scour depth

Analysis of the sheet-wall vane, as schematised in Figure 7.5, is carried out with the aid of program SPW2004, which is based upon theory for a beam with elastic support. The sheet pile wall is considered as a bending beam. Actions and reactions of the soil are described by non-linear springs. For relatively small displacements, the soil stress is proportional to the displacement. The maximum and minimum horizontal effective stresses are determined by coefficient of passive lateral stress K_p and active lateral stress coefficient K_a, respectively. In the elastic branch, the soil stiffness is determined by the displacement difference between passive and active conditions. Computations are executed for a Larssen 21 sheet pile profile, properties of which are given in Table 7.2. Other input parameters are presented in Table 7.3; it is assumed that W_s = 20 kN/m^3, K_a = 0.5, K_n = 1.0, K_p = 2.5 and D_w = 0.020 m.

Larssen 21 StSp37			
b	= 500 mm		
h	= 220 mm		
t	= 8.2 mm		
A	= 1.21·10^4 mm^4/m		
W	= 78.0 kN/m	EI	= 1.617·10^4 kNm^2/m
i	= 7.98·10^{-2} m	M_{adm}	= 98.0 kNm/m
A	= area of cross-section	EI	= flexural rigidity
W	= volumetric weight of material	M_{adm}	= maximum bending moment admissable
i	= radius of inertia		

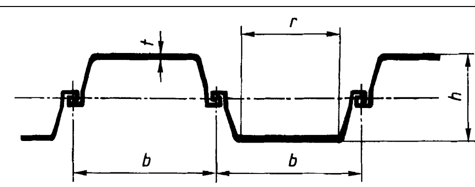

Table 7.2: Properties of a Larssen 21 StSp37 sheet pile profile

Input program SPW2004			
F'	= 7.5 kN/m	K_a	= 0.5
y_m	= 3.0 m	K_n	= 1.0
H_{v0}	= 2.7 m	K_p	= 2.5
d_d	= 3.5 m	D_w	= 0.020 m
W_s	= 20 kN/m^3		

Output program SPW2004			
w	= 0.154 m (abs. maximum)	Q	= 29.6 kN/m (maximum)
M	= 47.1 kNm/m (maximum)	f	= 51.6 kN/m^2 (abs. maximum)

K_a	= coefficient of active lateral stress	W_s	= volumetric weight of bed material in saturated condition
K_n	= coefficient of neutral lateral stress	w	= lateral displacement
K_p	= coefficient of passive lateral stress	M	= bending moment
D_w	= lateral displacement difference between the generation of active and passive lateral stress	Q	= shear force
		f	= resultant soil pressure

Table 7.3: Input and output parameters program SPW2004

Table 7.3 and Figure 7.6 present output data. It is seen that a Larssen 21 StSp37 profile not only assures stability, the profile also satisfies the aforementioned specification with regard to the lateral displacement, if d_d = 3.5 m (see Figure 7.5). The maximum lateral displacement occurs at the top elevation of the schematised vane and equals 0.154 m. Computations indicate that installation depth d_i should minimally equal 6.5 m (see Figure 7.5), so that the minimum total length of the sheet piles equals 9.2 m.

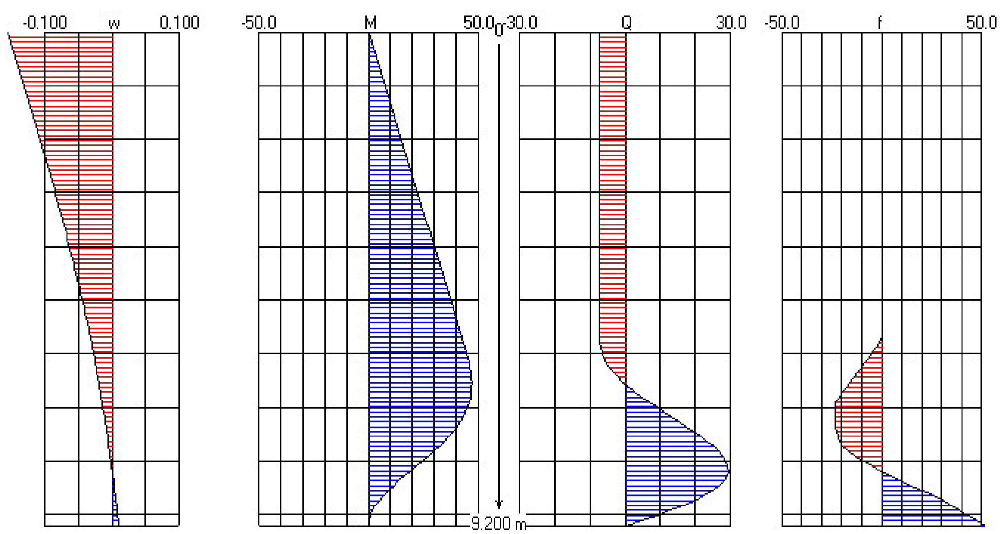

Figure 7.6: Computational results: lateral displacement *w* (in [m]), bending moment *M* (in [kNm/m]), shear force *Q* (in [kN/m]) and resultant soil pressure *f* (in [kN/m^2])

8 CONCLUSIONS AND RECOMMENDATIONS

8.1 INTRODUCTION

In the present chapter, conclusions and recommendations are enumerated, accompanied with important findings of the analyses of velocity and local scour measurements. The reader is reminded that the findings hold for the tested vanes in experiments carried out in the outdoor facility at BUET in the period of March till June 2003. Experimentation comprised mobile bed tests for single thin, flat vanes at varying initial vane height and angle of attack for steady flow in a straight, rectangular channel.

Figure 8.1 presents a schematic of the outline, which was already displayed alternatively as Figure 1.2. In order to supply recommendations with regard to vane design, information is required about two important and interrelated issues: the physics of the flow past vanes and the development of local scour at submerged vanes.

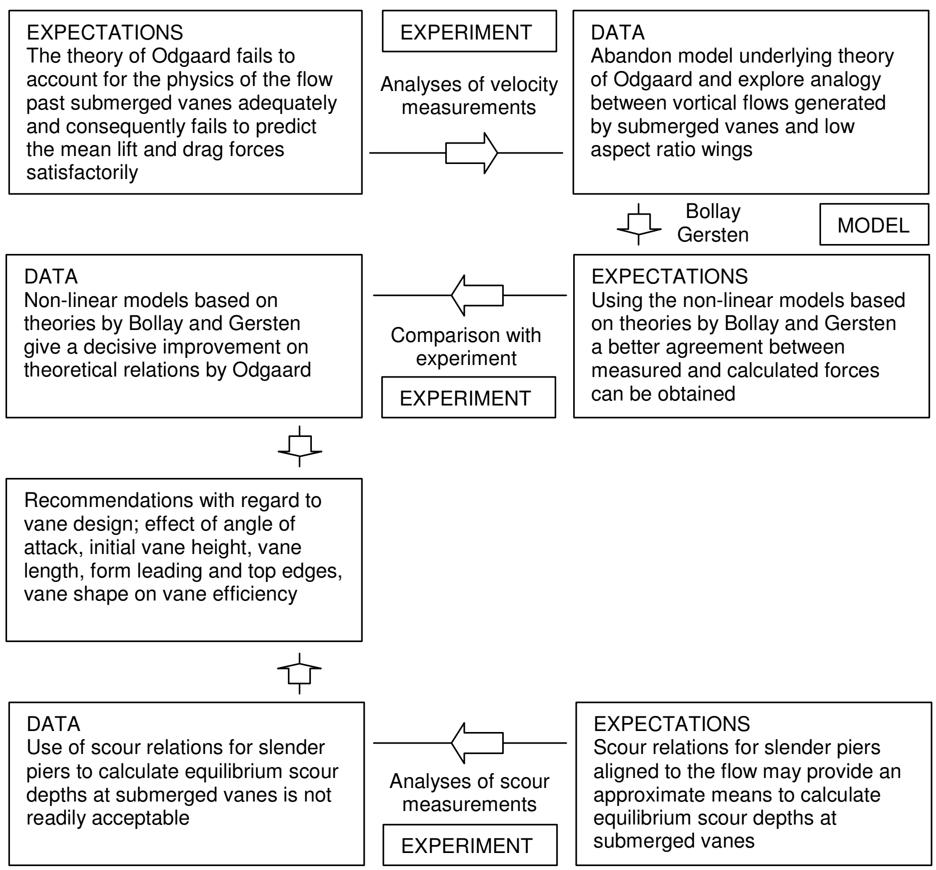

Figure 8.1: Outline

On the basis of results of recent studies [11; 24; 30], the hypothesis was raised that the existing and widely adopted theory developed by Odgaard et al. does not account for the physics of the flow past submerged vanes adequately and consequently fails to predict the lift and drag forces exerted on vanes (as found experimentally) satisfactorily. The time-averaged results of near vane velocity measurements are used to test the hypothesis. It is demonstrated that the hypothesis is well founded. Consequently, the model underlying the theory of Odgaard, the classical lifting line theory for finite wings by Prandtl, is abandoned. Instead, the analogy between vortical flows generated by submerged vanes and slender low aspect ratio wings is explored. In Section 5.3, non-linear models are described based on theories developed by Bollay and Gersten. From comparison with experiment, it is concluded that the non-linear models give a decisive improvement on the theoretical relations by Odgaard et al. By the observed agreement between measured and calculated lift and drag coefficients, confidence is gained that the hypothesis that the leading edge of a submerged vane plays an important role in the generation of the primary vortex and that the primary vortex is a so-called ‘leading edge vortex’, as observed on low aspect ratio wings, is founded.

Referring to the lack of information about local scour at submerged vanes, Hoffmans and Verheij [19] proposed to use scour relations for slender bridge piers aligned to the flow to predict equilibrium scour depths at submerged vanes. The current data sets of scour depths provide a means to evaluate the use of scour relations for bridge piers. The agreement between measured and calculated equilibrium scour depths is rather unsatisfactory. Use of scour relations for slender bridge piers aligned to the flow is not readily acceptable.

By combining information about the development of local scour and the physics of the flow, gained accordingly, a number of recommendations with regard to vane design can be derived. The results of analyses of velocity and local scour measurements and the results of the non-linear models for prediction of the mean lift and drag forces can be used to investigate the effects of several parameters on vane efficiency.

8.2 CONCLUSIONS

8.2.1 Analyses of velocity measurements

- Flow separation occurs along the sharp leading and top edges. Regions of depressed streamwise velocity component exist in the lee of the vane, which expand and intensify with increasing angle of attack and initial vane height. For vanes at relatively low angles of attack, the flow along the suction side reattaches at some distance downstream of the leading edge, while for vanes at the higher angles of attack and for vanes protruding relatively high above the bed, layers of more or less adhering flow can be observed underneath the regions of depressed streamwise velocity component. Along the pressure side near the top edge, the flow is directed upward. At and above the top elevation of the vane, there is flow over the top edge of the vane. The amounts of fluid masses involved in tip flow enlarge with increasing angle of attack and to a lesser extent with increasing initial vane height. It appears that the intersecting flows separated from the leading and top edges give rise to the generation of the primary vortex in the lee of the vane at some distance from the leading edge. Further development of the primary vortex is observed downstream of that position along the suction side. Within the regions of depressed streamwise velocity component, considerable masses of fluid are put into spiral motion. The centre of the vortex core is well inboard.
- Measurements suggest that the centre of the core of the primary vortex at $X = X_{TE} + 3.0$ cm is averagely at about $Y = 0$. It appears that the centre shifts slightly toward Y_{LE} with increasing angle of attack and to a lesser extent with increasing initial vane height, while the centre shifts toward Y_{TE} with decreasing initial vane height. These findings suggest that the primary vortex leaves from the surface of the suction side at a distance from the leading edge, which decreases with increasing angle of attack and increases with decreasing initial vane height.
- The strength of the primary vortex increases with increasing angle of attack. Both induced velocity components and core diameter enlarge with increasing angle of attack. As the vortex travels downstream, its strength decays and the depression of the streamwise velocities becomes less pronounced.
- The core of the primary vortex appears to have a more ellipsoidal shape for vanes at relatively low initial vane height, probably as a result of boundary effects. The presence of the free surface may affect the shape of the core for vanes protruding high above the bed.
- Experimental results show that as the vortex travels downstream, the vortex filament tends to centre at mid-depth, thus confirming observations for low ratios of vane height to flow depth reported by Wang [53]. Noteworthy, results also indicate that the effect of the primary vortex on transverse transport of bed material for vanes at high ratio of vane height to flow depth is highest at some distance downstream of the vane as the vortex filament relocates toward mid-depth and near bed transverse induced velocities gradually increase with distance downstream of the vane.

- Vortex motion is seen to bring about modifications of the velocity distribution. Outside of the core of the primary vortex, where the vertical velocity component is directed toward the bed, the higher velocities are brought down toward the bed due to the induced vertical velocities, resulting in higher local streamwise bed shear stresses than in the flow field where the vertical velocity component is directed toward the free surface. The effect of re-distribution of the higher velocities toward the bed by vortex motion enlarges with increasing angle of attack as submerged vanes at the higher ranges of angle of attack induce larger vertical velocity components.
- Measurements indicate that, at an angle of attack of 20°, vane effectiveness in terms of induced near bed transverse velocity component is distinctly poor if the ratio of vane height to flow depth is restricted to 0.2. At an angle of attack of 30°, on the other hand, single vanes appear to be quite effective, even at low ratios of vane height to flow depth.
- For the tested vanes at an angle of attack of 30° and 40°, the presence of a horseshoe vortex is identified. Marelius and Sinha already reported the presence of a horseshoe vortex for a single vane at an angle of attack of 40° [30], but results of the current research suggest that such a vortex is also generated at angles of attack as low as 30°. Adopting nomenclature by Marelius and Sinha, the presence of the weaker suction vortex and the vortex leg leaving from the leading edge have not been found, probably due to the use of inferior instruments and a less detailed measuring project. However, the experimental results confirm the presence of the counter rotating (compared to the sense of direction of the primary vortex) horseshoe vortex leg leaving from the trailing edge, the strength of which increases with increasing angle of attack. In conformance with observations by Marelius and Sinha [30], measurements suggest that the horseshoe vortex leg leaving from the trailing edge decays within about twice the vane length downstream of the midst of the vane.
- Despite enlarged risks of probe-induced disturbances to the flow, valuable information about the generation of the primary vortex may be obtained from measurements of the velocity components in planes parallel to the pressure and suction sides of the vane. It is observed that the directions of measured velocity vectors in the plane parallel to the pressure side qualitatively correspond to directions of strings attached to the vane as presented by Marelius and Sinha [30]. Near the top edges of the tested vanes, the flow is directed upward, while the flow is largely directed toward the bed over the most portion of the exposed surface. In the plane parallel to the suction side, measured velocity vectors at elevation of the top edge of the vane consistently have downward directions near the leading edge, while at greater distance from the leading edge the flow is directed toward the free surface. These findings indicate that the leading edge plays an important role in the generation of the primary vortex. Regions of stagnated and even reversed flow exist below the top elevation of the vane near the leading edge for vanes at the higher angles of attack (30° and 40°). A smoother type of flow is observed for vanes at the lower angles of attack (10° and 20°). It appears that there is a more or less adhering near bed flow along the suction side for vanes protruding relatively high above the bed and for vanes at the higher angles of attack.

Experimental results of the current research do not support the description of the flow past submerged vanes as presumed in favour of the theory of Odgaard, in which the vortex sheet (resulting from an upward velocity component along the pressure side and a downward velocity component along the suction side) at the trailing edge rolls up to form a large vortex springing from a position near the top of the vane (tip vortex). The hypothesis that the theory of Odgaard does not account for the physics of the flow about submerged vanes adequately seems well founded:

- The theory of Odgaard is developed for non-separated flow past vanes, where the strength of the circulation about the vane is calculated by assuming that the rear stagnation point is shifted to the trailing edge. The Kutta condition implies that there can be no velocity discontinuity at the trailing edge. Results of the current research demonstrate that the assumption that the circulation about the vane is established by the Kutta condition cannot be expected to hold for angles of attack higher than about 10°. In reality, significant flow separation occurs for vanes at conventional and higher angles of attack.
- The centre of the core of the primary vortex in the cross-section near the trailing edge is not at Y_{TE}, but rather the centre of the core is situated at about the centreline, shifting

slightly toward Y_{LE} with increasing angle of attack and to a lesser extent with increasing initial vane height and shifting slightly toward Y_{TE} with decreasing initial vane height (for given dimensions and orientation of the tested vanes; vane length: 0.40 m). The findings suggest that the primary vortex leaves from the surface of the suction side at a distance from the leading edge, which decreases with increasing angle of attack and increases with decreasing initial vane height.

- In tests with a deformable bed, Marelius and Sinha found that the strength of the primary vortex at a downstream cross-section is a maximum at about 40° (vane length: 0.24 m; initial vane height: 0.12 m; flow depth: 0.40 m) [30]. The model underlying the theory of Odgaard, the classical lifting line theory for finite wings by Prandtl, is appropriate for wings at moderate to high aspect ratio, which generally stall at an angle of attack of 20° to 25°. Apparently, the lift force exerted on a submerged vane increases for ranges of angle of attack of up to 40°.
- Force measurements conducted at WL | Delft Hydraulics [11; 24] show that the theory of Odgaard fails to predict the lift and drag forces exerted on a vane at an angle of attack of 17.5° (for varying vane lengths and vane heights) satisfactorily. Because force measuring provides an excellent means to test the validity of the theoretical description of the flow past submerged vanes, support is found for the hypothesis that the theory of Odgaard does not account for the physics of the flow adequately.
- Measurements of the velocity components in planes parallel to the suction side suggest that the leading edge plays an important role in the generation of the primary vortex, seemingly similar to the effect of the leading edge on the physics of the flow about low aspect ratio rectangular wings.

8.2.2 Non-linear models based on theories by Bollay and Gersten

The main shortcoming of the theory of Odgaard with regard to the mean lift and drag forces is that the classical lifting line theory by Prandtl is inappropriate for wings (and submerged vanes) at low aspect ratio. In Section 5.3, non-linear models are described for prediction of the mean lift and drag forces exerted on a sharp-edged slender vane protruding above a rigid bed. The models are based on theories for low aspect ratio wings developed by Bollay and Gersten. The mathematical models by Bollay and Gersten assume pre-determined shape and position of the separated vortex flow over the lifting surface in the vortex wake, the latter of which is modelled as a wake composed of straight line vortices inclined at an angle with respect to the lifting surface (Figure 8.2). The validity of the non-linear models is tested by comparison with experiment, using available results of measurements of the lift and drag forces on vanes protruding above rigid beds (measurements OS1986 [30], OS1989 [38], WL1998 [11] and WL2001 [24]):

- Lift coefficients calculated with the non-linear models are seen to agree reasonably to good with experimental results at low and higher ranges of angle of attack, particularly with measurements WL1998 and WL2001 and to a lesser extent with measurements OS1986. A comparison with measurements OS1989 at the higher angles of attack shows a poor agreement between measured and calculated lift coefficients. Possibly, given the relatively low vane height of the tested vane, the discrepancies may be partly explained by disturbances to the primary vortex caused by the presence of the bed. The remaining part must be attributed to measuring inaccuracies, differences between experimental equipment and procedures, and corrections to data for shear forces exerted on the vane mount and zero-shifts.
- Induced drag coefficients calculated with the non-linear models agree well with measured drag coefficients for measurements WL1998 and WL2001, and for measurements OS1986 and OS1989 at low angles of attack. Note that the non-linear models account for induced drag only; profile drag has to be added to obtain total drag.
- Measurements OS1986 and OS1989 show relatively low measured drag coefficients. As a result, the measurements suggest high vane efficiency in terms of lift to drag. Results of experiments conducted at WL | Delft Hydraulics, however, indicate that the curvature of polars (lift versus drag) approximately corresponds to the expected non-linear behaviour of the lift and drag forces exerted on a sharp-edged, slender vane: the primary vortex influences the pressure distribution on the suction side and gives rise to a substantial non-linear lift contribution that partially compensates for the additional drag due to the loss of the leading edge suction force.

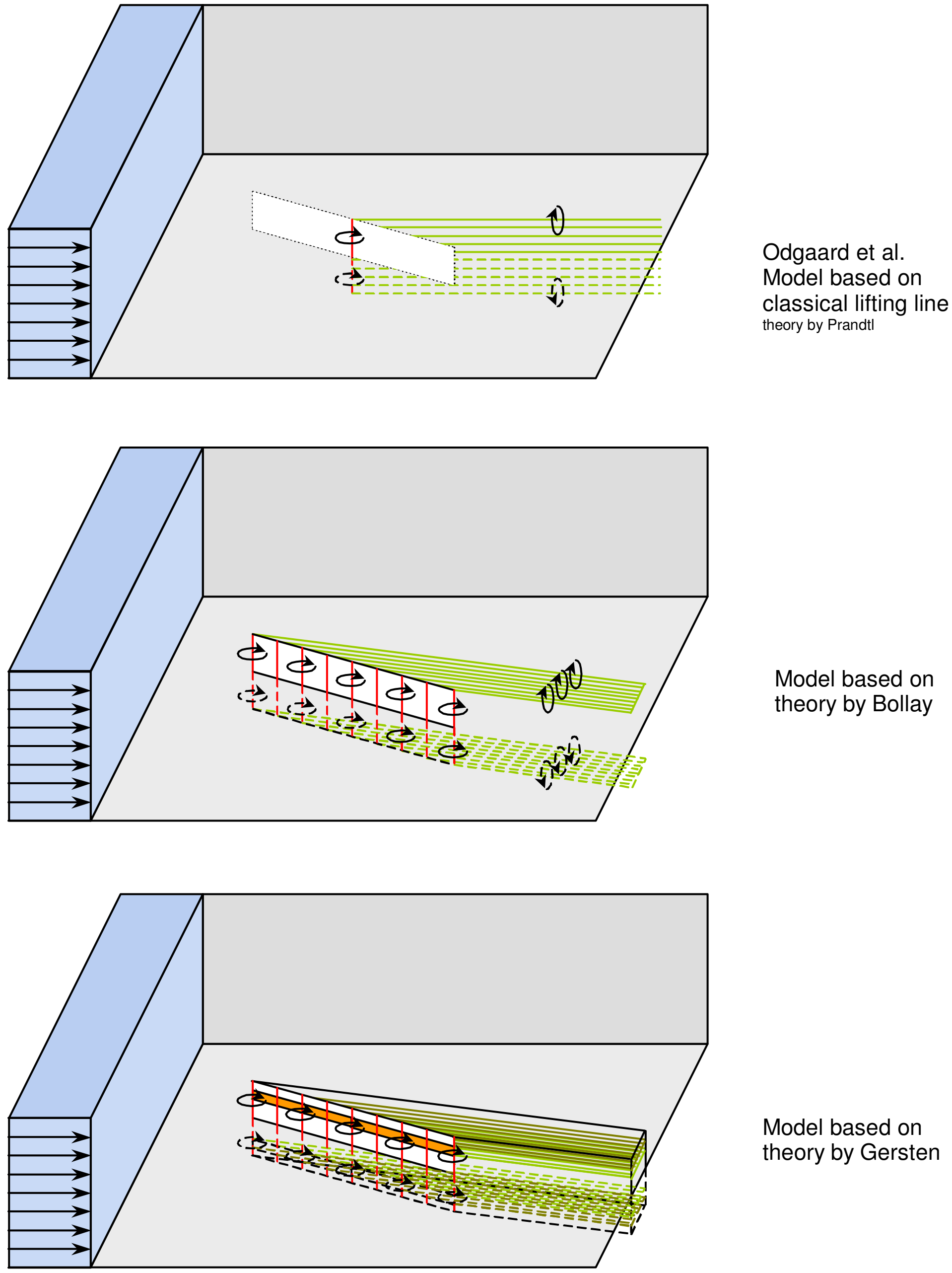

Figure 8.2: Mathematical models based on theory by Prandtl (Odgaard et al.), Bollay and Gersten

Use of the model model based on theory by Bollay is advised for ratios of vane height to vane length lower than about 0.1. At higher ratios of vane height to vane length, the model based on theory by Gersten gives more accurate results. Because the assumption that a single reflection of the bound and trailing vorticity in the plane of the bed by the method of images is sufficient to account for boundary interference effects breaks down with increasing ratio of vane height to flow depth, the ratio of vane height to flow depth should not be all too high. At present, the upper limit of the validity ranges of both models is confined to an angle of attack of about 20° due to the lack of experimental results for the higher ranges of angle of attack. The model based on theory by Gersten is seen to hold approximately for ratios of vane height to flow depth up to at least 0.6

Because the flow on the suction side is mostly separated at practical ranges of angle of attack and flow separation is fixed along the sharp leading and top edge, it is assessed that the mean lift and drag forces exerted on thin, flat vanes do not depend strongly on Reynolds chord number and regular levels of free stream turbulence. Submerged vanes at yaw angle may induce inboard secondary and/or tertiary separation. The pressure side of a submerged vane is essentially a stream surface. The suction side, on the contrary, is predominately covered with vortex layers and is therefore subject to a non-uniform and time-varying pressure distribution. Based on results of surface pressure measurements for low aspect ratio wings by Wickens [54] and Winter [55], it is foreseen that the hydrodynamic load on a slender sharp-edged submerged vanes includes large pressure peaks in regions near the leading edge and near the top edge next to the core of the primary vortex and that intense pressure fluctuations occur in these regions. At the higher angles of attack, the presence of strongly developed horseshoe vortices may give rise to an expansion of the regions at which pressure fluctuations are augmented.

8.2.3 Analyses of local scour measurements

- Scour development commences near the leading edge of the submerged vane. Soon after commencement of scouring, a relatively shallow scour pattern is formed around the leading edge of the vane, taking the shape of a spherical shell with increasing radius. As a result of flow separation at the upstream rim of the scour hole excavated by the downflow, a horseshoe vortex develops. Particularly for vanes at angles of attack of 30° and higher, it is observed that the strength of the horseshoe vortex leg along the pressure side of the vane is such that the vortex becomes effective in transporting material away from the scour hole. The eroded material is then transported downstream by the combined action of accelerated flow and the spiral motion of the horseshoe vortex leg along the pressure side of the vane. At a distance of twice the vane length downstream of the midst of the vane, the horseshoe vortex leg leaving from the trailing edge loses its identity and converts into general turbulence.
- The local scour depth is seen to depend strongly on the alignment to flow. Hence, the scour depth is a function of the projected width of the submerged vane (width normal to the flow). With increasing angle of attack, the location of maximum scour moves along the exposed pressure side of the vane towards the trailing edge. For the tested vanes, the scour depth at the rear ultimately exceeded the scour depth at the front for angles of attack of 30° and higher. In general, the upstream part of the scour hole stabilizes first. At the midst of the vane and at the trailing edge along the pressure side, scouring takes place in the later stages of scour development.
- At an angle of attack of 20°, the maximum scour depth is seen to increase with increasing initial vane height. Strikingly, an increase in the ratio of vane height to flow depth from 0.4 to 0.6 resulted in an increase in local scour depth that is disproportionate to the increase in scour depth for an increase of the ratio from 0.2 to 0.4. Apparently, as velocity measurements do not indicate the presence of a strongly developed horseshoe vortex leg leaving from the trailing edge at a ratio of vane height to flow depth of 0.6, the observed increase in scour depth must be attributed to a disproportionate increase in downflow.
- At a ratio of vane height to flow depth of 0.4, the scour depths for angles of attack of 10° and 20° are seen to differ only marginally. However, for angles of attack of 30° and 40°, strong increases in scour depth are observed, demonstrating clearly the capacity of a strongly developed horseshoe vortex to transport bed material downstream.
- The result for the tested vane at an angle of attack of 40° agrees well with the equilibrium scour depth as found by Marelius and Sinha [30], which supports the hypothesis that the equilibrium scour depth is a function of angle of attack and of initial vane height mainly. The comparison seems to indicate that vane length plays a less dominant role with regard to scour and although the current experiments were not designed to test the effect of vane length on local scour, the expectancy is proclaimed that the effect of vane length on local scour is considerably subordinate to the effects of angle of attack and initial vane height.
- Results for angles of attack of 30° and 40° suggest that the assumption by Hoffmans and Verheij [19] that submerged vanes cause less scour than bridge piers and that a reduction factor may be applied to the calculated scour depth using relations for scour at slender bridge piers does not hold for vanes at the higher ranges of angle of attack.

The use of scour relations for slender bridge piers to predict equilibrium scour depths for submerged vanes, as proposed by Hoffmans and Verheij [19], is evaluated using maximum scour depths obtained from bed level measurements as estimates of the equilibrium scour depths (a state of equilibrium scour has not been reached for all experiments). In general, the agreement between calculated and measured scour depth is rather unsatisfactory. For given test conditions, the CSU method is seen to predict the equilibrium scour depths better than the relation for scour at slender bridge piers according to Breusers et al.

The use of scour relations for slender bridge piers aligned to the flow to calculate equilibrium scour depths for submerged vanes is not readily acceptable:

- The extreme values of the ratio of length to thickness for submerged vanes do not relate to values for slender bridge piers. It can be anticipated that, at relatively low angles of attack, the extent of flow separation in front of the structure is larger for (slender) bridge piers than for submerged vanes. At the higher ranges of angle of attack, the agreement between flows along the exposed sides of bridge piers and submerged vanes improves. For angles of attack higher than about 30°, the presence of strongly developed horseshoe vortices can be observed for both bridge piers and submerged vanes. With increasing angle of attack, the effect of pier width on scour diminishes and scour depth becomes a function of the projected width (width of the structure normal to the flow) mainly. Hence, it can be expected that scour relations for slender bridge piers aligned to the flow give more accurate predictions of the equilibrium scour depths for submerged vanes at the higher ranges of angle of attack than at the lower ranges of angle of attack.
- In contrast to submerged vanes, bridge piers cause surface rollers, which become more dominant with decreasing flow depth and weaken the downflow. On the other hand, for vanes at low angles of attack, the upward flow near the top edge along the pressure side may cover a relatively large portion of the exposed surface and hence, application of a reduction factor seems justified (supporting the proposal by Hoffmans and Verheij [19], although possibly on different grounds).
- Scour relations for slender bridge piers do not account for submergence, whereas results of the current research indicate that the scour hole dimensions depend on the initial vane height (at least for low angles of attack).

8.2.4 Vane shape, dimensions and orientation

The performance of a system of vanes that intends to meet the design objectives in terms of induced bed shear stresses by the generation of a secondary circulation in the downstream flow field can be evaluated by the capability to induce strong and stable primary vortices at design stage. By approximation, the results of analyses of the physics of the flow past submerged vanes and the non-linear models for prediction of the mean lift and drag forces may be used to proclaim expectancies with regard to the effectiveness of a system of equally sized and equally angled vanes in the field.

Because submerged vanes aim to generate a secondary circulation, preferably at a minimum of flow resistance, and because the strength of primary vortices is related to the lift force, vane efficiency can be expressed in terms of ratio of lift to drag. However, it is assessed that the effect of trailing vorticity associated with linear lift is negligible. Non-linear lift (or vortex lift) is an enhanced measure of the strength of the vane-induced circulation and vane efficiency is expressed more correctly in terms of non-linear lift to drag. Due to profile drag, deficiencies associated with structural width and form of leading and top edges, and vane interaction, vane efficiency will generally be lower than predicted by the non-linear models.

Angle of attack

According to the model based on theory by Gersten, the ratio of non-linear lift to drag decreases with increasing angle of attack and increasing ratio of vane height to vane length. Theoretically, vortex lift and thus, the strength of the primary vortex increases non-linearly with increasing angle of attack, however, accompanied with enlarged flow resistance. Unacceptable flow resistance and scour depths will generally confine the upper limit to the angle of attack. The lower limit to the angle of attack may be defined by effectiveness of individual vanes and initial vane height. Measures ought to be taken to ensure that the angle of incidence remains constant and to prevent adverse flanking in meandering rivers [39]. Continuously evolving flow field and topographical features may result in vanes at different ranges of angle of attack than originally intended [30].

Initial vane height and vane length

With decreasing ratio of vane height to vane length, tip flow predominates the flow on the suction side more and more and an increase in diameter of the rolled up primary vortex can be observed. However, for vanes protruding relatively low above the bed, only a small 'vortex cushion' can be built up. It appears that the presence of a layer of more or less adhering flow underneath the regions of depressed streamwise velocity component is beneficial to the development of the primary vortex. Such layers of mainly adhering flow accompanied with flow separation occur for vanes protruding sufficiently high above the bed (from experiment: at angles of attack up to 20°, ratios of flow depth to vane height lower than about 3 to 4) and for vanes at the higher angles of attack emplaced in deformable beds. If, for practical reasons, the initial vane height is bound to a relatively low maximum, it is advised to consider applying a higher angle of attack, as experimental results for vanes at low initial vane height demonstrate that the conditions for the development of the primary vortex improve at the higher ranges of angle of attack due to bed level changes along the suction side caused by the combined effects of the horseshoe vortex and the primary vortex. In case of relatively long vanes, the diameter of the core of the primary vortex can hypothetically augment up to a degree, where apparently no more fluid can be rolled up and the after parts of the rolled up primary vortex become unstable, eventually resulting in the breaking off of the primary vortex. Hence, there are upper and lower limits to initial vane height and vane length. Odgaard and Spoljaric suggested that the ratio of vane height to vane length should be in the range from 0.1 to 0.5 [37]. It is stated that the given range is adequate, be it that the theoretical non-linear lift contribution at ratios of vane height to vane length of the order of 0.5 is clearly more inefficient.

Form of leading and top edges

Because non-linear effects are due to flow separation and generation of trailing vortices at the leading and top edges, the non-linear lift contribution is larger for sharp-edged vanes than for vanes with rounded edges. Rounding of the top edge probably brings about a small detrimental effect on the non-linear lift. An increase of the distance between pressure and suction side results in a decrease in tip flow and hence, a decrease in non-linear effects. Submerged vanes should preferably be equipped with sharp leading and top edges and the structural width should be reduced to a minimum.

Vane shape

Cambering and twist probably do not improve the lift characteristics of vanes. The effect of camber is to bring about a 'smoother' type of flow over a larger portion of the suction side. For a predominantly more or less adhering flow, however, the formation of vortices is reduced. Furthermore, relative to thin, flat vanes, the distance between pressure and suction side is increased by the profile thickness. Compared to thin, flat-plates, sheet-wall vanes generate less lift and distinctly more drag. The relative increase in drag for sheet-wall vanes may be explained largely by an increase in profile drag. The conclusion cannot be drawn that sheet-wall vanes generate much weaker primary vortices. Especially for sheet-wall vanes protruding not too low above the bed, measured lift forces agree reasonably with measured lift forces on thin, flat vanes of equal dimensions (measurements WL2001 [24]). Like thin, flat-plates, sheet-wall vanes are equipped with sharp leading and top edges, so that the location of flow separation is fixed. Hence, in principle, slender sheet-wall vanes comply with key ingredients to the generation of strong primary vortices. However, as a consequence of the relative increase in drag, the efficiency of a sheet-wall vane is clearly poorer.

It is recognized that vanes require structural width, which may increase with increasing angle of attack as a result of enlarged load and scour depths. Consequently, vane efficiency is lower than predicted by the non-linear models based on theories by Bollay and Gersten. Therefore, the application of arrays of vanes at conventional angles of attack may not always lead to adequate and satisfying results. The detrimental effects of structural width on tip flow can be compensated for by selecting a higher angle of attack.

8.3 RECOMMENDATIONS

The limited number of measurements of the lift and drag forces exerted on submerged vanes imposes restrictions to the drawing of conclusions. It is recommended to conduct additional force measurements for thin, flat vanes and to use the results to verify findings with regard to the mean lift and drag forces presented in this report. Preferably, measuring projects should include force measurements at high angles of attack up to 50°. With the aid of experimental force data for vanes at high angles of attack, the validity ranges of the non-linear models based on theories by Bollay and Gersten can be defined. At present, the upper limit of the validity ranges is confined to an angle of attack of about 20°. Special attention should be paid to the effect of horseshoe vortices on measured forces. If a strongly developed horseshoe vortex is present in the near vane flow field, measured transverse forces cannot be justifiably treated as equivalent to the lift forces exerted on the tested vanes.

Based on analyses of the experimental results, the author supports views by Marelius and Sinha [30] and feels that future experiments should concentrate on vanes at the higher ranges of angle of attack, despite enlarged scour holes, increased resistance to flow and the presence of additional vortical structures. At present, the extent to which the horseshoe vortex and possibly other vortices are counterproductive forces within the system governing the transverse transport of sediment has not been fully explored. Experimentally, it has been shown that these vortices decay downstream within a few vane lengths, while the primary vortex dominates over a much longer distance downstream of the vane. In case of a vane array, the strength of the horseshoe vortices in a state of equilibrium may be less than the strength of the horseshoe vortex for a single vane as the scour holes of neighbouring vanes may overlap. It is stressed that the suitability of scour holes to aid the intended purpose must not be ignored. To a certain degree, the presence of the scour hole leads to vortex stretching in transverse direction, thus increasing the effective width of each vane. It can be anticipated that for a system of vanes at high angles of attack both the transverse and longitudinal vane spacing may be enlarged. Hence, a smaller number of vanes may be sufficient to meet design objectives in terms of induced bed shear stresses than in the case that the vanes are laid out at conventional angles of attack. Furthermore, because of practical restrictions to minimum structural width and initial vane height, arrays of vanes at conventional angles of attack may not always lead to adequate and satisfying results. Finally, the effect of a vane system on induced change in energy slope is still uncertain and calls for further investigation. Existing relations need revision and improved relations are required to evaluate the effect of vane systems on flow resistance.

In order to suppress flow separation from the leading edge, the application of a small nose flap can be considered. The suitability of a nose flap to reduce pressure fluctuations and induced drag for submerged vanes has not been investigated as of yet, but may be an interesting research objective for future experiments.

At present, the limited number of available experimental results for scour at submerged vanes does not allow for the development of alternative scour relations. However, experimentation in the framework of the BUET-DUT linkage project has been continued at BUET after Zijlstra and Van Zwol ended their stay in Dhaka, Bangladesh, and is currently still ongoing. It is highly recommended to collect the experimental data of these scour tests and to re-evaluate the use of scour relations for slender bridge piers to predict the equilibrium scour depths at vanes.

An explanation for the reasonable agreement between measured and calculated induced velocity components as observed in Section 4.5, is that, at low angles of attack, the non-linear lift coefficient is approximately of the order of the lift coefficient calculated with the theoretical relations by Odgaard et al. Efforts should be undertaken to investigate whether the theory of Odgaard can be improved by implementation of the relations for lift and drag given by the model based on theory by Gersten, by which the strength of the circulation is related to the non-linear lift coefficient.

REFERENCES

[1] Anderson, J.D., 1991, *Fundamentals of aerodynamics*, Second edition.

[2] Blenk, H., 1925, Zeitschrift für Angewandte Mathematik und Mechanik, Vol. 5, pp. 36 (in German).

[3] Bollay, W., 1937, *A theory for rectangular wings of small aspect ratio*, Journal of Aeronautical Sciences, Vol. 4, pp. 294-296.

[4] Bollay, W., 1939, *A non-linear wing theory and its application to rectangular wings of small aspect ratio*, Zeitschrift Angew. Math. Mech., Vol. 19, pp. 21-35.

[5] Breusers, H.N.C., A.J. Raudkivi, 1991, *Scouring*, IAHR, Hydraulic design considerations, ISBN 90-6191-983-5.

[6] Breusers, H.N.C., G. Nicolet, H.W. Shen, 1977, *Local scour around cylindrical piers*, Journal of Hydraulic Research, IAHR, Vol. 15, pp. 211-252.

[7] BUET/Delft Cluster, 2001, *Capacity Building in the field of water resources engineering and management in Bangladesh*, Inception report.

[8] BUET-DUT, 2001, *Review report on bottom vanes*, (not published).

[9] Davey, A., 1961, *Boundary layer flow at a saddle point of attachment*, Journal of Fluid Mechanics, Vol. 10, pp. 593-610.

[10] Ermelenko, S.D., M.T. Barinov, 1966, *Calculation of the stream deflection angles behind rectangular wings of small aspect ratio at subsonic speed using non-linear theory*, Reports of the Higher Educational Institutes, No. 3, pp. 3-10 (in Russian).

[11] Flokstra, C., F. de Groot, N. Struiksma, 1998a, *Optimalisatie lengte bodemschermen; Deel 1: Krachtmetingen*, WL | Delft Hydraulics, Report Q2418 (in Dutch).

[12] Flokstra, C., F. de Groot, N. Struiksma, 1998b, *Optimalisatie lengte bodemschermen; Deel 2: Stroomsnelheidsmetingen*, WL | Delft Hydraulics, Report Q2418 (in Dutch).

[13] Froehlich, D.C., 1988, *Analysis of on site measurements of scour at piers*, Proceedings ASCE, National hydraulic engineering conference, Colorada Springs, Colorado.

[14] Fukuoka, S., A. Wattanabe, 1989, *New bank protection methods against erosion in the river*, Proceedings of the Japan-China joint seminar on Natural Hazard Mittigation, Kyoto, Japan, pp. 439-448.

[15] Garner, H.C., D.E. Lehrian, 1963, *Non-linear theory of steady forces on wings with leading-edge flow separation*, A.R.C R&M, No. 3375.

[16] Gersten, K., 1961, *Nichtlineare Tragflächentheorie insbesondere für Tragflügel mit kleinem Seitenverhältnis*, Ingenieur Archiv, Vol. 30, pp. 431-452 (in German).

[17] Gersten, K., 1963, *A non-linear lifting surface theory specially for low aspect ratio wings*, AIAA Journal, Vol. 1, No. 4, pp. 924-925.

[18] Glauert, H., 1926, *The elements of airfoil and airscrew theory*, Cambridge University Press, London.

[19] Hoffmans, G.J.C.M., H.J. Verheij, 1997, *Scour manual*, ISBN 90-5410-673-5.

[20] Hossain, M.M., J.J.P. Lambeek, BUET-DUT, 2002, *Research proposal* (not published).

[21] Ikeda, S., T. Nishimura, 1985, *Bed topography in bends of sand-silt rivers*, Journal of Hydraulic Engineering, ASCE, Vol. 111, No. 11.

[22] Jansen, P.Ph., L. van Bendegom, J. van den Berg, M. de Vries, A. Zanen, 1979, *Principles of river engineering; The non-tidal alluvial river*, Pitman, London.

[23] Johnson, P.A., 1992, Reliability-based pier scour engineering, Journal of Hydraulic Engineering, ASCE, Vol. 118, pp. 1344-1358.

[24] Jongeling, T.H.G., C. Flokstra, 2001, *Bodemschermen: Stromingskrachten en snelheidsveld bij variatie van de schermhoogte*, Delft Cluster Report (in Dutch).

[25] Kuethe, A.M., C.-Y. Chow, 1986, *Foundations of aerodynamics, Bases of aerodynamic design*, Fourth edition.

[26] Laursen, E.M., A. Toch, 1956, *Scour around bridge piers and abutments*, Bulletin 4, Iowa Highway Research Board, State University of Iowa.

[27] Legendre, R., 1965, *Lignes de courant d'un écoulement continu*, Rech. Aérosp., No. 105, pp. 3-9 (in French).

[28] Lighthill, M.J., 1963, *Attachment and separation in three-dimensional flow*, in: Laminar boundary layers, Section II 2.6, L. Rosenhead (ed.), 1963, pp. 72-82.

[29] Marelius, F., 2001, *Experimental investigation of submerged vanes as means of beach protection*, Coastal Engineering, 42 1-16.

[30] Marelius, F., S.K. Sinha, 1998, *Experimental investigations on flow past submerged vanes*, Journal of Hydraulic Engineering, Vol.124, No. 5.

[31] Multhopp, H., 1938, *Die Berechnung der Auftriebsverteilung von Tragflügeln*, Luftfahrt-forschung 15, S.153 (in German).
[32] Multhopp, H., 1950, *Methods for calculating the lift distribution of wings (Subsonic lifting surface theory)*, A.R.C. R&M, No. 2884.
[33] Nakagawa, H., K. Suzuki, 1976, *Local scour around bridge pier in tidal current*, Coastal Engineering in Japan, Vol. 19, pp. 89-100.
[34] Naudascher, E., 1991, *Hydrodynamic forces*, IAHR, Hydraulic structures design manual, Hydraulic design considerations, ISBN 90-6191-993-2.
[35] Odgaard A.J., A. Spoljaric, 1986, *Lift and drag on small-aspect ratio foils*, Proceedings of the ASCE Specialty Conference on Advancements in Aerodynamics, Fluid Mechanics and Hydraulics, University of Minnesota, Minneapolis, June 3-6, 1986.
[36] Odgaard, A.J., 1989, *River-meander model, I: Development*, Journal of Hydraulic Engineering, ASCE, Vol. 115, No. 11.
[37] Odgaard, A.J., A. Spoljaric, 1986, *Sediment control by submerged vanes*, Journal of Hydraulic Engineering, Vol. 112, No. 12.
[38] Odgaard, A.J., A. Spoljaric, 1989, *Sediment control by submerged vanes; Design basis*, in: Ikeda, S., G. Parker, River meandering, Water Resources Monograph 12, 1989, American Geophysical Union.
[39] Odgaard, A.J., C.E. Mosconi, 1987, *Streambank protection by submerged vanes*, Journal of Hydraulic Engineering, ACSE, Vol. 113, No. 4, pp. 520-536.
[40] Odgaard, A.J., R.J. DeWitt, 1989, *Sediment control by submerged vanes*, Proceedings of the twentieth annual conference of the International Erosion Control Association, Vancouver, Canada.
[41] Odgaard, A.J., Y. Wang, 1991, *Sediment management with submerged vanes*, I: Theory, Journal of Hydraulic Engineering, ACSE, Vol. 117, No. 3, pp. 267-283.
[42] Odgaard, A.J., Y. Wang, 1991, *Sediment management with submerged vanes, II: Applications*, Journal of Hydraulic Engineering, ACSE, Vol. 117, No. 3, pp. 284-302.
[43] Peake, D.J., M. Tobak, 1967, *Three-dimensional interactions and vortical flows with emphasis on high speeds*, NATO, AGARD, AGARD-AG-252.
[44] Pelletier, A., T.J. Mueller, 2000, *Low Reynolds number aerodynamics of low aspect ratio thin/flat/cambered-plate wings*, Journal of Aircraft, Vol. 37, No. 5, pp. 825-832.
[45] Rom, J., 1991, *High angle of attack aerodynamics: subsonic, transonic and supersonic flows*, ISBN 0-387-97672-8.
[46] Rom. J., C. Zorea, R. Gordon, 1974, *On the calculation of non-linear aerodynamic characteristics and the near vortex wake*, ICAS paper 74-27.
[47] Rozovskii, I.L., 1957, *Flow of water in bends of open channels*, Academy of Sciences of the Ukrainian SSR, Kiev, Soviet Union (in Russian) (Israel Program for Scientific Translation, 1961, Jerusalem, Israel, translated to English).
[48] Sinha, S.K., F. Marelius, 2000, *Analysis of flow past submerged vanes*, Journal of Hydraulic Research, IAHR, Vol. 38, No. 1, pp. 65-71.
[49] Truckenbrodt, E., 1953, *Tragflächentheorie bei inkompressibler Strömung*, Wissen. Gesell. Lüftfahrt-Jahrbuch, pp. 40-65 (in German).
[50] Vriend, H.J. de, 1995, *Bodemschermen in rivierbochten; werking vanuit Newtons perspectief gezien*, Delft University of Technology, The Netherlands (in Dutch).
[51] Wang, Y., 1989, *Bank protection with submerged vanes*, Proceedings twenty-third Congress of International Association for Hydraulic Research, Vol. S, pp. 17-23.
[52] Wang, Y., 1990, *Sediment control with submerged vanes*, Ph.D. thesis, University of Iowa, Iowa.
[53] Wang, Y., A.J. Odgaard, 1993, *Flow control with vorticity*, Journal of Hydraulic Research, IAHR, Vol. 31, No. 4.
[54] Wickens, R.H., 1967, *The vortex wake and aerodynamic load distribution of slender rectangular plates*, Canadian Aeronautics and Space Journal, Vol.13, pp. 247-260.
[55] Winter, H., 1935, *Strömungsvorgänge an Platten und profilierten Körpern bei kleinen Spannweiten*, Forsch. auf dem Gebiete des Ingen.wesens, Vol. 6, pp. 40-50, 67-71 (in German)
[56] Zijlstra, R., 2003, *The morphological effect of bottom vanes, An experimental and a mathematical study*, M.Sc. thesis, Delft University of Technology, The Netherlands.
[57] Zijlstra, R., J.A. van Zwol, 2003, Measuring report, Experimental study of submerged vanes in the outdoor facility at BUET, Delft University of Technology, The Netherlands.